université PARIS-SACLAY

Prototyping of innovative cryogenic detectors for the detection of coherent elastic neutrino-nucleus scattering

Etude et prototypage des détecteurs cryogéniques innovants pour la détection de la diffusion cohérente des neutrinos sur noyaux

Thèse de doctorat de l'université Paris-Saclay

École doctorale n° 576, Particules, Hadrons, Energie, Noyau, Instrumentation, Imagerie, Cosmos et Simulation (PHENIICS)
Spécialité de doctorat: Physique des particules
Graduate School : Physique, Référent : Faculté des sciences d'Orsay

Thèse préparée dans les unités de recherche Département de Physique des Particules (Université Paris-Saclay, CEA), Laboratoire National Henri Becquerel (Université Paris-Saclay, CEA) et IJClab (Université Paris-Saclay, CNRS), sous la direction de Claudia NONES, Chercheuse, CEA-Saclay (DPhP), et le co-encadrement de Martin LOIDL, Directeur de recherche, CEA-Paris Saclay (LNHB)

Thèse soutenue à Paris-Saclay, le 22 Novembre 2022, par

Beatrice MAURI

Composition du jury

Jules GASCON Professeur, IP2I, Université Claude Bernard Lyon 1	Président
Loredana GASTALDO Professeure, Kirchhoff-Institute for Physics, Universität Heidelberg	Rapporteur & Examinatrice
Luca SCOTTO LAVINA Directeur de recherche, LPNHE, Sorbonne Université	Rapporteur & Examinateur
Esther FERRER RIBAS Directrice de recherche, CEA/IRFU/DEDIP, Université Paris-Saclay	Examinatrice
Claudia NONES Chercheuse, CEA/IRFU/DPhP, Université Paris-Saclay	Directrice de thèse

THESE DE DOCTORAT
NNT : 2022UPASP126

université PARIS-SACLAY

ÉCOLE DOCTORALE
Particules, hadrons, énergie et noyau: instrumentation, imagerie, cosmos et simulation (PHENIICS)

Titre: Etude et prototypage des détecteurs cryogéniques innovants pour la détection de la diffusion cohérente des neutrinos sur noyaux

Mots clés: Détecteurs à basse température, Bolomètres, Veto cryogénique, Diffusion cohérente des neutrinos sur les noyaux,

Résumé: La détection de la diffusion cohérente des neutrinos sur les noyaux (CEνNS) représente un défi expérimental en raison de sa signature unique : un recul nucléaire de faible énergie de l'ordre de 10-100 eV en moyenne. Ce processus, largement inexploré jusqu'à aujourd'hui, pourrait sonder la physique au-delà du modèle standard. NUCLEUS est une expérience de neutrino de réacteur nucléaire conçue pour la détection de CEνNS en utilisant un nouveau type de calorimètres cryogéniques à très bas seuil d'énergie (inférieur à 20 eV) basés sur la technologie CRESST. Il sera installé dans le Very Near Site (VNS), un hall expérimental à faible profondeur situé entre les deux réacteurs nucléaires de la centrale de Chooz B en France, avec des distances entre réacteurs de 72 m et 102 m. Par conséquent, un système de suppression du bruit de fond très efficace est fondamental. Dans cette thèse, le prototype du veto externe cryogénique de NUCLEUS et les essais correspondants réalisés à IJClab (Orsay, France) sont présentés afin de valider la technique utilisée pour l'identification et l'élimination des neutrons et des rayons gamma les plus pénétrants constituant la radioactivité de fond. En outre, cette thèse couvre également l'activité BASKET (Bolometers At Sub KeV Energy Threshold), un projet de R&D visant le développement de détecteurs cryogéniques innovants pour la détection de CEνNS. Nous avons couplé différents capteurs thermiques aux cristaux de Li_2WO_4. Dans cette thèse sont rapportés les principaux résultats obtenus jusqu'à présent.

Title: Prototyping of innovative cryogenic detectors for the detection of coherent elastic neutrino-nucleus scattering

Keywords: Low-temperature detectors, Calorimeters, Cryogenic veto, Coherent elastic neutrino-nucleus scattering

Abstract: The detection of Coherent Elastic Neutrino-Nucleus Scattering (CEνNS) represents an experimental challenge because of its unique signature: a low-energy nuclear recoil in the range of 10-100 eV on average. This process, largely unexplored until today, could probe physics beyond the Standard Model. NUCLEUS is a nuclear reactor neutrino experiment conceived for CEνNS detection using a new type of ultra-low energy threshold (below 20 eV) cryogenic calorimeters based on the CRESST technology. It will be installed at the Very Near Site (VNS), a shallow depth experimental hall located in between the 2 nuclear reactors of the Chooz B power plant in France, with reactor baselines of 72 m, and 102 m. Therefore, a highly efficient background suppression system is fundamental. In this thesis, we present the cryogenic outer veto prototype and the corresponding tests carried out at IJClab (Orsay, France) that validated the technique used for the identification and rejection of the most penetrating neutrons and gamma rays constituting background radioactivity. In addition, this thesis also covers the BASKET (Bolometers At Sub KeV Energy Threshold) activity, an R&D project aiming at the development of innovative cryogenic detectors for the CEνNS detection. We coupled different thermal sensors to Li_2WO_4 crystals. In this thesis, we report the main results obtained so far.

Université Paris-Saclay
Espace Technologique / Immeuble Discovery
Route de l'Orme aux Merisiers RD 128 / 91190 Saint-Aubin, France

"There is nothing like looking, if you want to find something.
You certainly usually find something, if you look,
but it is not always quite the something you were after."
J. R. R. Tolkien

Contents

Acknowledgements

It is my pleasure to conclude this journey by thanking the people who have accompanied me during these years.

I would like to begin by thanking all the members of my defense jury: Jules Gascon, Loredana Gastaldo, Luca Scotto Lavina, and Esther Ferrer Ribas for their time and dedication to carefully reading my manuscript. Next, I want to thank Claudia Nones and Martin Loidl, my supervisors, for believing in me offering me the opportunity to work in their research groups, and for pushing me to challenge myself every day allowing me to grow as a researcher and as a person. I will never forget your valuable lessons. A big thank you should also go to Matias Rodrigues, Matthieu Vivier, Edoardo Mazzucato, and Stefanos Marnieros for always being available to help discuss my doubts and provide essential insights.

You are too many to cite one by one, but I would also like to thank the colleagues from IJClab, IRFU, and C2N who have made this journey unique in many ways. In particular, I want to thank Les Becquerels Fusionnés, Les Becquerels Spontanés et Les Becquerels Fissionnés (i.e. LNHB) thank you for welcome me as if I had always been part of your lab and for all the unforgettable moments that I will jealously guard.

Some people come into your life and have such a beautiful impact on it that you can even remember hoe it was without them. I was incredibly lucky to share my Ph.D. journey with my wonderful colleagues and friends Dounia Helis and Arshjot Kaur, very special people that always listened to and cheered me. A heartfelt thanks.

Thanks also to Jack Holguin, Lorna Day, Toby Dixon and Federico Panciera for all the good times spent together at Arkose, Fontainebleau, and La Troche, and the inestimable climbing advices.

Un ringraziamento va anche alle mie amiche storiche, quelle che mi hanno accompagnata in questo viaggio fin dal primissimo giorno di università: Claudia Delogu, Giulia

Marcucci e Stephanie Cancelli. Vi ringrazio per esserci sempre state nonostante la distanza e per tutte le risate che mi avete strappato in questi anni.

Un ringraziamento speciale va a Eleonora Villa, Gianfranco Pecoraro e Michelangelo Al Rajhi, la mia seconda famiglia. Grazie per la costante presenza e per i meravigliosi momenti di convivialità ad ogni mio ritorno in patria.

Qualche parola va anche al mio compagno di cordata, Michele Peresano. Grazie per essere stato sempre al mio fianco e per avere sempre creduto in me. Grazie per numerosi i viaggi fatti solo per poter restare insieme qualche giorno in più. Non ci sono parole per esprime quanto io sia grata ad averti nella mia vita. Non vedo l'ora di scoprire quali altre avventure ci attendo.

Ovviamente, non posso non ringraziare Gemma e Roberto Peresano. Grazie per i vostri consigli e aiuto, per le lezioni di friulano e fornese ma, soprattutto, per avermi accolta come una figlia.

Last but certainly not least, un immenso ringraziamento va ai miei genitori. Con il loro amore incondizionato mi hanno sempre appoggiata in qualsiasi mia decisione, incoraggiandomi a vivere le esperienze che mi hanno reso la persona che sono oggi. Nulla li ripagherà mai di tutti i sacrifici fatti. Questo traguardo è anche il loro.

Un ricordo è certamente dovuto anche ai miei amati nonni che mi hanno sempre incoraggiata a seguire il mio sogno di diventare una ricercatrice, insegnandomi ad infischiarmene di quello che la gente pensa, a lottare sfoderando gli artigli, ed a farmi strada nel mondo a colpi di macete. Avete così tanto atteso questo giorno ma purtroppo eravate troppo di fretta...

I almost forgot! I would also like to thank myself. I am proud of what I have achieved with my own strength and spirit of sacrifice. I am ready and excited to start a new chapter of my scientific career.

Résumé en français

L'étude des processus rares devient de plus en plus cruciale afin d'avoir accès à la physique au-delà du Modèle Standard.

Cette thèse se concentre sur une classe particulière de processus rares : la diffusion cohérente élastique de neutrino sur noyau (CEνNS). La détection de ce processus

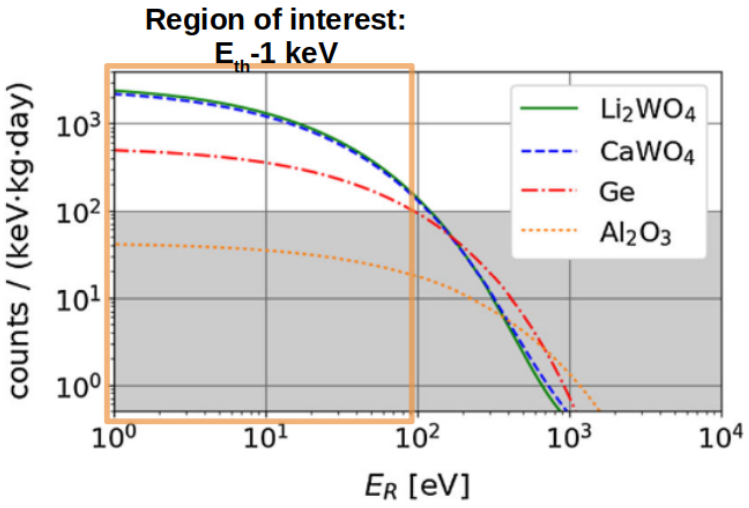

Figure 1: Taux de comptage différentiel CEνNS sur Li_2WO_4 (ligne verte), $CaWO_4$ (ligne bleue), germanium (ligne rouge) et Al_2O_3 (ligne orange pointillée), calculé avec le flux d'anti-neutrinos attendu sur le site expérimental. L'expérience NUCLEUS vise à atteindre un taux de comptage du bruit de fond de 100 coups/(keV kg jour) (bande grise) [1].

représente un défi expérimental en raison de sa signature unique : un recul nucléaire de faible énergie, de l'ordre de 10 à 100 eV en moyenne. Ce processus a été postulé il y a plus de 40 ans par D.Z. Freedman, comme un "act of hubris" en raison des limitations de

la reduction du bruit de fond, du faible taux d'interaction et parce que les technologies conventionnelles de l'époque n'atteignaient que des seuils en énergie de l'ordre du MeV.

Aujourd'hui, grâce à une synergie avec les recherches sur la matière noire, nous avons développé des technologies très sensibles capables d'atteindre un seuil d'énergie de quelques eV. C'est dans ce contexte que s'inscrit NUCLEUS, une expérience de neutrinos de réacteurs qui relève le défi, en développant une nouvelle approche de détection du CEνNS basée sur un dispositif expérimental complet et innovant. Il sera installé dans le Very Near Site (VNS), un hall expérimental à faible profondeur situé entre les deux réacteurs nucléaires de la centrale de Chooz B en France, avec des distances entre réacteurs de 72 m et 102 m. Par conséquent, un système de suppression du bruit de fond très efficace est fondamental. Dans l'expérience NUCLEUS, le niveau de bruit de fond désiré est de 100 coups/(keV kg jour) (figure 1).

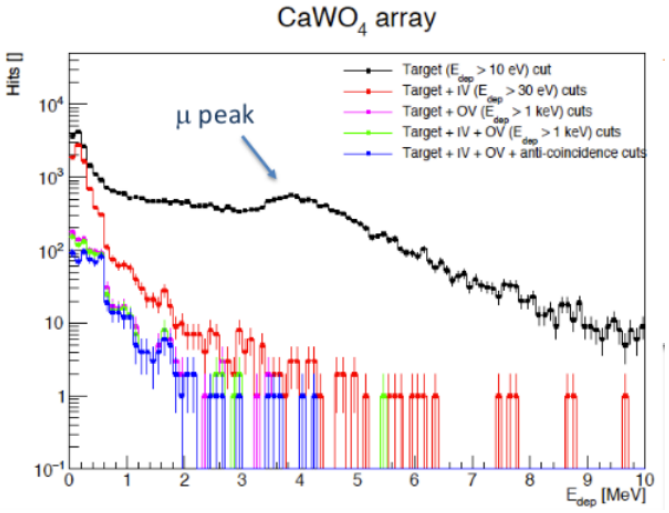

Figure 2: En noir, le spectre d'énergie attendu de la cible. En bleu, le spectre d'énergie de la cible en tenant compte de tous les vétos actifs et du COV travaillant en anti-coïncidence [2].

Aujourd'hui, NUCLEUS a entièrement conçu le dispositif expérimental composé de systèmes complexes de réduction des bruits de fond (vétos et blindages) ainsi que des détecteurs capables d'atteindre un seuil d'énergie de recul nucléaire ultra-faible ($\mathcal{O} \leq$ 10 eV) pour avoir la chance d'observer sans équivoque la signature qui nous intéresse.

Selon les simulations Monte Carlo (figure 2), l'un des systèmes de véto les plus importants de NUCLEUS pour la détection et le rejet efficaces des événements de bruits

Figure 3: Le prototype de véto extérieur cryogénique (COV) conçu et développé pendant mon activité de doctorat.

de fond (principalement dus aux rayonnements gammas les plus pénétrants) est le véto cryogénique externe (COV): il permettra de rejeter les muons atmosphériques à 90% (en tenant compte du système de blindage) et les gammas ambiants à 95% dans la région d'intérêt (0,1-1 keV).

Dans la configuration finale, le COV sera composé de deux cristaux cylindriques et de quatre cristaux de germanium de forme parallélépipédique disposés pour former une boîte, entourant et abritant complètement les détecteurs internes. Afin de travailler en anti-coïncidence avec les détecteurs cibles (c'est-à-dire les cristaux Al_2O_3 et $CaWO_4$ équipés avec des Transition Edge Sensors), le COV doit avoir un temps de réponse au moins aussi rapide que les détecteurs cibles ($\sim$300 μs). Cette exigence peut être satisfaite en utilisant le signal d'ionisation.

Au cours de mon activité de doctorat, j'ai travaillé sur le prototype du COV de NUCLEUS, une version simplifiée du COV final, composé de deux cristaux HPGe. Chaque cristal est équipé d'électrodes en aluminium évaporées sur les surfaces supérieure et inférieure afin de collecter les charges libres produites par les particules en interaction (figure 3). Entre les deux, un cristal de Li_2WO_4 équipé d'un capteur Neutron Transmu-

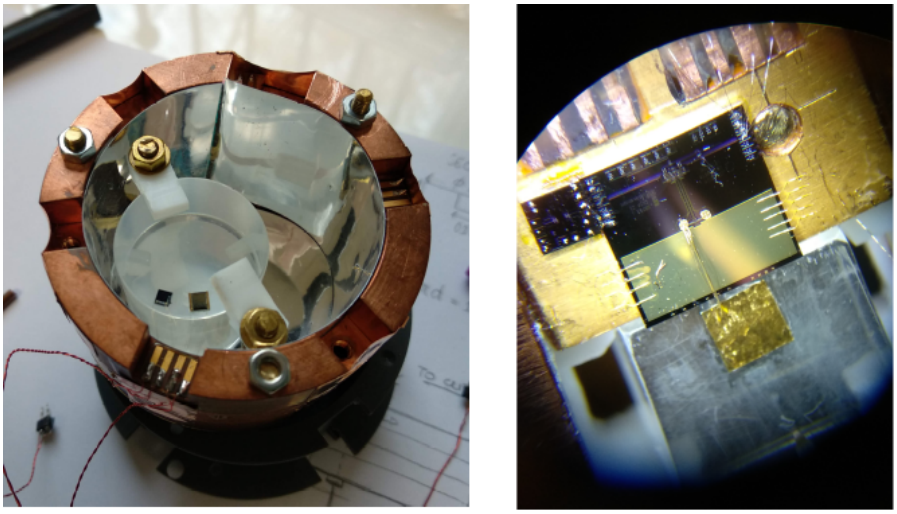

Figure 4: *Gauche*: Exemple de prototype de détecteur BASKET composé d'un cristal cylindrique de Li_2WO_4 équipé d'un capteur Neutron Transmutation Doped (NTD) et d'un chauffage. *Droit*: exemple de prototype de détecteur BASKET composé d'un cristal cubique de Li_2WO_4 connecté à un Calorimètre Magnétique Métallique (MMC)

tation Doped (NTD) a été ajouté entre les deux HPGe afin d'étudier les coïncidences entre ce détecteur cible et le prototype du COV. Afin de vérifier et de valider l'efficacité de ce système de rejet du bruit de fond et de définir les prérequis pour fonctionner dans les meilleures conditions, j'ai effectué plusieurs tests dans différentes conditions au Laboratoire Irène-Joliot Curie (IJCLab, Orsay, France) en utilisant deux réfrigérateurs à dilution sèche équipés de différentes électroniques. Dans le chapitre 5, je rapporte la procédure d'analyse et les résultats obtenus pour valider le principe de fonctionnement du COV pour l'expérience NUCLEUS.

En parallèle des travaux de développement du COV, j'ai également participé durant mon doctorat au développement de détecteurs cryogéniques innovants dans le cadre du projet BASKET (Bolometers At Sub KeV Energy Threshold). Il s'agit d'une R&D démarrée en 2017 dont l'objectif est de développer des détecteurs bolométriques innovants pour la détection de CEνNS en utilisant de nouveaux cristaux scintillants comme matériaux absorbants.. Le principal candidat absorbeur est le tungstate de lithium dopé au molybdène ($Li_2(Mo^{0,05})W_{0,95}O_4$), un composé très prometteur. En effet, en exploitant l'affinité entre W et Mo, des études antérieures sur le composé Li_2MoO_4 ont prouvé

que la teneur naturelle en ^{6}Li (8% dans les cristaux utilisés pour nos prototypes) révèle d'excellentes capacités d'identification des particules permettant le suivi du fond neutronique par la réaction ^{6}Li(n,t)α. De plus, étant donné que la section efficace de CEνNS varie avec le carré du nombre de neutron du noyau cible,la présence de tungstène (N autour de 110) augmente la probabilité d'interactions CEνNS. L'objectif final de BASKET est de développer des détecteurs cryogéniques très sensibles avec un seuil d'énergie ultra-bas de O(10 eV) et un temps de montée de l'ordre de O(100 μs) afin qu'ils puissent être utilisés en surface près d'une centrale nucléaire. Nous avons testé différents capteurs thermiques (Ge NTD et MMC) pour lire le canal chaleur du cristal scintillant. Les configurations et les résultats sont présentés dans le chapitre 6 (BASKET avec NTD) et le chapitre 7 (BASKET avec MMC).

Introduction

The study of rare processes is becoming more and more crucial in order to have access to physics beyond the Standard Model. This thesis focuses on a particular class of rare processes: the Coherent Elastic Neutrino-Nucleus Scattering (CEνNS). The detection of this process represents an experimental challenge because of its unique signature: a low-energy nuclear recoil, of the order of 10 to 100 eV on average. This process was postulated more than 40 years ago by D.Z. Freedman, as an "act of hubris" because of limitations of the background reduction, the interaction rate, and the conventional detection technologies developed up to that time that was characterized by an energy threshold in the MeV range. Today, thanks to the synergy with the research on dark matter, we have developed very sensitive technologies capable of reaching an energy threshold of a few eV. It is in this context that NUCLEUS, a nuclear neutrino reactor experiment, has taken up the challenge by developing a new approach to the detection of CEνNS based on a complete and innovative experimental setup. It will be installed in the Very Near Site (VNS), a shallow experimental hall located between the two nuclear reactors of the Chooz B power plant in France, with distances between reactors of 72 m and 102 m. Therefore, a very efficient background suppression system is fundamental. The estimated target background level in NUCLEUS is 100 counts/(keV kg day). Today, NUCLEUS has fully designed the experimental setup composed of complex veto and shielding systems for background reduction and detectors able to reach an ultra-low nuclear recoil energy threshold ($\mathcal{O} \leq 10$ eV) to have the chance to observe unequivocally the signature of interest. According to Monte Carlo simulations, one of the most important NUCLEUS veto systems for the effective detection and rejection of background events (primarily due to the most penetrating γ radiation) is the cryogenic outer veto (COV): it will allow the rejection of the 90% atmospheric muons (taking into accont the shielding system) and the 95% ambient gammas in the Region of Interest (0.1-1 keV) In

the final configuration, the COV will be composed of two cylindrical crystals and four parallelepiped-shaped germanium crystals arranged to form a box, completely surrounding and housing the internal detectors. In order to work in anti-coincidence with the target detectors (i.e. Al_2O_3 and $CaWO_4$ crystals equipped with Transition Edge Sensors), the COV must be characterized by a response time at least as fast as the target detectors ($\sim$300 μs). This requirement can be met by using the ionization signal.

During my Ph.D. activity, I worked on the NUCLEUS COV prototype, a simplified version of the final COV, composed of two HPGe crystals, each of them equipped with aluminum electrodes evaporated onto the top and bottom surfaces to collect the free charges produced by the interacting particles. In between the two, a Li_2WO_4 crystal equipped with a Neutron Transmutation Doped (NTD) sensor was added between the HPGe in order to study the coincidences between the target detector and the COV prototype. To verify and validate the efficiency of this background rejection system and to define the "must-have" to operate in the best conditions, I have performed several tests in different conditions at the Irène-Joliot Curie Laboratory (IJCLab, Orsay, France) using two dry dilution refrigerators equipped with different electronics. In chapter 5, I report the following analysis procedure and the results obtained to validate the COV technique.

In parallel to the COV development work, during my Ph.D. I also participated in the development of innovative cryogenic detectors in the context of the BASKET (Bolometers At Sub KeV Energy Threshold) project. It is an R&D started in 2017 with the objective to develop innovative bolometric detectors for CEνNS detection using new scintillating crystals as absorber material. The main absorber candidate is molybdenum-doped lithium tungstate ($Li_2(Mo^{0.05})W_{0.95}O_4$), a very promising compound. In fact, by exploiting the affinity between W and Mo, previous studies on the compound Li_2MoO_4 have proven that the natural content of ^{6}Li (8% in the crystals used for our prototypes) reveals excellent particle identification capabilities allowing the tracking of the neutron background through the ^{6}Li(n,t)α reaction. Moreover, since the CEνNS cross-section varies with the number of neutrons as N^2, tungsten (N around 110) increases the CEνNS rate. The final goal of BASKET is to develop very sensitive cryogenic detectors with an ultra-low energy threshold of O(10 eV) and a rise time of the order of O(100 μs) so that they can be easily used on the surface near a nuclear power plant. We have tested different thermal sensors (Ge NTD and MMC) coupled to the scintillating compound.

The configurations and results are presented in chapter 6 (BASKET with NTD) and chapter 7 (BASKET with MMC).

Finally, in this thesis, a new activity started in June 2021 aiming at producing our own MMC sensors is also presented.

Chapter 1

Neutrino: an overview of this elusive particle

1.1 Chronology of a discovery

The neutrino existence was first theoretically postulated in 1930 by Wolfgang Pauli as a "desperate remedy" to justify the β-decay spectrum, a process in which a nucleus is transformed into a slightly lighter one with the emission of an electron [3]. Indeed, according to the two-body decay, a discrete spectrum was expected: a narrow distribution due to the energy carried away by the electron and corresponding to the energy difference between the initial and final states. On the contrary, it was observed a continuous energy spectrum with a maximum value at 1/3 of the Q-value[1]. Furthermore, subsequent experiments performed until 1957 proved a clear parity violation in this process. While Bohr was ready to sacrifice the energy conservation, for Pauli this law had to be valid to the point of introducing a new particle with no charge and with spin 1/2 (for the quantum numbers conservation) that is emitted with the electron. This particle was subsequently named *neutrino* by Enrico Fermi [4].

In 1933, Fermi introduced his theory of β *decay* in which he describes the interaction of four fermions at a single point. It was successfully used to explain many phenomena without changing the coupling constant g_L. He described β decay as a process in which a neutron is transformed into a proton while, at the same time, an electron is emitted

[1]The total kinetic energy available in the final state

(observed as a β particle) with a neutrino [5]:

$$n \rightarrow p + e^{-} + \nu \tag{1.1}$$

The prediction for the cross-section was first derived by Bethe and Peierls: influenced by Fermi's theory, it was suggested that, to verify the model, the neutrino could be detected by looking for the reverse process (namely the *inverse β decay*) in which an anti-neutrino interacts with a proton to form a neutron and a positron according to:

$$\bar{\nu_e} + p \rightarrow e^{+} + n \tag{1.2}$$

Considering neutrinos with energies of few MeV coming from a nuclear reactor, a typical cross-section was predicted to be $\sim 5 \times 10^{-44}\,\mathrm{cm}^2$. This prediction for cross-sections of reactor neutrinos is still accurate today.

1.1.1 The neutrino portrait

In the '50s, C. Cowan and F. Reines proved the neutrino existence through the β capture. The experimental set-up employed a water tank filled with a ^{108}Cd solution and surrounded by photomultiplier tubes and placed near the Savannah River nuclear reactor. The anti-neutrino, interacting with a proton, produces a positron and a neutron via inverse beta decay. The annihilation photons combined with the neutron capture photons revealed the presence of the anti-neutrino [6]. In 1995, Cowan and Reines received the Nobel Prize for neutrino detection.

In 1954, R. Davis realized a new experiment at the Homestake Gold Mine (1,5 meters underground) consisting of $380\,\mathrm{m}^3$ perchloroethylene tank exposed for a long time to solar neutrinos to prove that a neutron cannot capture an anti-neutrino [7]. Interacting with an electron neutrino, a ^{37}Cl atom becomes a ^{37}Ar radioactive isotope:

$$\nu_e + {}^{37}Cl \rightarrow e^{-} + {}^{37}Ar \tag{1.3}$$

The ^{37}Ar produced through this reaction was extracted and measured using miniaturized proportional counters. After more than 10 years of data taking, Davis could conclude that what was observed was not concordant with Bahcall's Solar Model predictions: just $\frac{1}{3}$ of the expected solar neutrino flux was detected [8, 9]. Later, other experiments (GALLEX/GNO, SAGE, Kamiokande, and SNO) confirmed this flux difference [10–12]. The same deficit was observed by Super-Kamiokande with atmospheric

neutrinos. In 2004, SNO and KamLAND experiments explained the deficit with a neutrino flavor change [13]. Moreover, by discovering the neutrino oscillation, they proved also that the neutrino is massive while in the Standard Model they are cataloged as mass-less particles.

Today, the neutrino is one of the Standard Model elementary particles. It is chargeless and experimentally observed in three different flavors (ν_e, ν_τ, ν_μ), each of them corresponding to a charged lepton (electron, tauon, and muon). According to the neutrino oscillation theory, each neutrino flavor is a combination of the neutrino mass eigenstates. Each neutrino type has a different mass and during its propagation in space-time its flavor changes periodically. Nevertheless, we have no information about absolute mass scale (*normal hierarchy* or *inverted hierarchy*) and which is the nature of these particles (Dirac or Majorana) [14, 15]. Moreover, a neutrino has a very low probability to interact with matter, because of the weak cross-section. Indeed, "*neutrinos of moderate energy could easily penetrate a thousand light-years of lead, [...] a comforting realization when you learn that hundreds of billions of neutrinos pass through every square inch of your body per second, night and day, coming from the Sun*" [16]. Since their first observation, an increasing number of experiments were conceived to define the main neutrino oscillation parameters, to investigate the properties of this elusive particle and the existence of the undetectable sterile neutrinos.

1.2 Coherent Elastic Neutrino Nucleus Scattering

On the basis of some experimental evidences of presence of a neutral current in neutrino-induced interactions obtained in Gargamelle experiment [17], Coherent Elastic Neutrino Nucleus Scattering (CEνNS) is a neutrino interaction postulated by D.Z. Freedman in 1974 [18], in which the neutrino scatters off a nucleus as a whole exchanging a Z boson (figure 1.1).

This suggestion was defined as an "act of hubris" since limitations of interaction rate, background suppression, and achievable energy threshold ($\sim$MeV) of the conventional detection technologies available at that time made the CEνNS detection a real challenge. Indeed, it required more than 40 years to measure it for the first time [19].

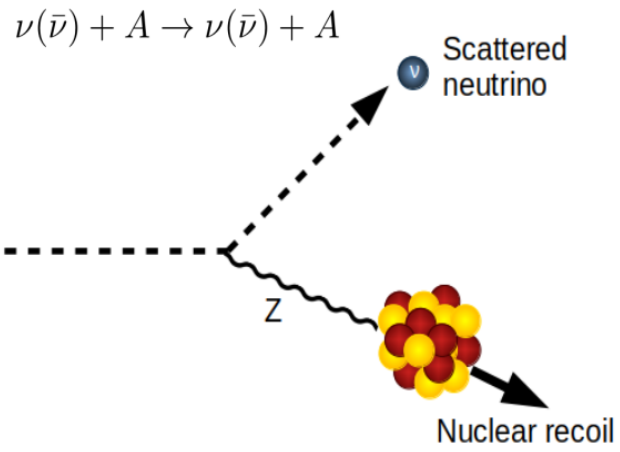

Figure 1.1: Representation of the coherent Elastic Neutrino Nucleus Scattering interaction.

1.2.1 CEνNS footprint

The coherence of this process implies that all the nucleons wave-functions in the target nucleus must be in phase with each other at low momentum transfer. As a consequence, the total cross-section can be evaluated by summing the amplitudes. The condition that must be satisfied so that CEνNS can happen is:

$$q \cdot R >> 1 \tag{1.4}$$

where q, defined as $\sqrt{2m_N E_r}$ (m_N and E_R are the mass of the target nucleus and the recoil energy respectively) is the three-momentum transfer and R the nuclear radius. Assuming medium size nuclei as the target, according to the condition 1.4, the coherence of the process is guaranteed for neutrinos with energy up to 50 MeV. The CEνNS cross-section is described in the Standard Model as [20, 21]:

$$\frac{d\sigma}{dE_R} \simeq \frac{G_F^2}{4\pi} Q_W^2 F^2(q^2) m_N \left(1 - \frac{E_R}{E_R^{max}}\right) \tag{1.5}$$

where G_F is the Fermi's constant, $F(q)$ is the form factor,E_R^{max} is the maximum recoil energy, and Q_W is the weak-charge which is defined as:

$$Q_W = N - Z(1 - 4sin^2\theta_W) \tag{1.6}$$

Neutron and proton numbers (N and Z) are the main contributions of the weak-charge Q_W, and therefore of the cross-section. Anyway, since Z is multiplied by the Weinberg angle θ_W, the term $(1 - 4sin^2\theta_W)$ is very small and we can assume that $(1 - 4sin^2\theta_W)Z \sim 0$. Therefore, we can approximate the term Q_W^2 in equation 1.5 with N^2. As a consequence, we will select target nuclei with an abundance of neutrons.
The CEνNS standalone fingerprint is the nuclear recoil energy, a quantity that can be measured experimentally. The maximum energy that can be released depends on the neutrino energy E_ν and the mass of the target nucleus m_N:

$$E_r^{max} \simeq \frac{2E_\nu^2}{(m_N + 2E_\nu)} \tag{1.7}$$

Equations 1.5 and 1.7 clearly show the boon and bane of this process. Because of the coherence effect, CEνNS has a quite large cross-section in the ν world (figure 1.2). Moreover, CEνNS can occur without a neutrino energy threshold. Therefore, choosing a target nucleus rich in neutrons is convenient to enhance the CEνNS rate. However, because of the coherence condition 1.4, from which $q << \frac{1}{R}$, we have nuclear recoils with energies typically in the keV range. To give an order of magnitude, assuming to have a neutrino source with $E_\nu \sim 50\,\text{MeV}$ and caesium nuclei as target, the maximum nuclear recoil energy E_r^{max} is $\sim$40 keV. Hence, it is necessary to find a compromise while selecting the target material. The conventional neutrino detectors used for other studies usually do have not a sufficiently low energy threshold to be sensitive to nuclear recoils in the CEνNS region of interest. This made the observation of CEνNS experimentally a challenge. Luckily, the technological improvements, taken place in the last decades for Dark Matter searches, allowed the development of new detectors very sensitive to low-energy events. These same technologies can be easily adapted for CEνNS searches to detect recoils from a few keV up to 10's of keV [22].

1.3 CEνNS and physics beyond the Standard Model

The study of CEνNS offers a unique possibility to open a new window to a multitude of physics observables, giving the possibility to answer many unresolved questions in the Standard Model and, eventually, to investigate the physics beyond it. Moreover, knowing better about this interaction could be particularly interesting for other searches as well, for example the Dark Matter search where a not negligible issue is the CEνNS scattering

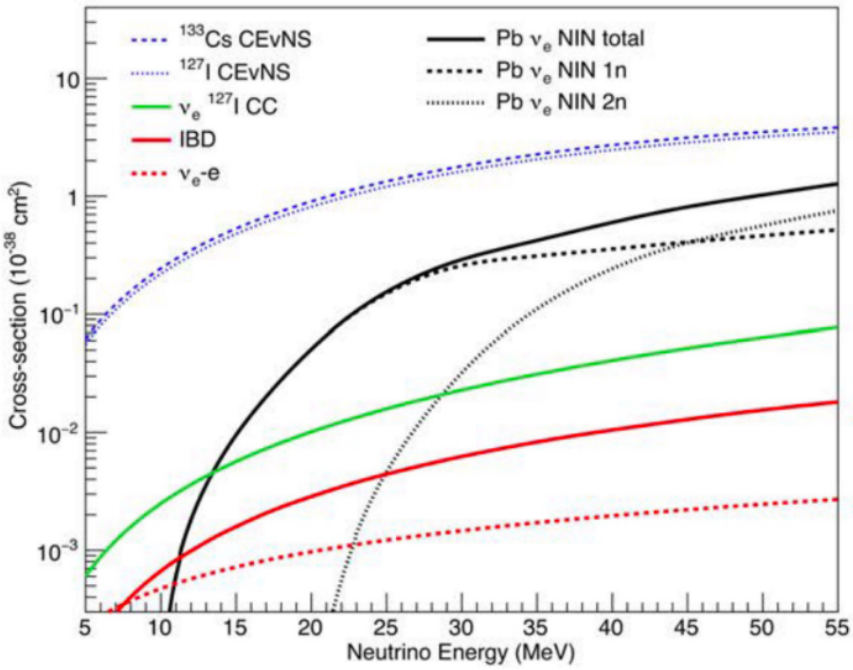

Figure 1.2: Cross-sections from CEνNS and some known neutrino couplings, such as inverse beta decay (IBD), neutrino electron scattering, charged-current (CC) interaction with iodine [19]. We can observe that not only the CEνNS cross-section is more than two orders of magnitude larger than for IBD, but no energy threshold exists if it is to occur.

of solar neutrinos.

Below, I will briefly present just some of the information that CEνNS could provide. More details are reported in reference [23].

Neutrino magnetic moment

The neutrino is classified in the Standard Model as a mass-less particle without magnetic dipole moment. Nevertheless, it has been proved that neutrino has mass [24] and the radiative corrections coming from new physics could rise the magnetic moment to detectable values. Moreover, we could even infer the neutrino nature from the order of magnitude of the magnetic moment [25]: if this value will be anomalously large ($\sim 10^{-12}\,\mu_B$ or larger) [26], it will be a hint of being a Majorana particle. Finally, a non-zero magnetic moment would play a role in the CEνNS cross-section, because of which the expected energy spectrum would change. The current magnetic moment constraints are widely reported in the PDG book [27].

Weinberg angle

The Weinberg angle θ_W, also called *weak mixing angle*, is a parameter of the electroweak interaction describing the spontaneous breaking of symmetry which results in a Z_0 boson and a γ [28]. It plays a role in the CEνNS cross-section (equation 1.6). This term is coupled to the number of the proton, therefore a target nucleus with a large atomic number is more suitable to measure the Weinberg angle even if we shouldn't forget that its contribution is small. The only way to become sensitive to the weak mixing angle is by collecting a large statistic in order to achieve a precision as higher as possible [29]. Until today, the most precise measurement of the angle θ_W is performed by combining the COHERENT with the atomic parity violation measurement on ^{133}Cs (more details are given in reference [30]). Improvements are still possible to reduce systematic errors; This could make the CEνNS a competitive process to achieve a larger accuracy [31].

Neutron form factor

The equation 1.5 takes into account the form factor for both protons and neutrons. While we already know the proton form factor $F_P(q^2)$, since the charge distribution can be tested via μ-spectroscopy and electron scattering, the neutron form factor $F_N(q^2)$ must still be investigated. Besides the model-dependent hadron scattering experiments,

the CEνNS experiments provide the opportunity to investigate the neutron form factor, and therefore the neutron distribution, because of the strong dependence of the cross-section on the neutron number (equation 1.8) [32, 33]. The neutron distribution radius and the neutron-skin[2], today unknown for many nuclei, could help to understand many processes in nuclear physics (such as the heavy ion collisions) and astrophysics (such as the structure and the evolution of neutron stars) [34–36].

$$F(q^2) = \frac{1}{Q_W}[NF_N(q^2) - (1 - 4sin^2\theta_W)ZF_P(q^2)] \tag{1.8}$$

New neutrino mediators

Non-standard neutrino interaction could have an impact on the neutrino coupling to proton and neutron, introducing new parameters that could tell us the magnitude of these interactions in proportion to the neutral-current weak interaction in the Standard Model [37, 38]. These couplings can be written as a function of the mediator mass and the momentum transfer.

In particular, if the momentum transfer q^2 is larger than the mediator mass, we are talking about a *"light" mediator*. In this case, the couplings become q^2 dependent and new physics can emerge, such as a new gauge symmetry with an additional vector mediator Z' or scalar mediator Φ.

Sterile neutrinos

In order to explain anomalies observed in neutrino oscillation experiments that are not compatible with the three-neutrino oscillation paradigm, the existence of at least a fourth neutrino with $\sim$1 eV mass has been hypothesized [39, 40]. This new fourth particle could mix with the already known active neutrinos (ν_e, ν_μ, ν_τ), having an effect also on the neutrinoless double beta-decay and dark matter at the keV scale [41, 42]. CEνNS, being a flavour-independent process could help in the probing of the sterile neutrino existence.

[2]The neutron-skin is defined as the difference between the neutron distribution radius R_n and the proton distribution radius R_p.

1.4 CEνNS experiments

Since when the COHERENT collaboration proved that the time has come for the CEνNS detection [19], there is increasing attention from the experimental and the theoretical point of view resulting in many proposed and under construction experiments (figure 1.3).

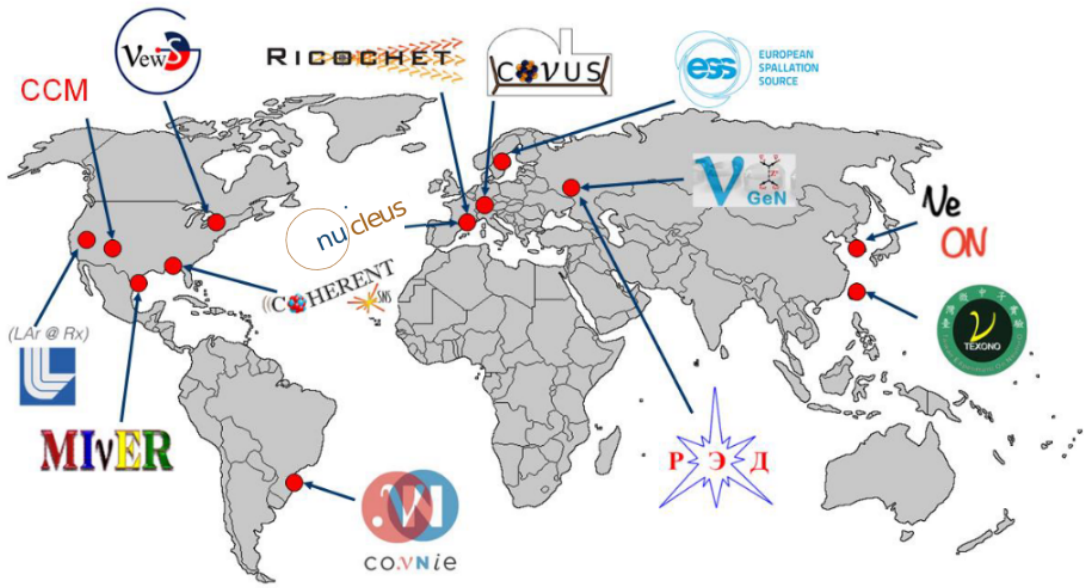

Figure 1.3: CEνNS experiments all around the world [43].

In this section, I will briefly introduce some of these experiments.

1.4.1 CEνNS neutrino sources

Keeping in mind that the CEνNS detection is our goal, we can make a list of the specifications we desire:

- high flux, to collect as many statistics as possible;
- well understood flux, to know how many neutrinos are interacting in the detector;
- pulsed flux or off-period of the flux, in order to facilitate the background rejection. In the first case, a pulsed flux allows the opening of acquisition windows that are

short in time, just when the neutrino flux is expected to come, globally reducing the background. In the second case, the background-only energy spectrum can be subtracted from the with flux energy spectrum;

- neutrino multiple flavors. Even if the CEνNS cross-section is flavor independent, a source with different neutrinos matched to a technique to distinguish their family (electron, muon, or tau) could help to study some neutrino properties;
- the produced neutrinos must have sufficient energy to generate detectable nuclear recoil but must not exceed in order that coherent elastic scattering is still the dominant process.

According to this wish list, we can identify mainly two neutrino sources that are particularly suitable for our purpose:

- **Stopped-pion sources**. The neutrinos are produced starting from energetic proton beams (figure 1.4) hitting a fixed target. In the collisions, the protons generate pairs of charged pions π^+ and π^- that lose their energy and decay at rest within the target: decaying in a few ns, they produce monoenergetic muons and muon neutrinos ($E_{\nu,\mu}$ ~30 MeV) according to the two-body reactions 1.9 [44].

$$\begin{aligned} \pi^+ &\rightarrow \mu^+ + \nu_\mu \\ \pi^- &\rightarrow \mu^- + \bar{\nu_\mu} \end{aligned} \tag{1.9}$$

  The muons are stopped within the target as well, where they decay in a few μs generating neutrinos following the three-body reactions [45]:

$$\begin{aligned} \mu^+ &\rightarrow e^+ + \bar{\nu_\mu} + \nu_e \\ \mu^- &\rightarrow e^- + \nu_\mu + \bar{\nu_e} \end{aligned} \tag{1.10}$$

  For each produced pion, three neutrinos of different flavors are produced and they will interact via CEνNS with the same cross-section for a given target nucleus. In particular, if the beam pulses are shorter compared to the μ lifetime (i.e. <2.2 μs), we can distinguish a prompt signal, namely the muon neutrino generated in reaction 1.9, and a delayed one due to the neutrinos generated in reaction 1.10.

- **Nuclear reactor**. A nuclear reactor provides an extremely high flux $\bar{\nu_e}$, ~ 2×10^{20} $\bar{\nu_e}$ per second per GW_{th} that is about four order of magnitude larger

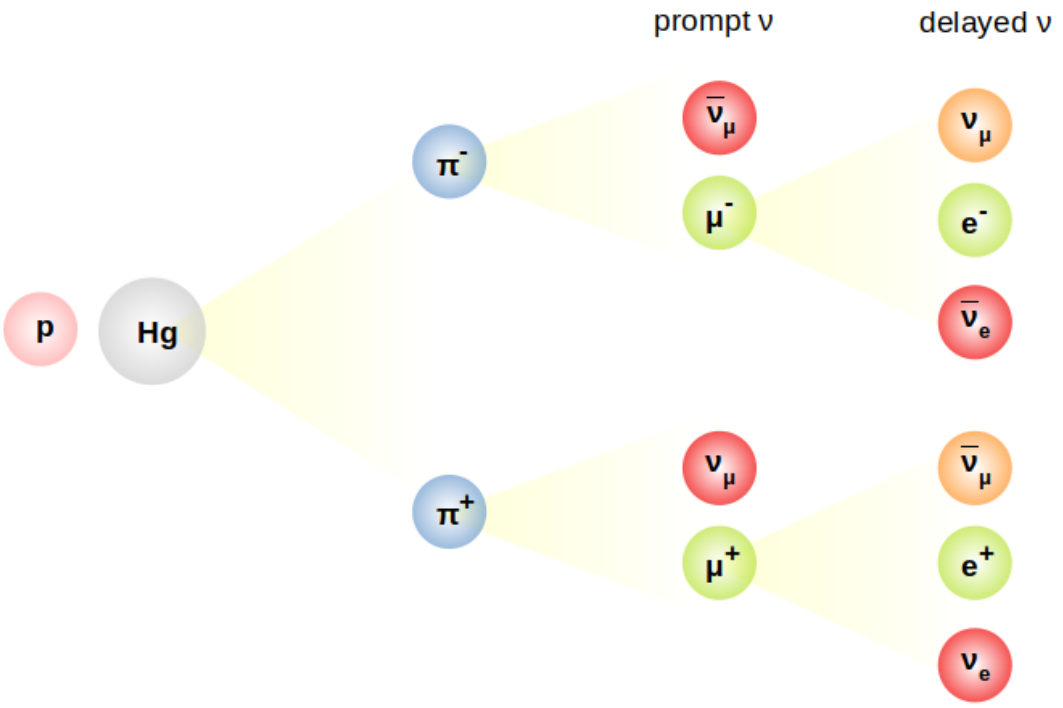

Figure 1.4: Starting from a proton beam hitting a target, the SNS offers the possibility to generate prompt and delayed neutrinos of different flavors through the reactions 1.9 and 1.10. This offers the additional possibility to perform studies on neutrinos of a different flavor.

compared to the stopped-pion sources. The $\bar{\nu_e}$ are produced by the β-decay of fission products, typically of ^{235}U, ^{238}U, ^{239}Pu and ^{241}Pu [46–48]. Nuclear reactors can generate $\bar{\nu_e}$ with energy much lower compared to the stopped-pion sources, determining smaller nucleus recoil energies to detect (equation 1.7). The advantage of this neutrino source is first of all the wide availability of already existent power or research nuclear reactors all around the world and almost complete freedom from the uncertainties due to the not well-known nuclear structure. As an example, the form factor $F(q^2)$ in equation 1.5 is about 1 at the neutrino reactor energies. Nevertheless, the intensity of the neutrino flux to which the detector will undergo depends strongly on its distance from the reactor core, as the emission is isotropic. Moreover, the reactor flux is not constant but it has been observed that it varies during the fuel burning cycle. The reactor-off periods provide the

unique possibility to make studies on the environmental radioactivity that can be subsequently used to apply a background subtraction on the reactor-on energy spectrum. Specifically, the off-periods of research reactors are usually longer and more frequent, allowing a more intense background characterization campaign even if we have to deal with the fact that, contrary to power reactors, their core power doesn't reach the GW_{th} (i.e. even smaller CEνNS signature).

Several other neutrino sources exist, since the processes at the origin of neutrino production are very common in nature [49]. Between them, we can mention the solar neutrinos, generated through thermonuclear fusion reactions in the core of the Sun [50], and geo-neutrinos, produced by the Earth's heart through natural radioactivity processes [51]. Anyway, even if the coherent elastic scattering regime is assured by the neutrino energy range, the too low flux makes these two sources unacquainted. Indeed, in order to become competitive in collecting enough CEνNS statistics, we would need a huge detector target mass such as the one used in SNO and Borexino [52, 53]. Moreover, the rejection of the background would be another critical point.

1.5 Overview on the CEνNS experiments

Hereinafter, some of the main CEνNS experiments are briefly presented to show how many techniques and setups can be designed in order to open new windows to probe physics beyond the Standard Model. In table 1.1, information about these experiments is reported in order to facilitate the comparison between them. NUCLEUS, the CEνNS experiment to which this thesis is partially dedicated, will be presented in chapter 4.

1.5.1 COHERENT

COHERENT is an experiment working in close proximity to the Spallation Neutron Source (SNS) at Oak Ridge National Laboratory (Tennessee, USA). The pulsed nature of the source allows delivering neutrinos in well-determined time windows, facilitating the background subtraction. Moreover, being a stopped-pion source, it provides prompt and delayed neutrinos offering the possibility to separate the different neutrino species (figure 1.4).

Based on a multi-target program to test the cross-section N^2 dependence, it confirmed Freedman's prediction by observing 2017 CEνNS events for the first time, using

14.6 kg of CsI scintillating crystal at 19.3 m from the source [19]. The COHERENT collaboration reconstructed 132±22 events with 6.7 σ significance, a value that is compatible with what was predicted by the Standard Model (figure 1.5). The data taking on CsI continued until June 2019, doubling the statistics. The results confirmed what had already been observed. The CEνNS cross-section was estimated $169^{+90}_{-26} \times 10^{-40}$ cm^2 to compare with the Standard Model prediction, i.e. $(189\pm6)\times10^{-40}$ cm^2 [54]. In 2020, the COHERENT collaboration started a measurement of CEνNS using 24 kg of liquid argon at 27.5 m from the spallation neutron source target. The achieved results once again are compatible with the Standard Model, showing a significance above 3 σ compared to the null hypothesis. This new run allowed us to verify the expected neutron number dependence of the cross-section, evaluated $(2.2\pm0.7)\times10^{-39}$ cm^2 on argon nuclei, and improved constraints on non-standard neutrino interactions [55]. In the future, the COHERENT experiment will include 16 kg of high-purity germanium detectors and a tonne-scale NaI scintillator array complementing each other to pursue richer physics.

1.5.2 CONUS

CONUS is the second most advanced CEνNS experiment, after COHERENT. It is located at 17 m distance from the 3.9 GW_{th} core of the commercial nuclear power plant in Brokdorf (Germany) [56]. The high duty cycle guarantees a constantly high antineutrino flux of energies up to 8 MeV. During the reactor-off periods, the background can be measured and therefore subtracted from the energy spectrum when the reactor is on. The CONUS detector, consists of 4 high purity point contact germanium crystals of 1 kg each exploiting the ionization technology of which the Max-Planck-Institut für Kernphysik (Heidelberg, Germany) has a deep knowledge [57]. The goal is to reach an energy threshold of ∼300 eV, a result achievable thanks to the contribution of electrical cryocoolers. The detectors are surrounded by a high-efficiency muon veto and compact shell-like passive shields enclosed in a radon-tight steel cage. This system draws inspiration from GIOVE (Germanium Inner Outer VEto), a high-purity germanium spectrometer setup developed at Max-Planck-Institut für Kernphysik in Heidelberg [58]. The active muon veto is composed of plastic scintillator plates equipped with photomultiplier tubes, while the passive shielding consists of several layers of lead (25 cm thick in total) alternated by borated polyethylene layers to moderate and capture neutrons. The data taking started in April 2018. A challenge for this experiment is the lack of information on the germa-

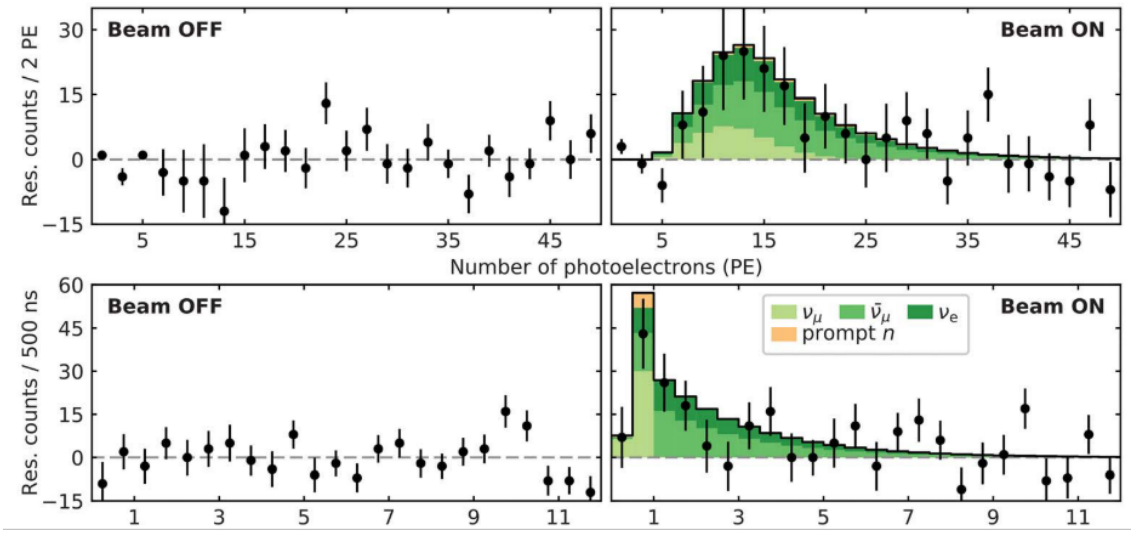

Figure 1.5: Observation of CEνNS by the COHERENT collaboration [19]. The plots show the differences in photon counts between the 12 μs after and before a beam trigger as a function of photon number (*top*) and arrival time (*bottom*). The "Beam OFF" data are accumulated during 153.5 live-days of SNS inactivity while the "Bean ON" during 308.1 live-days of neutrino production. An excess following the standard model CEνNS prediction (colored histograms on the *right*) was observed for periods of neutrino production only at a significance of 6.7σ.

nium quenching factor[3] at the CEνNS region of interest. Because of this not well-known parameter in germanium at low temperature, no hint for CEνNS signal can be observed in the acquired data. Any predictions on the CEνNS rate are strongly dependent on the quenching factor that can vary more than 1 order of magnitude in the investigated energy region (0.296-1.00 keV). Only an upper limit can be extracted. Assuming a quenching factor of 0.18, the CONUS collaboration determined an upper limit of 85 neutrino events in the region of interest at 90% confidence level, excluding quenching factors above 0.27 [59].

In 2021, a new data collection started. Following a series of improvements, a reduction of the statistical uncertainty and an improvement in the background understanding is expected [60].

1.5.3 RICOCHET

RICOCHET is a reactor neutrino observatory that will operate at 8.8 m from the 58.3 MW_{th} core of the Institut Laue Langevin (ILL) research reactor in Grenoble (France) [61]. The reactor cycles of about 50 days interspersed with reactor-off periods offer the possibility to launch periodical background measurements that contribute to the background mitigation of the reactor-on energy spectrum. The goal of the RICOCHET collaboration is to develop an experiment able to reach an energy threshold of ~50 eV (or lower). To achieve this result, RICOCHET will include a shielding system, based on a thick layer of lead and borated polyethylene, for a total weight of more than 15 tons, plus an active muon veto. It will exploit two detector arrays, the so-called CryoCube and QArray [62]. The CryoCube will consist of 27 detectors based on high purity germanium crystal, each of them with a mass of about 38 g equipped with a germanium neutron transmutation doped sensor for the heat signal, and aluminum electrodes for the ionization signal. The double read-out system will provide discrimination and an efficient rejection of the dominant γ and β backgrounds. Moreover, it will allow a direct measurement of the true nuclear recoil energy, avoiding any problems related to the quenching factor. After about 50 days, namely one reactor cycle, the CEνNS detection significance should be 4.3–17.3σ, depending on the background level achieved. The QArray will be an array of 9 cubes of superconducting zinc equipped with a transition edge sensor, devices that will

[3]This parameter is required to take into account the different amount of charges produced by nuclear recoils and electron recoils [59].

provide a detection threshold down to the binding energy of the Cooper pairs, and excellent background discrimination. The RICOCHET first CEνNS exposure is scheduled for 2023.

1.5.4 TEXONO

The Taiwan EXperiment On NeutrinO (TEXONO) collaboration was founded in 1997 to investigate the anomalous results obtained from the solar and atmospheric neutrino measurements [63]. In order to study the low-energy neutrino, the TEXONO collaboration identified the commercial power reactors as a suitable neutrino source to start a new research program. Today their priority is the detection of neutrino-nucleus elastic scattering. A dedicated experiment is realized at Kuo-Sheng Reactor Neutrino Laboratory (KSNL) which is located at 28 m from the 2.9 GW_{th} core-1 of the Kuo-Sheng Nuclear Power Station operated by the Taiwan Power Company. This reactor alternates 18 months of reactor-on with 50 days of reactor off. The design of the facility was initiated in 1997. It includes a 4π onionlike passive shielding (total mass 50 tons) composed of layers in oxygen-free high thermal conductivity copper, borated polyethylene, steel, lead, plus a muon veto scintillator. The TEXONO collaboration can boast of several results, among them limits on the neutrino magnetic moment achieved using a high-purity germanium detector (mass 1.06 kg) surrounded by scintillating NaI(Tl) and CsI(Tl) crystals as Compton vetos, with a detection threshold of 5 keV [64, 65]; constrains on the electroweak parameters and the electron neutrino charge radius, measured with a CsI(Tl) scintillating crystal array (total mass 187 kg) [66]. The TEXONO goal is now to lower the background rate and the energy threshold ($<$200 eV_{ee}) to make possible the CEνNS detection [67].

1.5.5 MINER

Mitchell Institute Neutrino Experiment at Reactor (MINER) is a reactor based experiment at the Nuclear Science Center (NSC) at Texas A&M University [68]. Their low-threshold $\sim$100 eV recoil energy) cryogenic detectors, based on high purity germanium, silicon and Al_2O_3, are developed starting from the knowledge inherited from the CDMS and SuperCDMS dark matter search [69]. The reactor is a 1 MW_{th} TRIGA (Training, Research, Isotopes, General Atomics) characterized by the possibility mobile core that allows the positioning of the detectors as close as $\sim$1 m from the neutrino source [70].

This feature makes MINER suitable for the for short-baseline sterile neutrino oscillation search, offering the possibility to remove the reactor flux uncertainty [71]. The Phase-1 of MINER, consisting of 2 kg payload at a distance of 4.5 m from the core, is ongoing. It will give some indications about the design of the Phase-2, where payload and flux will be 10 times the actual one and the background will be lowered by a factor 10 thanks to an hermetic shielding.

1.5.6 CONNIE

The Coherent Neutrino Nucleus Interaction Experiment (CONNIE) is based on an array of Charge Coupled Devices (CCDs), sensors fabricated on high-resistivity silicon. The experiment is located at 30 m from the 3.8 GW_{th} core of the Angra II nuclear reactor at the Almirante Álvaro Alberto nuclear power plant (Angra dos Reis, Brazil). The reactor cycle is 13 months followed by 1 month of shutdown. Installed in 2014, the CONNIE data taking started in 2016. After 3 years of data taking, it established a model-independent limit on CEνNS rate [72]. Moreover, it has proven to live up to the challenge of probing physics beyond the Standard Model. Indeed, in April 2020 it provided the first competitive beyond Standard Model constraints from CEνNS at reactors, setting limits on simplified extensions with light mediators [73]. In July 2021, the CONNIE detector was upgraded installing Skipper CCDs (768 x 1024 pixels each) [74, 75]. The advantage of these devices is the possibility to measure multiple times the charge in each pixel during data acquisition, allowing a reduction of the read-out noise according to the number of samplings N ($\sigma \sim 1/\sqrt{N}$), and allowing the detection of single electrons. The characterization of these devices at the sea-level background is fundamental considering that in the future there could be the possibility to install them inside the dome of the reactor, at a distance of 17 m from the core. [76].

1.5.7 RED-100

Russian Emission Detector 100 (RED-100) is a CEνNS reactor experiment started in 2012. The detector contains ∼200 kg of liquid xenon ((of which ∼160 kg is active volume)), exploiting the dual-phase noble gas emission [77], and the produced light is therefore detected by an array of 38 PMTs. This particle detection method was proposed for the first time by the Moscow Engineering Physics Institute in 1970 [78]. The strong point of this technique is the sensitivity to signals of ultra-small intensity, as to

be able to detect even single ionization electrons. Today, it is largely used for dark matter searches and neutrino detection in underground laboratories. The detector will be installed at a distance of 19 m from the 3.1 GW_{th} core of the VVER-1000 reactor, the fourth power unit of the Kalinin Nuclear Power Plant (KNPP) [79]. It will be shielded with 5 cm of copper and purified water contained in a water tank with a diameter of ∼10 m [55]. The first physical test of the RED-100 detector was performed in February 2019 in a ground-level laboratory and without any passive shielding. The achieved results, published in [80], show that the CEνNS detection using xenon nuclei as the target is possible and a threshold of 4 ionization electrons can be reached.

1.5.8 νGeN

The νGeN experiment consists of high-purity germanium detectors (active mass 1.41 kg) located at 11 m from the 3.1 GW_{th} core of Kalinin Nuclear Power Plant (Russia) for the coherent Neutrino–Ge Nucleus detection [81]. The detector shielding has an onionlike structure and it is composed of 5 cm of plastic scintillator as muon veto, 8 cm of borated polyethylene, 10 cm of lead, 8 cm of borated polyethylene, and 10 cm of oxygen-free copper; the most inner part is made of 3D printed nylon to avoid the radon issue. The first measurement was performed in 2022. A significant difference between the reactor on and off spectra was not observed, meaning that no positive signals for CEνNS were detected. More details are given in [82].

To summarize, CEνNS experiments based on different technologies are under construction or are already collecting data. The motivating force that will lead this research field for the next decade is the possibility to access physics beyond the Standard Model and face open questions from a different perspective, besides the prospect to shed light on this interaction. In conclusion, we are living right now at the beginning of an exciting time in CEνNS research.

Table 1.1: Presentation of the main CEνNS experiments: for each of them it is reported the chosen material for the detector, the kind and power of the neutrino source, the location, and a reference where more details on the experimental set-up are given.

Experiment	**Target detector material**	**Neutrino source**	**Power**	**Location**	**Reference**
COHERENT	CsI, Ar, Ge, NaI	SNS	1.4 MW	ORNL (Tennessee)	[83]
CONUS	Ge	reactor	3.9 GW_{th}	Brokdorf (Germany)	[56]
RICOCHET	Ge, Zn	reactor	58.3 MW_{th}	ILL (France)	[84]
TEXONO	Ge	reactor	2.9 GW_{th}	Kuo-Sheng Reactor (Taiwan)	[63]
MINER	Ge, Si, Al_2O_3	reactor	1 MW_{th}	NSC (Texas)	[68]
CONNIE	Si	reactor	3.8 GW_{th}	CNAAA (Brazil)	[85]
RED-100	LXe	reactor	3.1 GW_{th}	KNPP (Russia)	[86]
νGEN	Ge	reactor	3.1 GW_{th}	KNPP (Russia)	[81]
NUCLEUS	$CaWO_4$, Al_2O_3	reactor	4.25 GW_{th}	Chooz (France)	[87]

Chapter 2

Cryogenic calorimeters for the detection of rare events

A calorimeter is a device composed of a crystal acting as an energy absorber, and a thermal sensor glued on the crystal surface and working as a thermometer. When a particle interacts within the crystal, it releases energy that is absorbed by the crystal lattice and converted into phonons. This energy release is responsible for a temperature rise of the crystal. Thanks to a thermal sensor, we can convert the change of temperature into a signal readable by the electronics. The temperature change ΔT is inversely proportional to the detector heat capacity C:

$$\Delta T = \frac{\Delta E}{C} \tag{2.1}$$

A calorimetric measurement is therefore possible if we minimize as much as possible the crystal heat capacity. This can be achieved working at cryogenic temperature: lower is the base temperature of the detector, weaker is the heat capacity C, and larger is the temperature variation ΔT for the same amount of energy ΔE deposited in the crystal by the interacting particle. Indeed, the third law of thermodynamics establishes that the entropy S of a system becomes constant approaching the absolute zero, so, according to the equation 2.2, $C(T)$ must vanish.

$$dS = \frac{dQ}{T} = C(T) \cdot \frac{dT}{T} \tag{2.2}$$

The temperature variation we are speaking about is of the order of a few tens or hundreds of μK/MeV; for this reason, it is so important to cool down the detector at cryogenic temperatures (typically between 10-20 mK). The absorber is weakly connected to the

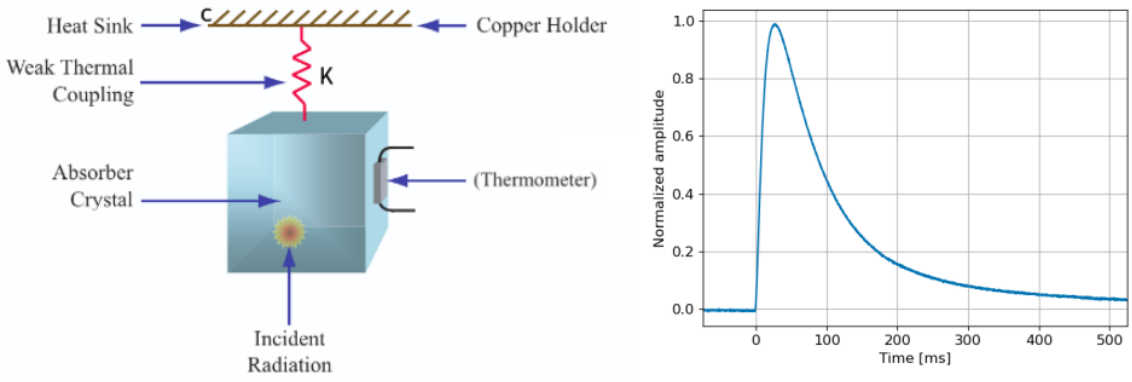

Figure 2.1: *Left:* simplified scheme of a calorimeter. A thermal sensor is glued to the absorber surface. The ensemble is thermally connected to the heat sink through a weak coupling of conductance K.
Right: example of a typical pulse shape. In general, the pulse amplitude (here normalized at 1) corresponds to the temperature variation ΔT while the decay time is the time required for the absorber to recover the base temperature, i.e $\tau = C/K$.

heat sink (usually the calorimeter copper holder) through a thermal coupling K to restore the base temperature after that a particle interaction heated up the detector:

$$\Delta T(t) = \frac{E}{C} \exp\left(-\frac{t}{\tau}\right) \tag{2.3}$$

The time τ required to restore the calorimeter absorber base temperature is defined as the ratio between the heat capacitance C and the thermal link conductance K between the detector and the heat sink. It usually corresponds to the pulse decay time.

2.1 The absorber heat capacity

The specific heat $c(T)$ of a crystal is a temperature dependent quantity and it is defined as the sum of two contributions: the specific heat coming from the crystal lattice $c_l(T)$ and the conduction electron system $c_e(T)$, as shown in equation 2.4.

$$c(T) = c_l(T) + c_e(T) \tag{2.4}$$

In case of a dielectric material, the $c_e(T)$ contribution is void and just the lattice component $c_l(T)$ plays a role. We can evaluate c_l thanks to the Debye law, assuming that

the condition $T << \theta_{Debye}$ is satisfied [88]. It is valid for dielectrics and semiconductors as well, and it is defined as [89]:

$$c_l = \frac{12\pi^4}{5} N k_B \left(\frac{T}{\theta_{Debye}}\right)^3 \tag{2.5}$$

where N is the number of atoms in the molecule, k_B the Boltzmann constant, T is the calorimeter temperature, m the absorber mass, m_{mol} the molar mass, and θ_{Debye} is the Debye temperature expressed as:

$$\theta_{Debye} = \frac{\hbar \cdot \omega_{Debye}}{k_B} \tag{2.6}$$

where $\hbar$ is the Planck constant and ω_{Debye} is the maximum acoustic phonon frequency.

Therefore, we can translate the specific heat of the lattice c_l into the absorber heat capacity C, according to equation 2.7 [90]:

$$C \simeq 1944 \cdot N \frac{m}{m_{mol}} \left(\frac{T}{\theta_{Debye}}\right)^3 \ [J/K] \tag{2.7}$$

where m is the crystal mass and m_{mol} is the molar mass. It is 374 K and 759 K for the germanium and Li_2WO_4 respectively. For example, assuming to have 1 cm^3 Li_2WO_4 crystal, through equation 2.7, we can evaluate a heat capacity of $5.43 \cdot 10^{-13}$ at 10 mK.

In the case of metallic materials, the conduction electrons' heat capacity $c_e(T)$ becomes dominant below 1 K. Since the system of conduction electrons can be approximated as a Fermi gas, we can evaluate the corresponding specific heat as:

$$c_e(T) = \frac{\pi^2}{\theta_{Debye}} Z R \frac{T}{\theta_{Fermi}} \tag{2.8}$$

where Z is the number of electrons in the atom, R is the perfect gas constant, and θ_{Fermi} is the Fermi temperature. However, the equation 2.8 is no more valid if we have to deal with a superconductive material at a temperature T lower than their critical temperature T_c. Indeed, in this particular case, c_e must be evaluated through the equation 2.9 and its contribution is negligible compared to the specific heat of the lattice.

$$c_e(T) \propto e^{-2\left(\frac{T_c}{T}\right)} \tag{2.9}$$

2.2 Double read-out detectors

In the search for rare events, we can identify three types of contaminations that contribute to the background:

- external contamination, rejected through a shielding system composed of passive layers (such as lead, polyethylene, borated polyethylene,...) and, if necessary, active veto systems;

- contamination in the absorber bulk, i.e. contaminations introduced during the crystal production. This contribution can be limited to selecting very radiopure materials;

- surface contaminations; the α particles, produced in the decay of nuclei surrounding the detector or coming from the surface detector itself, interact with the calorimeter producing signal. This kind of contamination is difficult to control.

A technique, largely used in Dark Matter and $0\nu2\beta$ experiments, that offers the possibility to reduce the α background, is the particle discrimination via double read-out [91–96].

The double read-out is obtained by coupling a 'main' calorimeter based on a scintillating crystal to a second cryogenic detector (i.e, the so-called *light detector*) that is sensitive to the scintillation light produced by the first one. The idea to construct calorimeters selecting scintillating crystals was adopted for the first time in 1982 by L. Gonzalez-Mester in an experiment aiming at the detection of magnetic monopoles of low-energy solar neutrinos [97]. In 1994, C. Bobin et al. proposed to collect the light emitted by the scintillating calorimeters introducing a second cryogenic detector characterized by a response time compatible with the order of magnitude of the main calorimeter [98]. They proved that the discrimination of α and γ particles is possible, combining 300 mg of scintillating $CaF_2(Eu)$ to a sapphire disk with a diameter of 9.2 mm and thickness of 230 μm, both equipped with a germanium Neutron Transmutation Doped sensor.

The working principle of this technique is based on the fact that different particles have different light output, depending on the energy loss mechanism of the particle, as described by the Birks formula [99, 100]:

$$\frac{dL}{dr} = S \cdot \frac{\frac{dE}{df}}{1 + k \cdot B \cdot \frac{dE}{dr'}} \tag{2.10}$$

where dL/dr is the specific scintillation yield per path length, S is the absolute scintillation efficiency, dE/dr the particle stopping power in the material, k the quenching parameter, and $B \cdot dE/dr'$ is the density of the excitation centers along the particle track.

In the case of α particles, the dE/dr is a large term, so the formula can be simplified as:

$$\frac{dL}{dr} = \frac{S}{k \cdot B} \tag{2.11}$$

Therefore, in most of the cases, the α particles emit a lower amount of light compared to β and γ particles [101].

The light detectors used in my doctoral work consist of highly pure germanium disks darkened with a thin layer of SiO_2 to increase the absorption of scintillation light; a Neutron Transmutation Doped sensor is epoxy glued on them. Some examples of particle discrimination exploiting the double read-out technique are presented in chapter 6.

This device, composed of a scintillating crystal and a light detector, is easy to reproduce and, therefore, it is particularly suitable in experiments where several of these modules necessary are required [102]. Moreover, during the last decades, they were optimized to reach a very low background rate: 10^{-4} counts/(keV·kg·y) in the ^{100}Mo region of interest ($\sim$17.9 MeV).

Figure 2.2 shows an example of a tower composed of 12 modules, designed compact in order to place each light detector very close to the corresponding scintillating crystal (0.5 mm gap). This tower, assembled at the IJClab (Orsay, France) clean room, is a CUPID demonstrator. According to the current baseline, CUPID will consist of an array of 1596 scintillating crystals (two calorimeters for each of the 14 floors arranged in 57 towers) separated by 1710 light detectors [103]. More details and results obtained with this prototype are reported in reference [104].

When the double read-out is chosen, the selection of the scintillating absorber material is a tipping point. Indeed, in order to have the chance to detect the physics interaction under investigation, the crystal must contain isotopes that enhance the rate of the searched events. In table 2.1, a list of rare event searches with corresponding suitable scintillating candidates as absorber material is reported. Reference [105] presents an exhaustive description of each scintillating compound and the process for which they are exploited.

2.3 Thermal sensors

The sensor has the task to convert any temperature variation, generated after a particle interaction within the crystal, into an another physical quantity according to the type of

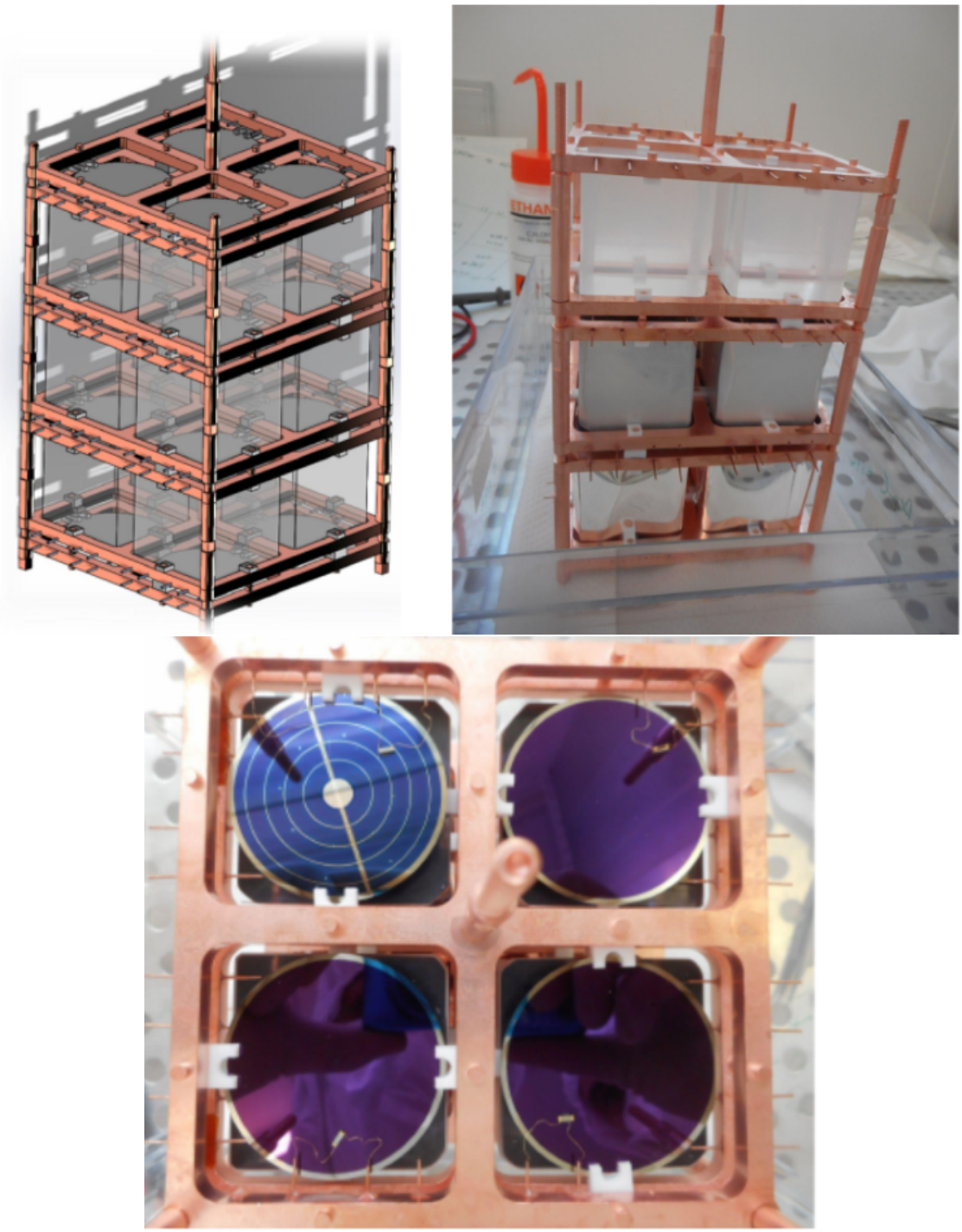

Figure 2.2: *Top left*: schematic view of the 12 modules (scintillating calorimeter + light detector). *Top right*: photo of the assembly. *Bottom*: top view of the 12 modules tower (light detectors in blue). More details are given in reference [104].

Table 2.1: List of rare event searches in which the bolometric technique is applied, and the corresponding most promising isotopes. More details are given in the reference [105].

Application	Main isotopes	References
CEνNS	isotopes with high atomic mass required to enhance the CEνNS rate	[106]
double β decay	^{48}Ca, ^{76}Ge, ^{82}Se, ^{96}Zr, ^{100}Mo, ^{110}Pd, ^{116}Cd, ^{124}Sn, ^{130}Te, ^{136}Xe, ^{150}Nd	[107]
rare β decay	^{50}V, ^{113}Cd, ^{115}In	[108]
rare α decay	^{144}Nd, ^{147,148,149}Sm, ^{151}Eu, ^{152}Gd, ^{174,176}Hf, ^{180}W, ^{184,186,187}Os, ^{190}Pt, ^{209}Bi	[108]
dark matter Weakly Interactive Massive Particles (WIMP)	^{7}Li, ^{11}B, ^{19}F, ^{23}Na, ^{27}Al, ^{73}Ge, ^{111,113}Cd, ^{127}I, ^{209}Bi, ^{155,157}Gd	[109]
solar and supernova neutrinos	^{82}Se, ^{100}Mo, ^{115}In, ^{116}Cd, ^{150}Nd, ^{160}Gd	[110–112]
solar axions	^{7}Li, ^{57}Fe, ^{83}Kr, ^{169}Tm	[113–116]
neutron detection in rare-event searches	^{6}Li, ^{10}B, ^{155,157}Gd	[117–119]

sensor. During my thesis, I had the possibility to work with germanium Neutron Transmutation Doped (NTD) thermistors [120], Magnetic Metallic Calorimeters (MMCs)[121] and doped silicon sensors [122]. The tests conducted with the latter will not be reported in this thesis, since they did not yield satisfactory results.

2.3.1 Neutron Transmutation Doped germanium thermistors

An NTD thermistor is produced starting from the selection of thin germanium wafers ($\sim$50 μm of thickness) characterized by a perfect lattice structure and a high purity, and then exposure to an intense neutrons flux (E_n = 25 eV) generated by a nuclear reactor. This technique, called precisely *Neutron Transmutation Doping*, promotes the neutron capture on stable germanium atoms (A = 70, 74, 76) forming acceptors (reaction 2.12), donors (reaction 2.13) or double donors (reaction 2.14) depending on the isotope involved in the reaction. Being the germanium isotopes identical from the chemical point of view, they are excellently randomly distributed. This, combined with the moderate cross-section that is a consequence of a uniform neutron flux throughout the wafer, ensures the reproducibility of the thermistor, guaranteeing a homogeneous concentration of dopants thanks to which it is possible to avoid resistance variations over many orders of magnitude [120, 123].

$$^{70}_{32}Ge + n \rightarrow ^{71}_{32}Ge \rightarrow ^{71}_{31}Ga + \nu_e \tag{2.12}$$

$$^{74}_{32}Ge + n \rightarrow ^{75}_{32}Ge \rightarrow ^{75}_{33}As + \bar{\nu_e} \tag{2.13}$$

$$\begin{aligned} ^{76}_{32}Ge + n \rightarrow ^{77}_{32}Ge \rightarrow ^{77}_{33}As + \bar{\nu_e} \\ \rightarrow ^{77}_{34}Se + \bar{\nu_e} \end{aligned} \tag{2.14}$$

The concentration of dopants in the wafer depends on the cross-section of the neutron capture and the natural abundance of the isotopes. While the Se concentration is negligible, the expected dopant concentrations are $2.94\times10^{-2}\,\mathrm{cm}^{-3}$ per neutron/cm^2/s and $8.37\times10^{-3}\,\mathrm{cm}^{-3}$per neutron/cm^2/s for Ga and As respectively. In order to produce low noise and highly sensitive sensors, it is important to fine-tune this concentration of dopants (hence, the duration of the exposition to the neutron source). Indeed, if the germanium wafer is poorly doped, at cryogenic temperatures it will behave as an

insulator. On the contrary, if it is excessively doped, it will develop metallic properties becoming insensitive to temperature variations. The perfect amount of dopants is achieved just before reaching the metal-insulator transition (MIT) concentration: the impurities donors (acceptors) introduced in the germanium wafer bring with them new energy levels immediately below the conduction (valence) band; when the concentration of dopants is very close to the MIT one, the wave functions of the conduction electrons start being overlapped. The device properties develop a temperature dependence of its resistance [124, 125]. This introduces a new electric conduction mechanism thanks to which the electrons can move through quantum mechanical tunneling between impurity sites, separated by the Coulomb potential barrier, by emission or absorption of phonons of adequate energy [126]. According to the temperature, we can identify two hopping mechanism regimes:

- at sufficiently high temperatures, the hopping mechanism occurs between the closest impurities empty sites. This case is called *nearest neighbor hopping* (NNH);
- at lower temperatures («10 K), since there is not an abundance of high energy phonons, the dominant mechanism is the *variable range hopping* (VRH): the electrons mainly jump to greater distances in order to find a impurity empty site at approximately the same energy.

The property we employ to monitor the thermistor temperature variations is the resistance $R(T)$ of the doped germanium and it obeys to [127]:

$$R(T) = R_0 \cdot exp\left(\frac{T_0}{T}\right)^{\gamma} \tag{2.15}$$

The equation 2.15 is derived from the resistivity law for VHR:

$$\rho(T) = \rho_0 \cdot exp\left(\frac{T_0}{T}\right)^{\gamma} \tag{2.16}$$

This γ exponent was initially evaluated to be 1/4 by Mott, assuming a constant density of states at the Fermi level. Later, in 975, A. L. Efros and B. I. Shklovskii showed that the Coulomb interactions between electrons are responsible for the formation of a gap in the state's density nearby the Fermi level [128], assigning to γ a value equal to 1/2. Therefore, the parameter γ in the equation 2.15 assumes value 1/2. The R_0 and T_0 parameters are determined experimentally and they characterize the thermistor. In particular, T_0

depends on the dopant concentration and it decreases for higher concentrations, while R_0, depending also on the geometry of the thermistor, is defined as:

$$R_0 = \rho_0 \cdot \frac{L}{S} \tag{2.17}$$

where ρ_0 is the resistivity, L is the distance between the contacts of the thermistor and S is its section. Another parameter characterizing the NTD is the sensitivity that tells us the ability of the device to translate a temperature variation of a fraction of mK into a resistance variation of the device itself. It is defined as:

$$A = \left|\frac{dlog(R(T))}{dlog(T)}\right| = \frac{T}{R(T)} \cdot \frac{dR(T)}{dT} \tag{2.18}$$

The NTDs mainly used for this thesis come from the Beeman (B) series, namely, they are produced following the procedure proposed for the first time in 1996 [123]: the wafer is subjected to a boron ion implantation, subsequent annealing, the deposition of a thin adhesion layer and finally the deposition of two thin gold films at the opposite sides of the thermistor for the electrical contacts.

Once the thermistor is ready, it can be glued directly onto the crystal surface. The glue interface determines the phonon transmission from the absorber to the sensor and, hence, the rise time and the amplitude of the recorded pulses. This is clearly a critical point since we do not have in our laboratory a device that allows a perfect reproducibility of the gluing. A different absorber-thermistor coupling means a different thermal contraction between the two at low temperatures. This leads to different stress on the sensors and, hence, a different resistance-temperature dependence. Moreover, the risk to produce cracks in the absorber increases. To mitigate this effect, the adopted technique to use a pogopin matrix to deposit isolated spots of glue instead of a uniform veil. More details on the gluing procedure and tests are reported in chapter 6.

2.3.2 Metallic Magnetic Calorimeters

Metallic Magnetic Calorimeters (MMCs, Figure 2.3) are envisaged to build microcalorimeter arrays for X-ray space telescopes but find applications also in rare event searches and spectroscopy of biological molecules.

They are a good alternative to NTDs when we need a temperature sensor able to provide a fast response time (below the μs at $T < 50\,mK$) that depends on:

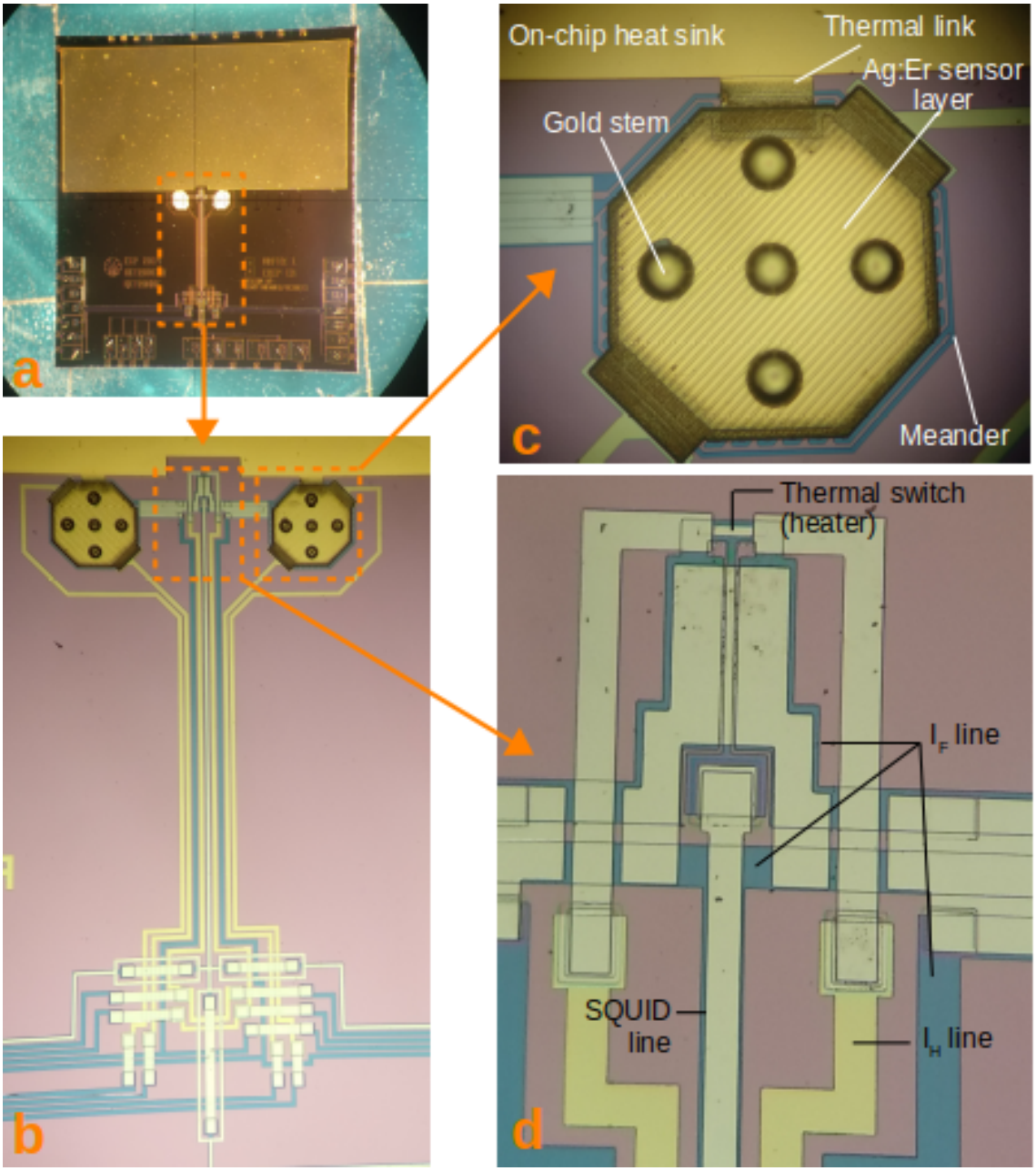

Figure 2.3: Photo of the entire MMC chip (*a*) and magnifications at the microscope (*b, c, d*).

- the properties of the sensor material (more details are given in section 2.3.2.1);
- the properties of the absorber material (very good results are achievable using metallic materials);
- the thermal link between the sensor and the absorber (for fastest response, the interface connecting the two-element must allow the carrying of the heat by the conduction electrons).

These devices are conceived starting from the observation that many materials show a magnetic behavior strongly dependent on the temperature. Of course, not all the materials showing magnetic properties can be used for this purpose: they must be carefully selected in order to optimize the response time and sensitivity of the device.

2.3.2.1 Sensor Materials

MMCs are devices exploiting the magnetization properties of paramagnetic ions diluted in a metallic host. The concentration of paramagnetic ions must be low to avoid spin-spin interactions that, otherwise, could critically affect the sensitivity of the device [129]. The first idea to exploit the *magnetic calorimetry* at low temperatures and the first tests found their origin in the '80s at the Walther Meissner Institut fur Tieftemperaturforschung (Munich, Germany) [130, 131]. The prototypes, based on $4f$ ions implanted into dielectric hosting materials, were not particularly attractive in the rare events search since the dielectrics are characterized by a weak coupling between magnetic moments and phonons that is responsible for a long response time at cryogenic temperatures.

This problem was investigated and faced in 1993, proposing to exploit the strong coupling of conduction electrons and localized $4f$ magnetic moments of metallic materials that can be used as hosts instead of the dielectric ones [132]. However, this choice presents some drawbacks that we have to accept if we want a fast detector response: a higher heat capacity due to the conduction electrons present in the metal, and a reduced magnetization dependence on the temperature variation due to a stronger interaction between the magnetic moments via the Rudermann-Kittel-Kasuja-Yoshida (RKKY) interaction, an indirect spin-spin interaction transmitted by the conduction electrons [133, 134]. Mitigation of these disadvantages can be applied, choosing ions characterized by a

weak interaction with conduction electrons, hence belonging to the $4f$ rare earth series instead of the $3d$ or $4d$ transition metal series and by adjusting the ion concentration.

The MMCs used for this thesis are composed of a few hundred parts per million of erbium ions Er^{3+} in Ag or Au host at the lattice sites.
Being a rare earth element, the paramagnetic property of the Er^{3+}has its origin in the not fully completed $4f$ shell. Moreover, its $4f$ shell being deeply inside the atom (at about 0.3 Å from the nucleus, to compare with the atom average radium is $\sim$1 Å), it is well protected by the $5s$ and $5p$ shells. From this, a strong spin-orbit coupling arises: the ions interact mainly with the external magnetic field. Ag:Er was introduced a few years ago in substitution of Au:Er. Indeed, even if Ag:Er has the disadvantage of a stronger RKKY interaction, it is still considered a better choice than Au:Er which has the more annoying disadvantage of a quadrupole moment of the Au nuclei that leads to an additional heat capacity and to a pulse shape with two-time constants. Another compound is Au:Er: despite it was introduced just few years ago, today it is nearly the only material in use. Even if it has the disadvantage of a stronger RKKY interaction, it is considered a better choice to Au:Er that has the more annoying disadvantage of a quadrupole moment of the Au nuclei, leading to an additional heat capacity and to a pulse shape with two time constants.

2.3.3 Detection principle of an MMC

When the detector absorbs an ionizing radiation, initially energetic electrons are produced. These electrons lose energy very quickly producing secondary electrons that in turn produce high frequency phonons. In metallic absorbers, these high frequency phonons thermalize interacting with the conduction electrons while in dielectrics this process is much slower since the high frequency phonons are mainly thermalized at the crystal surface. This produces a change of temperature ΔT in the absorber. Phonons are therefore thermalized generating a change of temperature also in the sensor. When the paramagnetic material of which the MMC is composed is exposed to a weak magnetic field at low temperatures, its magnetization is strongly sensitive to changes in temperatures, as visible in figure 2.4a: we can detect the particle interaction through the change of magnetization ΔM. With higher temperatures, the magnetization decreases, and vice-versa (figure 2.4). The MMC is magnetically coupled to a dc-SQUID (Superconducting QUantum Interference Device) through a magnetic flux transformer, namely a

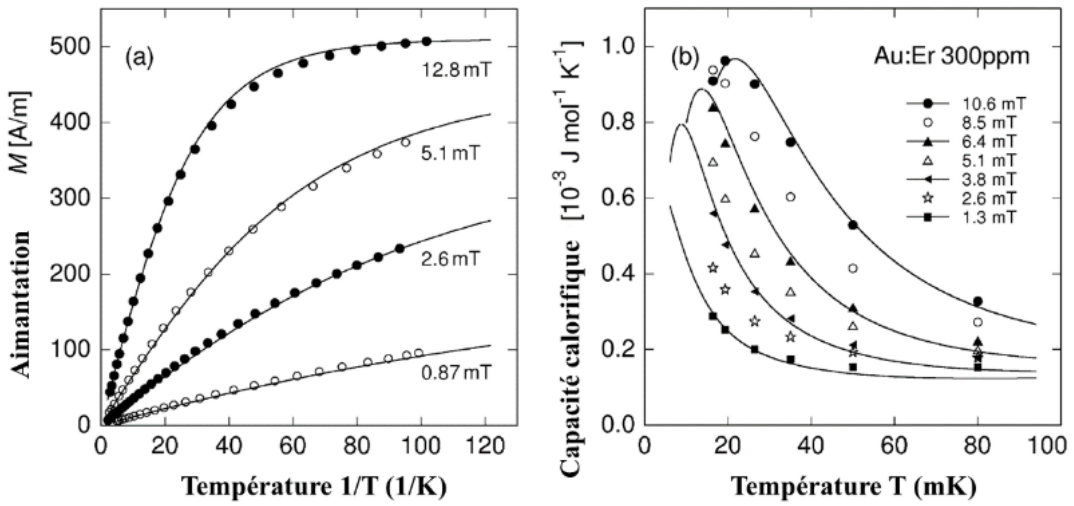

Figure 2.4: Magnetization and specific heat as a function of the temperature T and the inverted temperature $1/T$ respectively of a sensor based on Au:Er with 300 ppm enriched ^{166}Er at different applied magnetic field [135].

closed superconducting circuit composed of a pick-up coil and an input coil. The pick-up coil consists of a meander in superconductive material (generally made of niobium (T_c ~9.2 K) using the lithography technique) running along the MMC paramagnetic surface to maximize the magnetic coupling between the two (figure 2.5).

The meander reads the variation of magnetization ΔM and converts it into a magnetic flux variation $\Delta\Phi_s$ [135]:

$$\frac{\Delta\Phi_s}{\Delta E} = \frac{v}{C_a + C_s} \cdot \mu_0 \frac{G}{p} \cdot \frac{\Delta M}{\Delta T} \tag{2.19}$$

where v is the volume of the sensor, C_a is the absorber heat capacity, $< C_s >$ is the sensor heat capacity, G is the magnetic coupling constant that depends on the geometry of the sensor and input coil, p is the meander pitch, and μ_0 is the vacuum permeability. In order to magnetize the sensor, it is necessary to run a current I_F, the so-called *field current*, through the meander coil, thus generating a local magnetic field. I_F is injected and frozen with the help of a thermal switch (or heater). The change of flux in the pick-up coil is therefore translated into a flux change $\Delta\Phi_s$ through the SQUID loop by the input coil that is overlapped on the dc-SQUID. A dc-SQUIDs is a superconducting loop interrupted by two Josephson junctions (Figure 2.6 *a*), i.e. thin insulating barriers that

create a weak link between the two adjoined superconducting superconducting half-loops allowing the passage of Cooper pairs via the tunneling effect. Each Josephson junction has a shunt resistor R to avoid the hysteresis of the superconducting material and is characterized by a critical current I_c. When we apply to the SQUID a bias current I_b below I_c, the insulating barriers are thin enough to let pass the Cooper pairs via tunneling effect without having any dissipation effect. On the contrary, applying a I_b just above the critical one, a voltage across the tunnel barriers will appear (Figure 2.6, *b*). The critical current I_c and the voltage across the SQUID vary with the magnetic flux and this variation has a periodical behavior with a period equal to the flux quantum:

$$\Phi_0 = \frac{h}{2e} = 2.07 \times 10^{-15}\ Vs \tag{2.20}$$

Tuning I_b, we fix the working point w, namely the voltage at which the SQUID works properly (Figure 2.6, *c*).

Then, the voltage measured at SQUID ends is pre-amplified and integrated. The deviation of this voltage from the working point is transformed by a negative magnetic flux $-\Phi_{diff}$ by a resistor and a feedback coil to keep the working point to the fixed value, and to linearize the SQUID response.

2.4 Heater

Besides the NTD, a heater is glued like in the CUORE detector assembly [138]. The prototypes presented in this thesis consist of a heavily doped silicon semiconductor with typical dimensions of $2.33 \times 2.40 \times 0.52\,\mathrm{mm}^3$ silicon [139]. This element becomes very important in case of temperature fluctuations, in particular for long measurements, since it allows the temperature stabilization.
The heater is connected to a pulse. Periodically injecting signals of well-known voltage, therefore their amplitude, we create in the data acquisition a non-physical population thanks to which we can monitor the amplitude drift and, eventually, correct it. From this procedure, we can benefit an energy resolution improvement [140].
An example of a stabilization procedure is given in chapter 6.

2.5 Thermal model

A thermal model provides a valid description of the calorimeter behavior. It is usually used to predict the performances of the detector and, if necessary, which modification to introduce to improve them.

2.5.1 NTD based calorimeters

In figure 2.7, the thermal circuit of a calorimeter on which the model is based. It is composed of 3 nodes (absorber, sensor electron system and sensor lattice system), each of them characterized by a temperature (T_a, T_e and T_{ph} respectively) and a heat capacity (C_a, C_e and C_{ph}). In particular, C_a and C_{ph} follow the equation 2.7 while C_e is proportional to the temperature. The heat sink is at a base temperature T_b while its conductance is assumed infinite.

The model takes into account the electron-phonon decoupling among which we can imagine a finite thermal conductance G_{e-ph} whose value depends on the sensor size. The conductivity, described by equation 2.21, is shaped by the dimensionless exponent $\alpha \sim 5$ [141].

$$G(T) = g_0 T^{\alpha} \tag{2.21}$$

The conductance between the sensor and the lattice G_{glue} depends on the glue interface, hence on the reproducibility of the gluing procedure. Assuming to have perfect glue spots with 50 μm of thickness and 1 mm of diameter, we expect G_{glue} to be $2.6\times10^{-3}\ T[K]^{3.08}$ W/K [142].

G_{PTFE} is the conductance provided by the PTFE elements clamping the absorber to the copper holder (i.e. the heat sink). It depends on the conductance of the surfaces in contact with the PTFE, namely the copper holder and the crystal, and of the PTFE itself. Compared to the other conductances of the thermal model, it assumes very small values (i.e. weak conductance). Because of this, the thermal equilibrium between the absorber and the sensor is reachable before the heat produced in response to the particle interaction is released from the absorber to the heat sink. The measured G_{PTFE} value

for 10 g of material at T >30 mK is $1.2\times10^{-4}\ T[K]^{2.04}$ W/K [142].

G_{wire} is the conductance of the bonding wires that, in addition, provide the electrical connection of the calorimeter, and ensure a thermal connection between the heat sink and the sensor. In the specific case of the NTD, G_{wire} depends on the thermal boundary resistances[1] between the germanium (material of which the sensor is made), the gold deposited to make the Ohmic contacts, and the gold wires. It has been experimentally measured to be $3.6\times10^{-5}\ T[K]^{2.419}$ W/K/mm^2 [142].

2.5.1.1 Simulations

Ideally, all the components of the detector are at the same base temperature. In reality, there are some micro-vibrations due to background powers and electromagnetic influences responsible for eddy currents that lead to a not-perfect thermal equilibrium between all the components even in the static condition. A simulation can take into account all these complications in the thermal model providing us in advance the load curves, telling us the calorimeter working point (static behavior), and reconstructing the shape of the pulses (dynamic behavior). In figure 2.8, an example of a simulated IV curve and pulse shape obtained by means of a simulation program in C coding language, originally written for the CUORICINO experiment [144].

2.5.2 MMC based calorimeters

While in reality MMCs are more complicated devices compared to the NTDs, we can derive a thermal model considering an even more simplified detector as shown in figure 2.9: an absorber (heat capacity C_a), in which the particles interact, strongly thermally coupled to an MMC (heat capacity C_s) via a thermal conductance G_{as}. The sensor reads the temperature variation of the absorber: when the energy released in the absorber by the interacting particle is converted into heat, the detector experiences a change of temperature ΔT (equation 2.22). The sensor is linked to a heat sink at temperature T_0 via a weak thermal conductance G_{sb}. Each event in the crystal corresponds to a pulse, the structure of which is characterized by two time constants: a rise-time τ_r and (at least) a decay-time τ_d that depend on the thermal conductances and the heat capacities.

[1] ratio between the temperature discontinuity at an interface and the power per unit area flowing through the interface [143].

$$\Delta T = \frac{E}{C_a + C_s} = \frac{E}{C} \tag{2.22}$$

2.5.2.1 Two heat capacities model and signal size

A large signal size is required in order to achieve a high energy resolution. At the thermal equilibrium, figure 2.9 can be represented by the following system of differential equations:

$$\begin{cases} C_a \dot{T_a} = -(T_a - T_s) \cdot G_{as} \\ C_s \dot{T_s} = -(T_S - T_a) \cdot G_{as} - (T_S - T_0) \cdot G_{sb} \end{cases} \tag{2.23}$$

where T_a and T_s are the absorber and sensor temperatures respectively, and whose matrix of temperature variations with respect to T_0 is:

$$\begin{pmatrix} \Delta\dot{T_a} \\ \Delta\dot{T_s} \end{pmatrix} = \begin{pmatrix} -\frac{G_{as}}{C_a} & \frac{G_{as}}{C_a} \\ \frac{G_{as}}{C_s} & -\frac{G_{as}+G_{sb}}{C_s} \end{pmatrix} \begin{pmatrix} \Delta T_a \\ \Delta T_S \end{pmatrix} \tag{2.24}$$

The determinant of the matrix is:

$$\begin{aligned} det \begin{pmatrix} -\frac{G_{as}}{C_a} & \frac{G_{as}}{C_a} \\ \frac{G_{as}}{C_s} & -\frac{G_{as}+G_{sb}}{C_s} \end{pmatrix} &= \left(\frac{G_{as}}{Ca} \cdot \frac{G_{as}+G_{sb}}{C_s}\right) - \left(\frac{G_{as}}{C_a} \cdot \frac{G_{as}}{C_s}\right) = \\ &= \frac{G_{as}G_{sb}}{C_s C_a} > 0 \end{aligned} \tag{2.25}$$

Therefore:

- being the determinant non-zero, the solution of a system of differential equations is an exponential linear combination of the eigenvalues λ_1 and λ_2 of the matrix 2.25;
- being the determinant positive, the eigenvalues have the same sign;
- being the matrix trace negative, the eigenvalues are negative as well.

$$\begin{cases} \lambda_1 + \lambda_2 = -\left(\frac{G_{as}+G_{sb}}{C_s} + \frac{G_{as}}{C_a}\right) < 0 \\ \lambda_1 \cdot \lambda_2 = \frac{G_{as}G_{sb}}{C_s C_a} > 0 \end{cases} \tag{2.26}$$

Let's consider now a particle interacting with the absorber: it will release energy E in the crystal causing a temperature change in the detector ΔT_S that we can express as

a function of the detector thermal conductances, the heat capacities, and the time t as following:

$$\Delta T_S(t-t_0) = T_S(t-t_0) - T_0 = \frac{E}{C_a} \cdot \frac{\tau_r \cdot \tau_d}{\tau_r - \tau_d} \cdot \frac{G_{as}}{G_{sb}} \left(e^{-\frac{t-t_0}{\tau_r}} - e^{\frac{t-t_0}{\tau_d}} \right) \tag{2.27}$$

where the τ_r and τ_d are defined in equations 2.28 and 2.29 respectively.

$$\begin{aligned} \tau_r &= -\frac{1}{\lambda_1} = \\ &= 2 \left[\left(\frac{G_{as}}{C_a} + \frac{G_{as}+G_{sb}}{C_s} \right) + \sqrt{\left(\frac{G_{as}}{C_a} + \frac{G_{as}+G_{sb}}{C_s} \right)^2 - 4 \left(\frac{G_{as}+G_{sb}}{C_a \cdot C_s} \right)} \right]^{-1} \end{aligned} \tag{2.28}$$

$$\begin{aligned} \tau_d &= -\frac{1}{\lambda_2} = \\ &= 2 \left[\left(\frac{G_{as}}{C_a} + \frac{G_{as}+G_{sb}}{C_s} \right) - \sqrt{\left(\frac{G_{as}}{C_a} + \frac{G_{as}+G_{sb}}{C_s} \right)^2 - 4 \left(\frac{G_{as}+G_{sb}}{C_a \cdot C_s} \right)} \right]^{-1} \end{aligned} \tag{2.29}$$

According to the detector thermal conductances, we can distinguish two different pulse shapes and amplitudes:

- if $G_{as} >> G_{sb}$ and assuming $C_a = C_s = C/2$, the rise-time and decay-time expressions can be simplified as:

$$\begin{cases} \tau_r \approx \frac{C}{4G_{as}} \\ \tau_d \approx \frac{C}{G_{sb}} \end{cases} \tag{2.30}$$

  namely, the rise-time of the pulse depends on the thermal link between absorber and sensor. The maximum sensor temperature variation ΔT_S is equal to E/C. These conditions (i.e. $G_{as} >> G_{sb}$ combined to $C_a = C_s = C/2$) guarantees the best reachable energy resolution;

- on the contrary, if $G_{as} << G_{sb}$ we can approximate the expressions 2.28 and 2.29 as:

$$\begin{cases} \tau_r \approx \frac{C_s}{G_{sb}} \\ \tau_d \approx \frac{C_a}{G_{as}} \end{cases} \tag{2.31}$$

namely, the rise-time becomes dependent on the sensor and the thermal link between the heat sink and the sensor while the decay-time depends on the absorber and its thermal link with the sensor. This behavior is counterintuitive since in bolometry we use to think that the rise-time is determined by the link between sensor and absorber. Moreover, these dependencies are responsible for a signal amplitude reduction and, therefore, the energy resolution of the detector is degraded. An example of data interpretable with this behavior will be presented in chapter 7.

2.6 Dilution refrigerators

A cryostat is a cooling down system based on a refrigeration unit able to reach cryogenic temperatures. It is fundamental to operate calorimeters at low temperature since we need to reduce the detector heat capacity sufficiently to be sensitive to the change of temperatures of the absorber. The idea of the dilution refrigerator principle was suggested by H. London in 1952. The first prototype of a dilution refrigerator was conceived in 1962 and developed in 1964 in the Kamerlingh Onnes Laboratorium at the Leiden University. It was able to reach a base temperature of 220 mK [145]. The first commercial dilution refrigerator was realized by Oxford in 1967, asserting itself from that moment as one of the main cryostat producers. Since then, many the principles and methods of dilution refrigerators have been developed and improved up to reach base temperatures of a few mK [146].
The work reported in this thesis was realized using three different cryostats that we can summarize in two different families:

- a wet dilution refrigerator to perform the measurement of BASKET with MMC prototypes;
- two dry refrigerators to test the BASKET with NTD detectors and the NUCLEUS germanium outer veto prototype.

2.6.1 The ^{3}He/^{4}He mixture

Low temperatures are achieved thanks to a mixture obtained combining a Fermi liquid, the ^{3}He, with a superfluid, the ^{4}He, at low temperatures. The ^{4}He is a product of the petrol extraction and very abundant while the ^{3}He, produced from the tritium disintegration (reaction 2.32), is rare and very expensive ($\sim$3 k€/liter of gas at NTP).

$$\begin{aligned} {}^6Li + n \rightarrow {}^4He + \text{tritium} \\ \text{tritium} \rightarrow {}^3He + \beta \end{aligned} \tag{2.32}$$

To well understand the potential of this mixture, let's consider figure 2.10.

Let's assume to have a mixture at 2 K where just the 40 % is ^{3}He and let's start cooling down. In the beginning, the mixture is perfectly homogeneous. Both ^{3}He and ^{4}He show normal fluid behavior. At ∼1.5 K, the λ temperature T_λ is reached and the ^{4}He enters the superfluid regime. Continuing cooling down, we reach a critical temperature at ∼750 mK: the mixture starts to separate itself into two components:

- the *concentrated phase*: it is the lighter component rich of ^{3}He in the liquid state;
- the *dilute phase*: it is the heavier part. Here ^{3}He is in the gaseous state. The ^{4}He bulk is totally inert.

The concentration of ^{3}He in the two components depends on the temperature. At this stage, a thin layer of liquid composed of approximately 80% of ^{3}He will appear at the top of the mixture tank. Proceeding with the cooling down, the volume of the concentrated phase will increase and its percentage of ^{3}He as well, while they will decrease in the dilute phase. At 500 mK, the concentration of ^{3}He in the dilute and condensed phases are respectively 22% and 90%. At the absolute zero, they become 6.6% and 100%. The flowing of ^{3}He in the dilution unit is possible thanks to the superfluid nature of ^{4}He. Indeed, being in a superfluid state and at rest, it let easily pass through it the ^{3}He. While ^{3}He is pushed by a pressure gradient that balances the viscous forces, the ^{4}He is also subjected to an osmotic pressure gradient. The active role in the cooling down is played by the ^{3}He isotope.

2.6.2 The ^{3}He journey

In the light of the above consideration, namely that the working fluid is the ^{3}He, we will focus on its journey in the cryostat [148].

- the ^{3}He, stored in the mixture tank that is permanently connected to the cryostat, can flow in the cryogenic apparatus thanks to a system of pumps at room temperature that brings the mixture pressure to a few hundreds of mbar;

- after a pre-cooling at ∼4.2 K (in a cyclical way through a refrigerator cooler, usually a Pulse Tube (PT) -*dry dilution refrigerator*- or in a continuous way through a Liquid Helium (LHe) bath -*wet dilution refrigerator*), the ^{3}He enters the vacuum chamber;
- in the case of a wet cryostat, the ^{3}He reaches the 1 K pot where it is further down the at ∼1.2 K by a bath of pumped ^{4}He (i.e. 1 K bath). At this temperature, the ^{3}He starts condensing being its pressure much larger than the ^{3}He vapor pressure. The heat released during this change of state is removed through the 1 K bath. In the case of a dry dilution refrigerator, instead of the 1 K pot there is a Joule Thomson heat exchanger that cools down the ^{3}He via the homonymous effect;
- once condensed, the ^{3}He flows through the main impedance: a capillary tube characterized by a high flow resistance. The main impedance makes certain that the pressure is large enough so that the condensation can happen at 1.2 K;
- the ^{3}He reaches the still that is at ∼700 mK. Since at this temperature the pressure is large enough to let the ^{3}He boil again, in order to avoid it the ^{3}He pass through a secondary impedance characterized by a low impedance so that the pressure of the still heat exchanger is much larger than the vapor pressure;
- the ^{3}He flows through a counterflow heat exchanger. These devices, at temperatures above 50 mK, are usually double tube heat exchanger type, namely, it consists of two concentric tubes. In the inner one, the fluid we want to cool downflows, while in the outer one there is the refrigerating fluid (the ^{3}He that almost at the end of the journey, goes back to the still). At lower temperatures, they must have a larger surface area in order to reduce the Kapitza resistance;
- the ^{3}He, cooled down at a temperature of a few mK, enters the mixing chamber. Here the dilute and concentrated phases separate and the ^{3}He, passing the phase boundary, starts diluting;
- the diluted ^{3}He leaves the mixing chamber. During its ascent to the still, it cools the warmer ^{3}He in the concentrated phase that is going to the mixing chamber;
- when the ^{3}He arrives in the still, its presence in the dilute phase is reduced from 6.6% to 0.7%. The rest is ^{4}He. The continuous ^{3}He flow in the cryostat is ensured by a heating power applied to the still.

2.6.3 How the magic happens

During the work presented in this thesis, three different cryostats were used.

The first one, the so-called *Ulysse*, is a dilution refrigerator at IJClab (Orsay, France). It is designed in 1999 by CNRS and Air Liquide and made operational in 2003 at the laboratory of Insubria (Como, Italy). Ulysse is a dry cryostat based on a pulse tube cryocooler. Some improvements were applied to the condensing system in 2012 in order to make faster the mixture condensation. Ulysse is composed of four copper screens, each one fixed to a specific temperature stage. The most external one is the Outer Vacuum Chamber (OVC) screen. It is kept at room temperature. Thanks to the high vacuum to which it is subjected, it provides the first insulation safeguarding the inner vessels against heat convection and conduction originated from the experimental environment. However, it doesn't protect the cryogenic volume from the 300 K radiation, therefore a multi-layer insulation system similar to the one used in dewars is needed. It consists of several thin layers ($\sim$6 μm) of reflecting material, Kapton or Mylar, coated on one or both sides with a thin metallic layer, usually aluminum or silver. It presents a perforated structure to facilitate high vacuum pumping. In order to reduce the conductance between each reflecting layer, there is a net-like textiles interlayer made of a low thermally conductive material.

Immediately after the OVC, we find in sequence the 80 K screen and the Inner Vacuum Chamber (IVC). The IVC is a second high vacuum room kept at 4 K thanks to the pulse tube cryocooler. This volume contains the dilution unit circuit and, therefore, the 1 K, 50 mK vessels and the mixing chamber where the calorimeters are fixed and kept at the base temperature.

The second cryostat, named *Actuator*, is also located at IJClab. It is a dry cryostat with similar features to Ulysse but it has just one Vacuum Chamber.

The third cryostat, located at the LNHB laboratory (LIST/CEA, Saclay, France) is a wet dilution refrigerator. As Ulysse, it has the Double Vacuum Chamber. Clearly, being a wet dilution refrigerator, the procedure followed to cool down the cryostat is different. To avoid to loose too much helium in evaporation, first of all, we need to fill the helium bath with nitrogen, which is less expensive and has a boiling temperature of 77 K. Some helium in the gaseous state is injected into the IVC to create a thermal bridge between the vessel and the elements in the chamber. Then, approximately 3 hours after, we are

ready to remove the residual nitrogen and fill the helium bath with liquid helium.

2.6.4 Wet dilution refrigerators vs. dry dilution refrigerators

In this section, a comparison between the two types of dilution refrigerators is reported, taking into account different aspects.

- **costs**
  Compared to dry cryostats, the necessity to pre-cool an entire cryogenic system is a not negligible cost in the long run. Indeed, while the ^{3}He/^{4}He mixture, flowing in a closed system, is bought only once, the liquid helium used for the helium bath is a recurring charge. During its transfer in the cryostat, despite careful handling of the cryogenic fluid liquid, part of it is inevitably lost because of the low evaporation temperature. Moreover, once the liquid helium is delivered by the producer, a countdown starts: even if it is stored in a proper dewar, there is always slow evaporation of the liquid helium. The amount of liquid helium used is approximately 10 liters/day;

- **necessity of refilling**
  The helium evaporates very easily (the boiling temperature at atmospheric pressure: 4.2 K), therefore it is necessary to refill the LHe bath very often (approximately every 4 days) to avoid the natural heating up of the cryostat and the impairment of the data acquisition. In short, a wet dilution refrigerator needs continuous maintenance. Furthermore, each refilling of the cryostat takes time and often the data taken during the refill must be removed. On the contrary, a dry cryostat doesn't need so often maintenance since it is just necessary to plug the pulse tube into the current and forget about it;

- **vibrations**
  In a wet dilution refrigerator, the only possible source of vibration coming from the cryostat itself is due to the boiling of the liquid helium. In the case of a dry cryostat, the mechanical vibrations are the dominant noise and very much stronger than those in a wet refrigerator. They are produced by the repetitive expansion and contraction of stainless steel tubes induced by the compressed and decompressed gas inside [149].

2.7 Noise mitigation in the cryogenic system

It is fundamental to minimize the source of noise that could affect the low-frequency region where the bolometric signal is expected (a few tens of Hz) [150].

We can distinguish two different families of noise:

- **intrinsic noise**, inevitable since it is characteristic of the detector itself. There are two main contributions. The first one is the Johnson noise, and it is due to the charge carriers fluctuations in the conductive elements. The second one is the thermodynamic noise: in the case of complete thermalization, the intrinsic energy resolution is limited by fluctuations of the number of thermal phonons exchanged with the heat sink through the conductance K. This causes energy fluctuations, hence temperature fluctuations in the absorber and, therefore, an intrinsic detector noise. The intrinsic noise sets the lowest achievable theoretical limit for the energy resolution [151];

- **extrinsic noise**. It is generated by vibrations introduced by the cryogenic system, the read-out systems, electromagnetic interferences, microphonism, or activities external to the laboratory.

In this section, we want to discuss the main cautions one should take into account in order to minimize the probability to be affected by some extra noise source generated by the cryogenic system.

Decoupling system

Any mechanical vibrations can affect the detector performance. The adoption of a system decoupling the calorimeters from the cryostat mixing chamber can drastically mitigate them. It is made up of springs carefully chosen in terms of elastic constants, to uphold the detector weight, and elongation, to avoid any contact between the detector itself and the mixing chamber vessel that could potentially introduce a thermal short [152–154]. When the calorimeters are decoupled from the mixing chamber, it is therefore important the introduction of a strong thermal link to bring the calorimeters to the base temperature. It can be ensured through some soft conducting elements, such as copper bands or braids.

Absorber fastening

During the detector assembly phase, we must verify that the crystal is well fixed with materials not heavily sensitive to thermal contractions at cryogenic temperatures. In fact, if the absorber is not properly fastened, it will experience more strongly any vibrations, affecting its performance. Examples of materials used to ensure a good clamping are small shaped elements in polytetrafluoroethylene (the solution chosen for all the prototypes described in this thesis) or small spheres in sapphire [155, 156].

Cabling

The wires vibration can introduce some friction responsible for the formation of random charges that are responsible for extra noise. Therefore, it is good practice to fix the wires with the help of some copper tape or Teflon tape, in order to make sure that the detector wires are not free to move

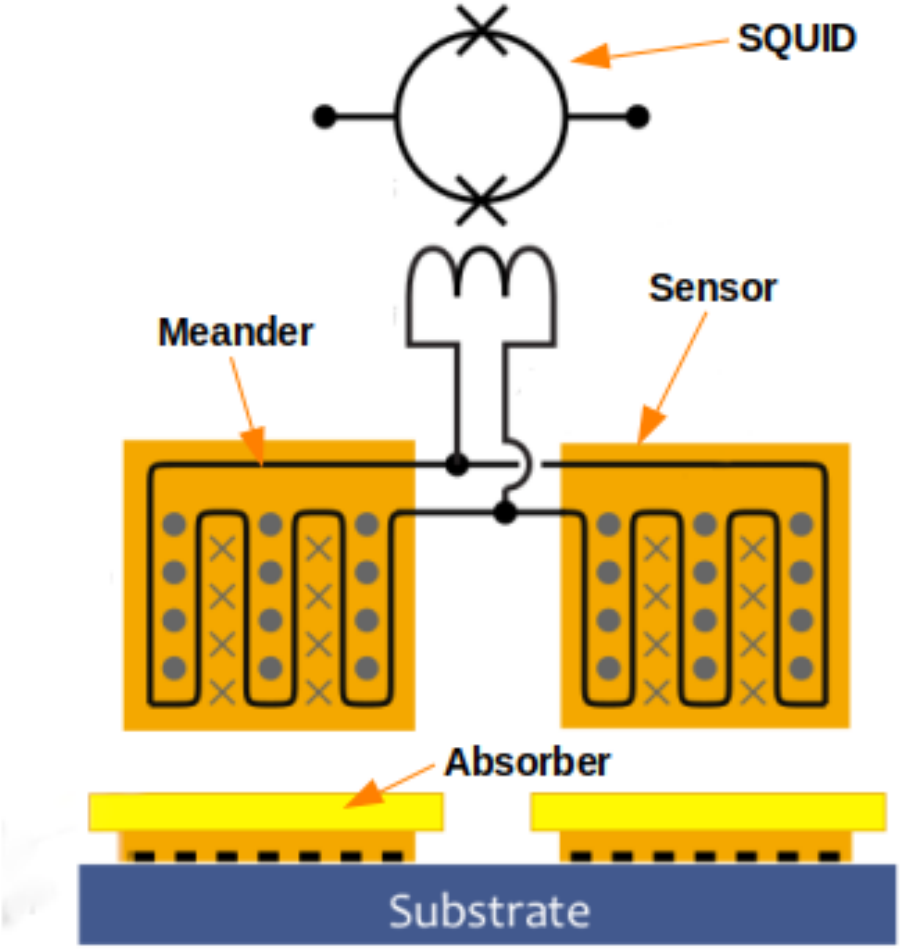

Figure 2.5: Schematic rappresentation of an MMC sensor onto two meander-shaped pick up coils, magnetically coupled to a dc-SQUID [136]. The MMC chips used for this thesis have two paramagnetic sensors, each one with its own pick-up coil. The double meander is used to freeze the field current I_F in the circuit (formed by the two meanders) and avoid I_F flowing in the input coil. The magnetic flux corresponding to the two meanders has an opposite sign. For our applications, just one of them was thermally linked to the absorber.

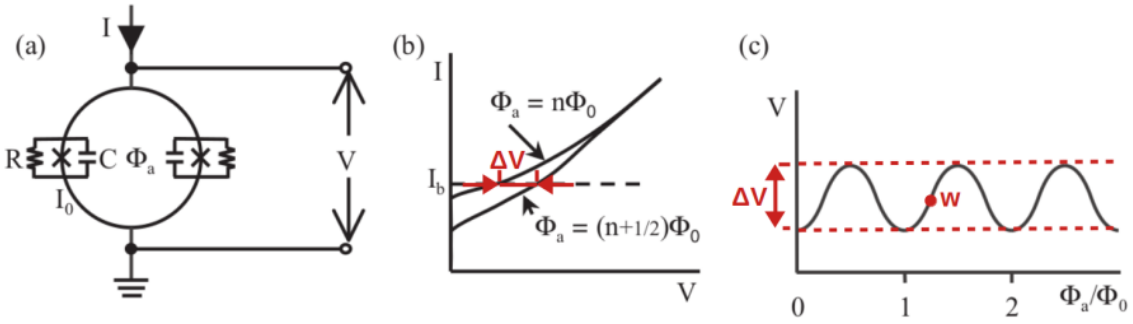

Figure 2.6: *a*: schematic representation of a dc-SQUID; *b*: current-voltage characteristics at integer and half-integer values of applied flux. Set a current $I_b > I_c$, a voltage difference ΔV appears; *c*: voltage vs. flux Φ_a/Φ_0 for constant bias current I_b. The working point w is set by I_b [137].

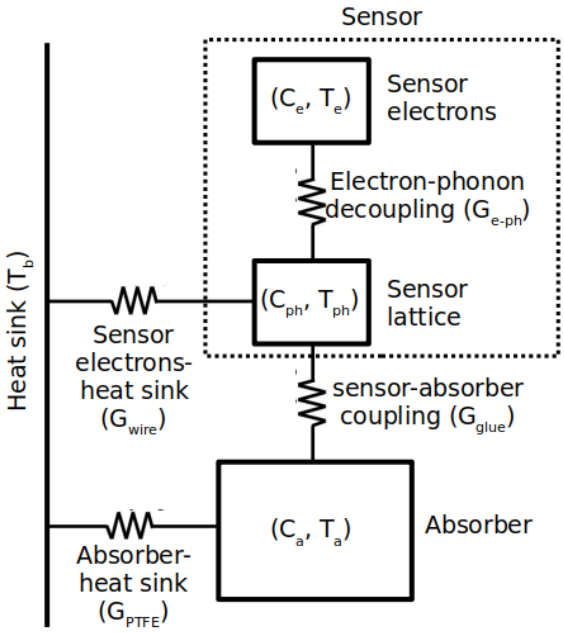

Figure 2.7: Thermal scheme of a calorimeter with NTD sensor. More details in the text.

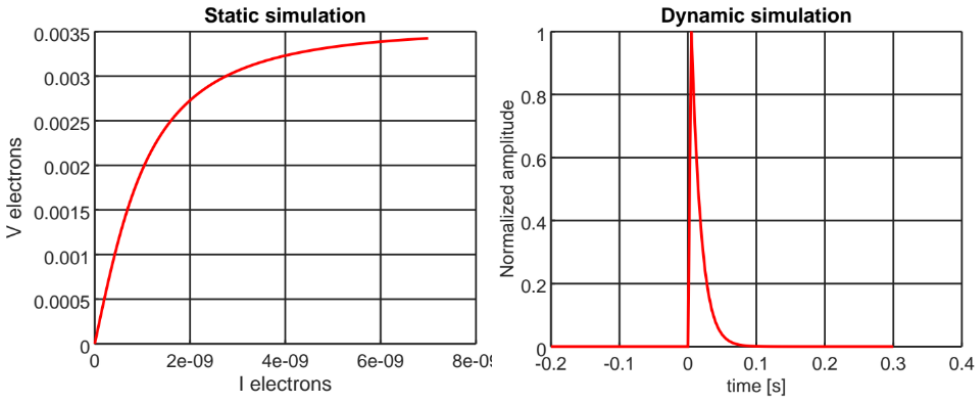

Figure 2.8: Example of static and dynamic simulations for a calorimeter composed of 1 cm^3 Li_2WO_4 crystal coupled to a 34B NTD (T-shaped) series through 1 glue spot.

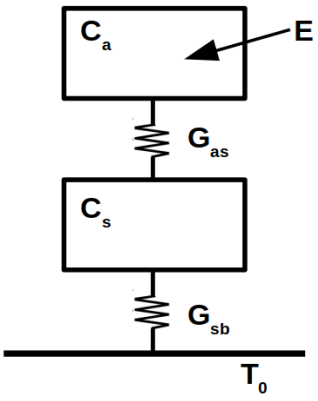

Figure 2.9: Scheme of a simplified cryogenic assuming to have an MMC sensor as the thermometer.

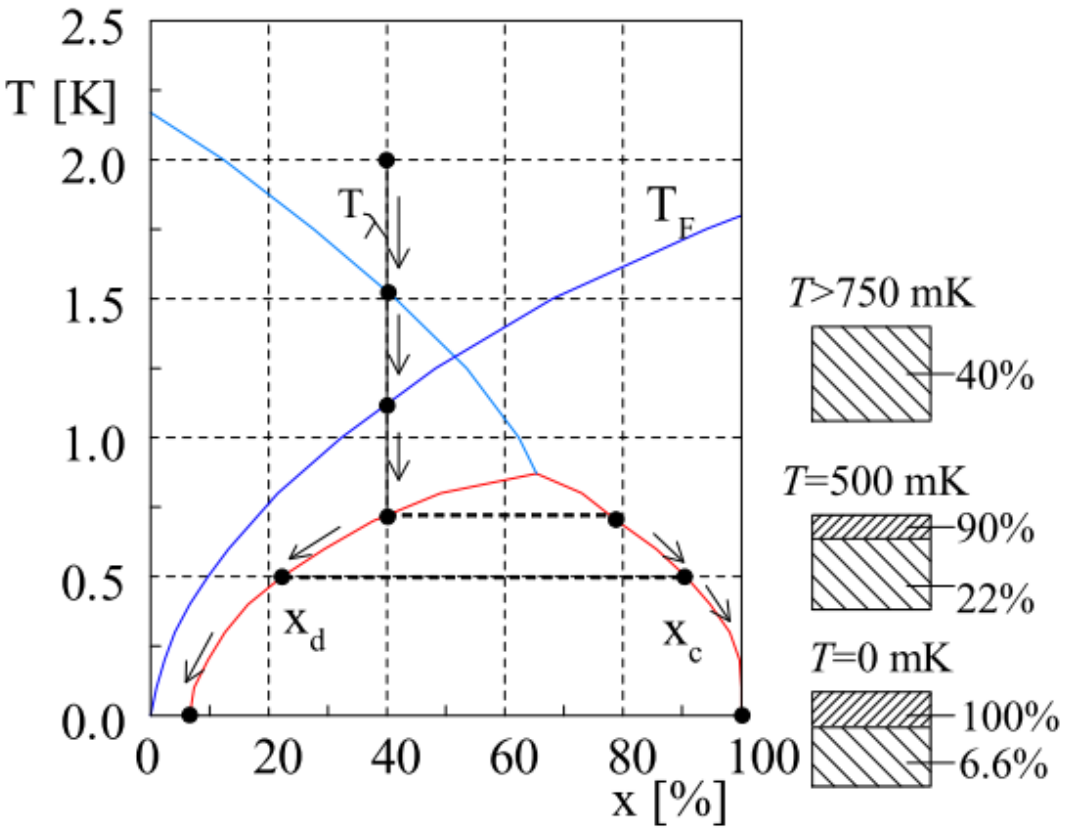

Figure 2.10: Phase diagram of the ^{3}He/^{4}He mixture: the λ line describe the ^{4}He superfluid transition temperature T_λ, while the ^{3}He is well described by the Fermi temperature line T_F [147].

Chapter 3

Analysis tools

All the data for this thesis are collected with the streaming technique: the data are recorded continuously, providing the full information in the output. This method is useful since allows checking and reprocessing of data but, compared to the triggering technique, it requires more memory space and time for the analysis.
In this chapter, I present the main analysis tools used to reconstruct the main information of the stored physical events.

3.1 Argonauts software

Argonauts is an offline analysis software based on Matlab and developed at IJCLab [157]. It is based on the Gatti-Manfredi optimum filter, a method that does not preserve the pulse shape but allows to maximize the signal-to-noise ratio and, hence, extract the best evaluation of the amplitude of the pulses [158].
The data are processed in the following way:

- we set the length of the pulse window: it must be sufficiently large to contain completely a single thermal pulse;

- we build a mean pulse by selecting manually a certain number of pulses belonging to a chosen energy region (in our case, the gamma energy region) and averaging them to minimize the impact of noise (figure 3.1). Similarly, the mean noise power spectrum is built by averaging the power spectra of a set of data windows free from any signals. This step is fundamental in order to provide the noise and

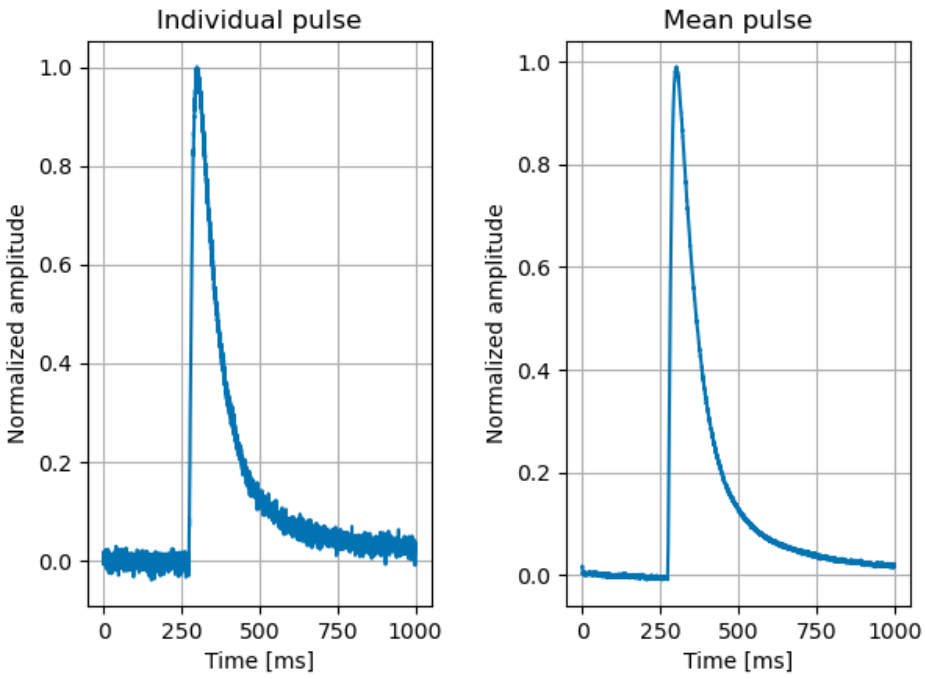

Figure 3.1: *Left*: example of individual pulse eligible for the signal template. *Right*: example of mean pulse built with 15 pulse candidates and used as template in the analysis.

signal templates used to build the optimum filter, and determine the quality of the analysis;

- the entire data acquisition is scanned to identify pulses and tag them as events. This is possible by carefully setting an amplitude *threshold*. It must be sufficiently low to detect also the smallest pulses. During this phase, we must be careful to not pick up also any noise fluctuations from the baseline, such as cross-talks or electrical spikes. We usually set a threshold that is five times the standard deviation of the baseline RMS. In order to improve the signal-to-noise ratio, the triggered events then undergo the Gatti-Manfredi optimum filter, meaning the transfer function:

$$H(\omega) = \frac{S_m(\omega)}{|N(\omega)^2|} e^{-i\omega\tau_m} \tag{3.1}$$

where $S_m(\omega)$ is the Fourier transform of a mean pulse, $N(\omega)$ is the noise power spectrum. We do not have to manually tune any parameter at this stage. A fast

Fourier transformation is automatically applied to the recorded data thanks to an algorithm that is widely described in reference [157]. The effect of the Gatti-Manfredi is the symmetrization of the pulse with respect to the maximum. If a high energy pulse is triggered, after the filtering it could show symmetrical lobes above zero. To avoid this effect, a second parameter, the *Pearson correlation coefficient*, is set: it expresses with a value between 0 and 1 how much similar are a transformed individual pulse above the threshold and the pulse template. Only the events with correlation above the chosen value are registered as events. Since different interacting particles show different pulse shapes, the correlation must be chosen carefully.

The output file is an n-tuple where each line corresponds to an event described by fourteen parameters, derived from both the raw and the filtered pulse. Since the filtered pulse is symmetrical, the extraction of the main information is easier compared to the raw pulse [159]. The main parameters used to characterize the detectors presented in this thesis are analysis are the following:

- the *trigger position*, i.e. the position of the maximum of the pulse in the data stream. It can be used to derive the time information;
- the *raw amplitude* is an average value evaluated around the maximum amplitude of the raw pulse;
- the *filtered amplitude* is the maximum amplitude of the filtered pulse in the time domain;
- the *baseline level* is the signal average in a time window before a pulse (to avoid any contribution of pulses tail);
- the *fitted baseline* is the linear fit constant term of the individual filtered pulse as a function of the filtered reference pulse;
- the *correlation parameter* expresses how close the individual filtered pulse is to the reference one;
- the *decay time* corresponds to the time necessary for the signal to decrease from 90% of the maximum amplitude to 30%;

- the *rise time* is the time necessary for the signal to reach the 90% of the maximum amplitude from the 10%. It depends on the sensor sensitivity to athermal or thermal phonons: athermal phonon sensitive thermistors usually show events featured by a rise-time shorter compared to the ones of thermal phonons sensitive thermistors;

- the *fitted amplitude*. It is obtained starting from an individual pulse and an averaged pulse (usually dominated by the contribution of bulk events) with maximum amplitude normalized to 1. They are synchronized at their maximum (figure 3.2) [151]. At every instant t_i, the amplitudes of mean pulse $m_i = m(t_i)$ and individual pulse $r_i = r(t_i)$ are sampled. By plotting the r_i amplitudes versus the corresponding m_i values, we obtain roughly a straight distribution to which a linear fit ($r = k_1 \cdot m + k_2$) is applied. Consequently, we found two parameters:

  - the fit intercept k_2 that assumes null value when the mean pulse and the individual pulse have exactly the same shape;
  - the fit slope k_1, namely the so-called fitted amplitude. Ideally, if the individual pulse has a shape identical to one of the mean pulse, the fitted and the filtered amplitudes have the same value.

Among all these parameters, rise-time and fitted amplitude are the two most suitable parameters to perform a particle discrimination since α particles generate pulses very different in shape from the γ and β one. Studies on $0\nu\beta\beta$ detector prototypes entirely based on these two parameters are reported in reference [160]. In this thesis, examples of particle discrimination are presented as well, for the identification of ^{6}Li(n,t)α events.

If the double read-out is adopted, the procedure to follow for the light detector data treatment is slightly different. First, the heat channel is processed as described above, and then it is the turn of the light channel. Indeed, if the double read-out technique is chosen, it means that we are interested to search for heat-light coincidences. This is possible by uploading directly in Argonauts the heat trigger file (namely, a file automatically generated during the identification of the events) in which the position of the tagged pulses in the data stream is recorded. Since the light is emitted secondly, after the deposition of energy in the calorimeter absorber and its conversion into heat, we need to set a parameter that takes into account this time delay between the two detectors. No threshold or correlation levels are set at this stage. This implies that the

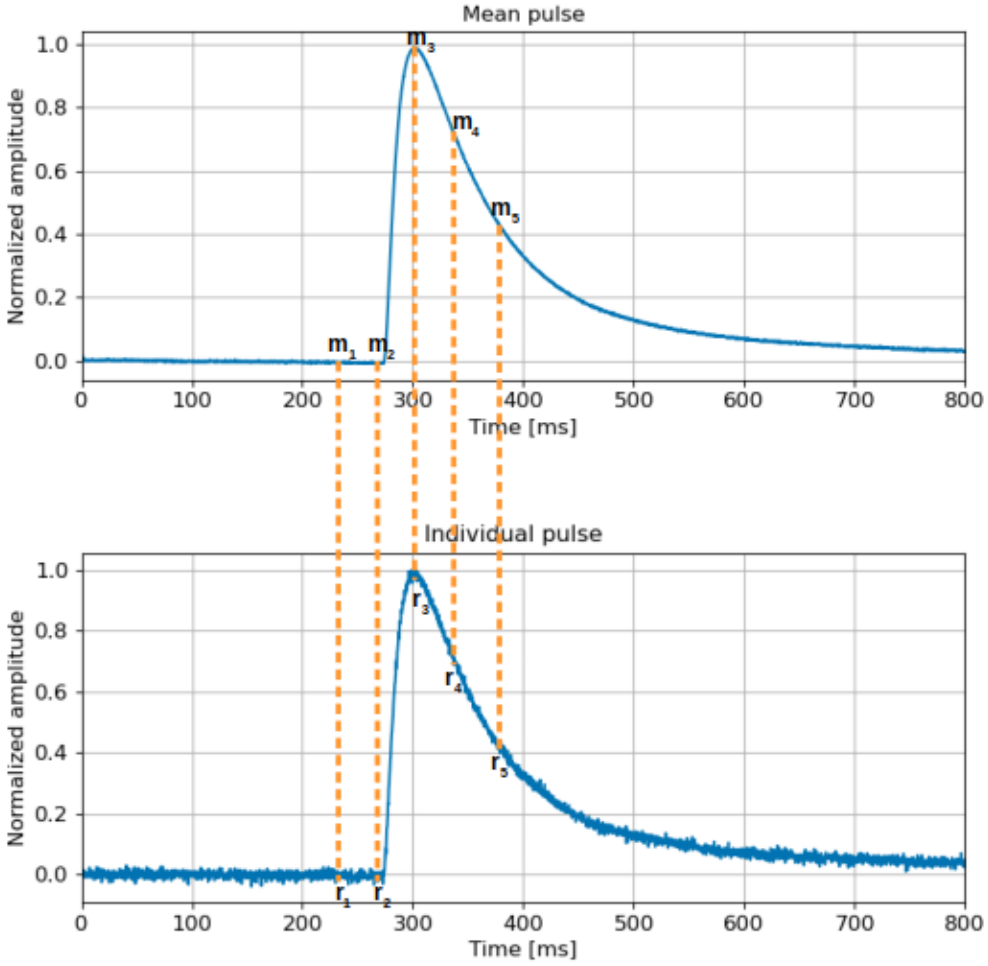

Figure 3.2: Representation of the amplitudes sampling behind the fitted amplitude parameter. At each instant t_i, the amplitudes m_i and r_i of the mean and individual pulses respectively are sampled. The slope of the linear fit performed with the points (m_i,r_i) corresponds to the fitted amplitude and it is an estimator filtered pulse amplitude.

light channel n-tuple will be a list of amplitudes recorded at the moment in which a heat event was detected rather than a selection of good light events. As a consequence:

- we will not have the full collection of light events;
- in the light output file, there will be also amplitudes not corresponding to any physics events: the amplitude reported will correspond to the baseline level (no

light emission detected by the light detector matching the triggered heat pulse).

3.2 The new analysis tool for ionization signals

In this thesis, besides the analysis dedicated to calorimeters, we have also a chapter dedicated to a cryogenic veto based on ionization signals. Argonauts, being developed especially for calorimeters that are based on NTDs working in mitigated background condition, is particularly suitable for pulses with a duration of a few tens of ms and in absence of a strong pile-up. Furthermore, it allows studying coincidences just between two detectors (typically a 'main' calorimeter and a light detector that is also coupled to an NTD thermometer). All these features cannot allow Argonauts to provide more than just a preliminary evaluation of the cryogenic veto, where we are interested in more than a double coincidence.
For this reason, we developed a completely new analysis tool based on C++ and Root framework, able to detect fast signals (rise time of order of few μs) and not biased by a high pile-up rate. For our purpose, it is built to process at the same time four ionization channels and one heat channel but it can be modified to increase or decrease the number of input files. It offers a faster and simplified way to process heavy data files using the bin-to-bin method. After combining anode and cathode signals (in the case of the ionization channel), a derivative over bins of 10 μs is computed throughout the data file (figure 3.3). The advantage of this approach, instead of using a pulse template, is to flatten the baseline becoming almost completely insensitive to fluctuations. This feature makes easier the task of selecting the trigger threshold value, reducing the risk to lose the smallest pulses while trying to avoid picking up noise structures in the baseline. Furthermore, the bin-to-bin technique allows recognizing pulses even if affected by pile-up, without necessarily rejecting them or pretreating data by applying a Butterworth filter. A similar procedure is followed also for the heat channel, taking into account that NTD signals are usually slower and could present some undershoots at their tail (figure 3.3).

All the information we need to reconstruct the energy of the pulse is contained in the rise of the pulse (figure 3.3, *top*). After applying the bin-to-bin method, the area under each few bins peak is proportional to the energy of the event (figure 3.3, *bottom*).

As will be explained in chapter 5, the NTD readout adopts the 1 kHz square modulation method in order to optimize the noise amplifier improving the signal-to-noise

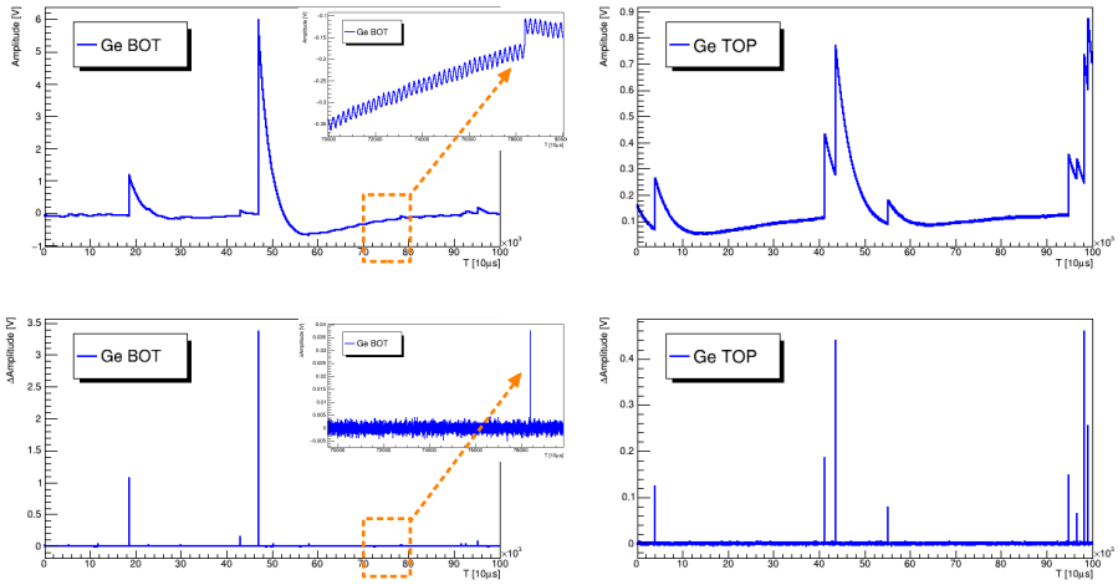

Figure 3.3: *Top:* examples of ionization data (measurement details in section 5.4). *Bottom:* the same data after applying the bin-to-bin method. We immediately see that the effect is to flatten the baseline without losing the possibility to detect even the smallest pulses (*insets*). Moreover, we are able to distinguish each pulse even if affected by pile-up.

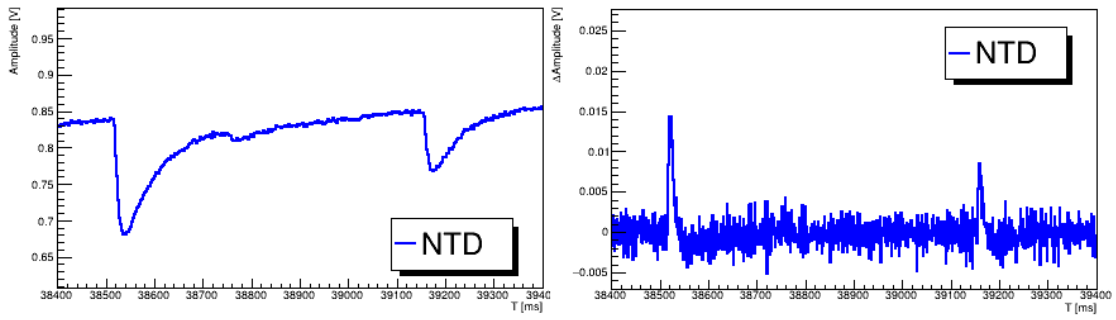

Figure 3.4: Example of heat signal before (*left*) and after (*right*) applying the bin-to-bin technique.

ratio. This current modulation is responsible for 1 kHz cross-talk in the ionization channels (figures 3.5a and 3.5b): every 1 ms we have a spike above thresholds that can be triggered and treated as a normal pulse. Since this cryogenic veto system is developed aiming at the CEνNS detection, we are particularly interested in the reduction of this events family. This is achieved by removing all the pulses with amplitude included in an adequately chosen energy band (precisely 4-7 keV for the Ge BOT and 10-15 keV for the Ge TOP in the case of the COV) and that periodically in a precise instant. In figure 3.5c, an example of ionization energy spectrum at low energy (0-100 keV). The green elements are false pulses due to the 1kHz cross-talk that are detected and removed from the histogram.

The reconstruction efficiency of this analysis tool was tested. A reference pulse was built using the real data. Then, while the pulse template is periodically injected over the data stream, the data are processed. Knowing the number of pulses injected and the number of pulses detected at that precise energy, we can evaluate the efficiency. This procedure is repeated at different energies. In figure 3.6, the reconstruction efficiency plot for two cryogenic germanium detectors: the 50% of the efficiency is reached at 1.5 times the detectors energy threshold E_{th} (defined as $4\sigma_{RMS}$) while almost the 100% is reached at approx twice the E_{th}. These results prove that the reconstruction method of our analysis tool is robust.

3.3 MMC analysis tool

This software is developed at the Laboratoire National Henri Becquerel (LNHB, Saclay, France) appositely for the offline processing of MMC data streams recorded continuously and it is based on MATLAB [161]. The offline analysis offers the possibility to adapt the data processing to each specific case, according to the experimental conditions. The software processes the data following a few steps: detection of the pulse position in the data stream file, the building of a pulse and noise templates, pulse amplitude analysis and temperature fluctuation correction, and final data selection ad evaluation of the baseline resolution.

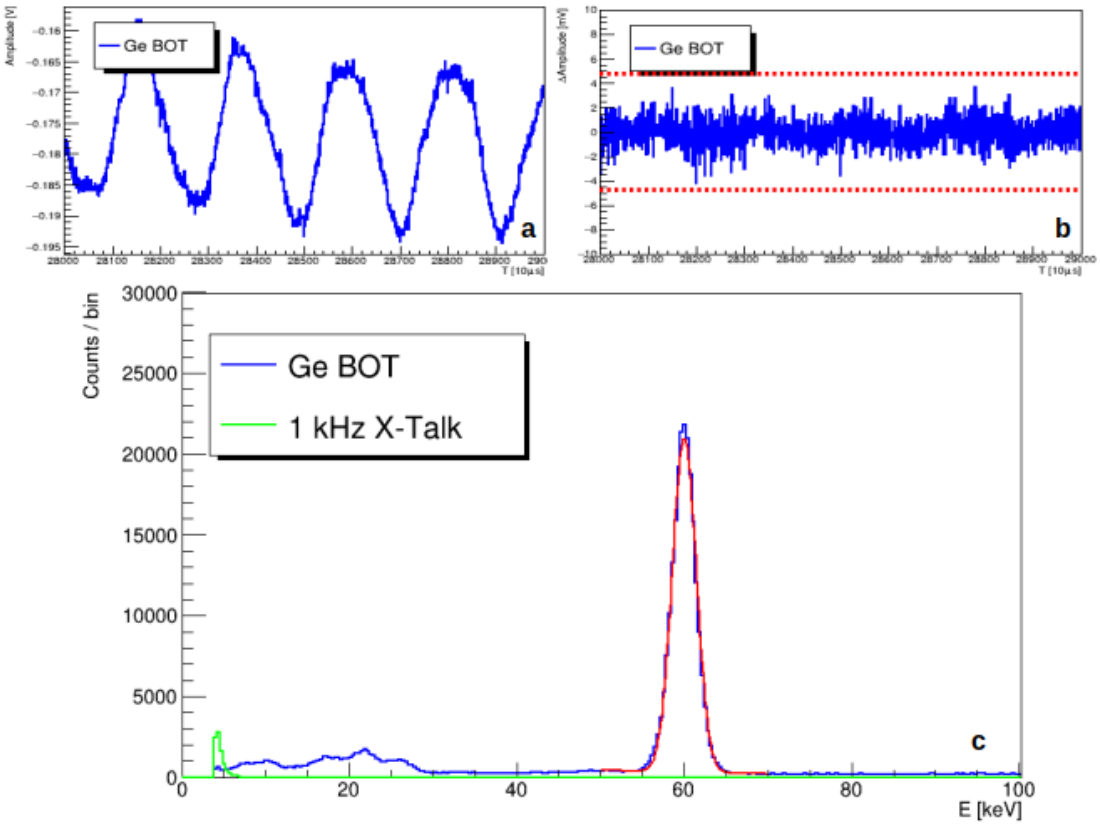

Figure 3.5: The plots *a* and *b* show a data stream window respectively before and after the bin-to-bin method. The baseline is affected by 1 kHz cross talk due to the NTD current modulation. Every 1 ms, a small non-physical pulse was observed. These events are recognized and removed (the green component in the plot *c*), leaving a corrected energy spectrum (blue distribution)

.

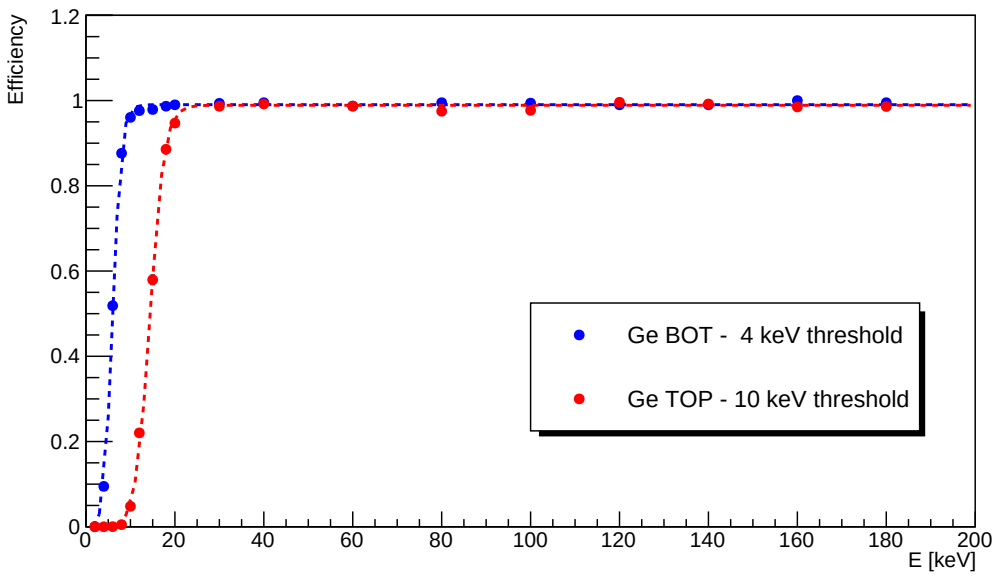

Figure 3.6: Reconstruction efficiency of the analysis tool, testing it with two cryogenic germanium detectors. Almost 100% of the efficiency is reached at approx twice the detector energy threshold.

3.3.1 Detection of the position of the pulses in the data stream file

At this stage, the data stream undergoes a first-order Butterworth band-pass filter. In the data analysis of the prototypes shown in this thesis, the chosen frequency cut values are:

- 250 Hz for the high-pass frequency cut. It allows the filtering of the pulses and the reduction of the pulse decay time. It is also responsible for an undershoot that is eliminated by applying a dead-time window;
- 450 Hz for the low-pass frequency cut. It filters the high-frequency noise and, as a consequence, increases the signal-to-noise ratio and allow to trigger smallest pulses.

This filter is used just at this step to determine the most suitable trigger level (figure 3.7). Whenever a pulse crosses the set threshold (ascending or descending), the respective positions in the stream file are registered (t_{start} and t_{stop}), giving us a time window where the pulse lies. To have a correct evaluation of the amplitudes, the baseline of the pulse must not be affected by the tail of a previous pulse. Therefore, there is a time window (so-named *dead time*) in which the calorimeter is not able to detect any pulses. The rejection of pulses belonging to the dead time window and so the determination of the detector active time (i.e. when the detector is ready to detect the next pulse) is performed through an algorithm: at each detected signal the algorithm evaluates a dead time window proportional to the pulse duration ($t_{stop} - t_{start}$). Since the triggered pulse duration is shorter compared to the real pulse, the time window ($t_{stop} - t_{start}$) is multiplied by a factor *dt* so that the dead time of the detector is at least as long as the recorded pulse. If a second pulse is triggered in this time window, it is removed from the list of detected events, and the dead time is extended by a factor equal to the duration of this second pulse.

3.3.2 Pulse height evaluation

The software allows evaluating the height of the pulses in both time and frequency domains. The evaluation in the time domain consists of a comparison between each detected pulse and a template pulse (also called reference pulse). The pulse template is built manually selecting 5 good pulses that are representative of the acquisition. From

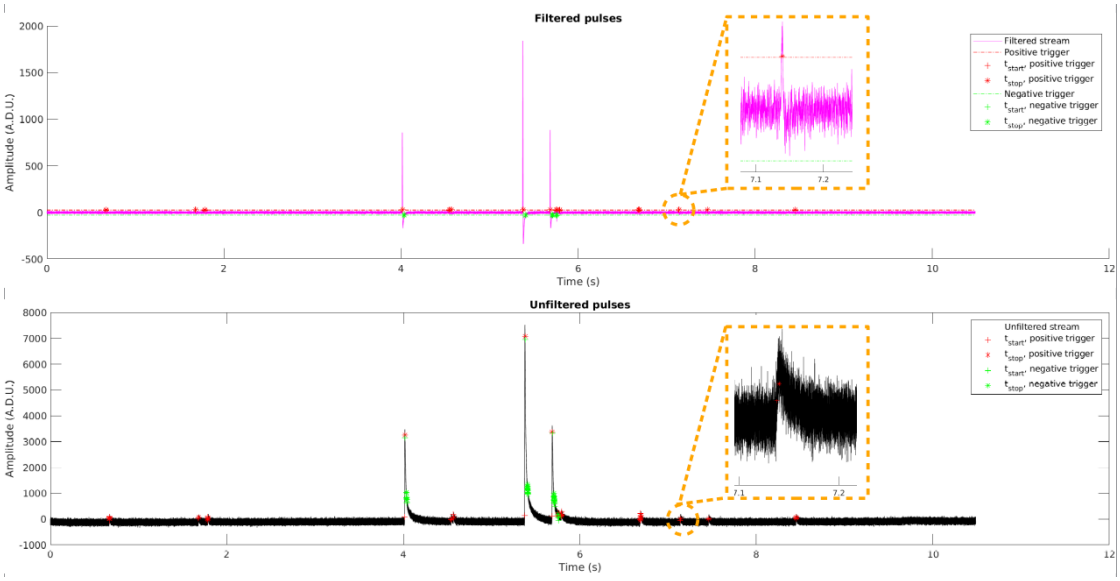

Figure 3.7: *Bottom*: example of 12 s window of the unfiltered data stream. *Top:* example of 12 s window of the data stream filtered with the 1^{st} order Butterworth band-pass filter. This plot is used to identify the most suitable trigger threshold in order to detect pulses of a few keV without triggering the baseline noise fluctuations.
In the insets a zoom of a small pulse ($\sim$ 6 keV, X-ray produced by a ^{55}Fe source), before and after the filtering. The red dashed line in the 'filtered' inset is the set trigger threshold.

them, χ^2 and RMS values are determined. These values are the limits for a selection and an average of 100 pulses;

The pulse template is composed of the baseline level before any pulse and the normalized average pulse.

3.3.3 Energy analysis and temperature fluctuations correction

The wet dilution refrigerator used for detectors with MMCs has the possibility to set and keep the cryostat at a chosen temperature. However, we have observed that the unavoidable small oscillations generated by the temperature control system (PID control) are more difficult to correct than the temperature drift without temperature control, affecting the energy resolution. For this reason, we decided to not use the PID control and, therefore, it is possible that during an acquisition there is temperature fluctuation $\sigma_{Temperature}$ of hundreds of μK. Since the pulse height is strongly dependent on the heat sink temperature, any fluctuations can degrade the energy resolution. For this reason, it is important to verify and, eventually, correct the temperature fluctuations.

The technique used is to select a dense population of events belonging to a well defined γ energy line as a function of time (figure 3.8), possibly not too low energy since the importance of pulse height fluctuations is proportional to the energy of the event (equation 3.2).

$$\sigma_{pulse\ height} = \frac{\sigma_{Temperature}}{T_0} \cdot Pulse\ height \tag{3.2}$$

A function $f(t)$ describing the pulse height fluctuations is obtained via interpolation with the spline function of the selected pulse heights as a function of time. Then, the height of all the detected pulses is corrected according to equation 3.3:

$$Pulse\ height_{corrected} = \frac{Pulse\ height}{f(t)} \tag{3.3}$$

In figure 3.8 an example of pulse heights as a function of triggering time before (*top*) and after (*bottom*) the temperature stabilization through the spline function (*center*).

This technique works in case of not very abrupt temperature fluctuations. If baseline jumps are present (for example due to helium refill), the corresponding events are removed.

The data analysis results, realized with this software, are presented in chapter 7.

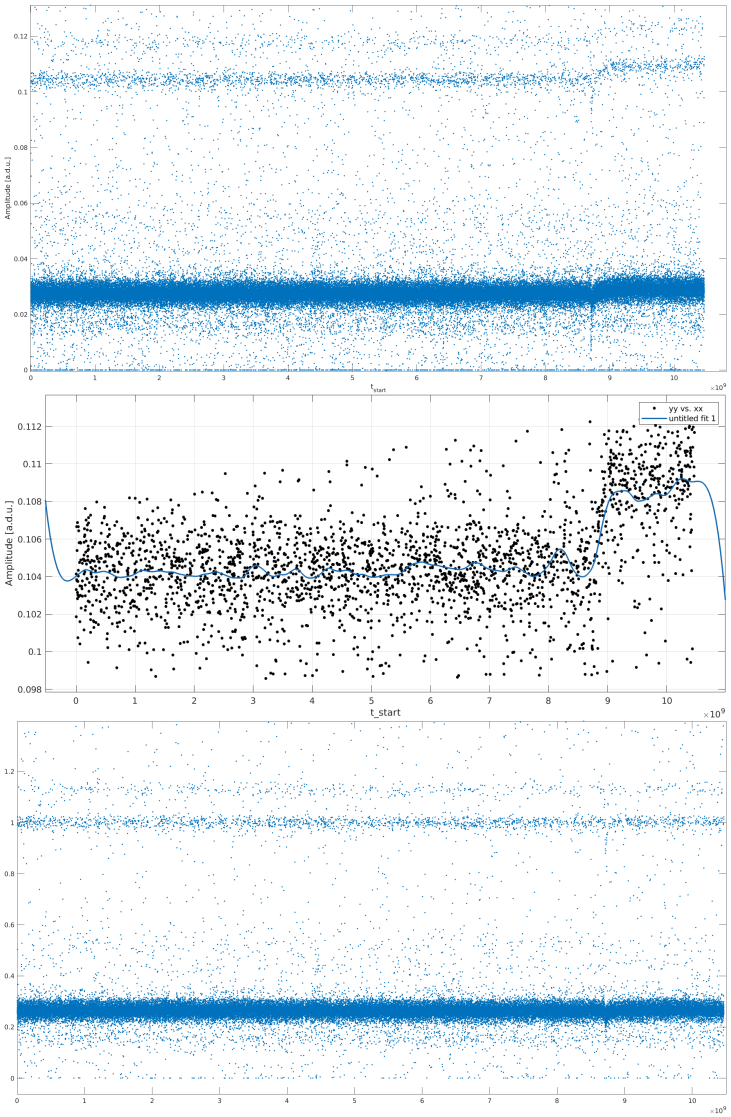

Figure 3.8: *Top*: above $t_{start} = 8 \times 10^9$, a pulse height fluctuation is visible. It is due to a temperature drift of the heat sink. In order to not affect the resolution, it is important to correct it. *Center*: the pulse height variation is corrected by selecting a population of events well defined in energy and interpolating them with a spline function (blue line). In this case, the selected population belongs to the 22 keV energy line. *Bottom*: the pulse height is stabilized, thus the drift is no more visible, except for the first instant where the temperature variation is too rapid. This short time period can be removed from the data.

Chapter 4

The NUCLEUS experiment

As mentioned in chapter 1, CEνNS offers a singular way to investigate neutrino properties and look for new physics beyond the Standard Model. Nevertheless, we should not forget that the small energy characterizing its unique signature makes arduous the detection of this process [18].
NUCLEUS is a neutrino nuclear reactor experiment that took up the challenge, developing a new CEνNS detection approach based on a complete innovative experimental apparatus [87].
The idea behind this experiment has its origin in 2016 at the Max- Planck-Institut für Physik in Munich where, in synergy with the CRESST collaboration, some preliminary tests were performed to validate the effectiveness of the technique [22].
The NUCLEUS collaboration was officially founded later, in 2018, and today it has fully designed the experimental apparatus composed of complex veto and shielding systems against the background in order to achieve the best performances.
Besides the background minimization, the NUCLEUS ambition is the development of target detectors able to reach an ultra-low nuclear recoil energy threshold ($\mathcal{O} \leq 10\,\mathrm{eV}$) to have the chance to unequivocally observe the signature of our interest.
NUCLEUS will progress in two phases [1]:

- phase 1: NUCLEUS-10g. A detector with a CEνNS target of 10 g (see section 4.1) will be employed. At this stage, all the facets of the experiment (background contributions studies, evaluation of the active and passive shields size, technique implemented with the different cryogenic detectors, etc.) must be validated at small scale. Despite the limited statistics over its complete run time, we expect to

observe CEνNS events;

- phase 2: NUCLEUS-1kg. The target detector will be upgraded to 1 kg total target mass, allowing a CEνNS precision measurement and expectedly opening a window on new physics.

In this chapter, I will provide an exhaustive description of the NUCLEUS experiment status.

4.1 The NUCLEUS target detectors development

In 2016, the CRESST-II experiment achieved for the first time an energy threshold of 307 keV using a $CaWO_4$ detector mass of 300 g, enhancing the sensitivity for nuclear recoils induced by the elastic scattering of dark matter particles [94]. This threshold was a limiting factor for the detection of rare events characterized by energies in the range from few keV up to 10's of keV. In particular, the calorimeters state-of-the-art was precluding the CEνNS detection at that time.
NUCLEUS already demonstrated its potential reaching an energy threshold of (19.7±0.9) eV using an Al_2O_3 prototype of 0.5 g, without shields against the environmental radioactivity, the cosmogenic background, and the radiation originated by materials inside the experimental volume [1, 22]. This is the lowest nuclear recoil energy threshold ever achieved by a massive cryogenic calorimeter based on a heat signal. Until today, the smallest neutrino detector that observed CEνNS events is the 14.6 kg CsI[Na] scintillator adopted by the COHERENT collaboration [19].
For the actual phase, NUCLEUS is developing 3×3 target arrays composed of a total target mass of 6.84 g for the $CaWO_4$ and 4.41 g for the Al_2O_3 (figure 4.1) [162].

All the crystals have dimensions $(5\times5\times5)\,mm^3$ and onto all of them a tungsten thin film (200 nm) Transition Edge Sensor (TES) with area $0.0061\,mm^2$ is evaporated. Moreover, an aluminum phonons collector with area $0.15\,mm^2$ is additionally evaporated: a larger phonon collection area grants a higher pulse without increasing the sensor heat capacity (figure 4.2). The TES is weakly thermally connected to the heat sink direct a gold strip (area $0.01\times7.0\,mm^2$, and thickness 20 nm).

The multi-target choice offers us the extraordinary possibility to enhance the sensitivity to the CEνNS signature. Indeed, as shown in figure 4.3, the heavy element in

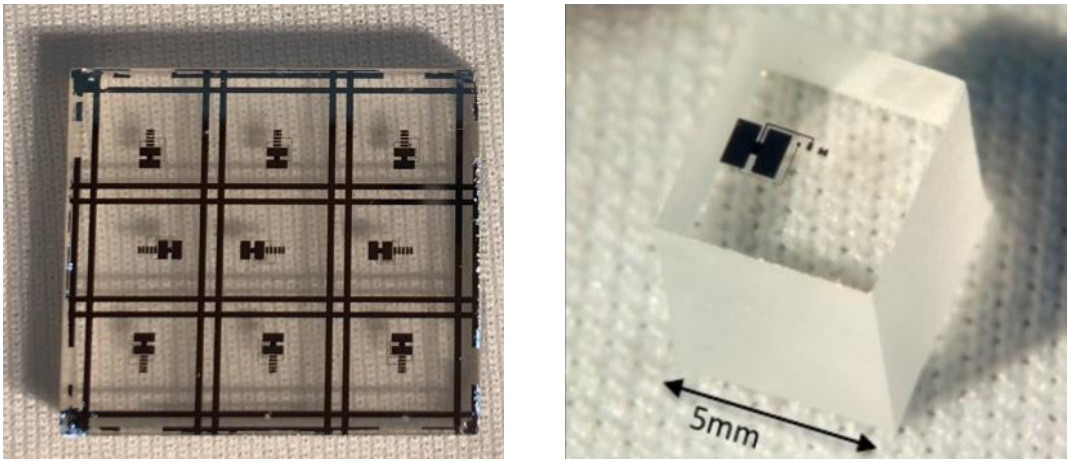

Figure 4.1: *On the left:* the 9 $CaWO_4$ crystals before the cutting, each of them already equipped with a TES sensor. *On the right:* an example of Al_2O_3 crystal.

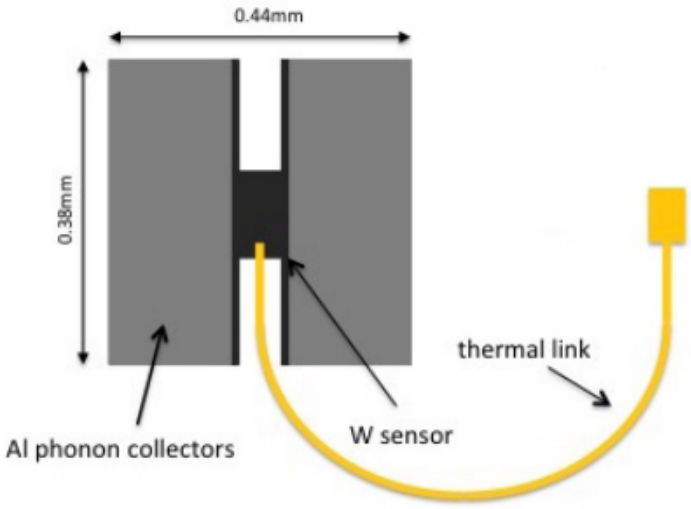

Figure 4.2: Schematic drawing of the W-TES evaporated directly on the surface of the crystals. Attached to the W film (thickness 200 nm), the Al pads allow a larger phonons collection area to improve the signal amplitude. Thanks to the thermal link provided by an Au strip weakly coupled to the heat sink, the thermal equilibrium is promptly restored [87].

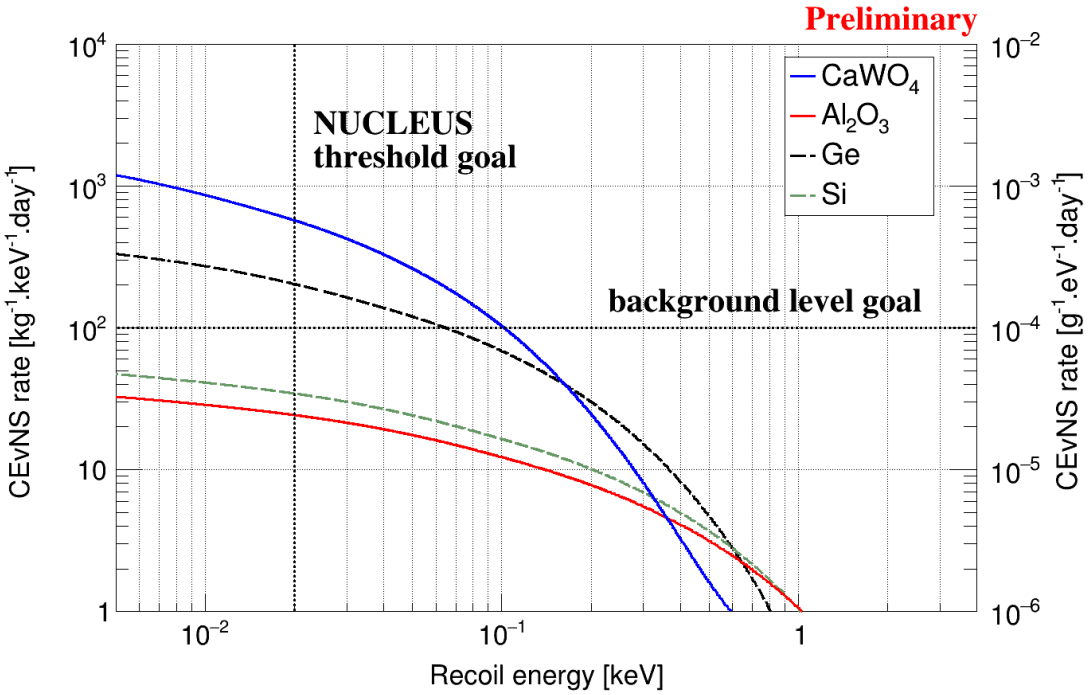

Figure 4.3: Preliminary plot showing the CEνNS rate as a function of the nuclear recoil energy for $CaWO_4$, Al_2O_3, Ge and Si. $CaWO_4$ and Al_2O_3 are the target compounds. Ge and Si are other two materials well known for their cryogenic properties; they are adopted for the active cryogenic veto systems (see sections 4.4.1 and 4.4.2), and they will be taken into consideration for the NUCLEUS upgrade from 10 g to 1 kg.

the $CaWO_4$ compound increases the CEνNS cross-section and as a consequence, we are assured to measure the signal of interest above the background level, at very small nuclear recoil energies too. At the same time, the Al_2O_3 compound is used to develop a common background model, being well below the background level goal.

The structure of the target detector draws inspiration from the so-called CRESST technology since it is very similar to the one used by CRESST for the dark matter search. Being the calorimeter irrespective of the kind of particle interaction, when any particle interacts with the detector, it releases and deposits energy in the detector absorber causing a change of temperature that will be read by the TES. In figure 4.4, examples of TES pulses of different energies. These devices are featured by a very fast response

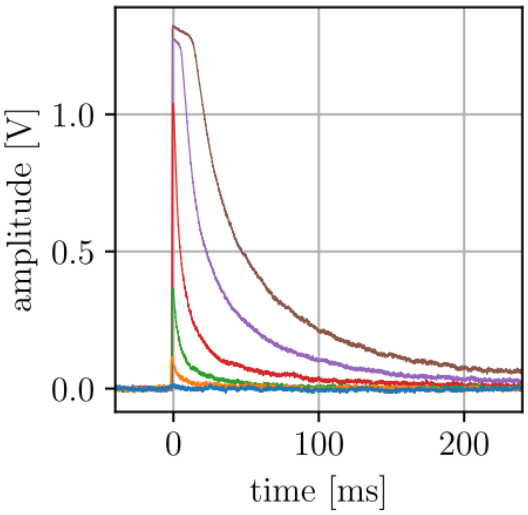

Figure 4.4: Examples of TES pulses of different energies (0.02 keV, 0.16 keV, 0.54 keV, 1.35 keV, 4.88 keV, 8.60 keV). They show the TES linear range and saturation region [163].

time: in the tests carried out on the NUCLEUS-1g prototype in 2017, the target detector showed pulses with rise-time of $\sim$300 μs [22].

We can make some predictions about the reachable energy threshold (see sub-section 4.1.1): approximately 4.0 eV for the Al_2O_3 and 7.0 eV for the $CaWO_4$.

4.1.1 The scaling law: a simple way to predict the energy threshold

The TES is a device primarily sensitive to the athermal phonons because of the weak thermal link between crystal and sensor due to the small electron-phonon decoupling at low temperatures. We expect two athermal components to compete: the athermal phonons that are thermalized at the surface of the absorber and the ones that thermalize in the TES film. Taking into account this, we can build a model to predict the achievable detector energy threshold [22, 163]. The model is a simplification and doesn't consider many aspects, some of which can be related to the detector target size (the main parameter playing a role in the prediction). When a particle interacts with the target, the TES film will experience a change of temperature equal to the fraction of deposited energy that is thermalized in the tungsten film ($\Delta E \cdot \epsilon$) divided by the heat capacity of the film electrons system (C_e):

$$\Delta T_{film} = \frac{\Delta E \cdot \epsilon}{C_e} \tag{4.1}$$

Since the fraction ϵ of energy is expressible as:

$$\epsilon = \frac{\kappa_{film} \cdot A_{film}}{\kappa_{absorber} \cdot A_{absorber}} \tag{4.2}$$

where κ_{film} and $\kappa_{absorber}$ are parameters including material properties, while A_{film} and $A_{absorber}$ are the surfaces respectively of the film and the target absorber.
Thanks to equation 4.2, we can express equation 4.1 as:

$$\Delta T_{film} = \frac{\kappa_{film} \cdot A_{film}}{\kappa_{absorber} \cdot A_{absorber}} \cdot \frac{\Delta E}{C_e} \tag{4.3}$$

Remembering that $C = c \cdot m = c \cdot \rho \cdot V_{film}$, then $C_e \propto V_{film} = h \cdot A_{film}$:

$$\Delta T_{film} \propto \frac{\kappa_{film} \cdot A_{film}}{\kappa_{absorber} \cdot A_{absorber}} \cdot \frac{\Delta E}{h \cdot A_{film}} \propto \frac{1}{A_{absorber}} \tag{4.4}$$

ΔT_{film} is inversely proportional to the absorber area. From this follows that the smaller the absorber size, the bigger the film temperature variation. The result is an increased signal amplitude and, as a consequence, a lower energy threshold. Therefore, the energy threshold is proportional to the absorber area. Considering cubic crystals, we can use the fact that $M \propto V = l^3$ to express the energy threshold E_{th} as follow:

$$E_{th} = k \cdot M^{\frac{2}{3}} \tag{4.5}$$

where k is a constant including materials and all the geometry factors except the size of the absorber.

Since NUCLEUS and CRESST detectors are very similar, we can apply a scaling law to the CRESST performances to have the prediction of how much low we can go with the energy threshold by playing with the dimension of the absorber.

4.2 The experimental site

The experimental site selected for NUCLEUS is the Chooz Nuclear Power Plant (France), where two N4 pressurized water reactors (B-1 and B-2) are driven by the power company Electricité de France (EDF). More precisely, the experiment will take place in a basement room ($24\,\mathrm{m}^2$) of an administrative building, nicknamed the *Very Near Site* in reference to

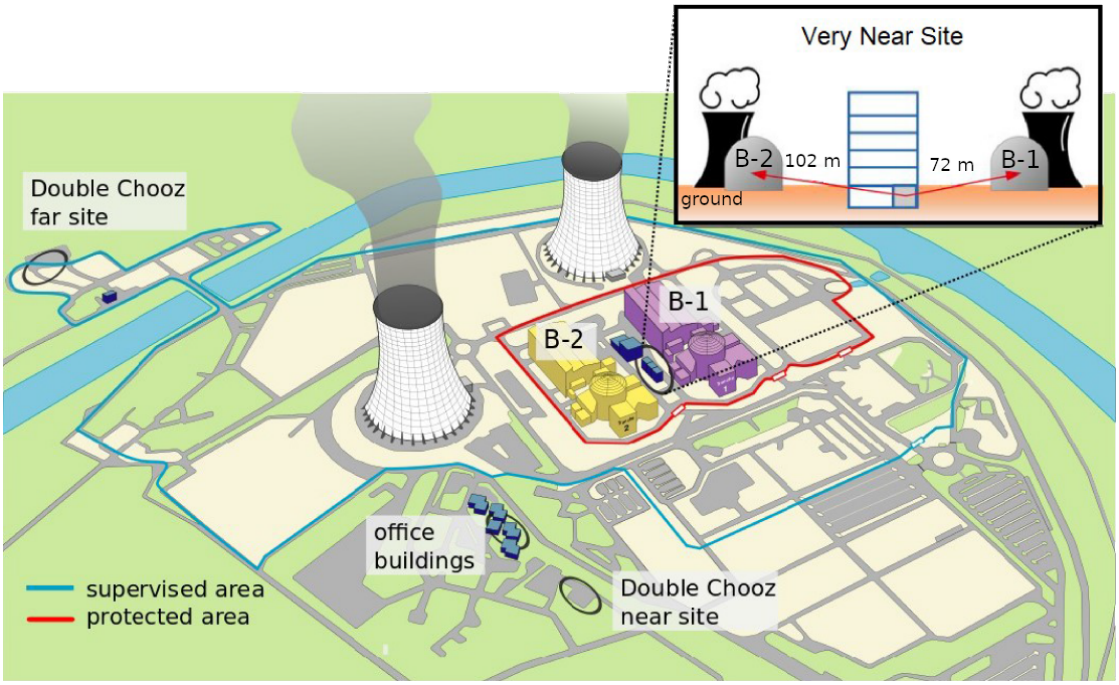

Figure 4.5: Schematic drawing of the Chooz Nuclear Power Plant. The inset shows the Very Near Site in the basement of an administrative building, situated between the nuclear reactors B-1 and B-2, respectively at a distance of 72 m, and 102 m from the two cores. The drawing additionally shows the position of the Double Chooz near and far sites.

the *Near Site* (∼400 m baseline) and *Far Site* (∼1 km baseline) where the Double Chooz experiment studied the neutrino oscillations via IBD (figure 4.5) [164]. The two nuclear reactors have a thermal power output of 4.25 GW_{th} each, with an overburden of about 3 meters of water equivalent (m.w.e). Their distance of 102 m and 72 m respectively from the experimental room, makes the Very Near Site particularly suitable due to the large neutrino flux [1]. The structural characteristics of the room impose a limit in terms of volume and weight ($\mathcal{O} \leq 10$ t) of the full experimental set-up. For this reason a weight support platform must be installed to sustain the load expected for the NUCLEUS shielding systems.

4.3 Background components at Chooz nuclear power plant

As already mentioned, the Very Near Site is a room located at a shallow depth, with an overburden of about 3 m.w.e. As a consequence, the background is an experimental issue that, if not carefully treated and faced, can potentially hinder the CEνNS detection. This background has many components with different origin and impact [165]. We can summarize them mainly in 4 categories:

- environmental radioactivity due to primordial radionuclides;
- internal contaminations;
- reactor correlated radioactivity;
- cosmic rays.

The primordial radionuclides are nuclides produced during the formation of the solar systems. The most commons are ^{40}K and the isotopes belonging to the ^{238}U (table 4.1), ^{232}Th (table 4.2), and ^{235}U decay chains. The nuclides α and β decays subsequently generating γ rays up to 2.6 MeV. These nuclides are present in the soil, rocks, and materials used in the construction of buildings (such as the Very Near Site). The γ's can be strongly reduced using a high-Z material shield of an adequate thickness since they interact mainly via Compton scattering [166]. Usually, the first choice is lead shielding as the most external layer.

An important source of airborne radioactivity is represented by ^{222}Rn, produced by the α decay of ^{226}Ra, a radionuclide belonging to the ^{238}U decay chain. Being non-volatile, the ^{222}Rn (half-life of 3.82 days) escapes by diffusion from the materials where it was produced. It α-decays in ^{218}Po which can deposit and contaminate the detector and the surrounding surfaces, determining a source of unwanted radioactivity. In the case of research activities where a low-radioactivity is fundamental, ^{222}Rn and its daughters represent a dangerous threat to the outcome of the experiment. To avoid any problems, the contamination level in the target crystals is monitored during the production phase, while the materials destined for components close to the target detectors are carefully selected with the help of γ-ray spectroscopy studies. Moreover, they are treated with special cleaning and purification procedures during the detector assembly

^{238}U decay chain		
Isotope	**Energy** [keV]	**Intensity** [%]
^{226}Ra	186.211	3.59
^{214}Pb	186.211	3.59
^{214}Pb	241.997	7.43
^{214}Pb	295.224	19.3
^{214}Bi	351.932	37.6
^{214}Bi	609.312	46.1
^{214}Bi	768.356	4.94
^{214}Bi	934.061	3.03
^{214}Bi	1120.287	15.1
^{214}Bi	1238.11	5.79
^{214}Bi	1377.669	4
^{214}Bi	1764.494	15.4
^{214}Bi	2204.21	5.08

Table 4.1: Main γ lines from the ^{238}U decay chain.

^{232} Th decay chain		
Isotope	**Energy** [keV]	**Intensity** [%]
^{228}Ac	338.32	11.27
^{228}Ac	911.204	25.8
^{228}Ac	968.971	15.8
^{212}Pb	238.632	43.3
^{208}Tl	727.33	6.58
^{208}Tl	277.351	6.31
^{208}Tl	510.77	22.6
^{208}Tl	583.191	84.5
^{208}Tl	860.564	12.42
^{208}Tl	2614.533	99

Table 4.2: Main γ lines from the ^{232}Th decay chain.

and installation [167, 168].
Another source of background is the nuclear reactor itself. Indeed, it is a source of a large number of fission neutrons. Most of them are immediately thermalized in the reactor, and the remaining fast neutrons are minor. As a consequence, the neutron background originated from the reactor core is negligible. This is inferred by making a scaling of the results obtained with a neutron reactor monitoring performed in the NUCIFER experiment [169]. This experiment was running at a distance of 7.2 m from the 7.0 MW_{th} Osiris core, a light water research reactor of open-core pool type that is located at the CEA-Saclay (France). The neutron elastic scattering rate on hydrogen in the gadolinium-loaded liquid scintillator, i.e. the NUCIFER target, was $4{\cdot}10^{-5}$ events/day at energies above 2 MeV [169, 170]. A further background product of a nuclear reactor is the γ-rays. They can be generated in different ways, during the fission process, in the neutron capture reaction in the fuel or other components of the reactor, or during the γ decay of the fission fragments after their β decay. In the case of NUCLEUS, this background is negligible as well, since the experimental set-up is located at a greater distance than 70 m from the cores and it is separated by about 10 m of rock. Moreover, the reactor vessel is surrounded by a thick layer of steel [1].

The most important component of the background is originated from cosmic-rays. Primary cosmic-ray particles are made up of 90% protons, 9% α's, and 1% heavy nuclei. Crashing with the Earth's atmosphere, showers of muons, neutrons, electrons, neutrinos, protons, γ-rays, and pions are created. The maximum concentration of these secondary particles is about at 13.7 km of altitude and then they progressively decrease [165]. While electrons, protons, γ-rays, and pions can be stopped by lead shieldings or the overburden offered by the building structure, some cosmic-rays products still have to be shielded:

- muons. They interact and lose their energy in rock by Bremßtrahlung, pair production, ionization, and nuclear interaction [166]. The classic technique adopted to veto this component is the introduction of an active muon veto, typically based on plastic scintillators, in the experimental set-up. All the events detected in coincidences with the muon veto are all events in coincidence with a muon event are removed;

- neutrons. They are slowed mainly via inelastic scattering and absorbed using materials with a high content of hydrogen and neutron-absorbing nuclei, such as

lithium or boron. Another component of neutrons is generated in the muon interaction with high-Z materials (for example, the lead shielding). This inconvenience can be overcome by avoiding high-Z shields in the proximity of the target detectors and high-efficiency muon veto.

A background characterization campaign was performed at the Very Near Site at Chooz between October 2017 and May 2018, observing a muon flux reduction by 29±1% compared to outside the building, and a neutron flux reduction by a factor of 8.1±0.4 for the range 100 keV_{ee}- 2 MeV_{ee}[1] [1]. GEANT4 MC simulations are ongoing to identify the best detectors and passive shielding configurations to minimize the background as much as possible. The NUCLEUS goal is to reach a background level of 100 counts(keV·kg·d). In table 4.3, the latest preliminary background and CEνNS rates are shown [171]. The background is simulated including in the passive shielding system a 4 cm thick B_4C. According to further simulations, this thickness should be sufficient to reduce the total background of a factor 6 and 12 for the $CaWO_4$ and Al_2O_3 respectively, in the 10-100 eV energy range. The atmospheric neutron rate at the Very Near Site is evaluated by applying a reduction factor 5 to the corresponding background estimated at the surface. According to the simulation, we should expect to detect with the 6 g $CaWO_4$ array approximately 1 CEνNS event in the 10-100 eV energy range every 5-6 days.

4.4 Cryogenic veto systems

NUCLEUS has developed a complex onion-like structure of shields to achieve the necessary background rejection allowing the detection of low-energy events, such as CEνNS In the following sections, I will present several cryogenic active veto systems and passive shieldings.

[1] keV_{ee} = keV electron equivalent. This unit is often used in experiments that measure ionization or scintillation in detectors. It is proportional to the actual nuclear recoil energy through a quenching factor.

Table 4.3: Simulated background components and CEνNS rates, including a 4 cm thick B_4C shield in the passive shielding system. These background estimations are very preliminary since the B_4C shield is still under discussion (difficult to produce with such thickness). The CEνNS rate in the 1-10 keV is negligible.

$CaWO_4$ array (rates in $kg^{-1}d^{-1}$)			
	10 -100 eV	**100 eV-1 keV**	**1-10 keV**
Atmospheric μ's	<1.9	<1.9	<1.9
Ambient γ's	1.7±0.2	5.3±0.4	∼45
Expected atmospheric neutrons at the Very Near Site	∼7	∼23	∼64
CEνNS	33.4	9.7	-

Al_2O_3 array (rates in $kg^{-1}d^{-1}$)			
Source	**10 -100 eV**	**100 eV-1 keV**	**1-10 keV**
Atmospheric μ's	<2.9	<2.9	<16±1.2
Ambient γ's	3.9±0.4	10.4±0.6	∼90
Expected atmospheric neutrons at the Very Near Site	∼1.5	∼15	∼44
CEνNS	2.0	4.3	-

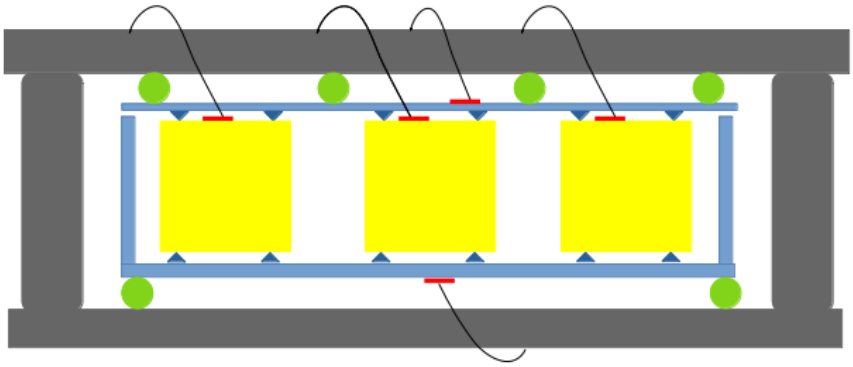

Figure 4.6: Schematic drawing of the inner veto. In light blue, the silicon slabs equipped with W-TES (red elements) acting as an active veto system and holder for the target detectors (yellow cubes). The point-like contact between the crystals and the silicon wafers is obtained thanks to pyramidal structures created via wet-etching. The holding strength is regulated using an external mechanical structure that touches the inner veto through Al_2O_3 spheres.

4.4.1 Active inner veto

The NUCLEUS inner veto is designed to face some problems encountered in the CRESST experiment [172, 173]. In order to be able to cool down the detectors at about 10 mK, we need to remove all the possible sources of microphonic noise that could transfer energy to the target detectors, heating up the cryostat. The most efficient way is to tighten solidly the detectors in a holder. The risk of fixing them with excessive force at rigid structure is to crack or fracture the crystals causing high-rate signals. To reduce the probability of this happening, NUCLEUS has developed a holding structure flexible and instrumented as an active veto system against the α's and β's due to the residual internal contamination of the target detectors (figure 4.7 *a*).

Figure 4.6 shows the schematic drawing of the inner veto, enclosing the target detectors. It is composed of a rigid silicon beaker (thickness $\sim$ 1-2 mm, figure 4.7 *c1*) and an elastic silicon wafers (thickness $\sim$ 200 μm, figure 4.7 *b1*) to cover the crystals (light blue elements in figure 4.6). This structure is exploited as active veto depositing TESs on the two silicon slabs. The top wafer has some laser-cut windows in order to let pass the bonding wires for thermal and electrical connections coming from the target detectors

(4.7 *c2*). Clearly, this will result in a not complete crystal coverage. In order to avoid a strong thermal contact between the silicon slabs and the crystals, the two are in contact through pyramid structures fabricated using the wet-etching technique (dark blue elements in figure 4.6 and figures 4.7 *b2* and 4.7 *c3*). The force with which the crystals are hold off is regulated using an external mechanical structure (grey element in figure 4.6), not sensitive to particle events, through some Al_2O_3 spheres (green elements in 4.6).

4.4.2 Outer veto

A primary issue to face, given the close vicinity to the nuclear reactors, is the suppression of neutrons and the most penetrating γ radiation. To satisfy this requirement, NUCLEUS has designed a cryogenic outer veto system enclosing the inner veto and, therefore, also the target detectors. In order to identify the interacting particles, the outer veto must have an energy threshold and a response time comparable with the target detectors (i.e. few keV and few μs respectively), since they will work in anti-coincidence. The final configuration of the outer veto will be a sort of a germanium box composed of two cylinders (Φ=100 mm and h= 25 mm) and four parallelepipeds (50 mm$\times$74.5 mm$\times$25 mm). On two opposite faces of all the crystals, aluminum electrodes will be evaporated to exploit the ionization signal generated by the interacting particles. The charge-readout is a technique that can answer our necessity to have a fast time response (order of μs) together with a good energy resolution [174]. More details will be given in a devoted chapter (chapter 5).

4.5 Passive shielding

Thanks to the presence of an active outer veto, the environmental γ radiation is suppressed of many orders of magnitude. As consequence, the passive shielding system can be simplified compared to traditional ones and it can be more focused on the attenuation of the neutrons produced by muons and γ's in the high Z materials, using just an external lead layer and inner polyethylene layers (figure 4.9). The shielding layers are designed to embrace the cryostat and they will be supported by rails to easily have access to the experimental volume. GEANT4 simulations allowed us to identify the optimal thickness of the different shields. The envisioned dimensions are reported in table 4.4.

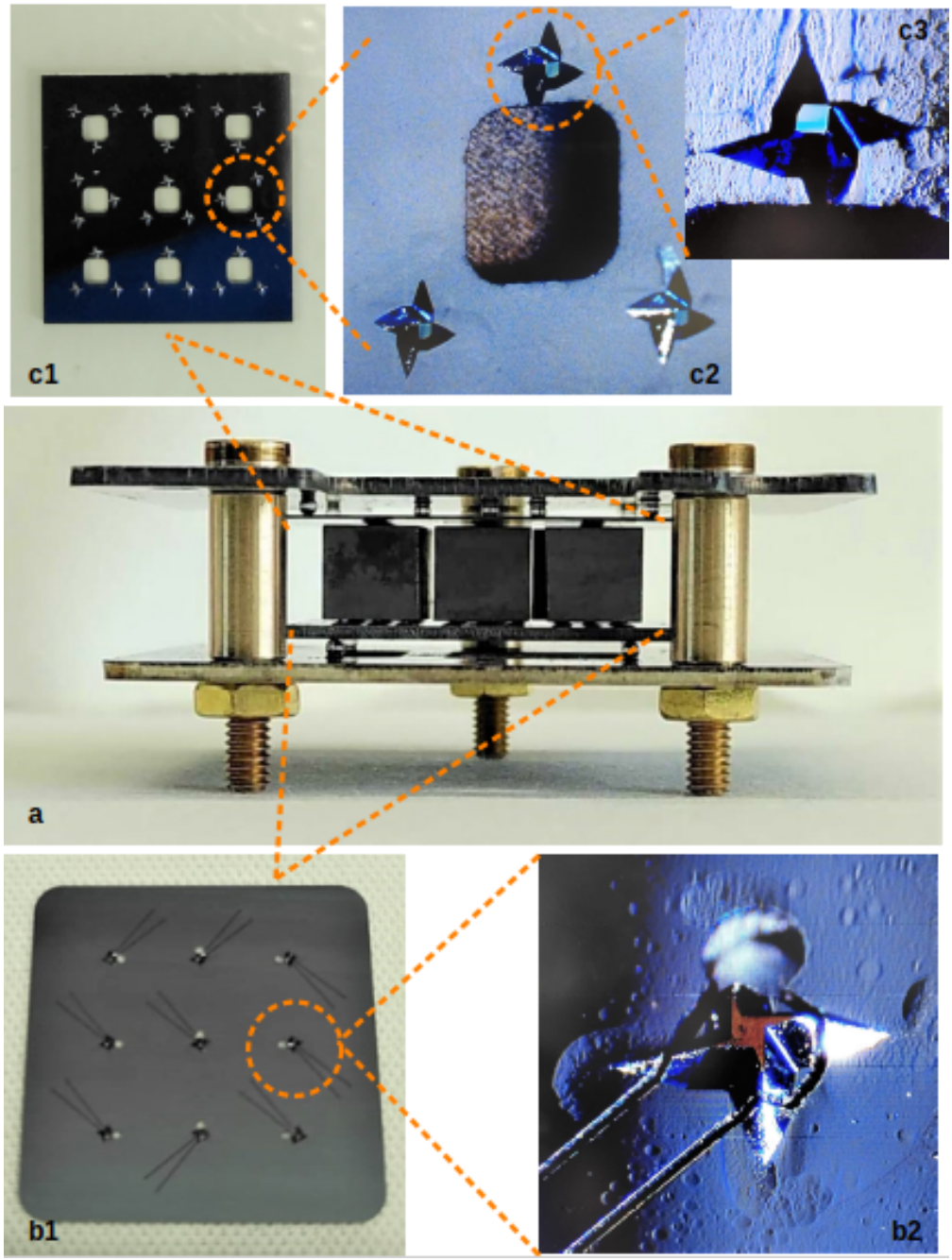

Figure 4.7: Inner veto enclosing the target detectors (*a*). The inner veto is composed of an elastic silicon wafer (*b1*) and a rigid silicon beaker (*c1*) with some laser-cut openings to allow the passage of the target detector wiring (*c2*). Both the silicon elements present pyramid structures that are realized with the wet-etching technique and ensure the fastening of the target crystals (*b2* and *c2*).

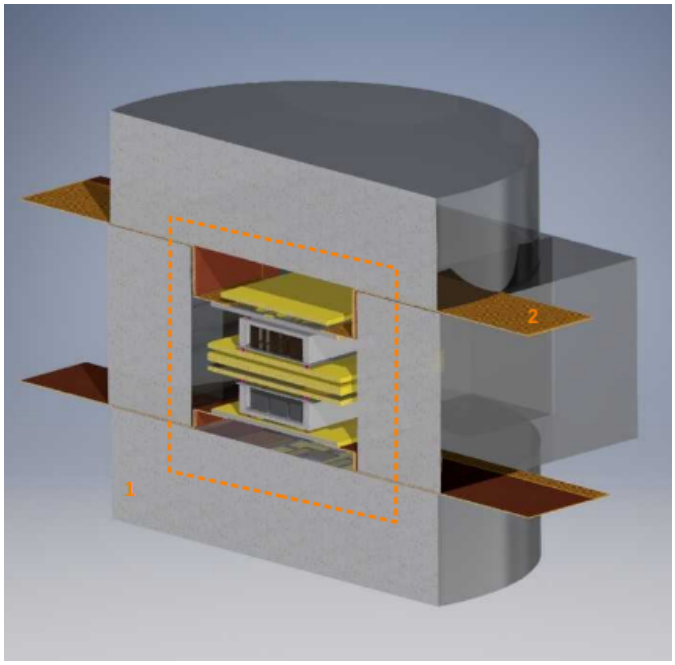

Figure 4.8: The schematic sketch shows the section of the 3 cryogenic detectors. The grey blocks (1) constitute the germanium outer veto. Inside the dashed area, the target detectors fixed in the inner veto are hosted. The germanium crystals are spaced with a small gab both for a charge collection reason and to let come out the electrical connection through a dedicated mechanical structure (2)

4.6 Muon anticoincidence veto

The largest component of the background is expected to be muon-induced neutrons. To detect a CEνSN event, we need to reduce this element of background by introducing an efficient muon veto. The goal of NUCLEUS is to reach the benchmark background index of 100 counts/(keV kg d), and the capability to identify muons at a rate of a hundred Hz in order to work as fast as the target detectors. At the final configuration, the muon veto will consist of several panels in BC-408 plastic scintillators, minimizing the dead areas and surrounding completely the lead shield, namely the most external passive shielding to reduce the probability of muon interaction with this latter.
The plastic scintillators will be read through wavelength shifting fibers connected to silicon photomultipliers [175].

Table 4.4: Envisioned dimensions of the NUCLEUS passive shields. These dimensions are the result of GEANT4 simulations aiming at the identification of the optimal thicknesses for the background suppression.

Shield	**Thickness**	**Application**
lead	5 cm	shielding against ambient γ's
5% borated polyethylene	20 cm	reduction of the impact of secondary neutrons and mitigation of the
boron carbide (B_4C)	4 cm	capture of thermal neutrons approaching to the target detectors

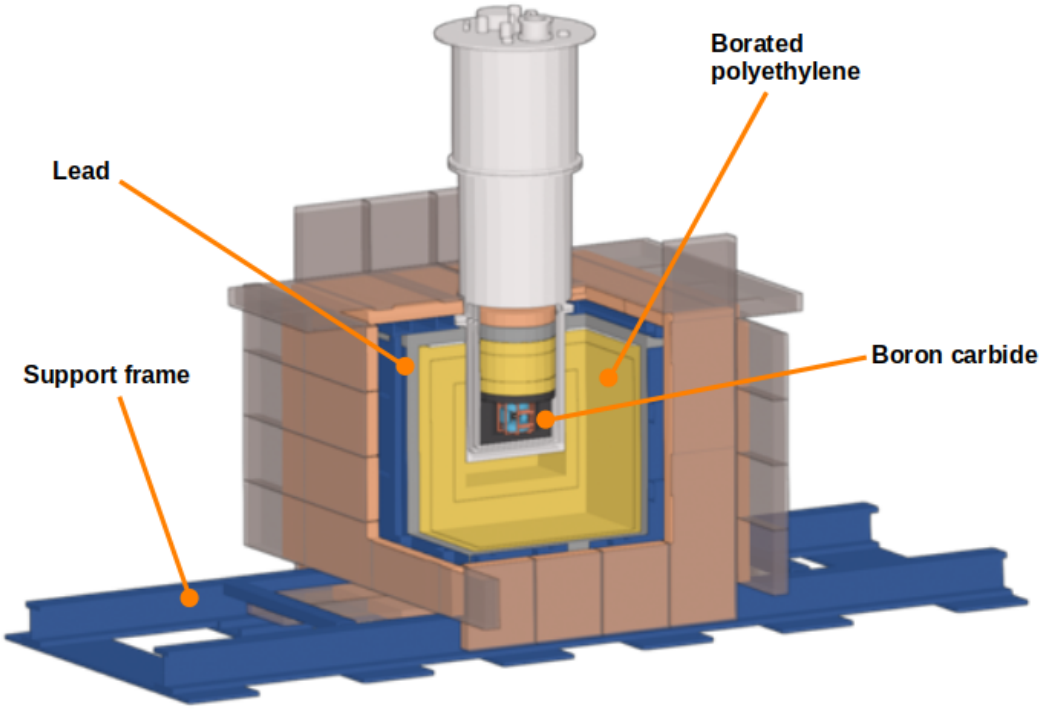

Figure 4.9: Schematic drawing showing a section of the passive shields that will be placed around the cryostat for the cryogenic detectors.

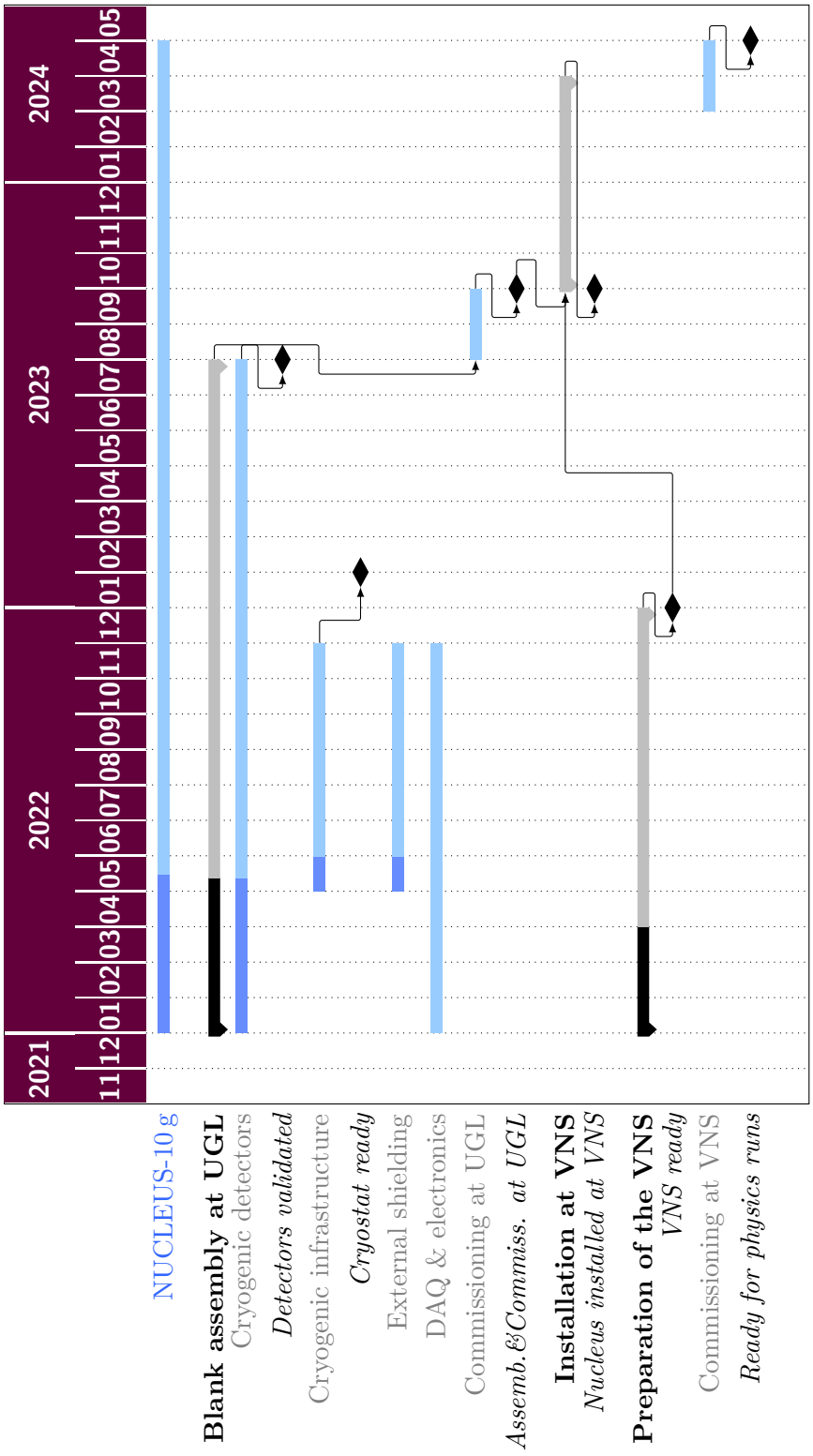

Figure 4.10: NUCLEUS-10g schedule.

4.7 NUCLEUS status and outlook

Due to the restricted access to the Chooz Nuclear Power plant for security reasons, the entire NUCLEUS experimental apparatus will be first assembled at the Technische Universität München (TUM) in a shallow underground laboratory, the so-called UGL, to optimize the cryogenic infrastructure, to study and validate the final detectors modules (namely, the cryogenic inner and outer vetos and the cryogenic target detector) doing a comprehensive calibration campaign and testing the rejection capability of a such sophisticated experimental set-up. According to the current NUCLEUS general planning (figure 4.10), the validation of the three detector modules at the UGL will be concluded within July 2023 [176]. The complete NUCLEUS assembling and commissioning at the UGL will be achieved within September 2023. Afterward, the installation of NUCLEUS at the Very Near Site (abbreviated VNS in figure 4.10) at Chooz is scheduled not later than February 2024. As a final milestone, the commissioning of NUCLEUS-10g should be finalized within April 2024, when the start of the first physics runs is scheduled.

Chapter 5

NUCLEUS cryogenic outer veto prototype

To reduce as much as possible the background level enhancing the possibility to detect and identify the CEνNS events, the NUCLEUS collaboration has conceived a cryogenic outer veto system composed of two cylindrical and four germanium parallelepiped-shaped crystals (figure 5.1) arranged as to form a box, completely surrounding and hosting the inner target detectors (see section 4.4.2). According to simulations dedicated to find the optimal crystal thickness, the two cylinders will have a diameter of 100 mm and a thickness of 25 mm whereas the four parallelepipeds will have dimensions 50 mm $\times$ 74.5 mm$\times$ $\times$ 5 mm, with a total mass of approximately 4 kg.

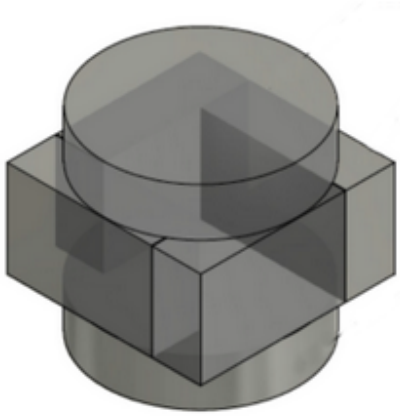

Figure 5.1: Simple schematic view of the designed NUCLEUS cryogenic outer veto.

To efficiently detect and reject background events (mainly due to neutrons and the most penetrating γ radiations), the outer veto must be featured by a response time at least as fast as the target detectors ($\sim$ 300 μs). This requirement can be fulfilled by

reading the ionization signal. Therefore, each germanium crystal will be equipped with aluminum electrodes evaporated onto the top and bottom surfaces to collect the free charges produced by the interacting particles.

To verify and validate the effectiveness of this background rejection system and define the *must-have* to operate in the best conditions, we gradually developed a cryogenic outer veto prototype at the Irène-Joliot Curie Lab (IJClab, Orsay, France).
In this chapter, I will describe the operating principles and I will show the results obtained in three measurement campaigns.

5.1 Principle of Germanium detectors

The idea of germanium crystals as solid-state detectors for particle physics research has its origin in 1963 with an investigation carried out by A.J. Tevendale and G.T. Ewan ([177, 178]) where they proved how efficacious germanium gamma-ray spectrometers can be. Indeed, germanium semiconductor detectors boast several advantages compared to the prior versions of crystal counters, such as exceptional energy resolution and fast timing features. Moreover, it is possible to produce easily crystals with a diameter of up to 10 cm.

Germanium is characterized by a bandgap of 0.661 eV. When a particle interacts within the crystal, it deposits energy exciting the local electrons. A valence electron could gain sufficient thermal energy to cross the bandgap into the conduction band: as a result, there will be a new electron in the conduction band and, a vacancy in the valence band. By a suited voltage bias applied to the electrodes, the electron and holes experience an electric field and drift to the electrode with opposite charge signs, where they are collected. The resulting signal is a current proportional to the interacting particle energy.
A single electron-hole pair needs average energy of 2.96 ± 0.02 eV [179] to be produced in germanium, a relatively small price that ensures a considerable amount of pairs and, therefore, good energy resolution and energy threshold .
In truth, electrons can jump from the valence to the conduction band also thanks to acquired thermal energy, causing thermal noise and jeopardizing the success of the experiment. To avoid this effect, the detector is efficiently cooled down at cryogenic tem-

peratures (10-20 mK).
The idea to exploit germanium crystals for the cryogenic outer veto system takes inspiration from the EDELWEISS experiment, where heat and ionization signals are both used with the goal to detect WIMP dark matter [180].

5.2 First test: single Ge crystal in the Actuator cryostat

5.2.1 Set-up and acquisition

The first test of the cryogenic outer veto was performed using a single germanium crystal (Φ=7 cm, h=2 cm and m=400 g) with planar electrodes evaporated onto the top and bottom surfaces, keeping a distance of 2 mm from the edges (figure 5.2). The procedure followed to deposit the electrodes consists of 3 steps:

- cleaning treatment of the crystal surface through 10 minutes of argon bombardment;
- surface passivation treatment realized with a 300 nm amorphous layer of hydrogenated Ge (a-Ge:H) deposited only onto the top and bottom surfaces. This process is important to reduce the electrical conductivity and, therefore, avoid surface leakage current. Indeed, the charges accumulated in traps close to the surfaces can be responsible for a leakage current of the order of 1 pA between two electrodes. As a consequence, a Joule heating of roughly 1 MeV/s can severely impact the CEνNS region of interest [181];
- electron beam evaporation in vacuum (10^{-7} bar) of 200 nm of aluminum.

The crystal was hosted in a copper holder structure (Φ=8.6 cm, h=2.7 cm) and kept well fixed through polytetrafluoroethylene (PTFE) elements. In general, PTFE has a very important role in all our assemblies. Indeed, additionally, to protect the crystals avoiding breaking or damaging them with the metallic structure, it works also as a weak thermal link between the crystal and the heat sink; without it, the crystal would be strongly thermally coupled to the heat sink avoiding the possibility to see changes of temperature, in case of heat read-out, or interfering to the charge collection in case of ionization read-out.
The germanium thermalization is guaranteed by two silicon squares (4 mm^2) glued directly on the crystal surface. Each of the squares has gold evaporation onto the surface

and is connected to the holder structure through several gold bonding wires (Φ=25 μm). The ionization signal is read by the electronics thanks to two aluminum wires (Φ=25 μm) that connect the electrodes to copper/kapton pads.

The detector was tested in the Actuator cryostat, a pulse tube refrigerator at IJClab (see section 2.6). Neither the detector nor the cryostat had an anti-vibration system included. During this test, the cryostat had not any lead shielding against the background radioactivity, hence we expected a high-event rate.

To lower the parasitic capacitance, we used cold electronics: 8 channel low noise JFET electronics compatible with voltage or charge amplification. The signal is amplified at room temperature with a 8-channel 2 MHz read-out acquisisystem (figure 5.3) [182].

To not affect the measurement with additional noise, we decided to make the detector cabling with low noise stainless steel cables.

The cryostat was closed and cooled down at the temperature of 17 mK. Reached the base temperature, one of the electrodes is biased with a voltage of 1.5 V while the second one is grounded. To make easier the subsequent characterization, a thoriated wire (i.e. a ^{232}Th source) was placed outside the cryostat in order to perform a gamma calibration.

A first evaluation of the signal was performed online, before starting the data acquisition. A huge pile-up was evident: in each 1 s window we detect 38 events on average, each of them with a rise-time of approximately 75 μs. This avalanche of events is probably due to the missing lead shield against the environmental background. Could not act against it, we made faster the detected pulses by modifying the operational amplifier cards unsoldering and removing the capacitors. This simple action guaranteed bandwidth of approx 2 μs, the speed limit of the amplifier. This means that even if we designed the detector to be faster, we are limited by our amplification card as long as we change it with one specially designed for very fast signals. For the purpose of the measurement, we don't need faster ones.

Furthermore, an elementary study of the noise spectra has revealed the necessity of some improvements to the experimental set-up to partially eliminate sources of microphonic noise. At the end of this operation, we observe similar noise spectra for anode and cathode where some structures are identifiable as microphonic noise (figure 5.4).

The original plan was to perform a measurement campaign using different bias voltages for the electrodes. Unfortunately, we performed just a measurement of one hour with 1.5 V voltage bias because of an unexpected problem with the cryostat. No more

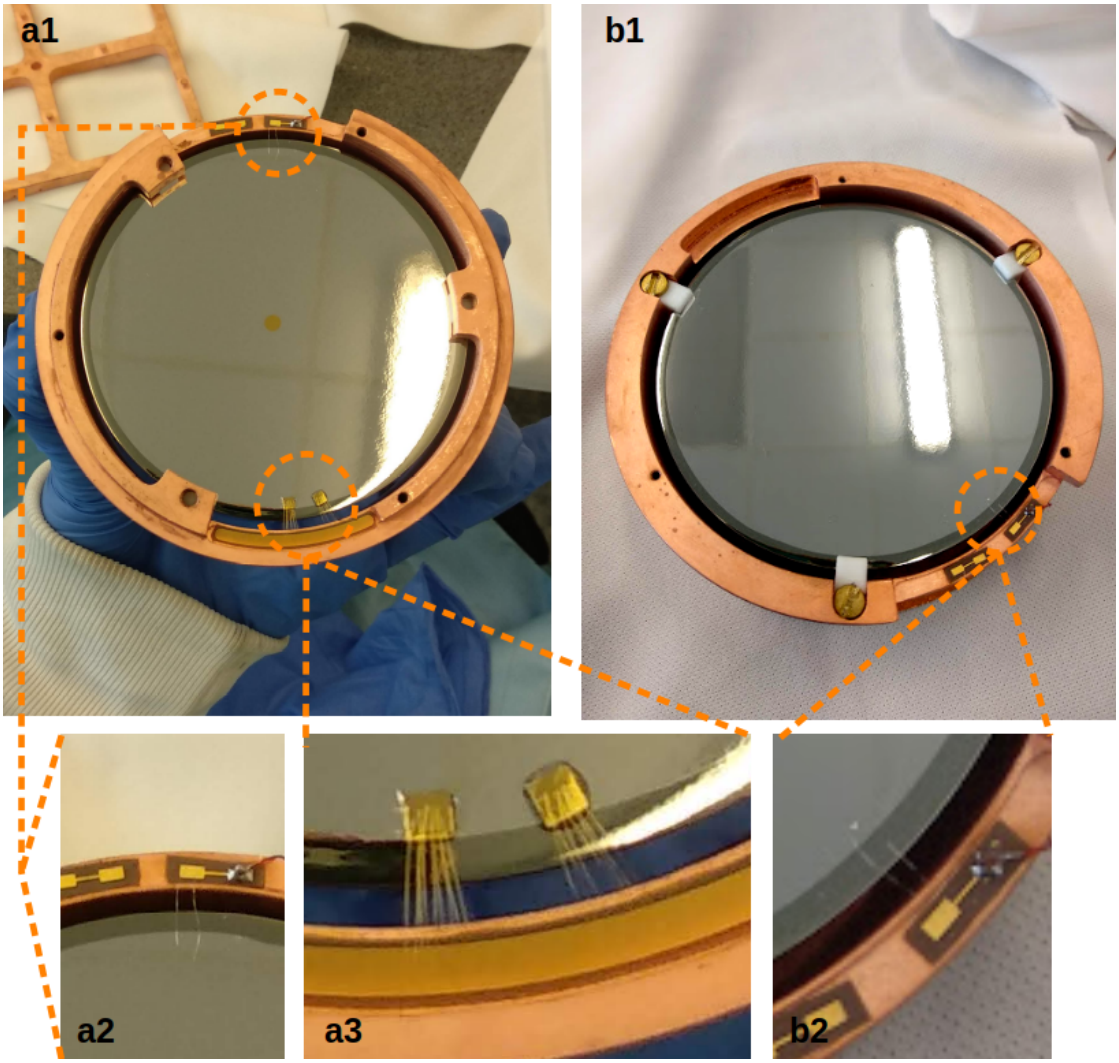

Figure 5.2: Figure *a1*: top surface of the germanium crystal; figure *b1*: bottom surface of the germanium crystal. Two silicon squares are glued and bonded to the heat sink to thermalize the crystal (figure *a3*). Each electrode is provided of two aluminum wires for the ionization readout (figures *a2* and *b2*).

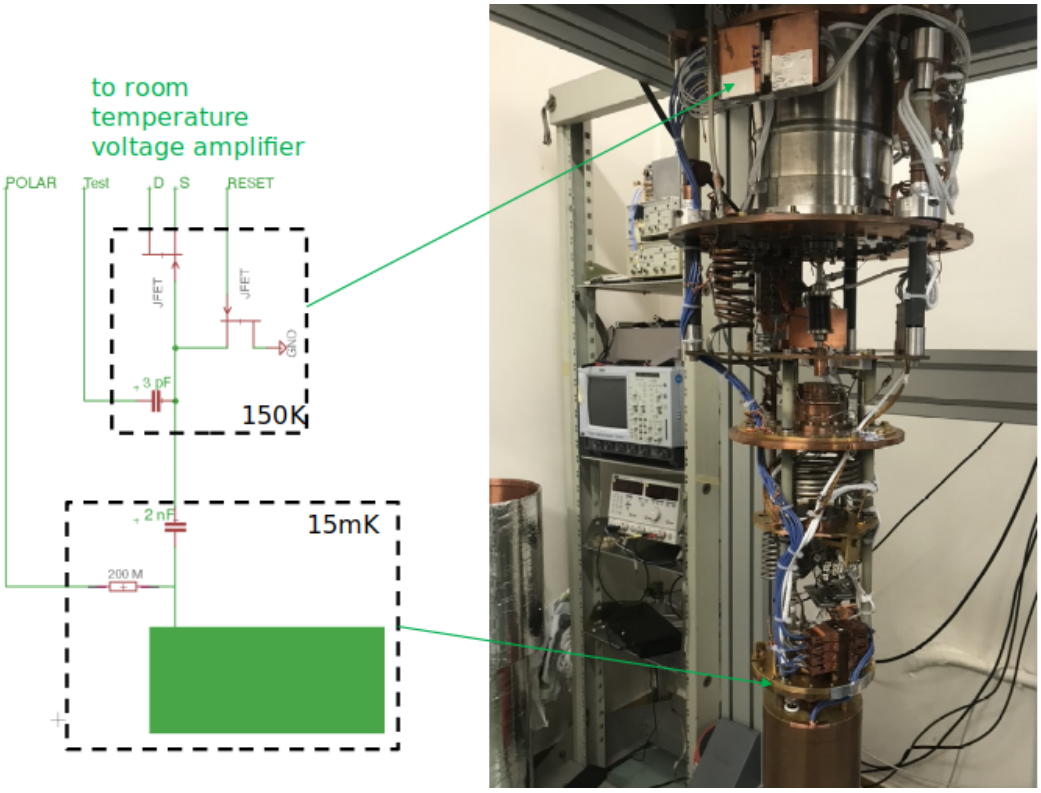

Figure 5.3: *Right*: the Actuator cryostat. *Left*: scheme of the read-out electronics.

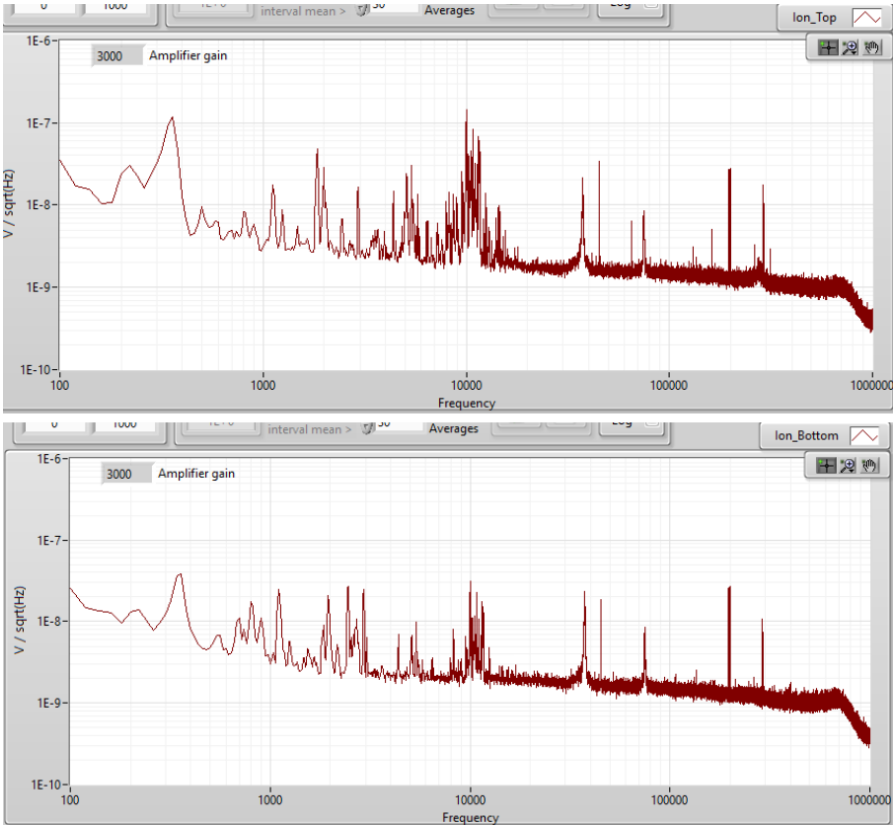

Figure 5.4: Noise spectra of the two electrodes after some modifications at the experimental set-up. The two channels present similar noise structures identifiable as microphonic noise. The strong similarity of the two noise spectra will be useful to simplify the analysis technique (see section 5.2.2), combining the two channels and processing them at once.

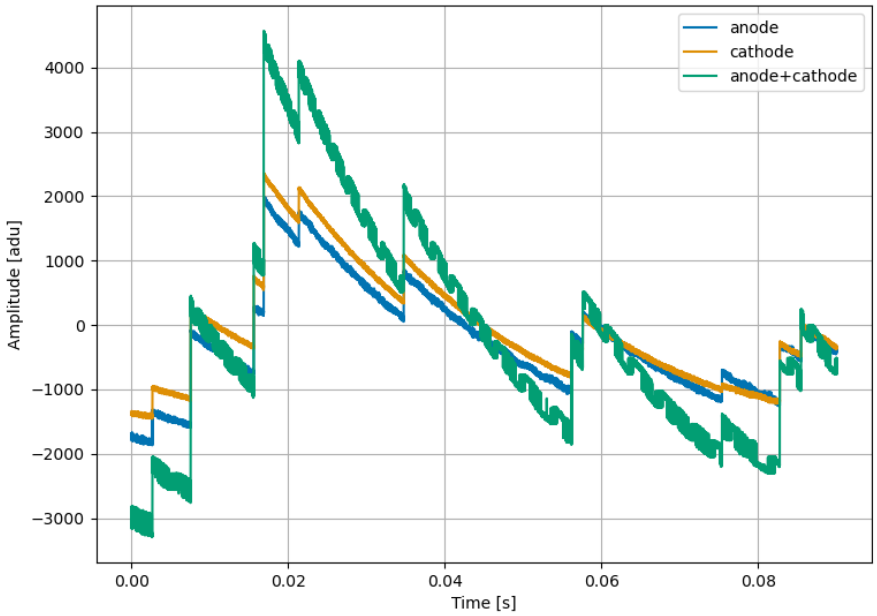

Figure 5.5: Comparison of the anode (*blue*) and cathode (*orange*) signals in an arbitrary time window. For both electrodes, we observe the same pulses characterized by the same amplitude. When the two are combined (action possible thanks to the similar noise spectrum), the result is a unique signal with a doubled amplitude.

measurements were possible. The data were streamed and stored continuously, with a sampling frequency of 5 kHz.

5.2.2 Analysis of the ionization signal

Data processing

As expected, a first look offline at the data reveals a significant pile-up. Since the noise spectra of the two ionization channels are similar and the amplifier cards have the same features, we decided to combine the anode and cathode signals: the signal with negative polarity is inverted and added to the one with positive polarity. As a result, we have a unique signal to process whose amplitude is increased by almost a factor of two, remembering that germanium has similar values for the holes and electrons mobility

(figure 5.5), and a reduction of the coherent noise.

The acquired data are processed and analyzed offline with Argonauts (see section 3.1), a software based on Matlab and developed at IJClab to process NTD signals.

To proceed with the analysis, it is indispensable to apply a filter directly to the raw data in order to recover quickly the baseline level. Hence, I developed a program in Matlab dedicated to the combination of anode and cathode signals and subsequently the filtering of the resulting signal with a high pass filter [183], simply defining two parameters:

- the cut-off frequency f_c, namely the frequency above which the signal can pass;
- the Nyquivst frequency f_n, defined as the sampling frequency/2.

A study on the effect of the filter is performed to compare and identify the most appropriate cut-off frequency (figure 5.6, *top*).

In the end, the chosen f_c is 1000 Hz, a value that turned out to be a good compromise between the pile-up rate and the preservation of the amplitude of the pulses (paying particular attention to the low energy region). In figure 5.6 *bottom*, we can observe the comparison between the unfiltered signal and the filtered one: thanks to the high pass filter, now the data stream is adjusted for the Argonauts data analysis.

Once the full data streams are filtered, we are ready to process them with Argonauts, starting from the building of the reference pulse. Figure 5.7 shows an example of an individual filtered pulse eligible for the reference pulse building and the reference pulse. As observed in the online preview, the pulses show a characteristic rise time of 2 μs and a decay time of $\sim$170 μs (value determined by the applied filter).

At the end of the process, we obtain an n-tuple file that contains the main information (between these, the raw amplitude, the filtered amplitude, the rise and decay times, the correlation, and the decay time) about each triggered event.

Data analysis

Once the n-tuple file is generated, it is important to check the stability of the baseline and eventually remove some jumps that can impact the analysis. In this case, since the

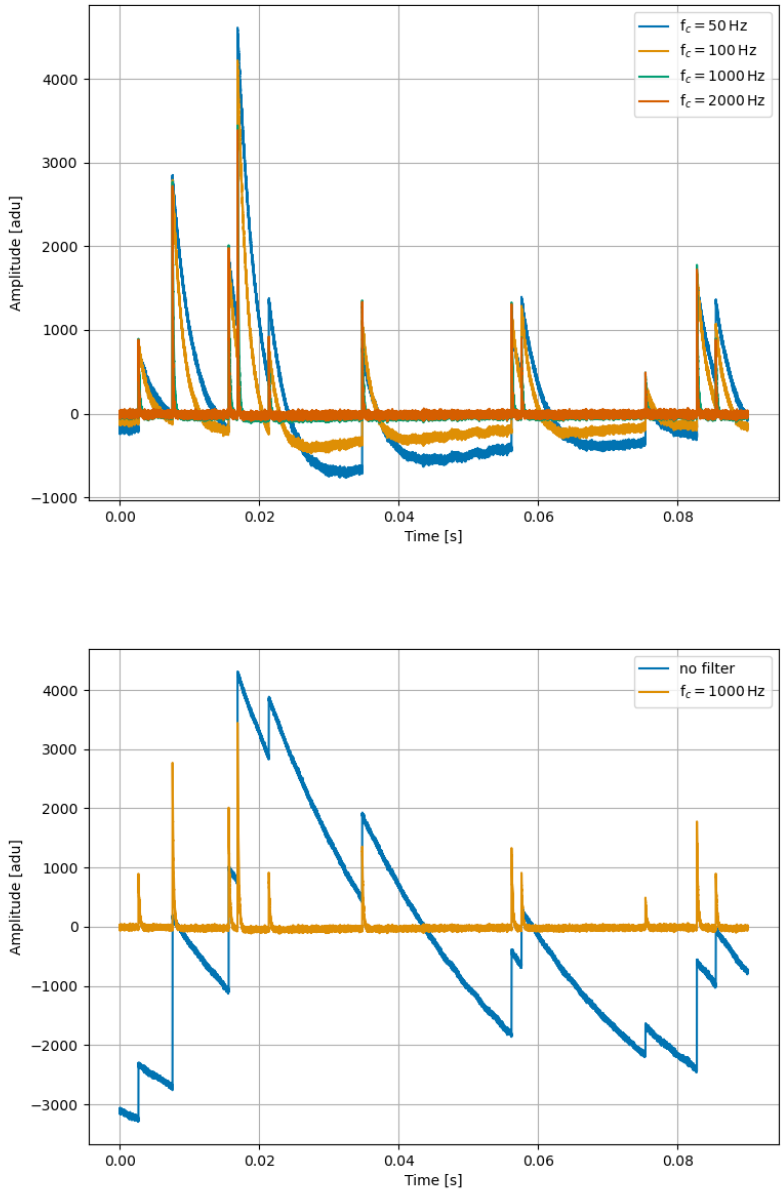

Figure 5.6: *Top*: an example of a time window of the acquired data stream that undergoes high pass filters with different frequency cut f_c values. This comparison clarified the magnitude of the effect of the filter increasing f_c. *Bottom*: comparison between the unfiltered signal and the same underwent to the high pass filter with f_c=1000 Hz.

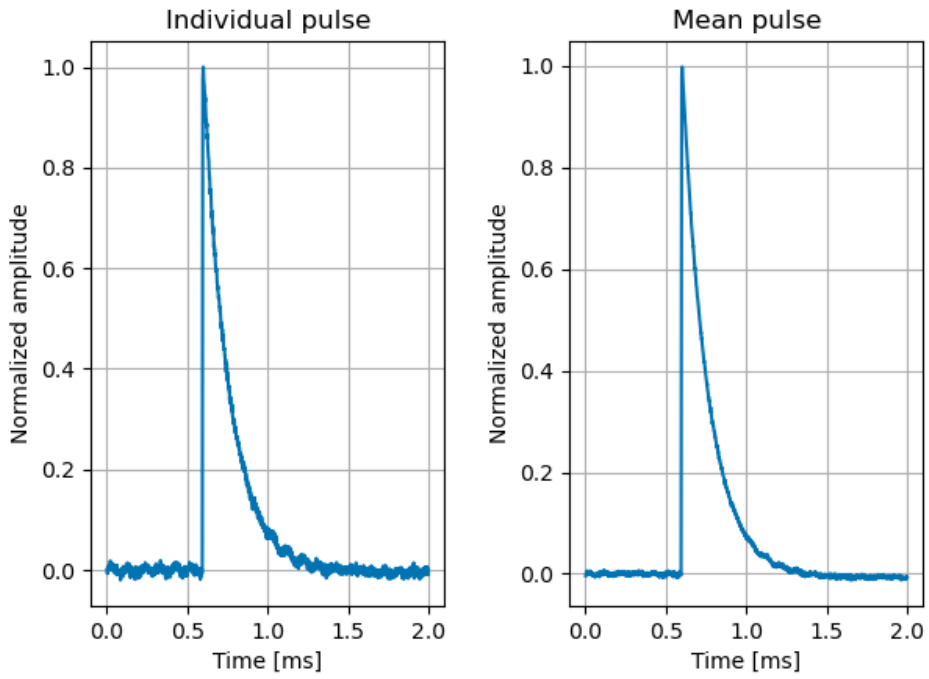

Figure 5.7: *Left*: example of individual pulse after the high pass filter; *Right*: reference pulse used as template in the analysis.

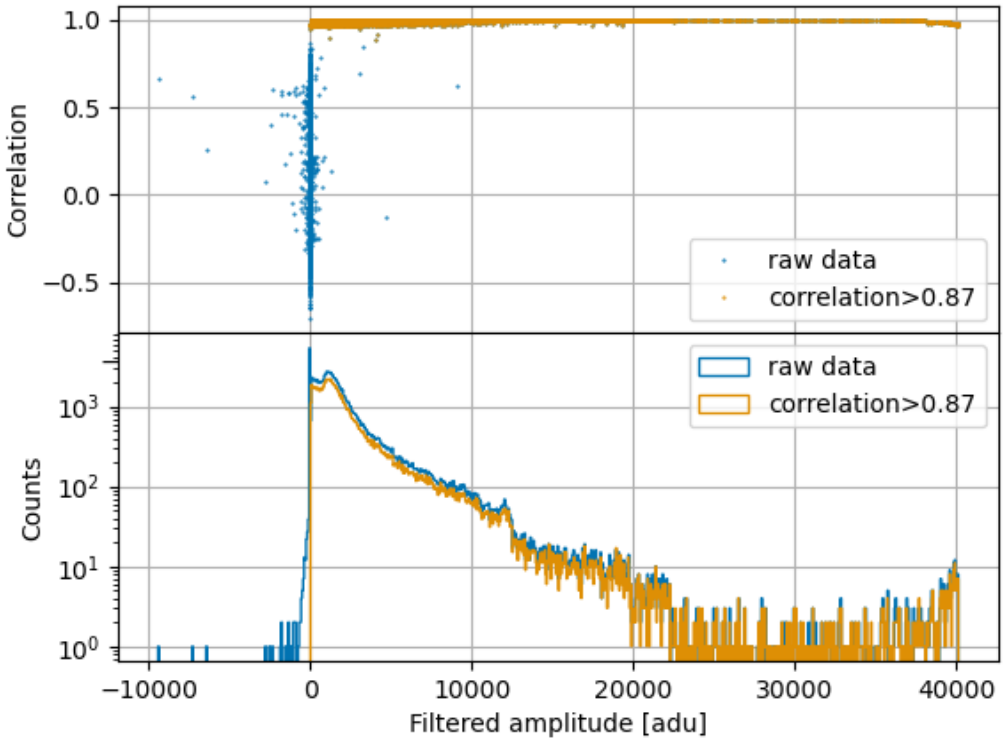

Figure 5.8: *Top:* correlation parameter vs. amplitude. For this analysis, we selected just events with an acceptable correlation value (0.87). *Bottom:* energy spectrum comparison before and after the correlation selection.

data are filtered with a high pass filter, the baseline is distributed around 0 adu (Analog to Digital Units); there is no reason to correct it.

Furthermore, in order to perform an optimized energy resolution, it is important to remove the events affected by pile-up or pathological events. A useful parameter to remove efficiently them is the correlation (defined in section 3.1), the parameter that quantifies how much the filtered pulse is similar to the mean pulse. In this case, it was set at 87 % (figure 5.8, *top*). In figure 5.8 *bottom*, the uncalibrated energy spectrum comparison between before and after the correlation.

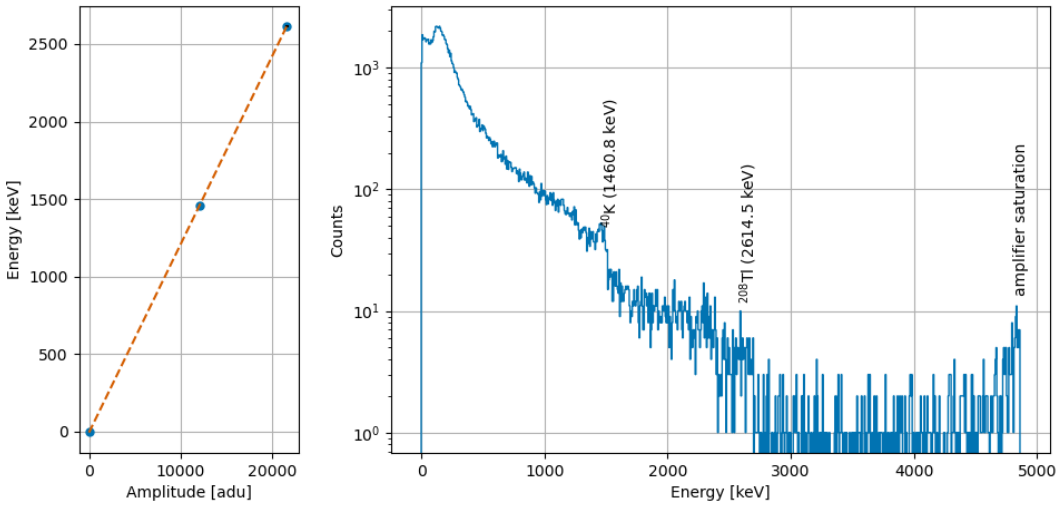

Figure 5.9: *Left*: energy calibration using the ^{40}K and the ^{208}Tl peaks. *Right*: the calibrated energy spectrum.

The detector calibration is performed using gamma peaks produced by the ^{232}Th source. Unfortunately, the acquisition was too short to see all the main gamma peaks of the thorium chain. Nevertheless, we were able to identify the end of the natural radioactivity coincident with the ^{208}Tl peak (2614.5 keV) (figure 5.9). Moreover, the 1460.8 keV γ line, due to the radionuclide ^{40}K, was visible because of the absence of any lead shielding.

The main results are reported in table 5.1. Despite the not optimized cryogenic conditions and the low statistics, we consider these results very promising. Indeed, they suggest that, combined with a sufficiently fast read-out system, the cryogenic outer veto prototype has the potential to satisfy the NUCLEUS requirements in terms of speed, energy threshold, and particle identification.

Table 5.1: Main results obtained from the data analysis

energy resolution (FWHM, at 1460.8 keV) [keV]	71±28
baseline resolution (FWHM) [keV]	1.1
sensitivity [nV/keV]	842
rise-time [μs]	2
energy threshold ($5\sigma_{RMS}$) [keV]	2.3

5.3 Second test: two Ge crystals in the Ulysse cryostat

5.3.1 Set-up and acquisition

The detector prototype

The detector used during the first test run is modified by adding a second germanium crystal. This detector has been previously used in the EDELWEISS experiment, and it has the same features of the germanium used in the first test: diameter of 7 cm, thickness of 2 cm, and mass of 400 g. The germanium is pretreated with 10 minutes of argon bombardment and passivation of the top and bottom surfaces realized with a 300 nm a-Ge:H; then, the electrodes are produced depositing 200 nm of aluminum via electron beam evaporation. The main difference between the two germanium crystals is represented by the geometry selected for the electrodes. Indeed, this detector, also called InterDigit, has concentric aluminum electrode rings evaporated onto the top and bottom surfaces [184]. For practical reasons, from now I will call 'Ge TOP' (or simply 'TOP') the ionization channel of the InterDigit detector and 'Ge BOT' (or 'BOT') the one of crystal with planar electrodes. The aluminum rings of the InterDigit detector are connected together forming a unique electrode in order to reproduce a geometry closer as much as possible to the planar one. Moreover, the InterDigit detector was already equipped with two NTDs (one per side). We decided to connect one of them to get also a comparison between the heat and ionization channels.
Lastly, we added also a Li_2WO_4 crystal between the two germanium working as a target detector to test the identification and rejection efficiency of the COV prototype. Onto the crystal, an NTD was glued. Unfortunately, the connection with the sensor was lost during the detector cooling down. Therefore, in total, we had four ionization channels (two electrodes per each of the two germanium crystals) and a heat channel (namely,

the NTD of the InterDigit detector).

Finally, the detector was wrapped with copper foil to protect it from infrared radiation. A lead castle 10 cm thick was shielding the entire cryostat.

Electronics and Cryostat

This second test was performed in the *Ulysse* cryostat at IJClab. This dilution refrigerator and its electronics are specifically designed to test crystals coupled to NTDs and, therefore, to read heat signals. The electronics was developed by the Milano-Bicocca group and has features very similar to the one used in the CUORICINO experiment: it is a room temperature fully differential voltage-sensitive preamplifier based on a pair of JFET transistors [185, 186]. In order to read the COV ionization signals, we can't just use these electronics like it is. We needed to add some components to our read-out system. Therefore, we designed an extra electronic box to be able to bias the germanium detectors and read at the same time the four ionization plus the NTD signals. Moreover, we added a resistors box at the cryostat cold plate level to reduce the thermal noise component of the bias resistors and, as consequence, the equivalent shot noise (figure 5.11).

In table 5.2, a comparison between the main set-up features of the first and second test measurements is given.

Germanium regeneration

A crucial moment is the regeneration of the germanium crystals. Indeed, no matter how pure the crystal may be, there are always contaminating atoms constituting the crystal lattice. When the electric field is established inside the crystal to allow the charge collection, some of the free charges originated in the crystal are captured by these intrinsic impurities, generating larger and larger trapping centers and forming in close vicinity of the electrodes an electric field with opposite sign. If the crystal is not periodically regenerated, the collecting field is progressively reduced and, as a consequence, the signal decreases until it disappears. To ensure the detector optimal performance avoiding this effect, it is important to neutralize the trapping centers by injecting charges in absence of collecting bias at the electrodes. The crystal regeneration can be obtained using an intense gamma source or infrared irradiation [187]. In our application, we decided to use a LED: an Agilent HFBR-1404 characterized by a wavelength of 820 nm based on the

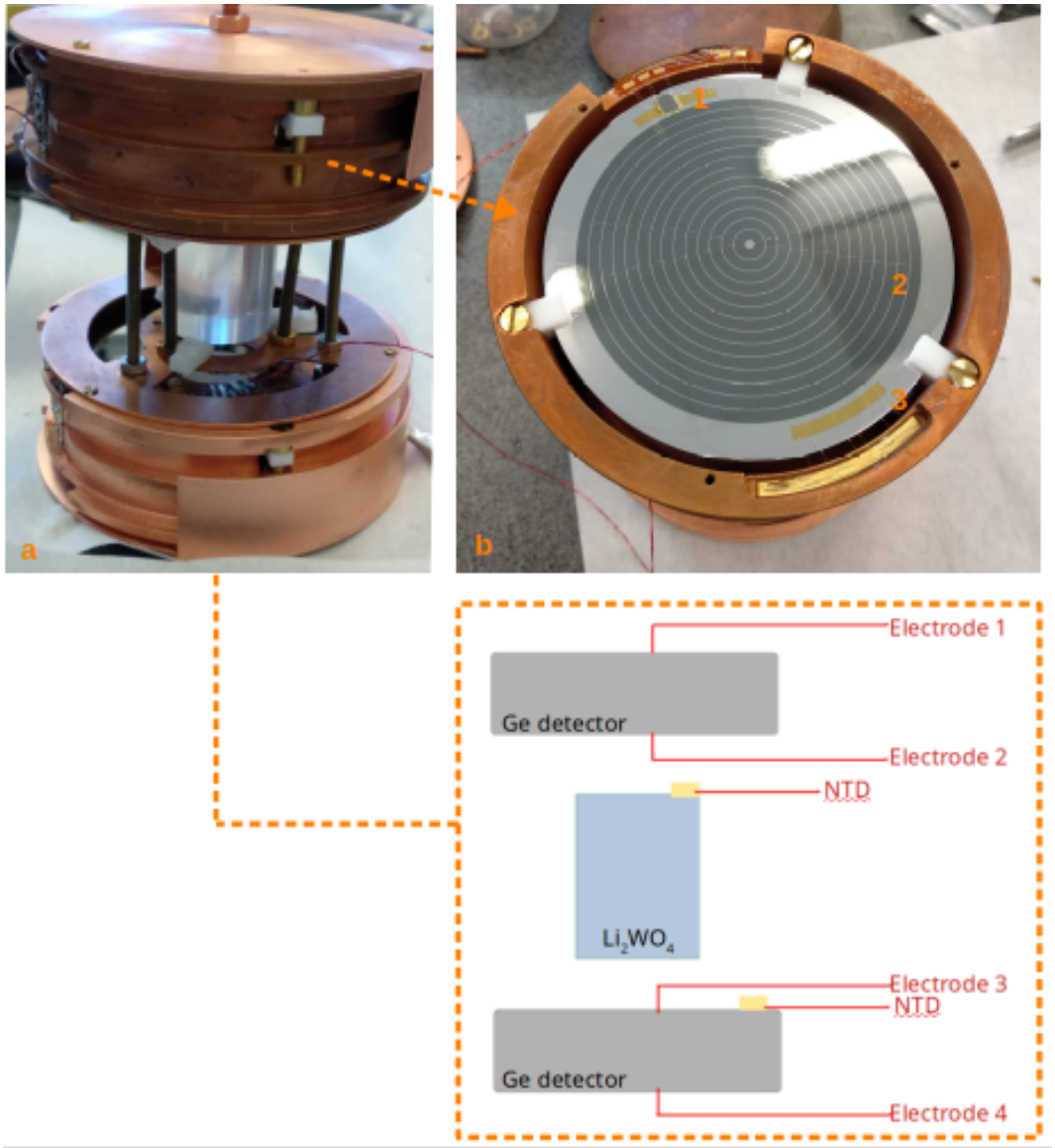

Figure 5.10: Photo and schema of the detector tested in the second test run. The added crystal is an Inter Digit, a detector largely used in the Edelweiss experiment [180].

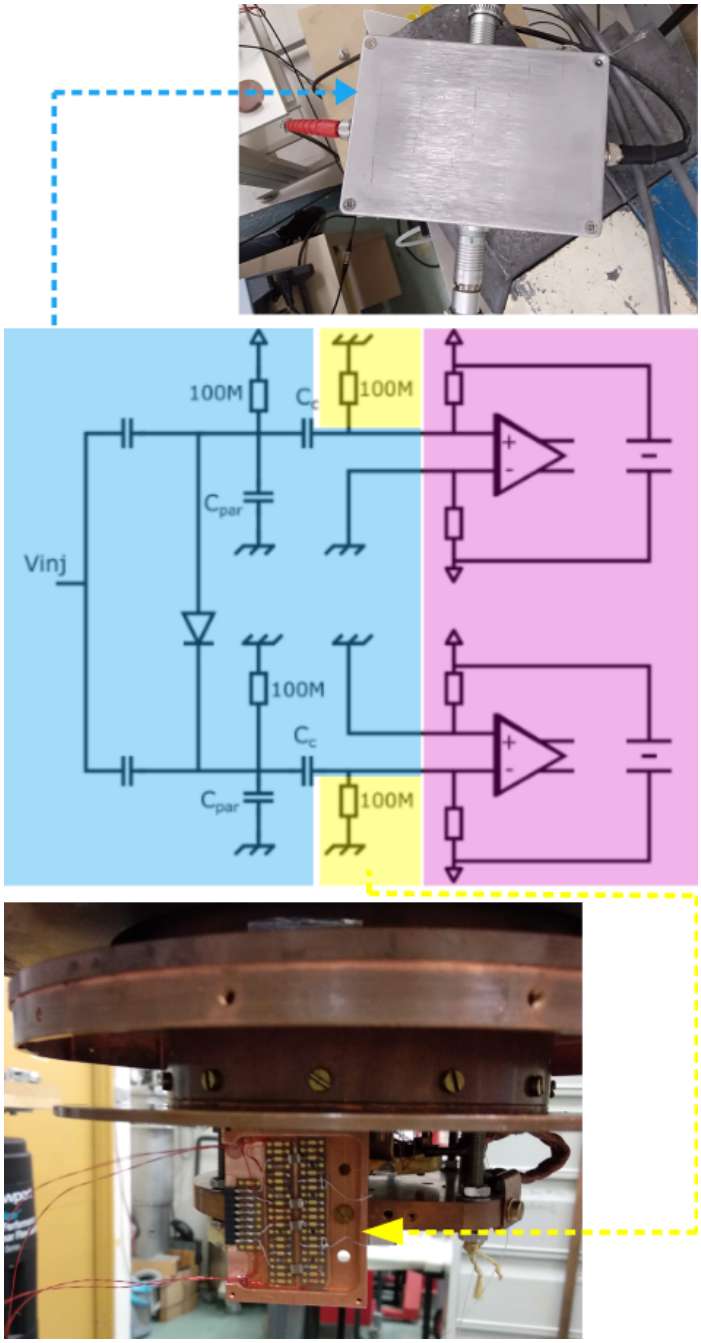

Figure 5.11: Schematic representation of the final read-out system. In pink, the already existing electronics. In yellow, the resistors placed in the box fixed at the cryostat cold plate. In blue, the additional electronics stage placed at room temperature.

Table 5.2: Summary of the main features of the Ulysse and Actuator set-ups.

	First test (Actuator)	**Second test (Ulysse)**
detector structure	BOT	TOP + Li_2WO_4 + BOT
electronics	cold electronics (BiFET for the heat channel and JFETs for the ionization channels)	Milano-Bicocca low noise voltage amplifier at room temperature + extra adaptation box
cryostat type	pulse tube cryostat (1 vacuum chamber)	pulse tube cryostat (2 vacuum chambers)
lead shield	no	yes
capacitance on which the charge is integrated	80 pF + 10 pF (detector itself)	>>500 pF

AlGaAs diode technology. The light is delivered to the cryostat mixing chamber, where the detector is fixed, thanks to an optical fiber. This LED provides a stable output that is regulated through a squared waveform in normal polarity with a width of 50 μs, and a frequency of 20 Hz. In order to accelerate the regeneration of the crystal, a voltage of the opposite sign is applied to the biased electrodes instead of grounding all of them. The regeneration process is monitored by checking the amplitude of the ionization signals.

5.3.2 Data taking and analysis

The measurement was performed at a cryostat base temperature of 20 mK, and with a sampling frequency of 20 kHz. For each germanium crystal, an electrode was biased with 10 V while the other one was grounded.

A ^{232}Th source was placed between the cryostat and the lead shield. The acquisition, interspersed with moments during which the data recording was stopped and the germanium crystals regenerated, was divided into three parts. Each measurement was analyzed separately and only at the end the obtained results were combined.

Table 5.3: Main results obtained in each of the 3 measurement partitions.

	Meas.3 (12 h)	**Meas.4 (19 h)**	**Meas.8 (24 h)**
energy resolution (FWHM) @ 2614.5 keV [keV]	54±3	36±4	43±3
threshold ($5\sigma_{RMS}$) [keV]	61.6	55.2	53
baseline resolution (FWHM) [keV]	29±2	26±2	25±1
sensitivity [nV/keV]	73	76	83.8

Data analysis

Taking a first look at the data, it is clear the necessity of reshaping the pulses: in addition to the slow recovery of the baseline, we observed an extra noise component not understood. Therefore, we applied a Butterworth band-pass filter (f_{low} = 20 Hz and f_{high}=250 Hz) [183]. Then, anode and cathode signals are combined obtaining in total three data files to process: two ionization signals (one for each germanium detector) and a heat signal (the InterDigit NTD). Then, an analysis procedure similar to the one described in section 5.2.2 is followed. Figure 5.12 shows the calibrated energy spectra obtained with the Ge TOP (in blue) and Ge BOT (in yellow) detectors, in the full energy scale (0-25 MeV) and γ energy region (0-3 MeV). In order to have a confirmation of the achieved energy spectra, the CRAB experiment team developed GEANT4 simulations of both the BOT and TOP germanium detectors [188]. Comparing the simulated muon bump maximum with the real data, they confirmed the energy calibration and the linearity of the electronics. Looking the table 5.3 we can estimate for the Ge TOP detector an energy resolution (FWHM) at 2614.5 keV of 38±2 keV and an energy threshold (evaluated as $5\sigma_{RMS}$) of approx 56 keV.

In table 5.4, a brief comparative summary of the features and results of the first and second tests is reported. We observe a very different sensitivity that can be explained by the different capacitance of the cables connected to the NTD.

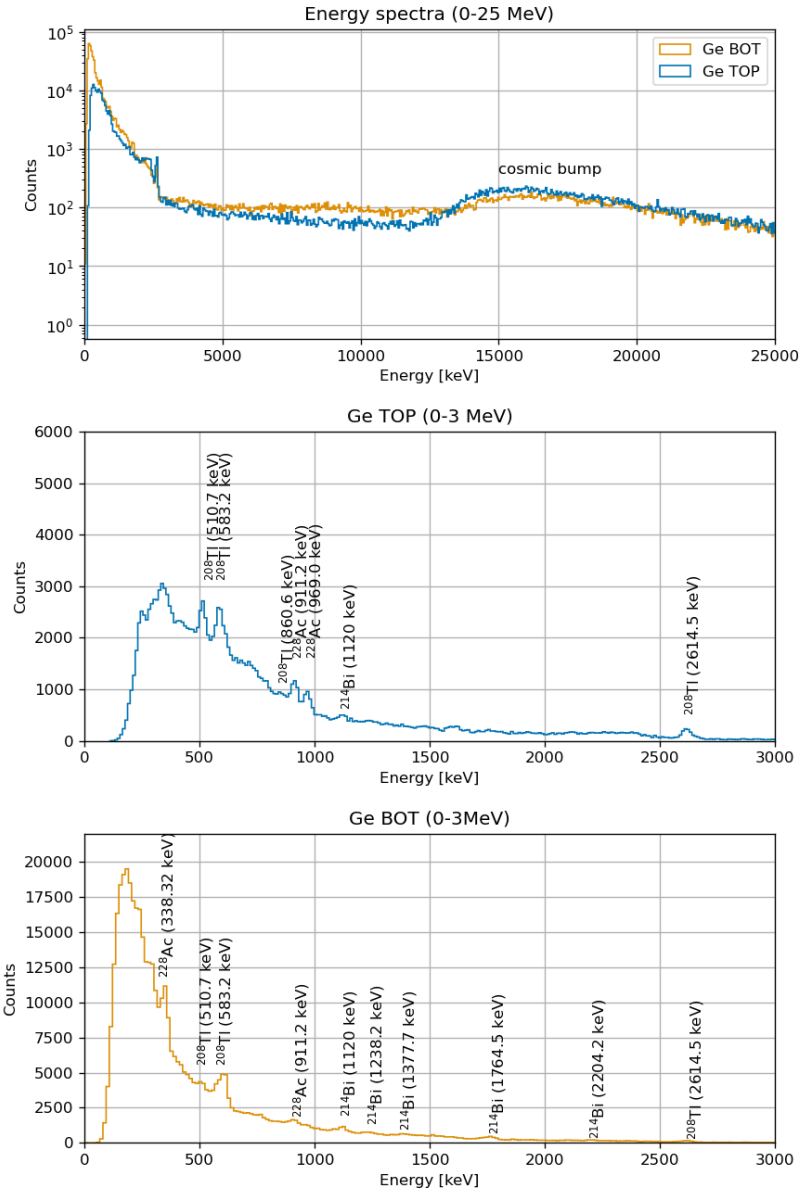

Figure 5.12: *Top*: Ge TOP (in blue) and Ge BOT (in yellow) energy spectra. In the inset, the 0-25 MeV energy region. *Center* and *bottom*: respectively the Ge TOP and Ge BOT energy spectra zoomed in the γ energy region (0-3 MeV). 124

Table 5.4: Comparison table between the first and second tests with Ge BOT.

BOT detector in:	1st test (Actuator)	2nd test (Ulisse)
main differences	capacitance: 100 pF bias voltage: 1.5 V filter: high-pass (1 kHz) + optimum filter	capacitance: >500 pF bias voltage: 10 V filter: band-pass (20-250 Hz) + optimum filter
energy resolution (FWHM) [keV]	71±28 @ 1460 keV	52.5±5 @ 2614 keV
threshold ($5\sigma_{RMS}$) [keV]	2.3	45
baseline resolution (FWHM) [keV]	1.1	21.3
sensitivity [nV/keV]	842	94.7
rise time [μs]	2	107

An additional study: the heat and ionization coincidences

After the characterization of the detector, we decided to exploit the NTD glued on the InterDigit detector to make an additional study between the two signals. The process is composed of two steps. First of all, remembering that an NTD is really much slower than the ionization signal (tens of ms versus a few tens of μs) we need to define the temporal shift between the answers of the two detectors. This is possible by processing the NTD data with a sufficiently high energy threshold in order to have muon events. This is important to reduce the number of events and make easier the identification of the NTD delay. Once this parameter is identified, the data are triggered again changing the high energy threshold to 5 times the baseline RMS standard deviation and setting the time correction.

The first plot of figure 5.13 shows the events seen by the NTD versus the Ge TOP in coincidence. As expected, being the NTD glued on the InterDigit detector, we have a linear behavior at lower energies (approx below the dashed line) between the two channels. At higher energies, the NTD linearity becomes progressively weaker: this happens when the signal is comparable with the calorimeter working voltage, and we have a saturation effect.

The same procedure was followed to verify the coincidences between the Ge BOT with the other two channels (second and third plots in figure 5.13). In contrast to the first plot in the same figure, here we clearly observe many accidental coincidences. Moreover, in both the plots, we can see a slope in the distribution of the events in coincidence probably due to a cross-talk between the two detectors.

5.4 Third test

The first two tests proved that the outer veto prototype can satisfy the NUCLEUS requirements in terms of speed and energy threshold despite not optimized cryogenic conditions, the little statistics, and the bias due to an analysis tool not shaping up for these specific measurements. Thanks to the first two tests, we can conclude that to achieve the best performances, it is fundamental that cold electronics are specifically developed to allow also the read-out of ionization signals. The achieved results encouraged us to embark on a third measurement campaign to fully understand the prototype and establish an indicative analysis procedure for the final NUCLEUS COV.

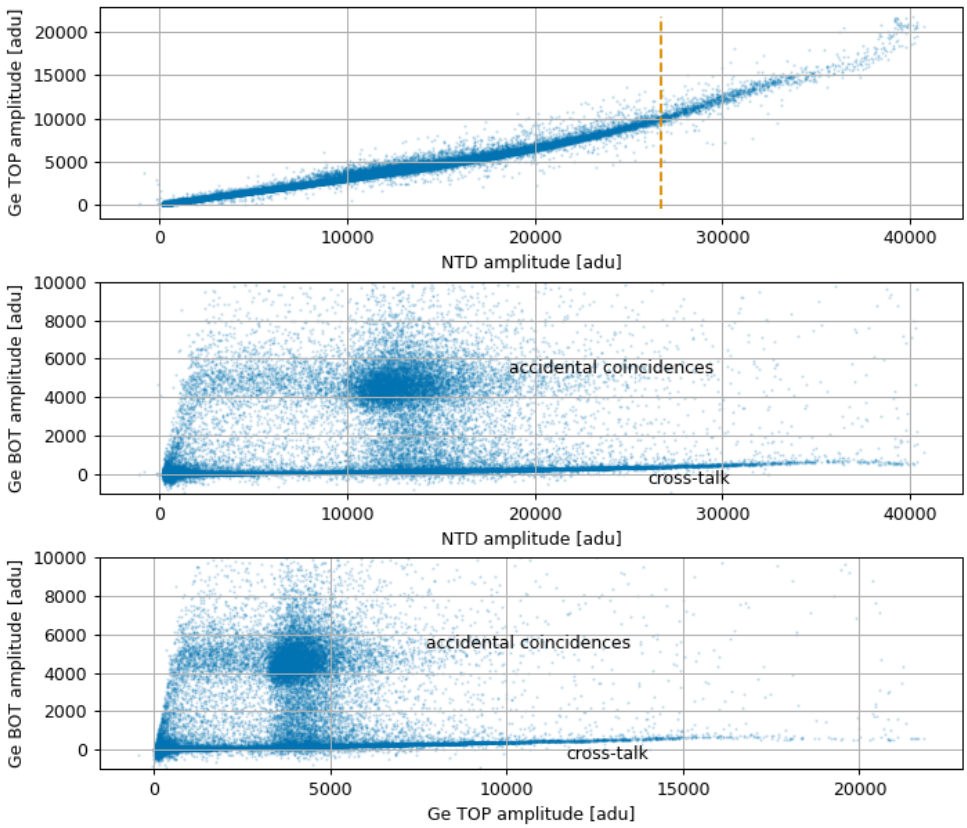

Figure 5.13: Comparisons between the Ge BOT, Ge TOP, and NTD. In the *first* plot, we can recognize a linear behavior between the NTD (glued to the TOP detector surface) and the Ge TOP that becomes progressively less strong with the energy increasing (more evident if we compare before and after the dashed line in orange). In the *second* and *third* plots, the comparisons between the events seen by the two different detectors. Independently if we look at the heat (i.e. NTD) or ionization (i.e. Ge TOP), we see clearly a concentration of accident events while the distribution of real events shows a slope probably a symptom of a cross-talk issue.

During this third test, we investigated and experienced the limits of the Argonauts software for this application which led us to the decision to build a completely new analysis tool (see section 3.2). Thanks to this new analysis technique it has been possible to completely understand and characterize the cryogenic outer veto prototype.

5.4.1 Set-up and acquisition

Detector and experimental set-up

The COV prototype used during the new test is the same already described in subsection 5.3.1: two germanium crystals providing in total 4 ionization channels and a Li_2WO_4 in the middle providing a heat channel. This Li_2WO_4 is added to make a coincidence study between the outer veto and the target detector, like in the NUCLEUS case. The NTD glued on the Li_2WO_4 crystal is biased using 1 kHz squared modulation, a method generally used in the EDELWEISS experiment [181]: instead of applying a constant current (DC bias), we inject a triangular waveform. Passing through a load capacitor, it is transformed into a squared one whose each cycle is composed of a positive and a negative section. The NTD resistance is obtained from the voltage difference between the positive and negative currents of each cycle. Before starting the data processing, we will need to demodulate the recorded signal, in order to recover its original shape, namely its temporal evolution: the negative sections will be reversed and the resulting signal will undergo a low pass filter. The alternate bias (AC bias), allows to shift the signal at a higher frequency and free from the low noise that is typical of the amplifiers. As a result, we can benefit from an improved signal-to-noise ratio. If we had used the DC bias, where the load capacitor is replaced by two load resistors, we would have potentially risked experiencing $1/f$ noise below the 200 Hz thus degrading the energy resolution. The choice to use 1 kHz as modulation frequency instead of a lower value is due to the fact that it plays a fundamental role in the rise-time of the recorded signal. Indeed, since the NTD is a slow device, a lower modulation frequency would lead to a lost of the pulse rise-time and hence a loss of the signal information.

To facilitate the regeneration of the germanium crystals, we glued an LED (1650 nm IR) onto the holder of the bottom detector. The regeneration procedure consists of illuminating the germanium crystals for 10 minutes and since the LED has the effect

Table 5.5: Main energy lines expected from the ^{241}Am source.

Energy [keV]	**Intensity [%]**	**Radiation**
13.9	13.02	Np Lα X-rays
17.0	18.6	Np Lβ X-rays
21.2	4.83	Np Lγ X-rays
26.3	2.31	γ
59.5	35.9	γ

to heat the system, leave the cryostat to recover the base temperature for approx 1 hour. At the bottom of the COV, we added an ^{241}Am source (table 5.5) wrapped with some copper tape to stop the alphas and have some gamma radiations at low energies. Given the importance of fast and low noise electronics, the detector was mounted in the Actuator cryostat (already introduced in subsection 5.2.1). We cooled down the detector to 18 mK and for two weeks we did different measurements (with natural radioactivity, ^{232}Th gamma or ^{252}Cf neutron sources), half without and half with 5 cm thick lead shield. For both the germanium detectors, we applied a bias voltage of 10 V to one electrode while the other one was grounded. The data were streamed and stored continuously with a sampling frequency of 100 kHz.

5.4.2 Data analysis

The following measurement is therefore entirely analyzed using a new analysis tool based on C++ and Root framework (already presented in section 3.2), tuned to study time coincidences.

Once all the data are processed, we can recover information about the detector performances just by setting a few parameters: rate above thresholds, calibration slopes, sensitivities, baselines RMS, and energy spectra.

The subsequent analysis is built in two steps: characterization of the three detectors and coincidences study.

Detector characterization

In figure 5.14 and 5.15 the main detector runs information. The baseline was stable for all the runs in the case of the ionization channels, while the NTD σ_{RMS} shows a varia-

Table 5.6: Averaged rates for each detector in different acquisitions and attenuation percentage between the case with and without lead shielding.

Type	**Channel**	**Not shielded** (Hz)	**Shielded** (Hz)	**Attenuation** (%)
background	NTD	6.0	2.3	62.2
	BOT	39.4	16.0	60.0
	TOP	27.0	8.2	69.6
gamma	NTD	6.9	2.1	69.1
	BOT	44.6	19.2	57.0
	TOP	31.6	9.6	69.5
neutron	NTD	6.5	2.3	64.3
	BOT	41.5	16.2	60.9
	TOP	28.6	8.7	69.6

tion within the 22% being this sensor more sensitive also to tiny temperature variations (figure 5.14, top). We can find another confirmation of the detector stability by looking at the calibration slope value (figure 5.14, bottom). This parameter is particularly useful because it allows an evaluation of the detector's sensitivity which is evaluated as calibration slope divided by the DAQ gain.

In figure 5.15, we can clearly see the effect of the lead shield; in table 5.6 the averaged rate of each detector during a background, gamma, and neutron calibration, with and without lead shield around the cryostat.

The difference between BOT and TOP rates is mainly due to the ^{241}Am source and the radioactivity coming from the ground that interacts mainly with the lower detector (i.e. BOT).

In figures 5.16 and 5.17, the comparison between the energy spectra of BOT and NTD with and without the lead shield surrounding the detector and a magnification of their low energy region (0-100 keV). All the plots are normalized at the same acquisition duration. On the right side of figure 5.16, we can observe the gamma peaks due to the radiation emitted by the ^{241}Am in tight contact with the BOT detector; the rate of the 60 keV was stable for all the run (variations less than 2%).

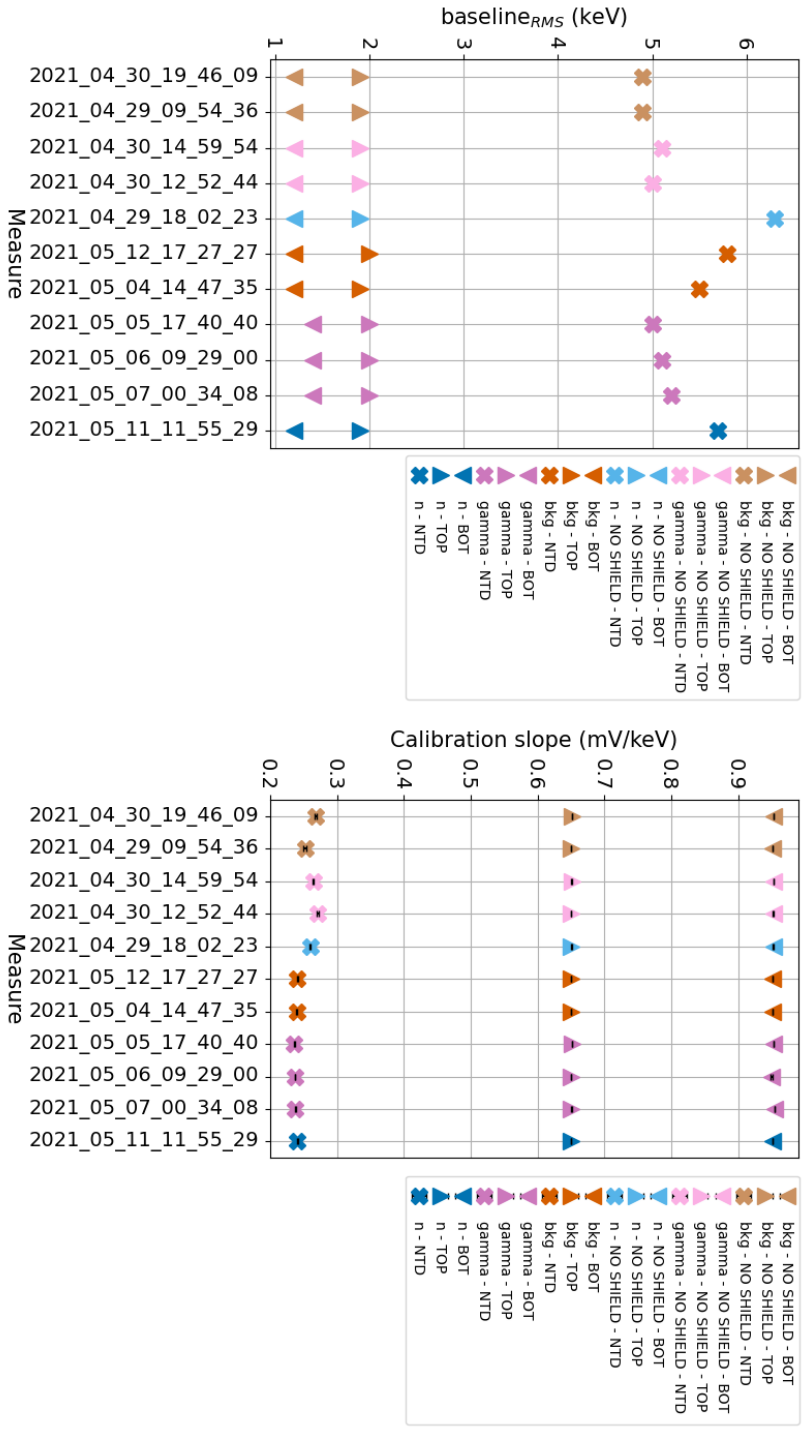

Figure 5.14: Baseline RMS (*top* plot) and energy calibration parameter (*bottom* plot) of Ge BOT (▽), Ge TOP (△) and NTD (×) in each measurement.

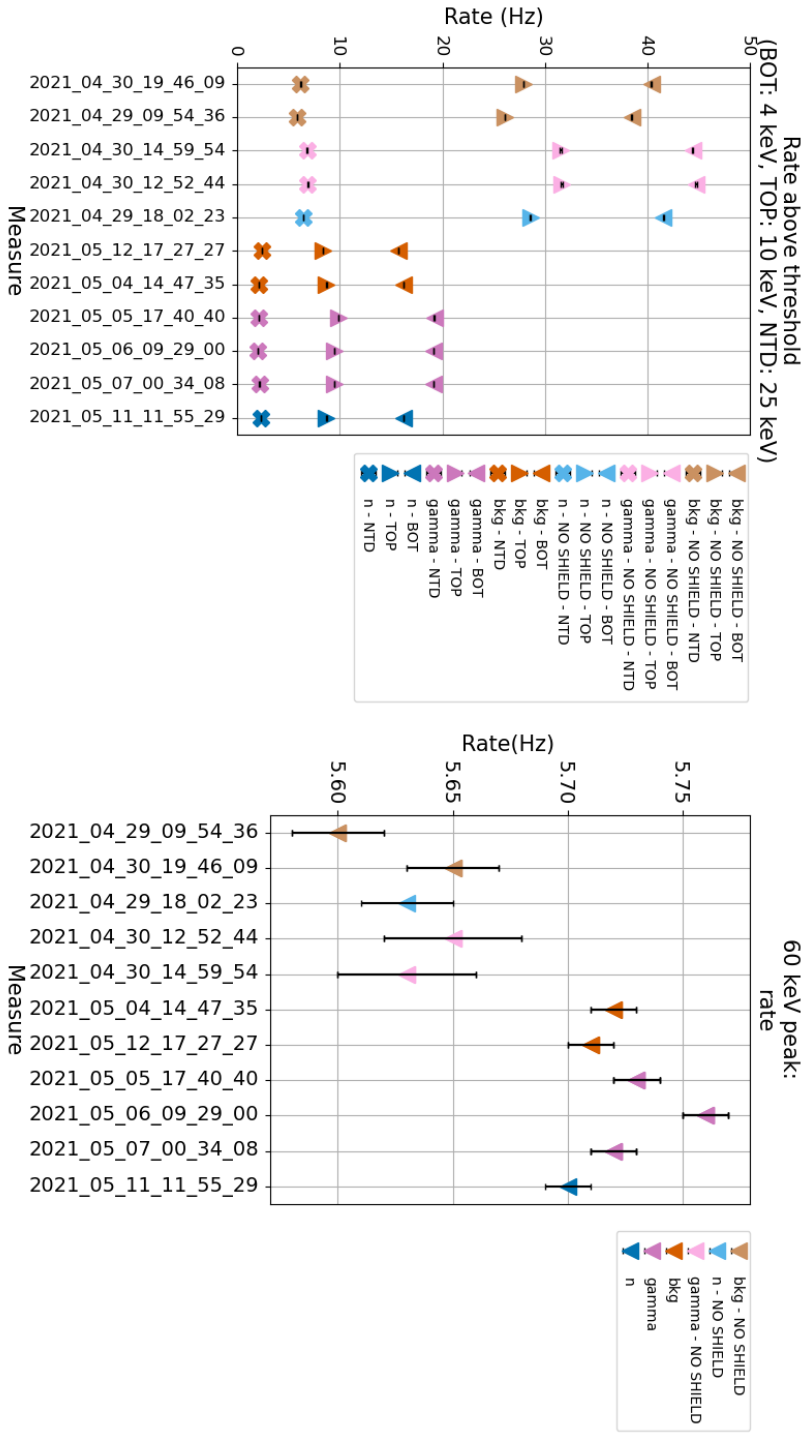

Figure 5.15: *Top*: rate above threshold of all the measures, specifically 4 keV for the Ge BOT (indicated with $\bigtriangledown$ in the plot), 10 keV for the Ge TOP ($\bigtriangleup$), and 25 keV for the Interdigit NTD ($\times$).

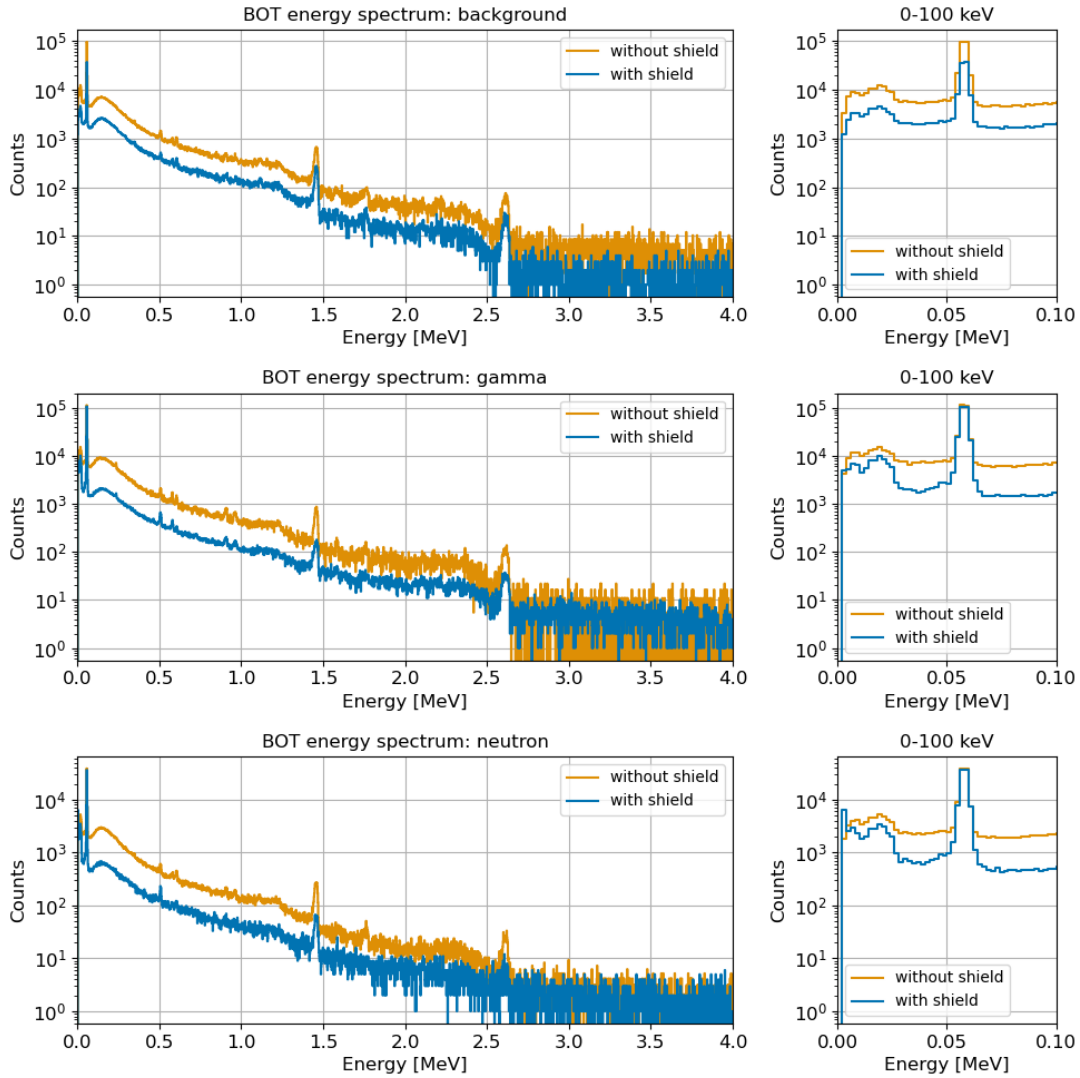

Figure 5.16: *Left*: energy spectra comparison of the BOT detector between the case with and without lead shielding in different conditions (background, gamma, and neutron sources). *Right*: low energy region (0-100 keV). We clearly recognize the gamma peaks due to the ^{241}Am source fixed at the bottom of the detector.

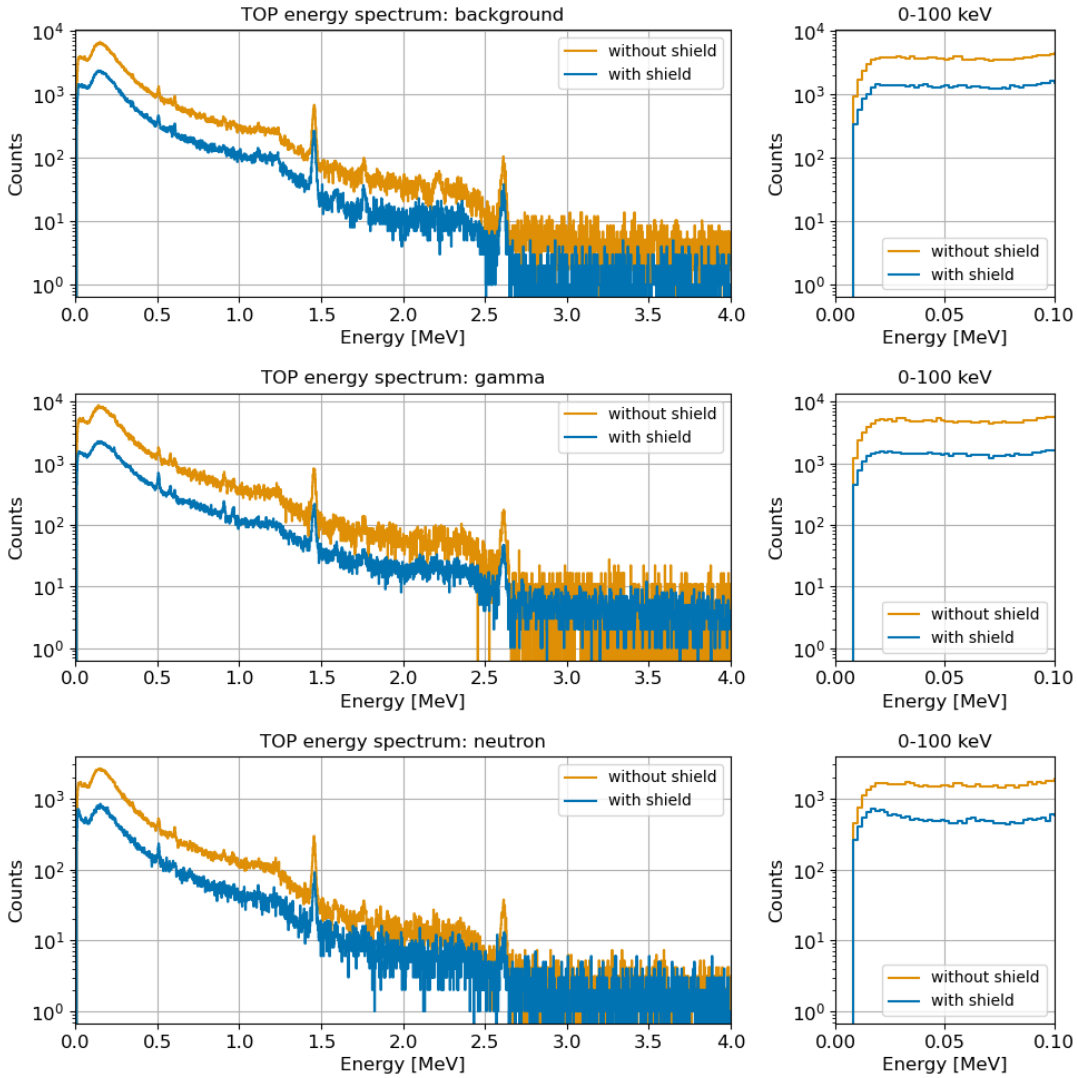

Figure 5.17: *Left*: energy spectra comparison of the TOP detector between the case with and without lead shielding in different conditions (background, gamma, and neutron sources). *Right*: low energy region (0-100 keV). Being fixed the ^{241}Am source at the bottom of the BOT detector, no gamma's can reach the TOP detector. As a consequence, the absence of any gamma peak in this region.

5.4.2.1 Coincidences study

Once the detectors are characterized, we can move to the heart of the analysis: the study of the time correlation between all the detectors. Indeed, we should not forget that the outer veto is designed and developed to identify and reject all the events originated by particles crossing one or more germanium crystals and the target detector. Knowing that the germanium detectors are perfectly in time between each other (coincidences in 10-20 μs window), the appositely developed analysis tool (described in section 3.2) identifies the coincidences in a carefully chosen time window between the ionization signal provided by the germanium detectors and the target detector heat signal, correcting the over-estimations in the rejection process. Since NTDs are intrinsically slow sensors compared to ionization, every time an event occurs, a suitable time window of a few ms (in the present case 6 ms) is used to verify if something is seen also by the germanium detectors. The closest ionization event in time between the two germanium detectors is considered as a coincidence if it falls inside the 6 ms time window. Even if in our prototype just two germanium detectors are involved, this technique allows performing a coincidence study between N germanium crystals, simplifying an N-dimension problem in a 1-dimension one. A histogram representing the coincidence correlation is built (figure 5.18): the peak represents the events that are in coincidence, and all the others are accidental coincidences. However, if we remove all the events inside the coincidence time window, we also remove accidental coincidences. A correction is required. This is done by applying a double exponential fit on the accidental coincidence distribution. Therefore, the number of events in true coincidence is the number of events in the coincidence time window minus the contribution due to accidentals under the coincidence peak that are estimated from the fit.

Since in the COV prototype we have just two germanium crystals, we can additionally plot the time correlations between NTD-BOT and NTD-TOP (figure 5.19). We can identify three different populations: the coincidences between the two germanium detectors diagonally crossing the plot, the coincidences between NTD-BOT (vertical population band) and NTD-TOP (horizontal population band). All the other events are accidental coincidences among the three detectors and they are uniformly distributed in the plot. Adopting this method, we vetoed 31.0% of the NTD events; if we had not corrected for accidentals, the vetoed events would have been 41.2%. These values are in agreement with Monte Carlo simulations taking into account the various detectors rate.

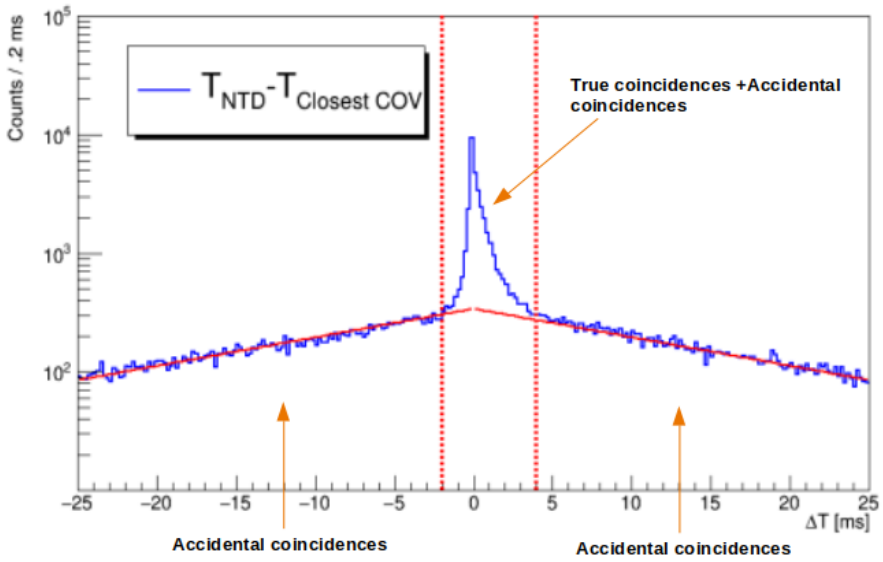

Figure 5.18: Time correlation between target detector and veto signals. The peak represents true coincidences, however, we can't remove simply them since accidental coincidences are also included. Therefore, a correction is needed: a double exponential fit on the accidental coincidences is applied. The number of events in coincidence is the number of events in the time window (area delimited by the red dotted lines) minus the contribution of the accidentals that is estimated from the fit.

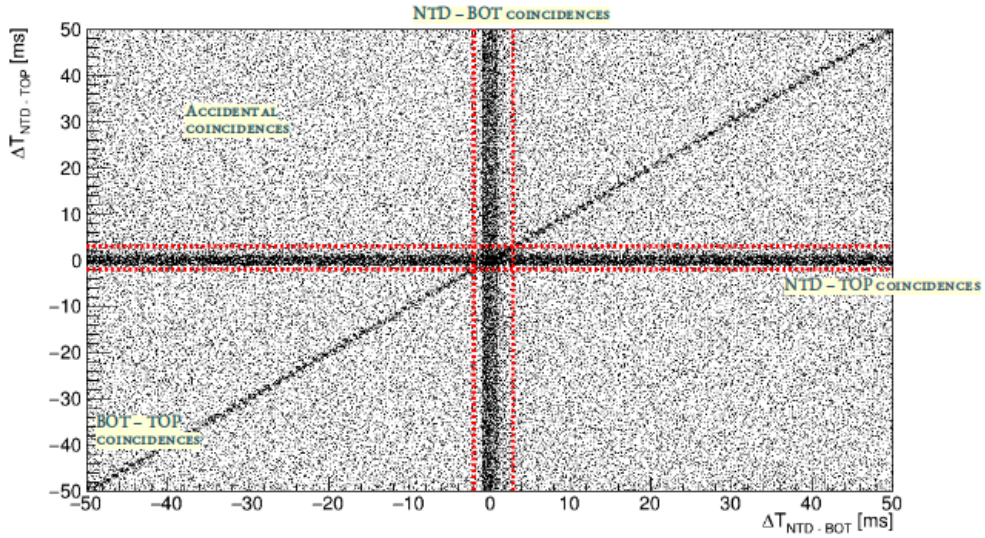

Figure 5.19: The time correlations between NTD-BOT and NTD-TOP are plotted one versus the other. The diagonal distribution is the TOP-BOT correlation while the vertical and horizontal populations delimited by the dashed red lines are the events in coincidence between NTD-TOP and NTD-BOT detectors respectively. The events located at the intersection of the three correlation bands correspond to the triple coincidences between the NTD and the two germanium detectors.

Table 5.7: Main results obtained from the first COV test using the new analysis tool and compared to the ones obtained with Argonauts.

	New tool	**Argonauts**
energy resolution (FWHM, at 1460.8 keV) [keV]	111±10	71±28
baseline RMS [keV]	2.3	1.1
sensitivity [nV/keV]	857	842
energy threshold set [keV]	4	2.3

At the end of this procedure, we obtain some parameters, such as NTD-ionization coincidences and fraction of vetoed NTD events (before and after the accidental correction), that allow characterizing completely the cryogenic veto system.

The plots in figure 5.20, show the coincidences rate between the BOT and NTD, and TOP and NTD respectively. In each plot, we immediately identify two sets because of the lead shield.

In figure 5.21, on the left the NTD energy spectrum after an over-estimation of events to reject, and on the right, the NTD energy spectrum after a correction for accidental events, both compared with the original NTD spectrum. What we can observe, is a veto rejection of $\simeq 31.0\%$. The rejected events are mainly muon interactions; as expected, the γ lines and $Li^6(n,t)\alpha$ are intact.

5.5 First test processed with the new analysis tool

With the aim to validate the analysis method proposed with the new analysis tool described in section 3.2, we decided to repeat the data processing of the first run. This technique allows faster and simpler data processing without being particularly sensitive to pile-ups, noise, and baseline fluctuations. Since it is not based on noise and reference templates, we are able to detect and keep the 10% more pulses without the obligation to apply a correlation selection. In figure 5.22, the calibrated energy spectrum obtained with the new method. In table 5.7 the main information are reported.

Considering the slightly different statistics to which we have access and the absence of the optimum filter with this second data analysis tool, we can say that the energy resolutions at 1460.8 keV and the sensitivities are in agreement between them.

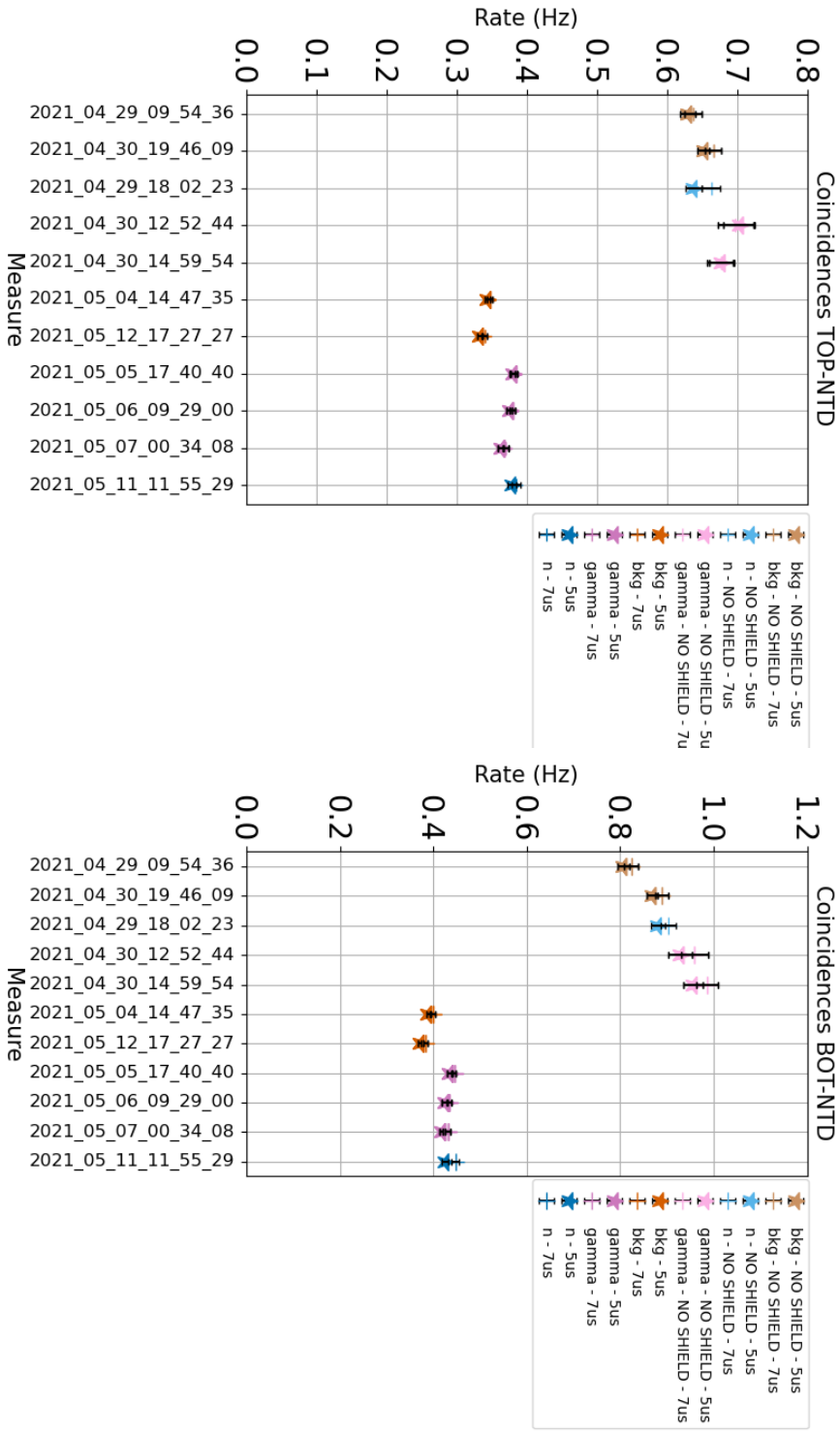

Figure 5.20: Rate of coincidences between TOP-NTD (*top*) and BOT-NTD (*bottom*).

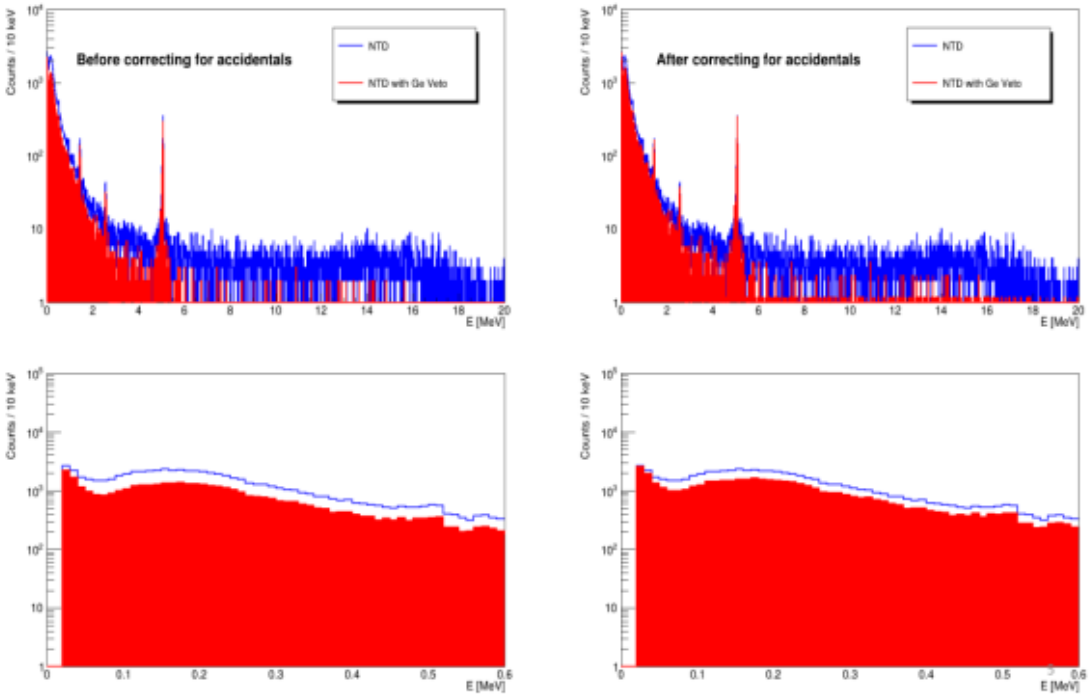

Figure 5.21: *Left:* in blue the original NTD energy spectrum. Overlapped in red, is the energy spectrum after removing all the events under the coincidence peak. *Right:* in red, the NTD energy spectrum corrected for accidentals overlapped to the original one (in blue). The bottom plots are an enlargement of the low energy region of the energy spectra. For more details about the corrections, see figure 5.19.

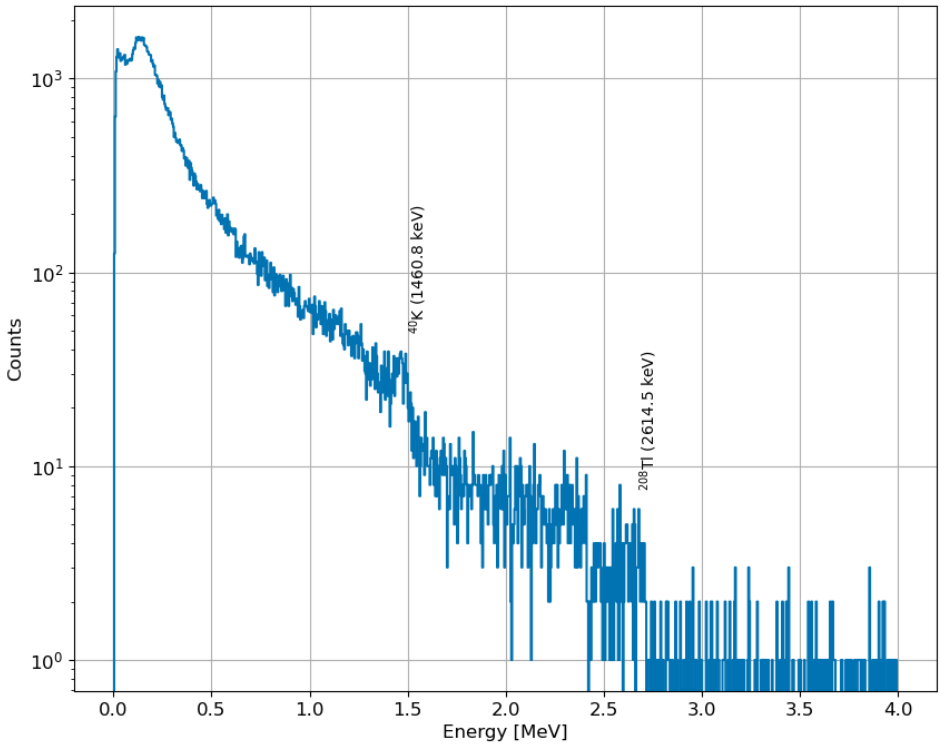

Figure 5.22: Energy spectrum obtained using the new data processing tool.

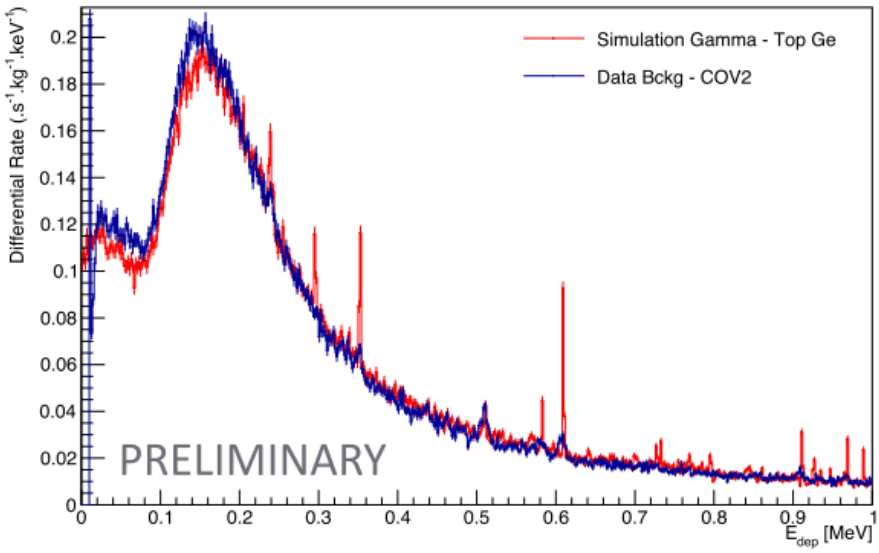

Figure 5.23: GEANT4 γ simulation (in red) compared to a background energy spectrum (in blue). The two events distributions are following the same behavior, except for the intensities of the γ peaks as expected.

5.6 Conclusions and next steps

We performed three COV prototype tests, in different conditions and using different set-ups. We can confirm that the detector works stably and solidly. In all the tests, it proved to be able to satisfy the requirements (in terms of time response, efficiency and energy threshold) demanded by the NUCLEUS experiment. We also observed that to optimize the detector performances, it is fundamental to have a shielding system surrounding the cryogenic veto. The reconstruction method proposed in this thesis demonstrated to be robust and to be able to reach an efficiency of $\simeq$100% at energies higher than twice the energy threshold. In parallel, preliminary GEANT4 MC simulations have been performed to cross-check these experimental results. In figure 5.23, we can observe a simulated γ energy spectrum (obtained generating the ^{232}Th decay chain in the GEANT4 program) matching a background measurement, with the exception as expected of the intensities of the γ peaks [189].

New COV tests have been carried out recently, with the purpose to test and characterize the final NUCLEUS cylindrical germanium crystals (figure 5.24 *a*). The two crystals were assembled together using a new copper cage design (figure 5.24 *b*). More-

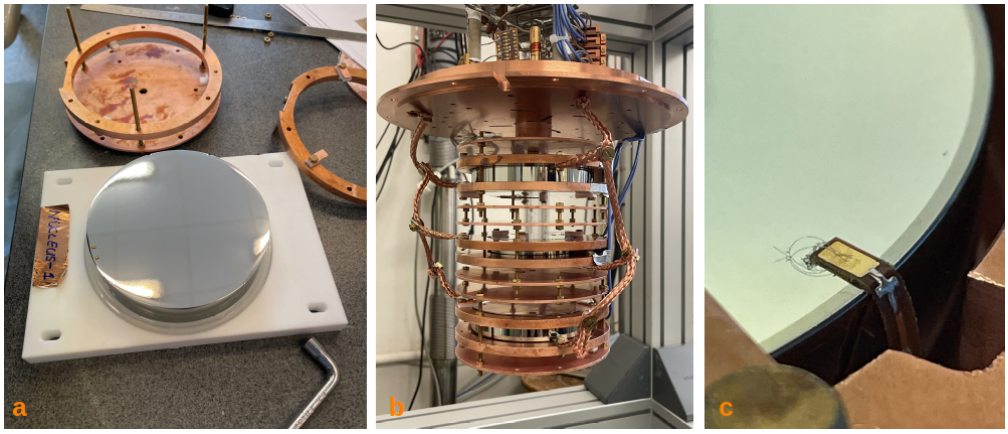

Figure 5.24: *a*: one of the two final cylindrical crystals for the NUCLEUS COV; *b*: new cage design conceived for the test of the NUCLEUS cylindrical crystals; *c*: adhesive kapton Printed Circuit Boards (PCBs) tested as an alternative solution to the evaporated gold spot or the golden silicon element glued onto the crystal

over, a third germanium crystal with a smaller thickness (2 cm) was added between the NUCLEUS ones; it was equipped with adhesive kapton Printed Circuit Boards (PCBs) for both the signal collection and the thermal link in order to test and validate this alternative solution to the one used in the COV measurements presented in this chapter (figure 5.24 *c*). The module was cooled down at 20 mK in the Actuator cryostat.

The final cylindrical crystals are validated: both showed an energy threshold below the 10 keV, good energy resolutions allowing the discrimination, and a sensitivity of 730 nV/keV. The analysis of this measurement is still ongoing in order to know more precisely the detectors performances. No additional tests are foreseen for these NUCLEUS germanium crystals [189]. The usage of the adhesive kapton PCBs worked well even if the adherence seems to not be guaranteed in the case of very long measurements. Indeed, three weeks after the end of the measurement, we observed that the PCBs started coming off. In experiments like NUCLEUS, where the measurements can run for months, we can't afford the risk to break the bonding wires and losing the contacts. For this reason, a new solution was proposed: non-adhesive kapton PCBs glued on the crystal with Araldite Rapid®.

The missing four rectangular crystals will be available at the beginning of December 2022. At the moment, they are under grinding treatment in Legnaro (Italy). Afterward,

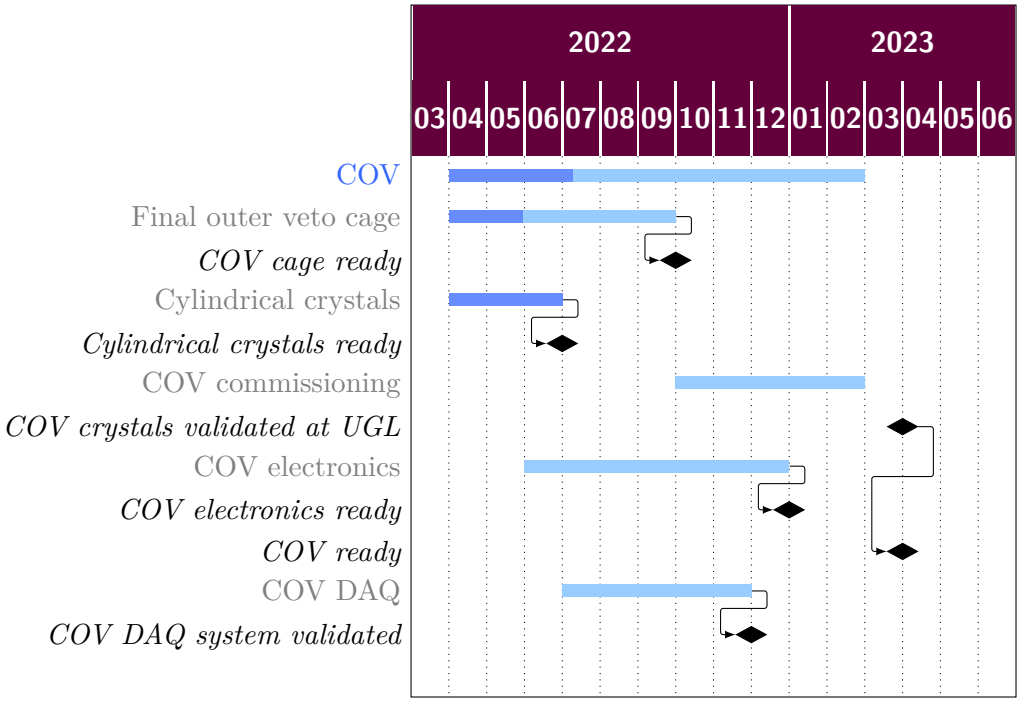

Figure 5.25: COV schedule: status and milestones.

they will be sent to Ferrara (Italy) for the etching treatment. The final validation of the COV will take place at the UGL by mid-February 2023, after that COV cold electronics and DAQ system will be ready and available. Figure 5.25 summarizes the COV schedule and milestones [190].

Chapter 6

BASKET with NTDs

BASKET (Bolometers At Sub KeV Energy Thresholds) is a CEA R&D project started in 2017 with the aim to develop innovative bolometric detectors for the CEνNS detection using new crystals as absorber material. The main absorber candidate is molybdenum doped lithium tungstate ($Li_2(Mo^{0.05})W_{0.95}O_4$), a very promising compound. Indeed, since the CEνNS cross-section scales with the number of neutrons as N^2, the tungsten (N around 110) strongly enhances the CEνNS rate. Moreover, exploiting the affinity between W and Mo, precedent studies on the Li_2MoO_4 compound proved that the natural content of ^{6}Li (8% in the crystals used for our prototypes) reveals excellent particle identification capabilities allowing the monitoring of the neutron background thanks to the ^{6}Li(n,t)α reaction [191].

The BASKET final goal is to develop very sensitive cryogenic detectors with an ultra low energy threshold of O(10 eV) and a rise time of the order of O(100 μs) so that they can easily be operated in above-ground conditions in close vicinity with a nuclear power plant.

All the Li_2WO_4 used in this thesis are produced at the Nikolaev Institute of Inorganic Chemistry (Novosibirsk, Russia) through the Czochralski method [191]. For our test we used mainly two crystal geometries: a 51.7 g crystal with cylindrical shape (Φ=25 mm, h=25 mm) and a 4.5 g crystal with cubic shape (l=10 mm). We tested different thermal sensors coupled to the scintillating compound: Ge NTD, MMC, and doped silicon sensors.

The development and characterization of the BASKET detectors using an NTD germanium thermistor were performed at IJClab (Orsay, France). All the detectors

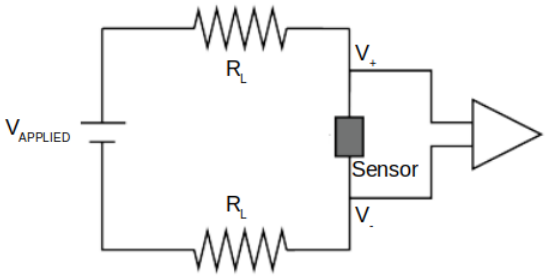

Figure 6.1: Scheme of the bias circuit for the NTD read-out.

shown in this paragraph were equipped with an additional silicon heater to eventually stabilize offline the baseline. Part of the measurements was performed using a light detector: a thin germanium disk equipped with an NTD (see section 2.2). The detectors were tested in the Ulysse dry pulse-tube cryostat using room temperature electronics, both already described in section 5.3.1. The cryostat was surrounded by 10 cm lead shielding to reduce the events rate due to the environmental radioactivity.

During my Ph.D. activity, I tested different detector configurations (different Li_2WO_4 crystals, different NTDs, with or without light detectors,..) under different conditions (base temperatures, voltage bias, type of glue,...). Therefore, I have decided to summarize my work by showing a measurement per type and the main observations.

6.0.1 IV characterization

Before starting data acquisition, it is fundamental to define at the beginning of each run the optimum working point of any detector, namely the bias current at which the signal-to-noise ratio is maximized. This is achieved by performing a static analysis (i.e. without any signal perturbing the equilibrium between the detector and the heat sink). In figure 6.1, the electric scheme of the thermistor bias circuit is shown. Applying a chosen constant bias voltage $V_{applied}$ using a DC power supply, a potential difference is generated across the sensor:

$$V_{bol} = \frac{|V_+ - V_-|}{G} \tag{6.1}$$

where V_- and V_+ are the voltage measured across the sensor and G is the selected gain. The thermistor is in series with two load resistors R_L with larger resistance compared

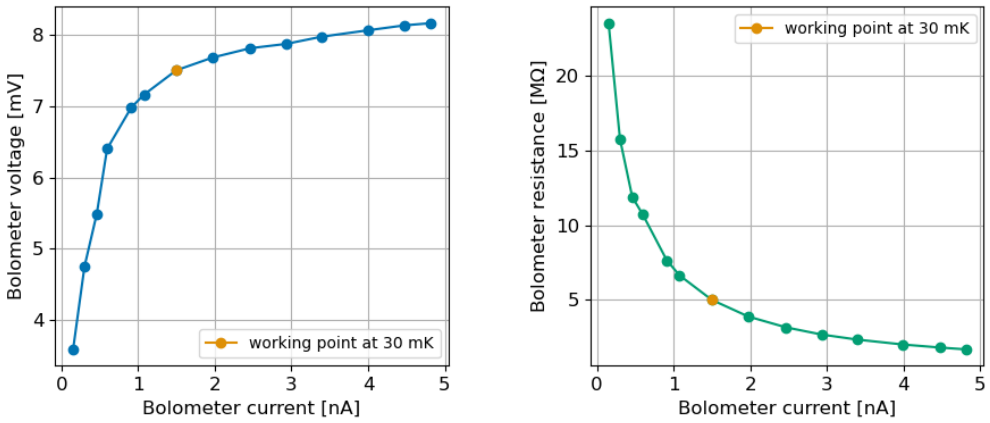

Figure 6.2: I-V and I-R curves at 30 mK. We can observe that lower is the T, higher is the V_{bol}. At lower voltages, since R_{bol} is almost constant, we observe a linear behavior. Increasing the voltage, we progressively start dissipating bias until reaching a plateau. We selected the working point (in yellow) right before the saturation of the curve.

to the calorimeter one, R_{bol}, so that we can approximate the injected current I as:

$$I = \frac{V_{applied}}{2R_L + R_{bol}} \sim \frac{V_{applied}}{2R_L} \tag{6.2}$$

Changing $V_{applied}$, we can collect a set of calorimeter currents I_{bol}, voltages V_{bol} and resistances R_{bol}. Since the NTD resistance is strongly dependent on temperature, it is important that the cryostat base temperature is stable all the time while collecting these parameters.

Figure 6.2 shows an example of I-V and I-R curves. We can identify a linear region justified by a more or less constant R_{bol}. It starts becoming less and less linear when we start dissipating power. As a consequence, the calorimeter starts heating, and the R_{bol} decreases. The plateau is reached when the power going to the heat sink and the dissipated power are comparable.

6.1 Background measurement with cylindrical crystal

6.1.1 Detector preparation

The detector presented in the following section was a cylindrical Li_2WO_4 crystal with 3x3x1 mm^3 germanium NTD (41B series), and silicon heater.

Gluing procedure

The NTD and the heater were glued to the crystal using six dots of Araldite® Rapid, a bicomponent epoxy glue produced by Huntsman Advanced Materials. This glue, already largely used in the CUORE experiment, is particularly suitable for calorimeters since it is characterized by low radioactivity (less than 2.2×10^{-10} g/g for ^{232}Th and 8.2×10^{-10}g/g for ^{238}U), good thermal conduction and a total drying time of approx one hour [192]. As already observed in many previous measurements, the quality of the glue interface between the thermistor and the absorber plays a role since it has an impact on the phonon collection and, hence, on the detector time response. To glue the sensor, we use a manual gluing system composed of a movable platform to adjust the crystal position, a pump holding the NTD, and a six pogopin matrix to immerse in the glue. Through the pogopin we deposit directly onto the crystal six glue dots then we carefully place the sensor on them. To not merge the dots while pressing the sensor, a 50 μm thick Mylar® mask was used (figure 6.3, left).

The same procedure is followed for silicon heater gluing.

Holder cleaning

For our measurements, the copper cleaning at each assembly clearly is not a mandatory point since the BASKET detectors are not working in a low radioactivity environment. Anyway, it become part of the detector assembly protocol at IJClab since most of the detectors build in this laboratory aim to the detection of double beta decay in underground conditions. The copper holder is cleaned using a specific recipe in order to avoid additional radioactivity originating from the surface contamination. It is based on the chemical etching technique:

- etching pre-treatment: the holder undergoes an ultrasonic bath in a mixture of

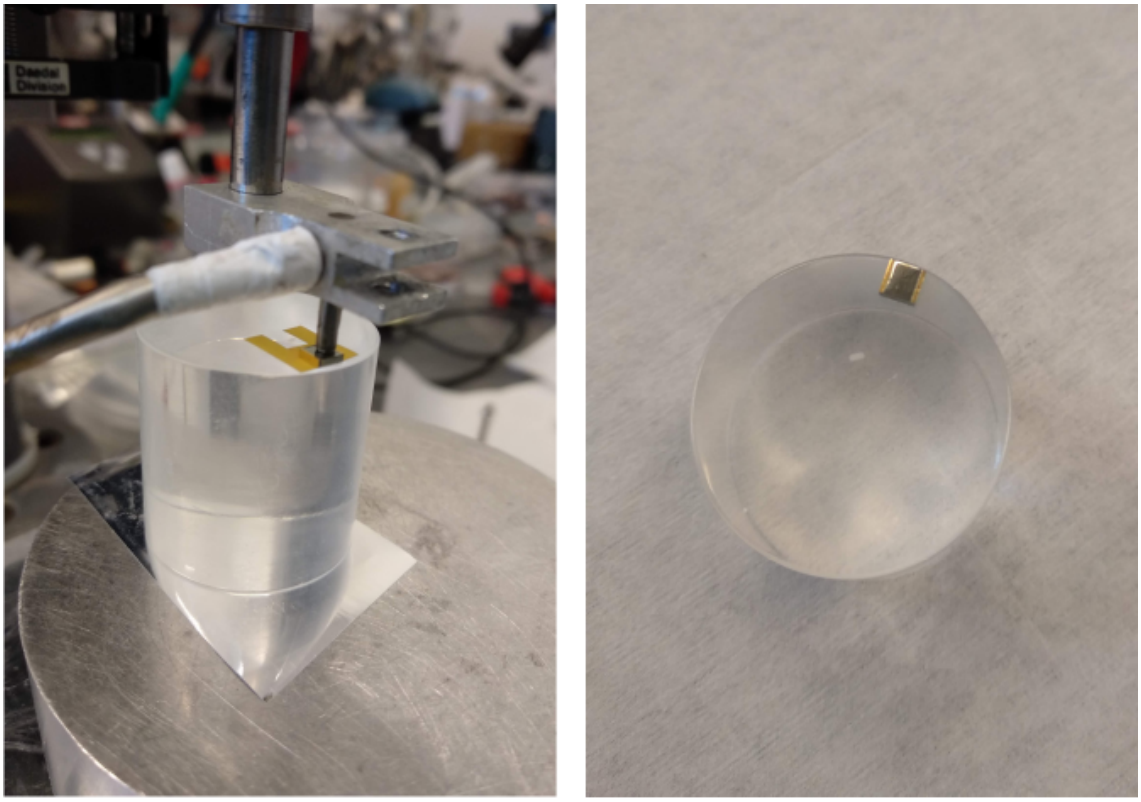

Figure 6.3: *Left:* gluing of the NTD sensor. The sensor is attached to the gluing machine by a vacuum pump. A Mylar mask is surrounding the six glue dots in order to not spread the glue. Then, the NTD is pressed over the mask. *Right*: the NTD glued on the crystal.

ultra-pure water and 5% Micro-90 soap at approx 50°C for 10-20 minutes. Then, it is rinsed with ultra-pure water;

- citric acid etching: the holder is exposed to another ultrasonic bath at 40-50°C, this time with ultra-pure water, 4%±2% of citric acid and hydrogen peroxide q.b. to activate the copper cleaning reaction. This procedure lasts 30-45 minutes depending on the holder size. Following this procedure, we should have removed about 10-20 μm of the surface. Then, the holder rinsed once again with ultra-pure water;

- the holder is treated with a second citric acid etching of 15 minutes with the same chemical agent and temperature to remove 3-5 μm more of copper;

- the copper is dried in the oven at 60-80°C for about one hour.

PTFE spacers

Some L-shaped PTFE (polytetrafluoroethylene) elements are used to block the crystal to the copper holder (figure 6.4, left). In addition, to compensate for the thermal contraction during the cooling down avoiding the breaking or damaging of the crystal, the PTFE works also as a weak thermal link between the absorber and the heat sink. Without these elements, the crystal would be strongly thermally coupled to the heat sink avoiding the possibility to see changes in temperature due to particle interactions in case of heat read-out (part of the heat will not reach the NTD but it will go directly to the heat sink). Moreover, the PTFE is a well known radiopure material, already largely used in many experiments such as CUORE, CUPID, and EDELWEISS [103, 155, 193]. Also, these elements need a treatment to be cleaned from surface contamination. The PTFE, being a soft material, is not eligible for an aggressive treatment like the chemical etching with citric acid. It is cleaned with an ultrasonic bath in ethanol.

6.1.1.1 Thermal and electrical contacts

The NTD electrical contacts are realized using two gold wires per side (Φ=25 μm) bonded to kapton-golden pads glued onto the copper holder, from which shielded copper wires are soldered and twisted in pairs for the outer electrical connection. These gold wires ensure also a weak thermal link to the heat sink.

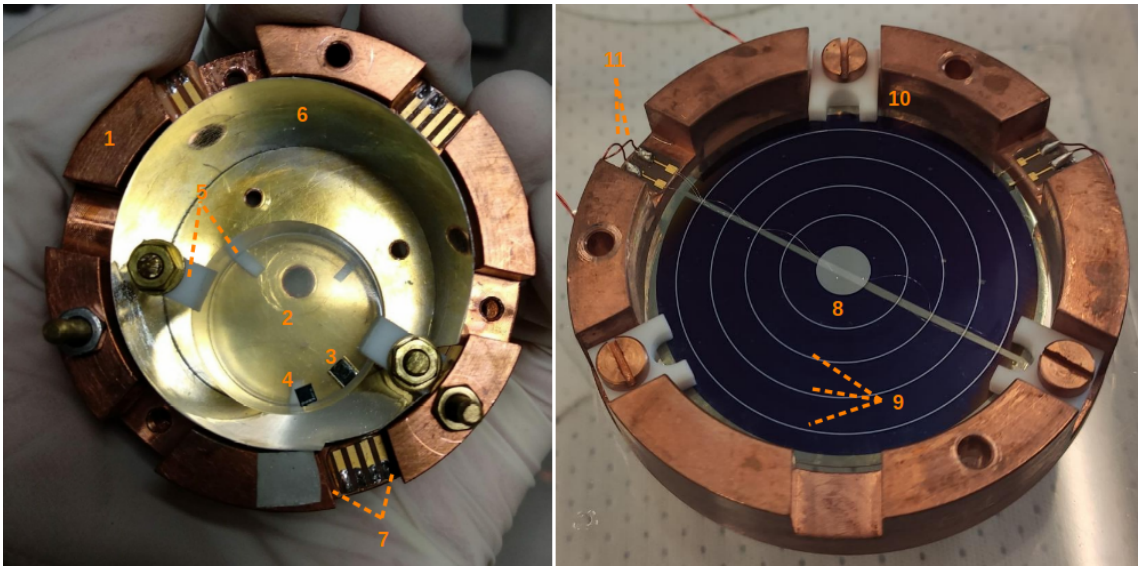

Figure 6.4: *Left:* 'main' calorimeter. On the cylindrical Li_2WO_4 crystal (2), the germanium NTD (3) and the silicon heater (4) are glued with Araldite® Rapid glue. The crystal is fixed to the copper holder (1) through brass fasteners and L-shaped PTFE elements (5) and wrapped with a reflecting foil (6) to increase the light collection. The electrical and thermal connection is realized through gold and aluminum wires bound to the golden pads (7). *Right*: light detector. The thin germanium wafer (8) has aluminum grids (9) deposited to enhance the charge collection. The wafer is fixed to the copper holder through PTFE clamps to avoid damaging it with thermal contractions. The aluminum wires are bonded to the golden pads. On the same pads, copper wires are soldered to allow the reading of the signal with the room temperature electronics.

Table 6.1: Main features of the background measurement using the cylindrical Li_2WO_4 aiming the background measurement.

Type	Background	γ+n
Sources	-	^{232}Th, ^{252}Cf
Mixing chamber temperature (mK)	22	15.5
Sampling frequency (kHz)	5	5
Duration (h)	33	18
NTD bias (nA)	3	2
NTD dynamic range (V)	$\pm$5	$\pm$1
NTD LD bias (nA)	3	2
LD dynamic range (V)	$\pm$1	$\pm$1

6.1.1.2 Light detector

The BASKET detector was coupled to a light detector produced at IJClab with the aim to make a coincidence analysis between them and therefore to better perform particle discrimination. The thin germanium slab was fixed to a copper holder with PTFE elements, acting as a clamp to avoid any wafer breaking (6.4, right).
In order to enhance the light collection, the crystal was carefully wrapped with a reflecting foil and the light detector was perfectly facing the crystal.

6.1.2 Data production

The detector was mounted and tested in Ulysse, the dry pulse-tube cryostat already introduced in section 5.3.1. The data was acquired in the stream mode with a sampling frequency of 5000 Hz. To facilitate the baseline stabilization, we injected through the silicon heater an artificial pulse with 200 mV amplitude every 60 s. In table 6.1 the main features of the acquisition are reported.

6.1.3 Data analysis

The data stream files of both the detectors are processed offline using Argonauts software (more details in section 3.1). While the BASKET data are processed in an independent

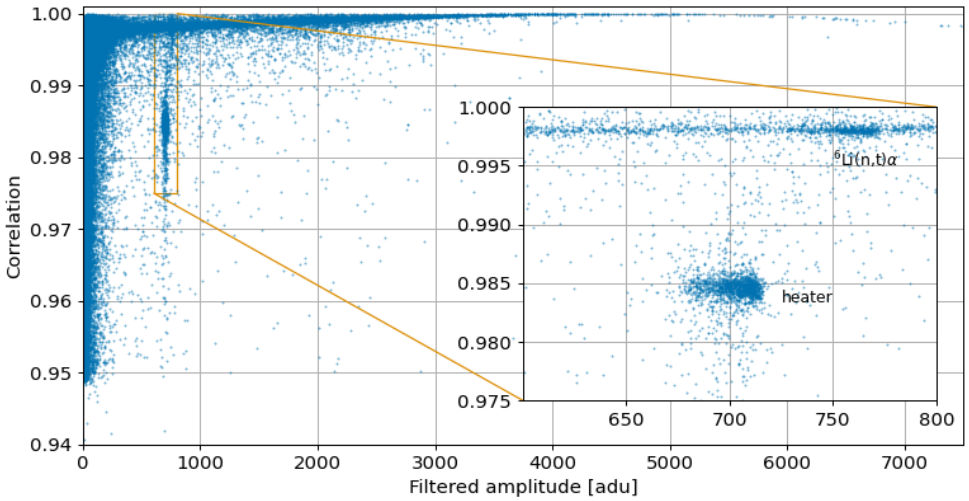

Figure 6.5: NTD correlation as a function of the filtered amplitude. In the inset, a zoomed on the heater and the ^{6}Li(n,t)α populations.

way, the light detector data are processed using the heat channel trigger file in order to have only light events in coincidences with the detector heat signals.

Data selections and amplitude stabilization

Once the heat channel n-tuple is produced, first of all, we need to verify if a data selection and/or a pulse amplitude correction is necessary. Indeed, cryostat temperature variations and instabilities can be responsible for baseline level drifts in time. If it is not corrected, it can severely affect the detector energy resolution. The first step is to verify if there are important baseline jumps to remove (figure 6.6). In this measurement, we did not observe any of them, so we did not remove any data time window. Another parameter to check is the correlation as a function of the filtered amplitude. Since the correlation parameter describes how much the individual filtered and the reference pulses are similar, we usually make a selection setting a high correlation threshold, being careful to preserve entirely the gamma, neutron capture, and heater populations (figure 6.5).

The next step is the amplitude stabilization. It is performed using a mono-energetic population of events, in our case the heater population (figure 6.7). Once selected these events, a linear fit is applied to them to know the slope m and the intercept q of the

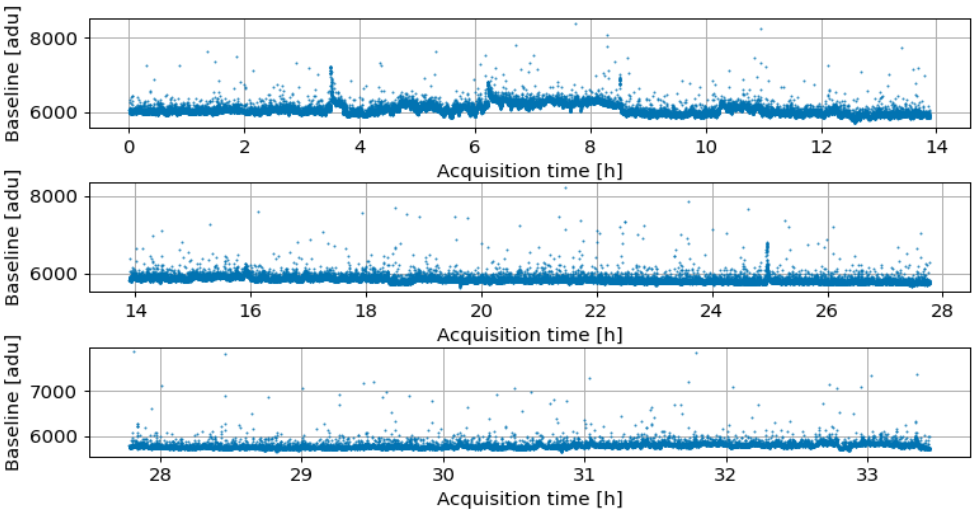

Figure 6.6: NTD baseline as a function of the time. It doesn't show any particular important jumps, therefore no data time window was removed.

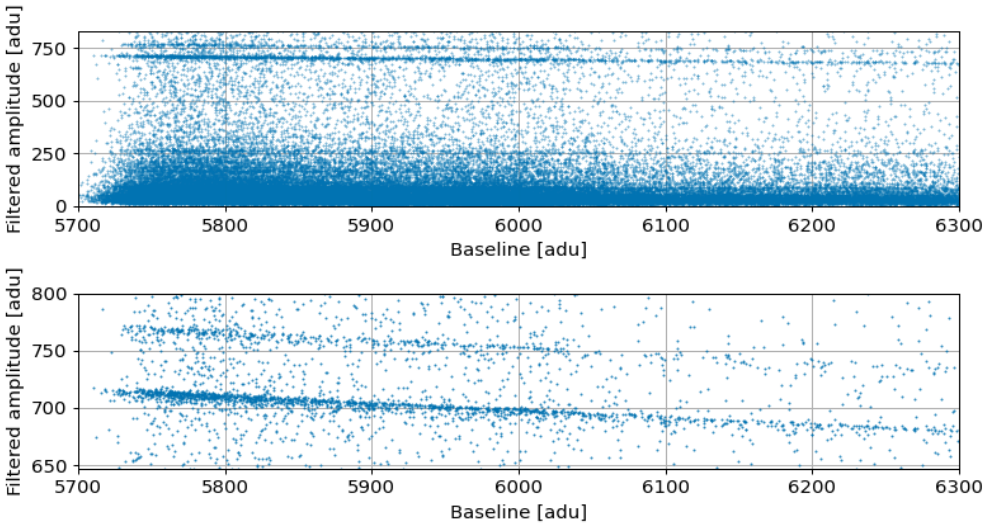

Figure 6.7: *Top:* filtered amplitude as a function of the baseline. *Bottom:* zoom on the heater (lower line) and the ^{6}Li(n,t)α (upper line) distributions.

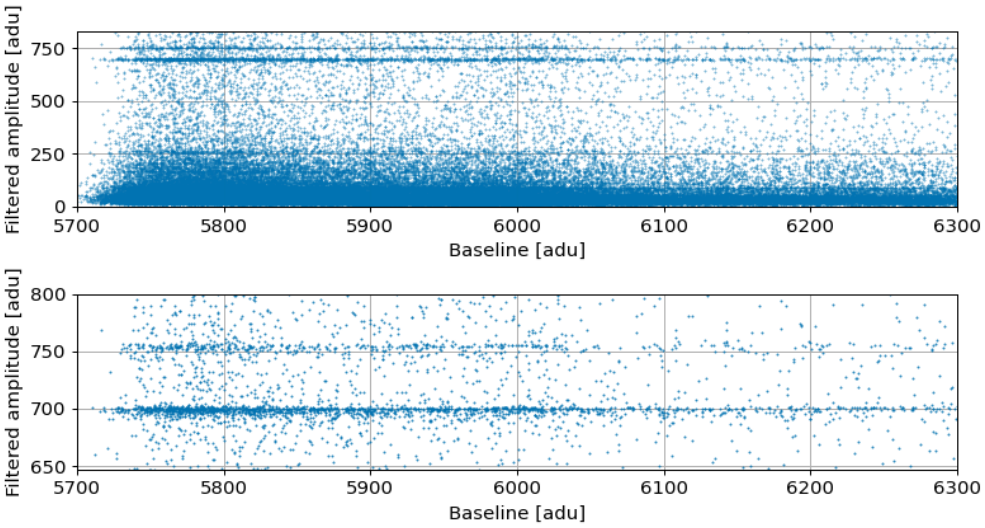

Figure 6.8: *Top:* Stabilized amplitudes as a function of the baseline. *Bottom:* zoom of the heater population (lower line) and neutron capture population (upper line) after the stabilization procedure.

distribution. Thereafter, all the amplitudes are stabilized as following (figure 6.8):

$$stabilized\ amplitude = A_{ref} \cdot \frac{filtered\ amplitude}{m \cdot baseline + q} \tag{6.3}$$

where A_{ref} is a constant used as the "fulcrum" of the stabilization and defined as:

$$A_{ref} = m \cdot \frac{B_{max\ heater} - B_{min\ heater}}{2} + q \tag{6.4}$$

with $B_{max\ heater}$ and $B_{min\ heater}$ respectively the maximum and minimum baseline values of the heater population selected for the calibration.

When the stabilization procedure is concluded, we can remove the heater population that does not correspond to physics events, verifying which parameters of the n-tuple file are more suitable for this task. In figure 6.9, an example of possible pairs of parameters we can check to remove the heater events. In this specific case, we decided to use the rise time as a function of the stabilized amplitude since it offers better discrimination between heater and physics events.

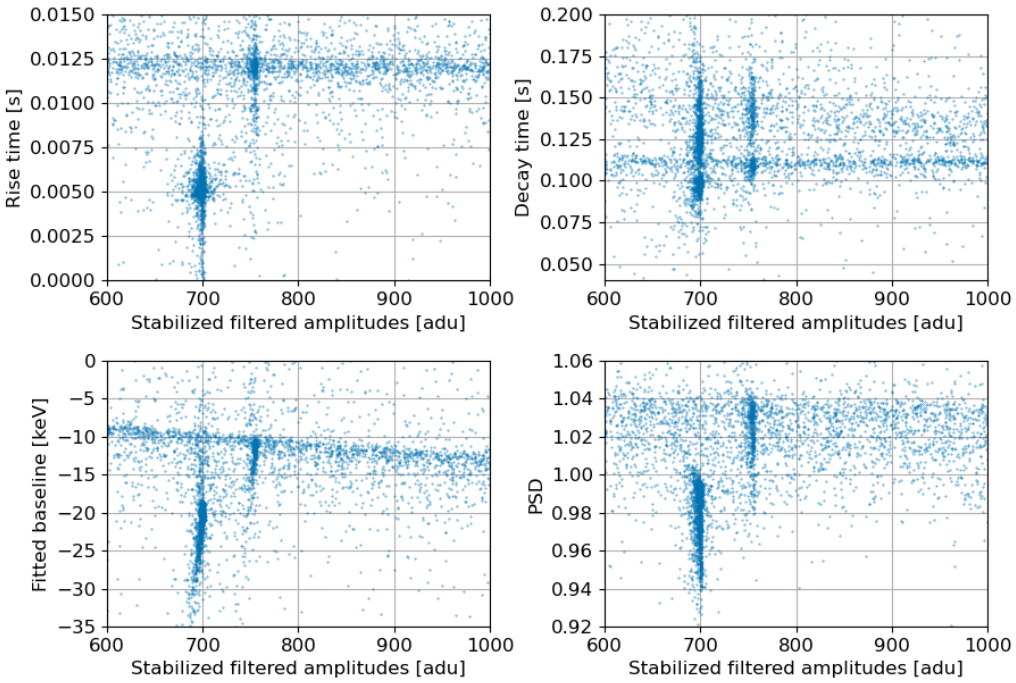

Figure 6.9: Example of parameters that can be used to remove the heater population. Among them, the rise-time versus the stabilized filtered amplitude offers a better discrimination and, as a consequence, an easier way to reject the heater population from the physics events.

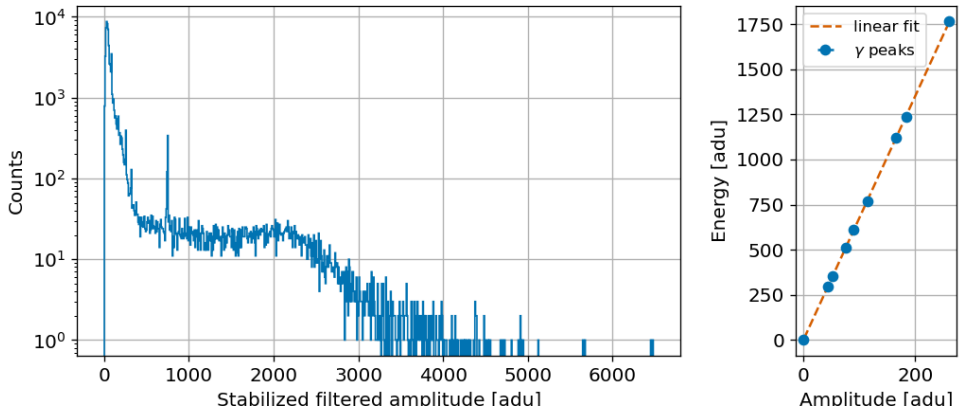

Figure 6.10: *Left:* stabilized amplitude histogram. We can immediately recognize some peaks typical of the background radioactivity (4.1) that we can exploit for the energy calibration. *Right:* first order polynomial fit using the main gamma peaks visible in the uncalibrated plot.

Energy calibration

At this point, we have a set of well-selected data. We are ready to calibrate them. The detector shows a linear behavior in particular in the gamma energy region. This suggests us to use a simple linear calibration to switch from a.d.u. units to keV. The conversion is possible by exploiting the most important γ peaks from the ^{232}Th and ^{238}U radioactive series, commonly present in the building materials surrounding the Ulysse cryostat and, hence, constituting the background radioactivity (figure 6.10).

In figure 6.11, the detector energy spectrum after the calibration is shown.

A fundamental parameter characterizing the detector is the energy resolution. For our application, it is important to develop a detector characterized by a high energy resolution since this implies a higher experiment sensitivity. The energy resolutions at the main γ energies are reported in table 6.2 . The baseline resolution (FWHM) is 11.1 $\pm$ 1.7 keV while the sensitivity is 20 nV/keV, evaluated as:

$$sensitivity = \frac{2 \cdot dynamic\ range \cdot 10^6 \cdot calibration\ factor}{2^{16} \cdot gain}\ [\mu V/keV] \qquad (6.5)$$

Thermal quenching of ^{6}Li(n,t)α, defined as the ratio between the peak position in the energy spectrum and its nominal value (4.8 MeV), is 1.1. We can explain the shift

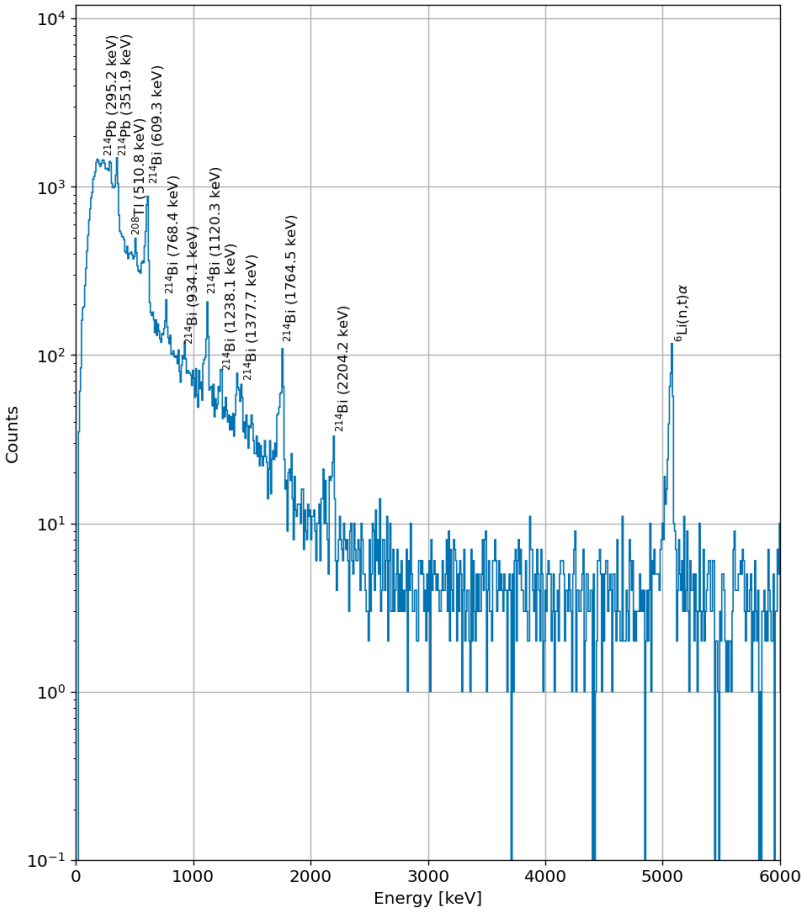

Figure 6.11: Energy spectrum of the background measurement.

Table 6.2: Energy resolutions at the dominant background γ peaks, and main parameters obtained from the detector characterization.

Energy line [keV]	**Energy resolution (FWHM)** [keV]
1764.5	21.9 ± 2.5
1238.1	13.0 ± 2.7
1120.3	15.4 ± 1.8
768.4	8.4 ± 2.4
609.3	19.4 ± 1.4
510.9	8.5 ± 1.8
351.9	16.9 ± 1.1
295.2	14 ± 4

baseline resolution (FWHM) [keV]	11.1 ± 1.7
sensitivity [nV/keV]	20
thermal quenching	1.1
DP	3.9 ± 0.2

of this peak from its nominal value to 5.0 MeV considering that the detector responds in a different way to heavy charged particles compared to γ's, namely two different pulse shapes. Since the amplitude reconstruction through the optimum filter adopted in Argonauts is based on a reference pulse built with γ pulses, we certainly have an aliasing in the amplitude evaluation of this kind of event.

A similar procedure is followed also for the light detector, with the difference that the amplitude is calibrated using the muon bump. The combination of light and heat information is a powerful technique. Indeed, if well implemented and improved, it could lead to the possibility to identify, isolate and reject the α component [160]. The parameter used is the light yield (LY), defined as the ratio between the energy of the emitted scintillation photons detected by the light detector and the energy deposited in the crystal and read by the NTD sensor (figure 6.12, left). Making a suitable selection of the data (for example, the dashed area in figure 6.12), we can build a light yield histogram that allows us to evaluate the discrimination power (DP) defined as:

$$DP = \frac{LY_{\beta\gamma} - LY_{\alpha}}{\sqrt{\sigma^2_{\beta\gamma} + \sigma^2_{\alpha}}} \tag{6.6}$$

It assumes high values when the distance between the $\beta\gamma$ and the α populations is high. In our case, we don't observe a complete separation between the two bands, but we can still recognise clearly the corresponding populations (figure 6.12, right). We evaluated a discrimination power of 3.9 $\pm$ 0.2 in the heat energy range of 4.5-10 MeV, while the light quenching factor, defined as the ratio between the $\beta\gamma$ and α light yields, is 0.3.

6.2 Neutron + gamma calibration with cylindrical crystal

The same detectors described in the previous section were used to perform a neutron + gamma calibration. The measurement was realized at 15.5 mK. A ^{232}Th source was placed between the lead shielding and the cryostat outer shield while a ^{252}Cf neutron source was positioned at 1 m distance far from the lead shielding. The data was acquired in the stream mode with a sampling frequency of 5000 Hz. Through the silicon heater, we injected artificial pulses with 200 mV amplitude every 60 s. Additional information

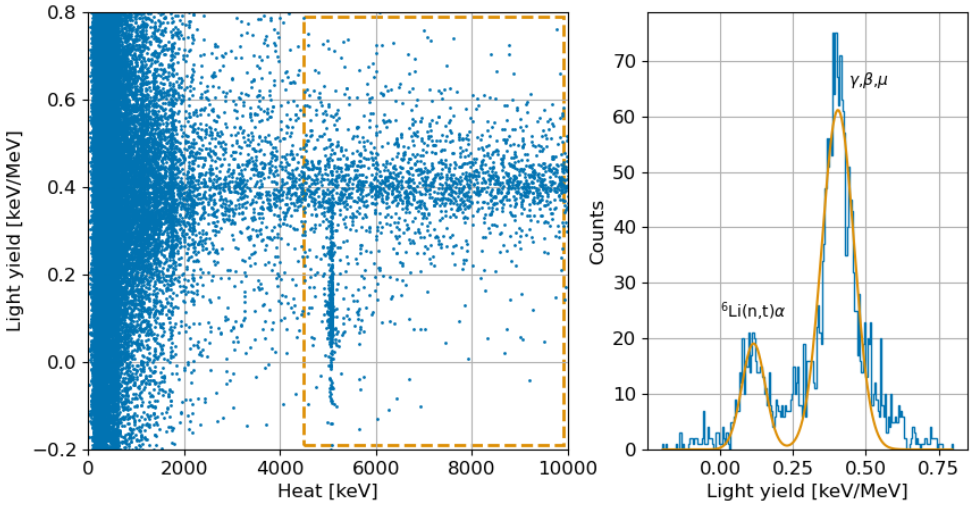

Figure 6.12: *Left:* Light yield as a function of the energy deposited in the crystal and read by the NTD. The events in the area surrounded by the dashed line are used to build a light yield histogram (*right*) and evaluate the discrimination power.

about the measurement are reported in table 6.1.

The procedure followed for the data production and analysis is the same described in paragraph 6.1.3. During the data processing, we observed a high pile-up rate due to the presence of the two intense sources at the same time so the correct identification of the peaks during the analysis was not an easy task. The figure 6.13 shows the calibrated energy spectrum. The energy resolutions were evaluated using the most defined γ peaks. They are reported in table 6.3 while the baseline resolution (FWHM) is 13.6±0.6 keV.

The evaluated sensitivity is 70 nV/keV.
Using the ^{252}Cf source, we observed more than 11 times of events under the neutron capture peak compared with the background measurement. The thermal quenching factor is 1.07. However, a complete discrimination between α and the β/γ populations is not possible (figure 6.14). With the help of the light detector, we still observed an overlapping between the two, evaluating a discrimination power of 2.0 ± 0.1 (figure 6.15).

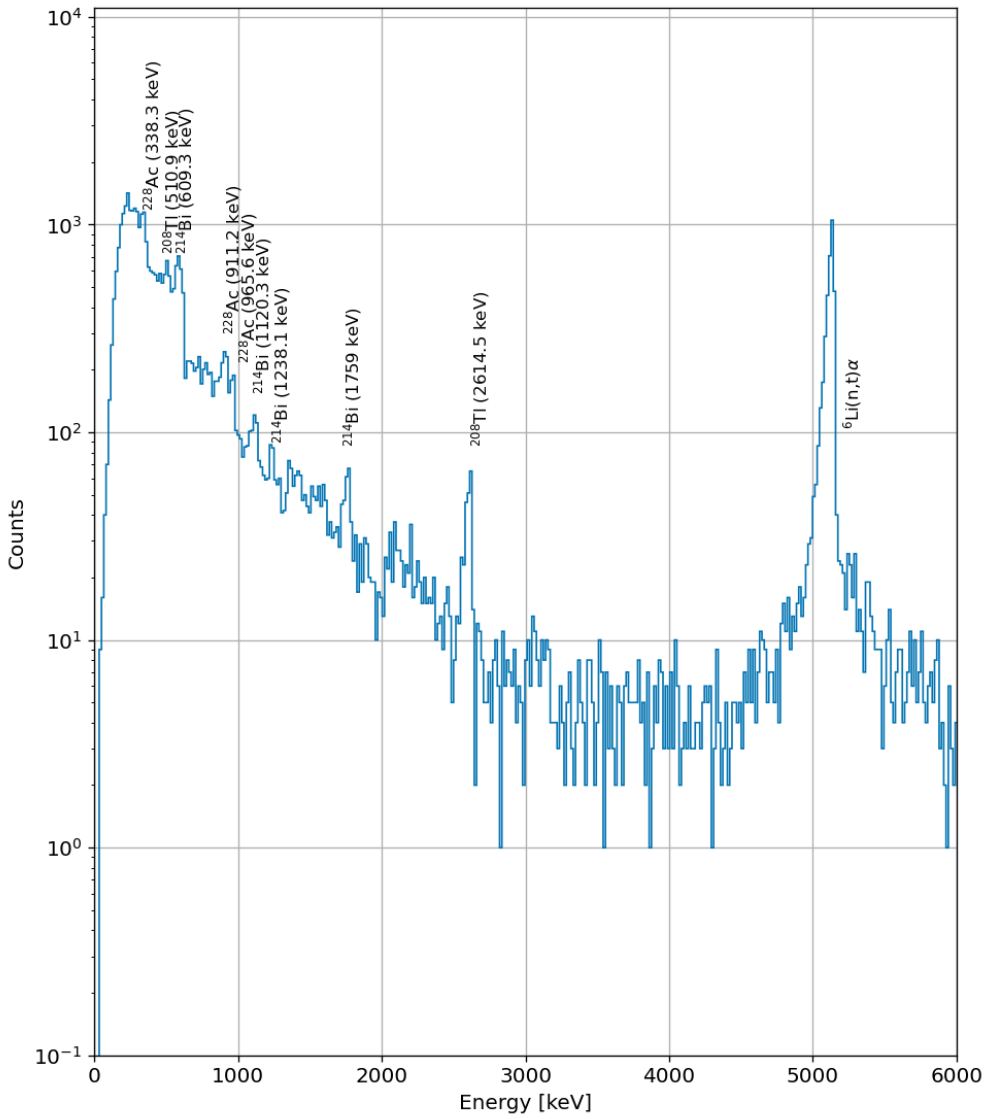

Figure 6.13: Energy spectrum of the neutron + γ measurement.

Table 6.3: Energy resolutions evaluated on the main gamma peaks and other parameters obtained from the detector characterization.

Energy line [keV]	**Energy resolution (FWHM)**[keV]
2614.5	25±5
1764.5	27±5
1120.3	30±8
911.2	34±12
510.9	20±6

baseline resolution (FWHM) [keV]	13.6 ± 0.6
sensitivity [nV/keV]	70
thermal quenching	1.1
DP	2.0 ± 0.1

6.3 Gamma calibration with cubic crystal

In this test, the detector was composed of a $1\,cm^3$ crystal equipped with a heater and a $1{\times}3{\times}1\,mm^3$ germanium NTD (T-shape 41B). The coupling between the thermistor and the absorber was done using 1 dot of Loctite® glue. We decided to use a different glue from Araldite® to test its effect on the detector performances (see section 6.4). The crystal was fixed to the copper holder with the help of four L-shaped PTFE elements (figure 6.16). As usual, the thermal and electrical connections are realized using gold and aluminum wires (Φ=25 μm).

The same light detector introduced in paragraph 6.1.1.2 was assisting the primary calorimeter. The module was completely wrapped with a reflecting foil to increase the light collection. The detectors were cooled down to 20.6 mK. Between the cryostat and the lead shielding, we placed a ^{232}Th source. In table 6.4 the main parameters of the acquisition are summarized.

The first thing we observed was a stronger non-linearity at energies higher than the γ energy region. We computed a baseline resolution (FWHM) of $1.1 \pm (1.2 \times 10^{-4})$ keV.

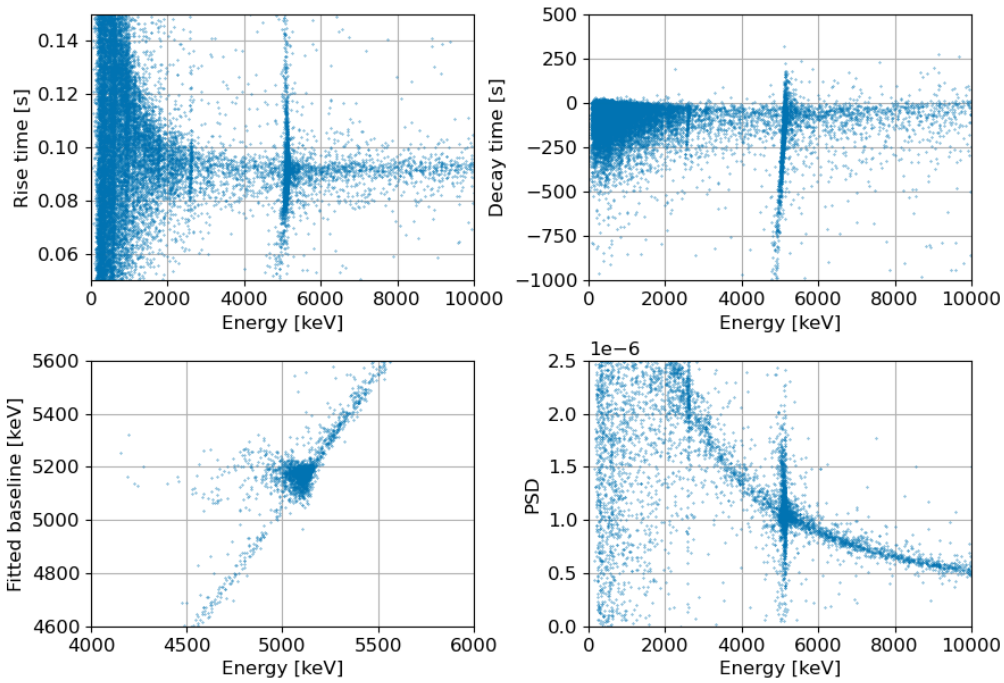

Figure 6.14: Some of the parameters used to verify if the discrimination between β/γ and α distributions is possible. In this case, no one of them allowed the rejection of α's.

The energy resolutions at different γ lines are listed in table 6.5. The experimental sensitivity is 181.8 nV. The thermal quenching factor was 1.1.

Despite the presence of a light detector, it was not possible to discriminate between the two populations or even make an estimation of the DP.

6.4 Glue Comparison

In parallel to the identification of the best detector configuration for BASKET, as previously mentioned, we decided to test a different glue applied to the bolometric technique and to study what impact it has on the detector performances. To carry out this task, we assembled two identical calorimeters except for the glue which was Araldite Rapid® in one case and Loctite® in the other one. Both of them are bi-component epoxy glues

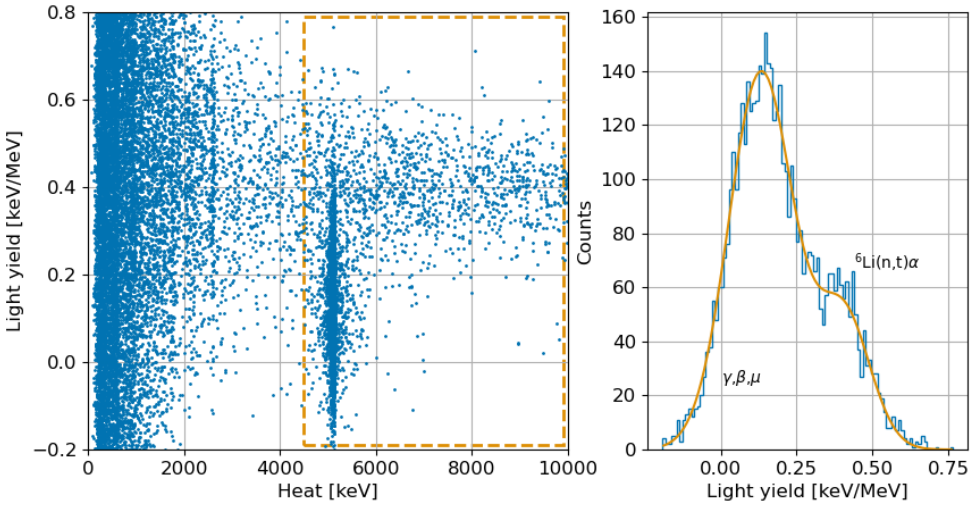

Figure 6.15: Light yield as a function of heat (*left*). The dashed area is used to build the light yield histogram (*right*). The corresponding discrimination power is 2.0 ± 0.1.

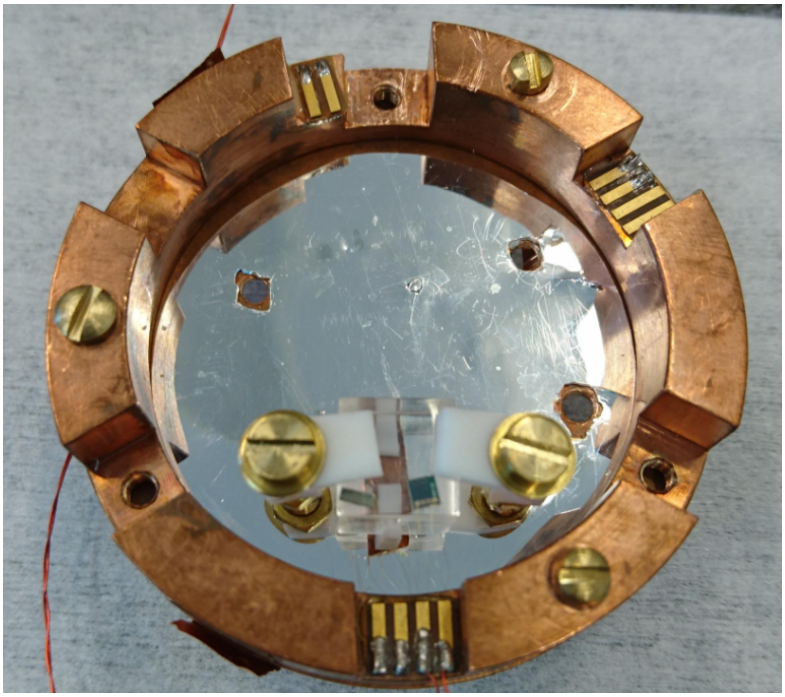

Figure 6.16: Calorimeter composed of a 1 cm^3 Li_2WO_4 cubic crystal with 1×3×1 mm^3 NTD and a heater.

Table 6.4: Main parameters of the acquisition performed with the cubic crystal.

Type	γ
Sources	^{232}Th
Mixing chamber temperature (mK)	20.6
Sampling frequency (kHz)	5
Duration (h)	17
NTD bias (nA)	3
NTD dynamic range (V)	$\pm$10
NTD LD bias (nA)	2.7
LD dynamic range (V)	$\pm$1

Table 6.5: Energy resolutions at main γ lines of the energy spectrum.

Energy line [keV]	**Energy resolution (FWHM)**[keV]
583.0	2.7 $\pm$ 0.1
510.9	3.5 $\pm$ 0.6
351.9	2.2 $\pm$ 0.3
338.3	4.0 $\pm$ 0.6
238.6	2.7 $\pm$ 0.2

baseline resolution (FWHM) [keV]	1.1
sensitivity [nV/keV]	181.8
thermal quenching	1.1

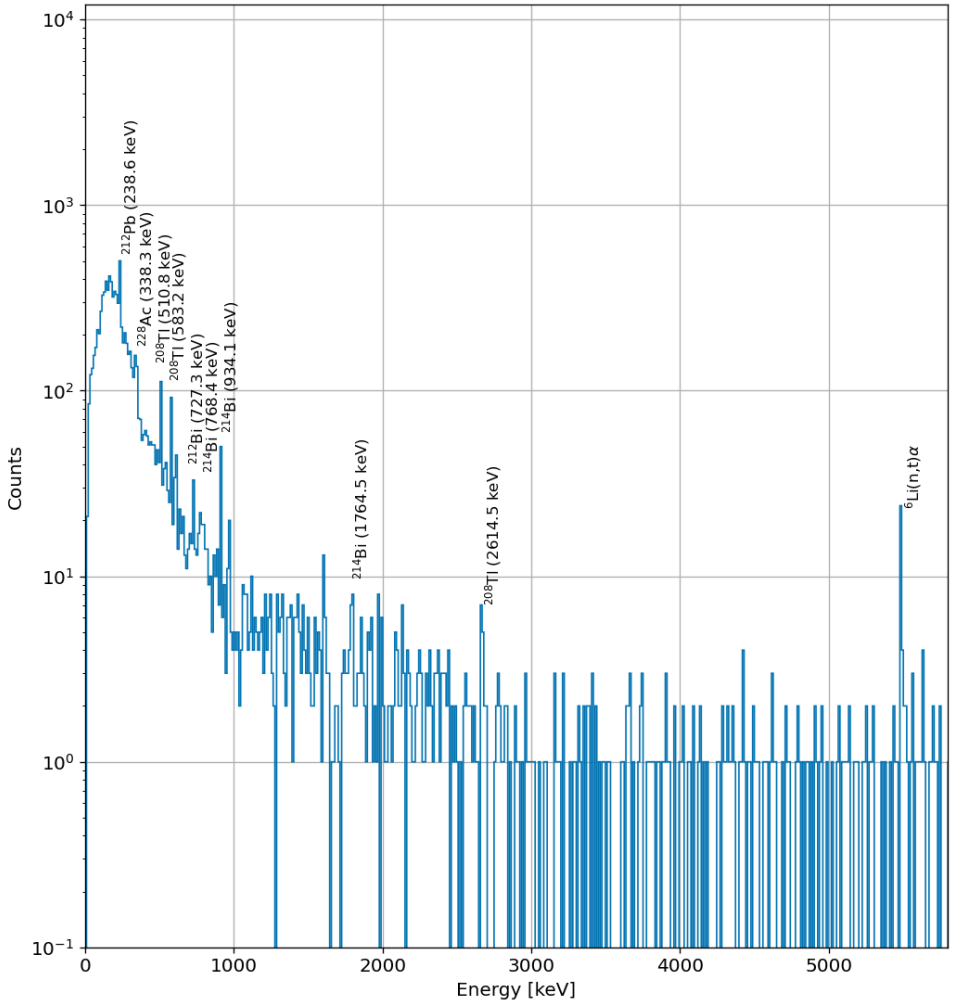

Figure 6.17: Energy spectrum of the γ measurement.

Table 6.6: Features of the glue test measurements.

Glue	Araldite Rapid®	Loctite®
Sources	-	-
Mixing chamber temperature (mK)	15.5	15.5
Sampling frequency (kHz)	5	5
Duration (h)	13	15
NTD bias (nA)	3	3
NTD dynamic range (V)	±10	±5

characterized by different properties at low temperatures that could determine an improvement or a worsening of the detector performance. The structure of the detector was the same already introduced in section 6.3: 1 cm^3 cubic Li_2WO_4 crystal coupled to a T-shaped 34B germanium NTD and a heater to allow the baseline stabilization. The two detectors were tested in the same cryostat and cooled down in two different runs. In order to be consistent, we tested the detectors in the same conditions (more details are given in table 6.6)

Once acquired and processed off-line the data with Argonauts, the first thing we did was to compare the pulse shape of events taken in the same energy range. We immediately observed that the different glue interface affects in a different way the heat transmission from the absorber to the sensor, determining a rise time of 7.2 ms and a decay time of 43.7 ms in the Araldite case, while using the Loctite glue we measured a rise time of 2.4 ms and a decay time of 15.9 ms (figure 6.18).

This difference is also reflected in the correlation parameter since it is very sensitive to the pulse shape. Indeed, in general, we observed lower correlation values and a much more strong not-linearity affecting the detector with the Loctite glue interface (figure 6.19). Figure 6.20 shows a direct comparison of the two calibrated energy spectra, after the amplitude stabilization. In both the plots we see the same γ lines but the main differences standing out are the shifted ^{6}Li(n,t)α peak at higher values (the thermal quenching factor is 0.9 for the upper plot and 1.1 for the lower one) and a lower muon contribution.

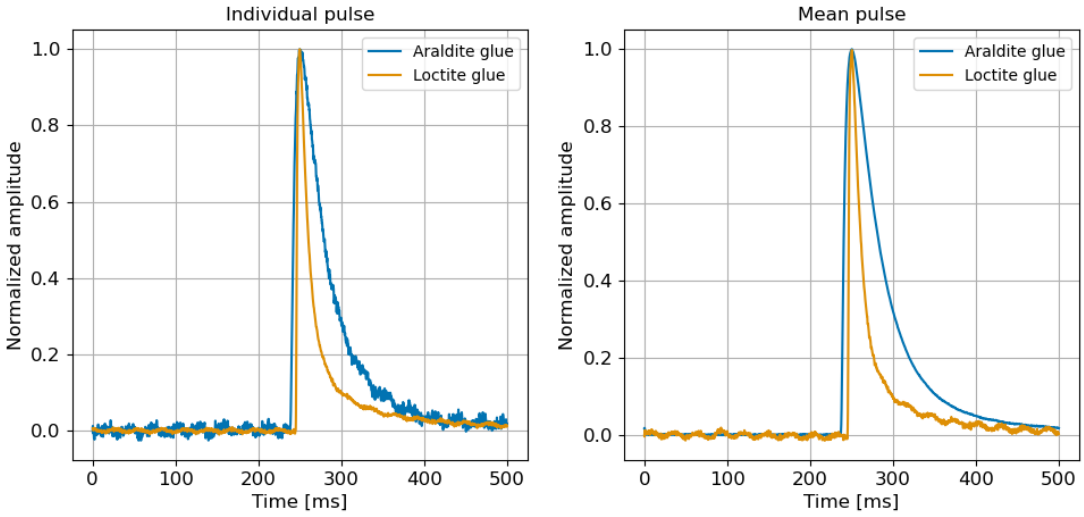

Figure 6.18: Individual (*left*) and mean (*right*) pulses, using two different glue interfaces between the absorber and the sensor.

We summarize and compare the main features of these detectors in table 6.7.

Using the light yield or any other discrimination parameters, it was not possible to evaluate the discrimination power between β/γ and α populations.

6.5 Conclusions

We performed different measurements testing different detector configurations. These prototypes showed to be excellent calorimeters and could be interesting, once optimized, to match them with a light detector with biased grids (namely, the Neganov-Luke mode [194]) to exploit them for neutron background monitoring. Indeed, it should improve the charge collection and could also improve the discrimination power. Despite this, there is still work to do in order to reach an energy threshold low enough to detect CEνNS events. Moreover, the NTD thermistor seems to not be enough fast to allow the application of these detectors in above-ground conditions, in particular, if the CEνNS source is a nuclear reactor. For this reason, additionally to "BASKET with NTD" we developed some prototypes with Magnetic Metallic Calorimeters (MMCs) presented in detail in chapter 7.

In parallel, we started a collaboration with a new partner at SiMAP in Grenoble

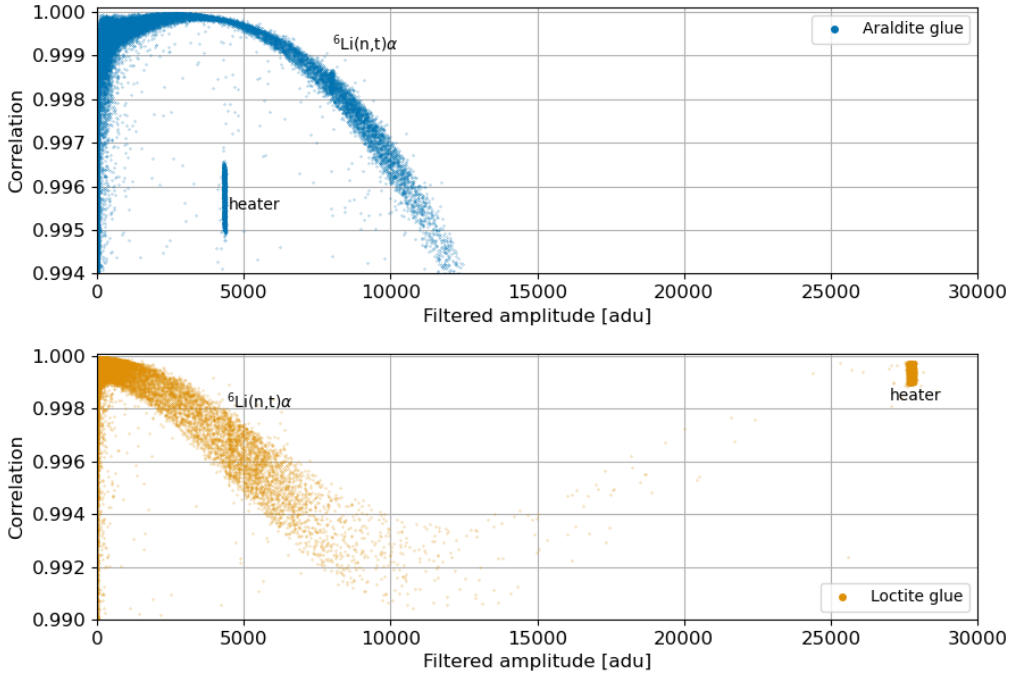

Figure 6.19: Correlation parameter as a function of the amplitude.

Table 6.7: Main features of the two detectors.

	Araldite Rapid®	**Loctite®**
Baseline resolution (FWHM) [keV]	1.56 ± 0.20	1.43 ± 0.02
Energy resolution (FWHM) at 609.3 keV [keV]	4.3 ± 0.7	4.6 ± 0.6
Sensitivity [nV/keV]	220	190
Rise-time [ms]	7.2	2.4
Decay-time [ms]	43.7	15.9

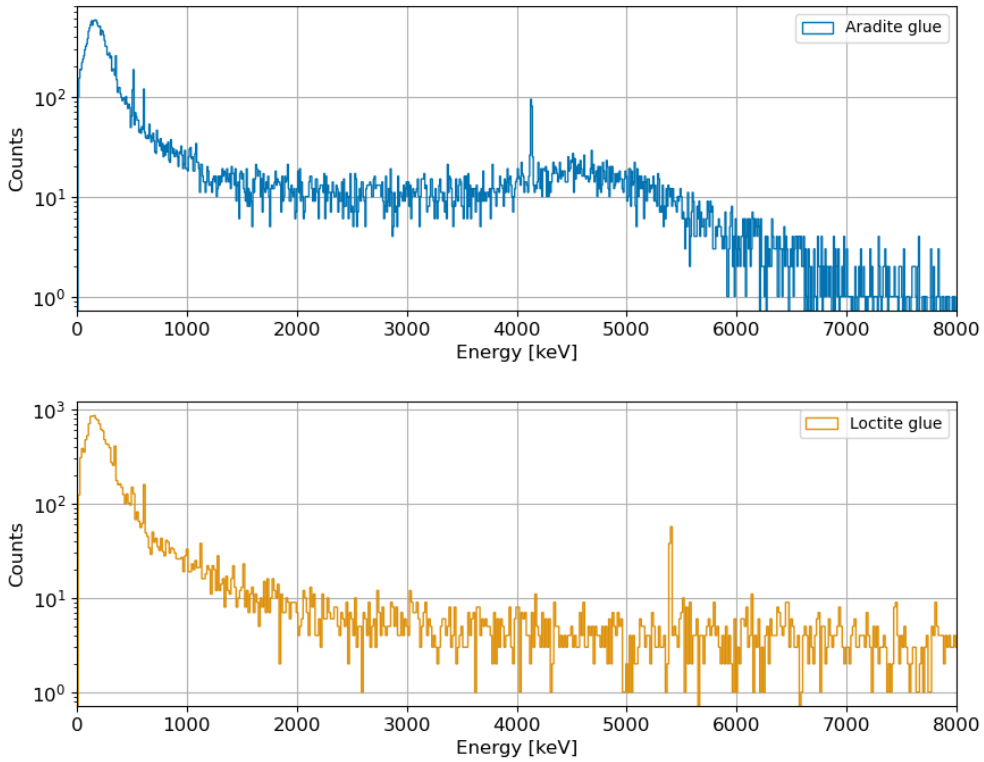

Figure 6.20: Comparison of calibrated energy spectra using Araldite® (*top*) and Loctite® (bottom) glues.

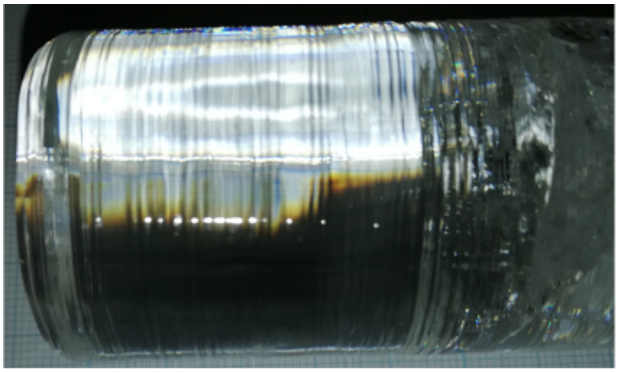
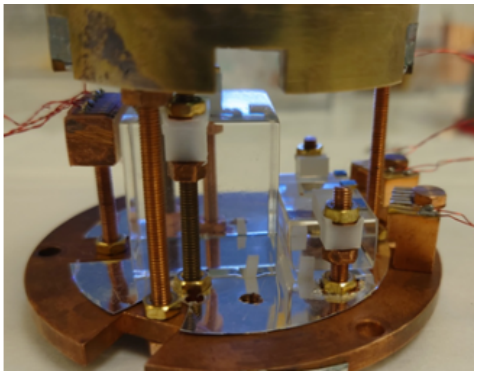

Figure 6.21: *Left*: Li_2WO_4 crystal (Φ=3.5 cm, h=3 cm) produced by the french partner. *Right*: two smaller elements (1.4×2.5×0.9 cm^3 and 2.5×2.7×2.5 cm^3) cut out from the Grenoble crystal and mounted as detector absorbers to test their performances.

(France) for a made in France crystal production. The need for a "local producer" is to simplify the purchase procedure. Indeed, since the natural content of ^{6}Li in Li_2WO_4 is ∼8 %, we need a ^{6}Li enrichment to produce absorbers to live up to the task. The bureaucratic procedure to purchase such crystals from Russia was complicated because ^{6}Li is an isotope with military applications for the fabrication of thermonuclear weapons. We received a first Li_2WO_4 crystal from Grenoble (figure 6.21, left), from which we cut out two smaller elements that have been already tested (figure 6.21, right). The data analysis is ongoing.

Chapter 7

BASKET with MMCs

In this chapter we present three detector configurations for the BASKET R&D project. As already explained in chapter 6, the absorber material chosen for the project (and therefore used in all the tests here presented) is Li_2WO_4.

7.1 First tests

7.1.1 Detector configurations

In this section, we introduce two detector configurations used in some of our tests and presented in figure 7.1. In both cases, the chosen absorber material is a $1\,cm^3$ cubic Li_2WO_4 crystal, element in common with all the BASKET detectors. The different opacity of the crystal is a consequence of the hygroscopic nature[1] of the Li_2WO_4. Between the two detector assemblies, the crystal underwent a mechanical lapping procedure, visible from the different opacity of the crystal. After each cleaning procedure, a Au-Ti pad ($5\,mm \times 5\,mm \times 200\,nm$) gold pad was evaporated directly onto the crystal surface in order to collect and thermalize the athermal phonons.

The crystal is fixed to a copper holder using a fastening system of PTFE clamps (Figure 7.2). The holder is designed with a gold plated copper pedestal where an Ag:Er MMC sensor and a dc-SQUID are manually glued with GE/IMI 7031 Varnish glue.

The MMC used in these tests is produced at the Kirchoff Institute of Physics of

[1]Because of the Li_2WO_4 hygroscopicity, the assembly process should minimize the crystal exposition to ambient air. Moreover, a periodical surface mechanical cleaning is necessary in order not to degrade the collection of athermal phonons into the gold film.

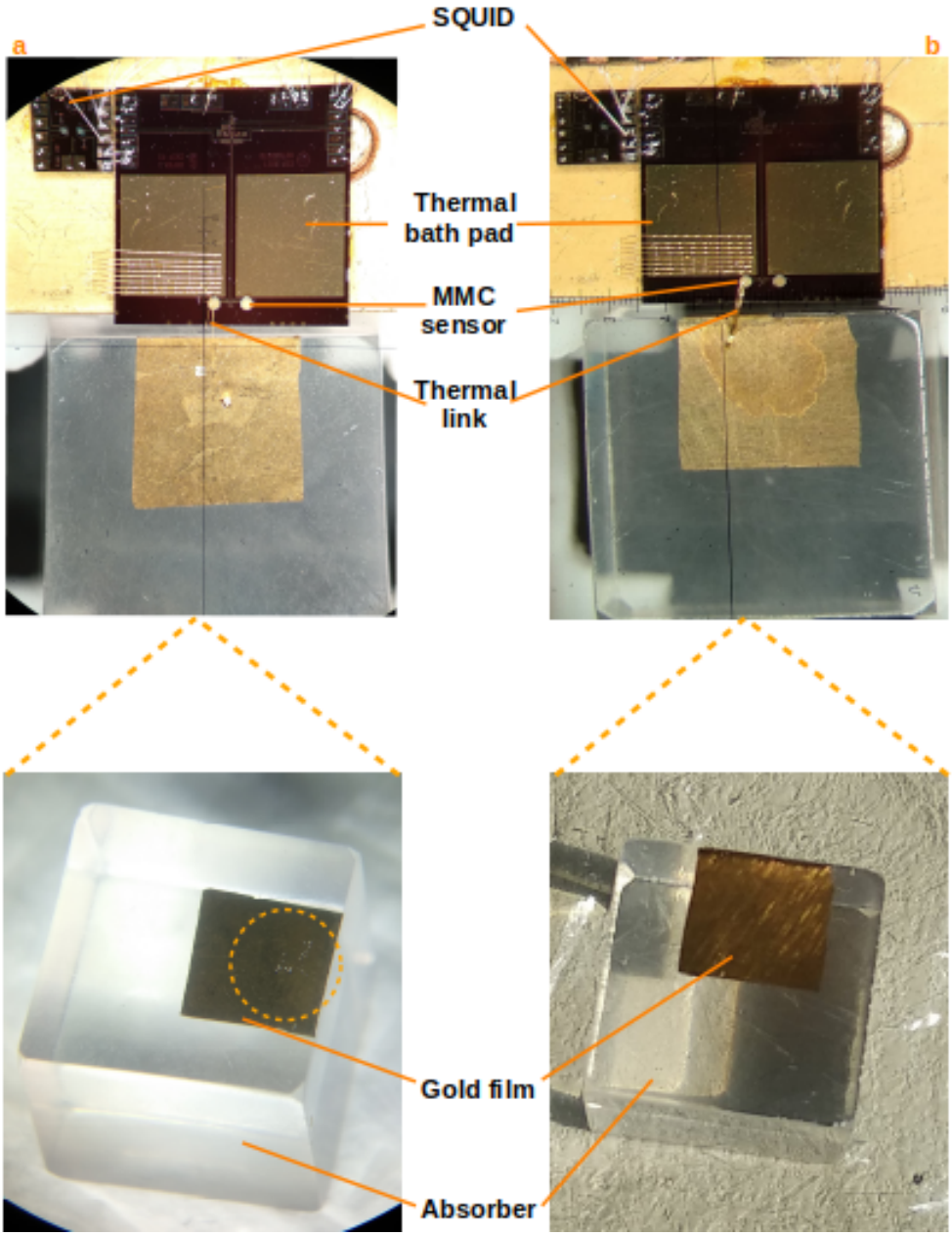

Figure 7.1: Detector configurations of the first tests. The main items are labeled in the figure.

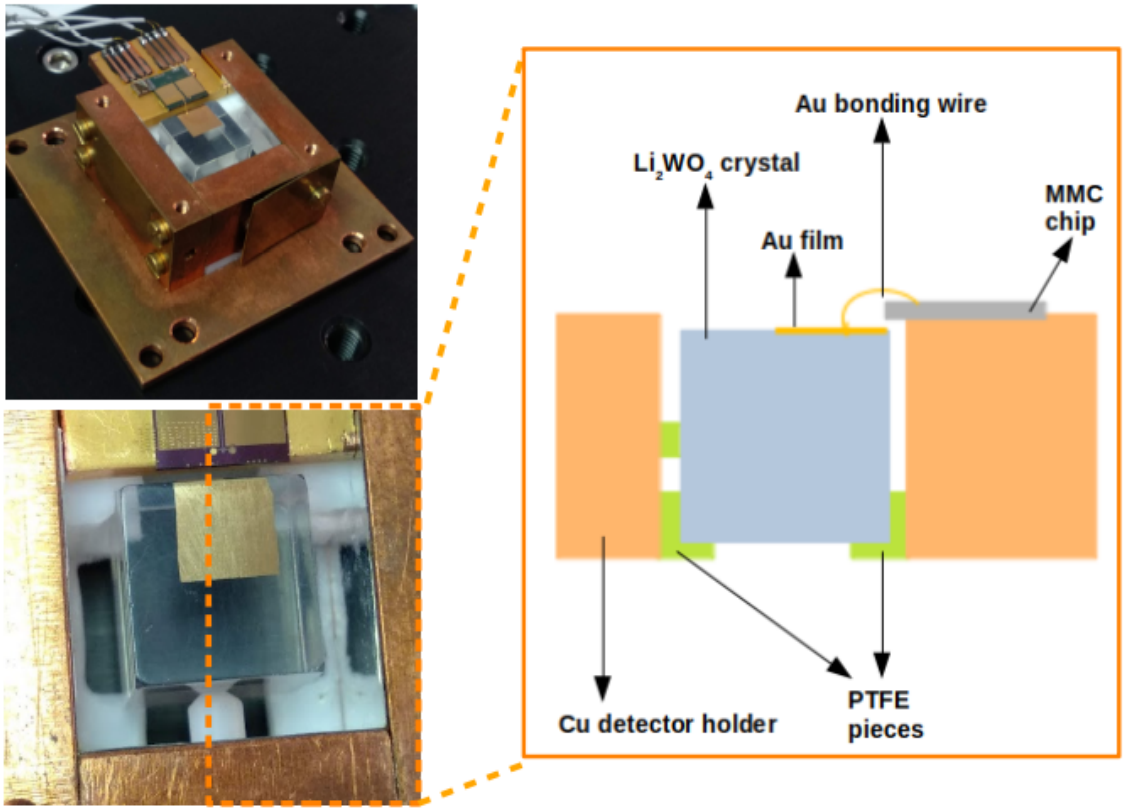

Figure 7.2: *Left top*: copper holder hosting the detector. *Left bottom:* in white, the PTFE system of clamps used for the crystal fastening. *Right*: Schematic cross sectional view of the detector.

Heidelberg University and it is optimized for an absorber heat capacity of 28 pJ/K at 20 mK. It is read by a single-stage dc-SQUID placed as close as possible to the MMC (the further it is, the smaller the signal size, due to the parasitic inductance of the leads between MMC and SQUID input coil). MMC meander and SQUID input coil are connected through aluminum bonding wires.
The thermal link between the gold phonon collector film on the absorber crystal surface and the MMC sensor was meant to be made by gold bonding wires. Anyway, a direct bonding on the evaporated pad was not possible, indeed any attempts left holes in the gold (*circled area* in figure 7.1. In order to avoid any weak link that could break during the cooling down procedure, we investigated other solutions:

- configuration 1 (figure 7.1 *a*): we bonded tiny pieces of gold foils (area 300 $\mu\times$300 μm and thickness thickness 3 μm) onto the gold pads thanks to a tool specific for ribbons included in the Kulicke&Soffa 4523 wedge bonder, and from them we bonded two gold wires to the Ag:Er MMC sensor;

- configuration 2 (figure 7.1 *b*): we used directly a thin gold foil as thermal link between the absorber and the MMC sensor;

The different thermal links employed in the detector were expected to have an impact on the rise-time of the detected pulses. Only one of the MMC meanders was used in the detector configurations.

The base temperature recovery is guaranteed by a small gold rectangle between the sensor octagon and the on-chip heat bath gold film (too small to be visible in figure 7.1, but it is the one labeled "thermal link" in figure 2.3). The on-chip heat bath is kept at the heat bath temperature thanks to a strong thermal link obtained by several gold wires running to the detector holder.

^{55}Fe-^{109}Cd energy calibration source (activity 6.49e3 Bq and 1.08e2 Bq for ^{55}Fe and ^{109}Cd respectively) is used and fixed outside the holder, facing directly the crystal through a breach in the holder (Figure 7.3). In the second configuration, an additional lead collimator was added to the source.

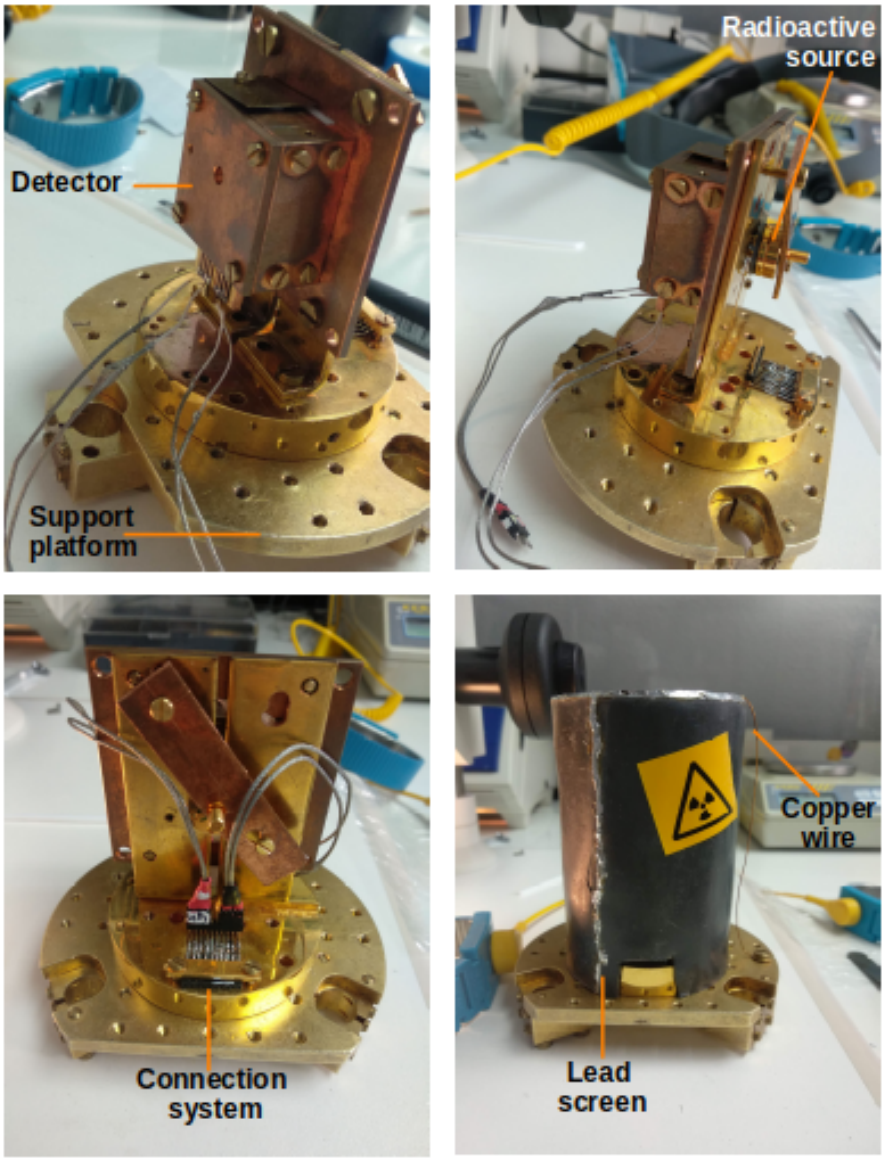

Figure 7.3: *Left top*: the detector is fixed on a gold plated copper support platform, necessary for the test in the dilution refrigerator. *Right top:* the platform allows to add a radioactive source directly facing the crystal through a breach in the holder. *Left bottom:* the platform has an integrated connection system for the read-out. *Right bottom*: the detector is shielded with a lead screen. The cooling down of the lead shield to the base temperature is assured by a copper wire.

7.1.2 Experimental set-up

The tests of the detectors are performed in a wet dilution refrigerator at the Laboratoire National Henri Becquerel (LNHB, Saclay, France) delivered by Cryoconcept (Figure 7.5): once the detector is placed in the experimental space underneath the mixing chamber and all the infrared screens are closed, and the dewar is filled first with liquid nitrogen (77 K) and then with liquid helium (4.2 K); all the stages in the IVC are cooled down to this temperature thanks to a thermal bridge created injecting a He exchange gas. More details about wet dilution refrigerators are given in chapter 2.
Reached the 4.2 K, we need to inject and freeze the field current in the meander to magnetize the sensor and allow the conversion of the temperature into a magnetization variation. This procedure is performed as followed:

- we inject a field current I_F=60 mA in the niobium superconductive circuit. This circuit splits into two branches: one that travels the double meander (black in figure 7.4, *a*) and a shorter one (orange in figure 7.4, *a*)) underneath the AuPd heater. I_F will flow in this second path since it is characterized by a lower inductance L_1 ($L_1 < L_m$);

- then, we heat the AuPd resistor switch injecting the heat current pulse I_H=4 mA through a battery. This thermal switch is a resistive element that heats up locally the niobium line L_1 to a higher temperature than the critical one T_c ∼9.2 K (Figure 7.4, *b*);

- since we created an electrical resistance (now locally the niobium is no more superconductive) in the I_F favorite path, I_F will start flowing through the meander with L_m where the resistance is zero;

- interrupting the current I_H, the meander circuit is now closed again and the field current I_F is permanently frozen in it creating a local magnetic field (Figure 7.4, *c*). Now the current injected from outside the cryostat can be switched off.

We cannot know if the field current is correctly frozen in the meander before reaching temperatures below 100 mK by observing the pulse heights or measuring the magnetization of the sensor.

The entire cooling down procedure takes about 2 days.

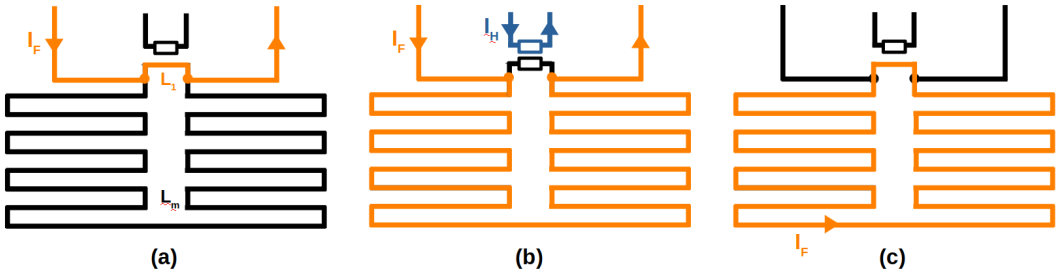

Figure 7.4: Steps followed in order to freeze field current in the meander.

The SQUID is biased and read out by a Magnicon XXF-1 SQUID Electronics. Then, the signal is filtered with a band-pass filter (0.1 kHz high-pass frequency and 30 kHz low-pass frequency) using a SR560 Low Noise Preamplifier. The data are recorded with a P25M PCI Express 16 bit digitizer card in continuous mode, with 100 kHz sampling frequency.

7.1.3 Data analysis

The recorded stream of data is processed with the analysis tool described in chapter 3. The pathological events are removed by cuts in the chi-square vs pulse height plot and the pulse height are corrected to suppress any temperature fluctuation that could affect the energy resolution. Below the main results and energy spectra are presented.

First configuration

We recorded data for almost two weeks, dividing it into two measurements characterized by a different dynamic range to have the opportunity to appreciate the neutron capture on Lithium (wide dynamic range (i.e. 0-8300 keV), ∼7 d) and have a better energy resolution in the CEνNS region of interest (short dynamic range (i.e. 0-185 keV), ∼3 d). As for all the analyses presented in this thesis, the calibration technique of the energy scale is based on the identification and gaussian-fitting of the main γ and X-rays peaks. In this case, we fixed on the detector a ^{55}Fe-^{109}Cd source facing the crystal. The most intense expected energy lines (and therefore usable for the energy calibration) are reported in table 7.1.

In both cases, we observed that the detector was characterized by a good linearity, allowing the calibration with a linear fit.

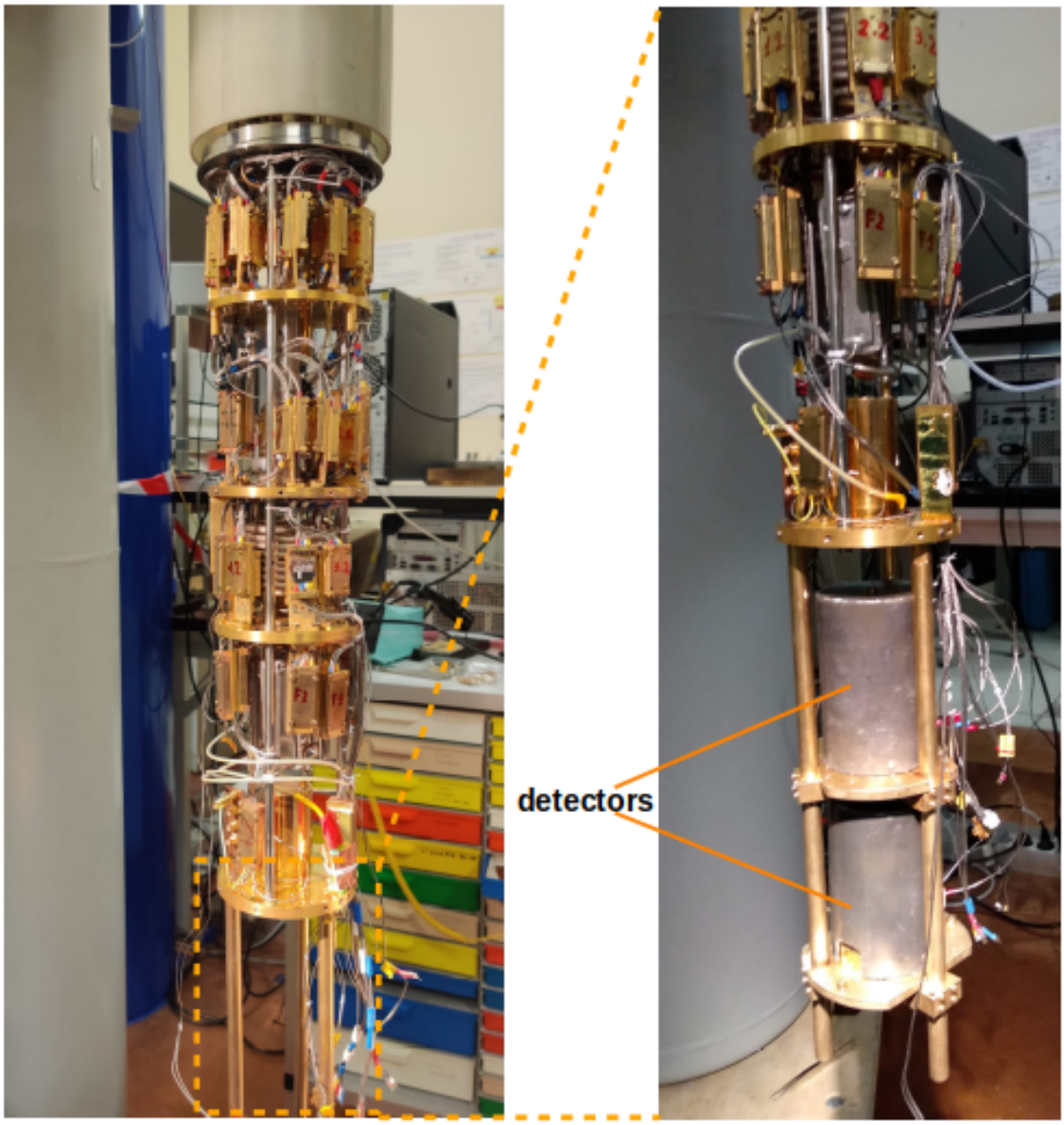

Figure 7.5: The wet dilution refrigerator at the LNHB. At the bottom part, the detector can be mounted using a suitable copper support platform. Depending on the size of the detectors, the cryostat can host up to a maximum of 3 detectors.

Figure 7.6 *top* shows the calibrated energy spectrum up to 150 keV (measurement with short dynamic range). The dominant peaks are the ones expected from the ^{55}Fe-

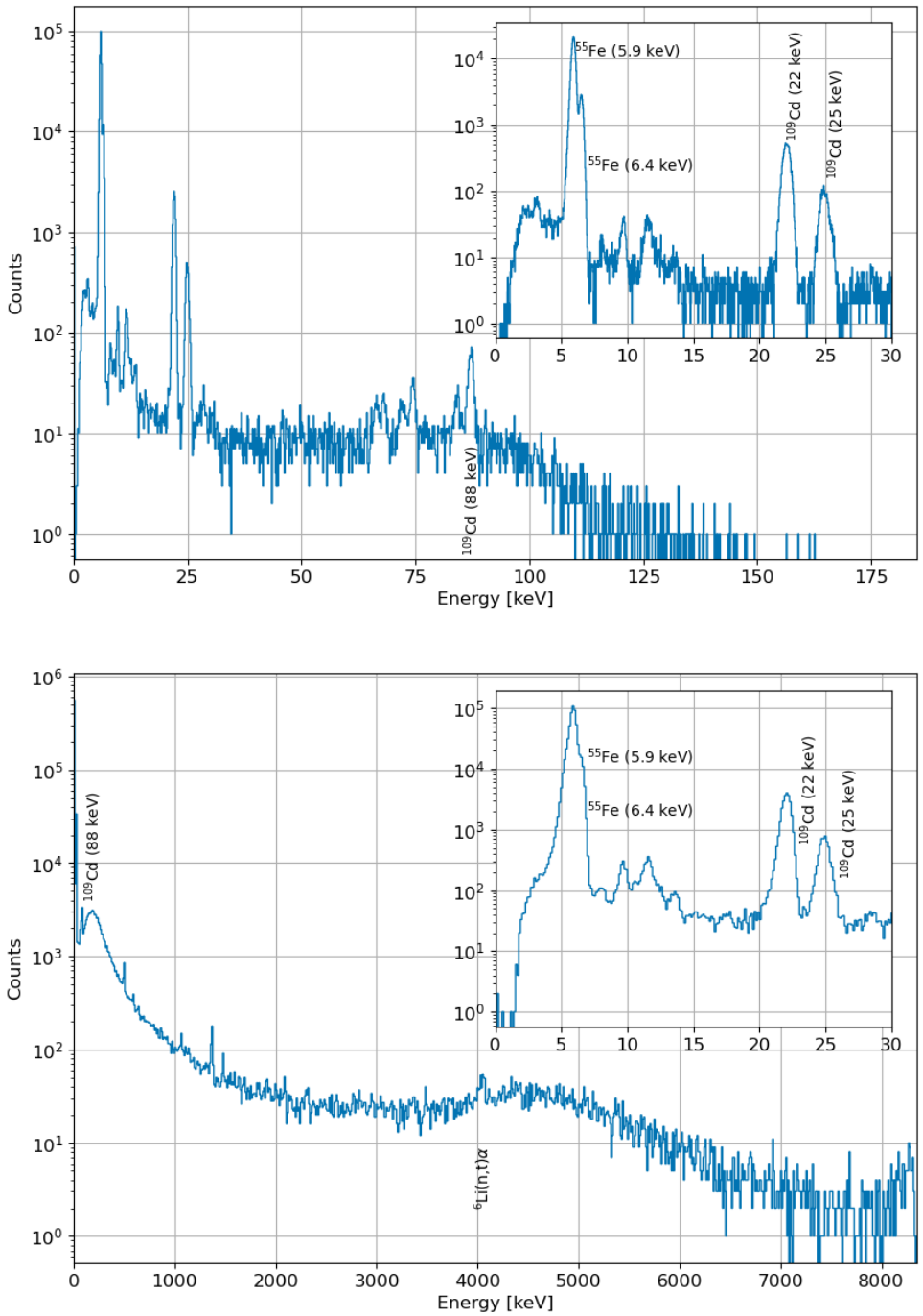

Figure 7.6: First detector configuration. *Top:* energy spectrum with short dynamic range. *Bottom*: energy spectrum with large dynamic range.

Table 7.1: Main photon energy lines provided by the ^{55}Fe-^{109}Cd source.

Energy [keV]	Source	Intensity [%]	Radiation
5.9	^{55}Fe	25%	Mn Kα X-rays
6.4	^{55}Fe	3.4%	Mn Kβ X-rays
22	^{109}Cd	55.1%	Ag Kα_1 X-rays
25	^{109}Cd	15.3%	Ag Kβ_1 X-rays
88	^{109}Cd	3.7%	γ-rays

^{109}Cd source. We did not identify the elements originating the other structures but they are mostly common to all the measurements performed with the same set-up so it seems reasonable to assume that it comes from the materials surrounding the detector.

Figure 7.6 *bottom* shows the energy spectrum extending up to 8.4 MeV (wide dynamic range). At the lower energy region (0-150 keV) we find the contribution of the same structures present in the case of the short dynamic range. At higher energies (150 keV- 3 MeV), we can clearly identify some other energy lines that are typical of the background natural radioactivity while at 4.1 MeV, we see the ^{6}Li(n,t)α peak characteristic of this absorber type. After the data selection, we evaluate approximately 31 n/d.

This detector was characterized by a sensitivity of 170 $\mu\Phi_0$/keV, while the FWHM baseline resolution is 194.1 eV. The rise-time of the 5.9 keV mean pulse is 1.6 ms while the decay-time is 5.9 ms. In table 7.2 are reported the FWHM energy resolutions evaluated at the main low energy peaks:

Table 7.2: FWHM energy resolutions evaluated at the most intense source peaks for both the fist and second detector configurations.

Energy [keV]	1^{st} config. E_{res} [eV]	2^{nd} config. E_{res} [eV]
5.9	326±1	375.0±6
6.4	309±7	354±18
22	622±4	710±40
25	722±26	960±240

Second configuration

As for the run of the first configuration, we recorded data dividing the measurement by a short dynamic range acquisition (27 hours) and a large dynamic range (9 days). We fixed on the detector a ^{55}Fe-^{109}Cd source facing the crystal by interposing a lead collimator in order to have better control of the events counts. Also in this case, we performed a linear calibration of the detector based on the identification and Gaussian fit of the main energy lines produced by the source. In figure 7.7 the short dynamic range energy spectrum (*top*) and the large dynamic range energy spectrum (*bottom*) are shown. From it, we can see immediately that the energy resolution of this second detector configuration is worse compared with the first one. The FWHM energy resolutions evaluated for the most main energy peaks are reported in table 7.2. Because of the presence of the lead collimator between the source and the absorber, the X-ray peaks are less intense, determining a larger uncertainty in the evaluation of the energy resolution. Moreover, we can observe that we are no more able to clearly identify the ^{6}Li(n,t)α peak due to a worsening of energy resolution as energy increases. We evaluated a sensitivity of 142 $\mu\Phi_0$/keV, while the FWHM baseline resolution is 233.7 keV. The rise-time of a 5.9 keV mean pulse was 1.6 ms while the decay-time was 16.6 ms.

7.1.4 First tests: conclusion

In this section, we presented two detector configurations in which the main difference was a different thermal link between the absorber and the sensor. Therefore, the expectation was to have two detectors characterized by a different rise-time. On the contrary, comparing the obtained results, we observed that both the configurations provide a rise-time of 1.6 ms but different decay-times: in the second case, it was almost 3 times the first case. These results, unforeseen and initially puzzling, can be explained by assuming that the thermal conductance between the heat sink and sensor (G_{sb}) is much larger than the thermal conductance between the sensor and the absorber (G_{as}). In fact, in the case $G_{as} << G_{sb}$, the rise time is inversely proportional to G_{sb}, instead the decay time is inversely proportional to G_{as}. So the rise time, that remains the same between both runs, depends on the thermal link between the sensor and the on-chip heat bath, micro-fabricated from a thin film and indeed unchanged. Also its value of 1.6 ms is very close to the design value of the decay time of these MMCs (1ms) that should normally be defined by the sensor-bath thermal link. More details about the theoretical explanation

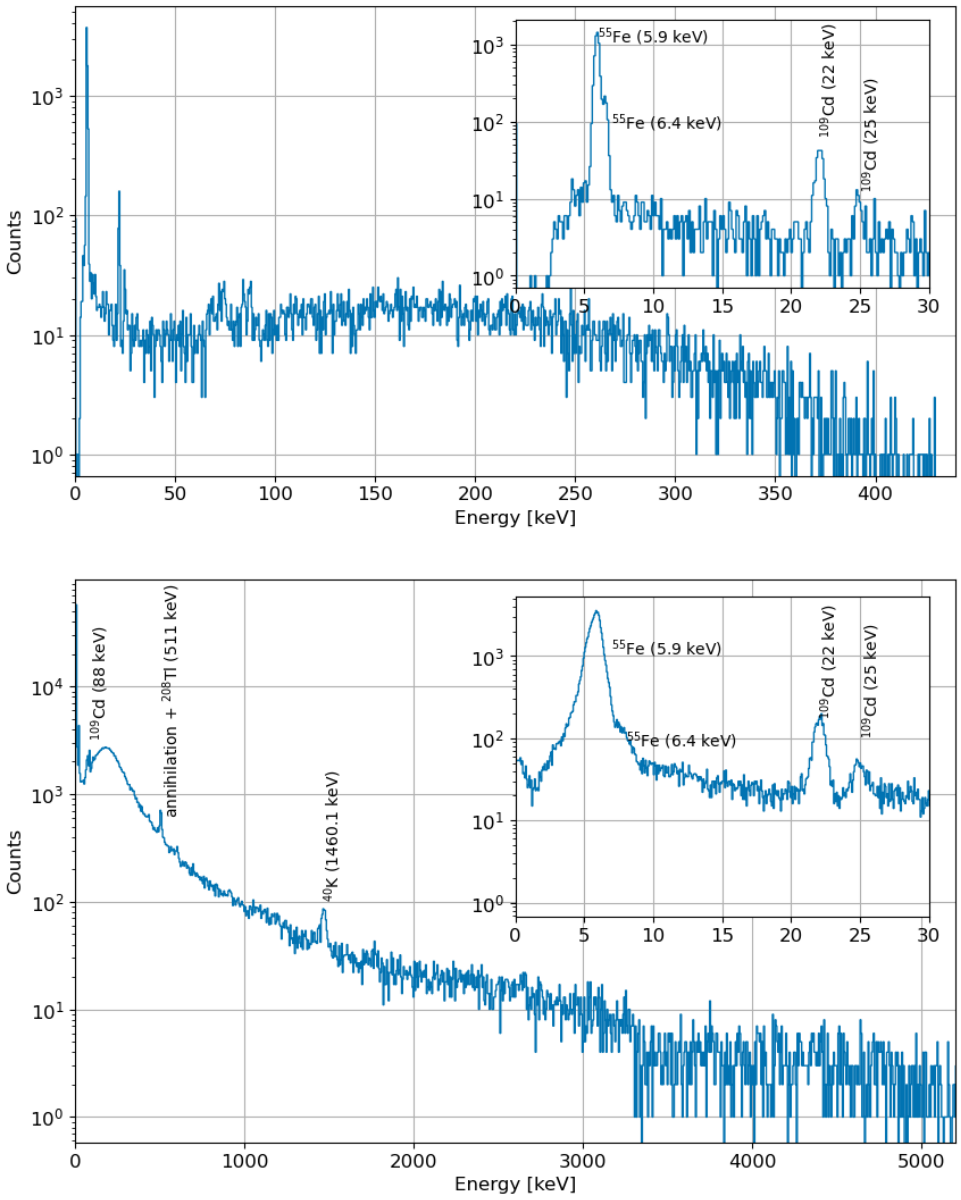

Figure 7.7: Detector second configuration. *Top*: energy spectrum setting a short dynamic range; *Bottom*: energy spectrum with a large dynamic range.

are given in section 2.5.2. This behavior, in addition to being counterintuitive (indeed with our cryogenic detectors we use to think that the rise-time is set by the thermal link between absorber and sensor), reduces the pulse height and thus degrades the energy resolution, which is indeed worse than expected.

7.2 Second tests

Detector configuration and experimental set-up

With the goal to overcome the difficulty to make a strong and reliable thermal link between sensor and absorber using the evaporated gold pad, we decided to try a different approach. The Li_2WO_4 crystal was once again mechanically lapped and the gold pad definitively removed. Instead of depositing a new gold layer, we glued directly onto the crystal surface a $3\,mm \times 3\,mm \times 3\,\mu m$ gold foil with Araldite Rapid® to improve the bonding of gold wires and increase the conductance between the absorber and the sensor. The gold foil dimensions are a constraint because the corresponding heat capacity (about five times larger than the one of the evaporated golf films, and in this detector configuration largely dominating the total detector heat capacity) plays a role in the pulse height and time response of the detector. The gold foil was carefully glued and left drying for 17 hours in a clamping system equipped with a specifically shaped PTFE mold pressing on it (figure 7.8). The development of a suitable clamping system is to answer the need to squeeze the excess ofAraldite Rapid® out of the crystal-gold interfaceobtaining a thin glue interface between crystal and phonon collector, and to avoid the wrinkling of the thin gold foil during the polymerization phase.

The thermal link between the absorber and the sensor was realized through three gold bonding wires (figure 7.9, *a*). The selected MMC and SQUID chips had the same features like the ones used in the first and second detector configurations (figure 7.9).

The experimental set-up and cooling down procedure are the same already presented for the first tests. Once the cryostat was at 4.2 K, we injected and froze in the meander a field current $I_F = 60\,mA$ opening the thermal switch with a heater current $I_H = 3.2\,mA$.

Data analysis

After reaching a stable temperature of 13.5 mK, we started recording data in continuous mode for two weeks, setting two different gain values (i.e. two different dynamic ranges):

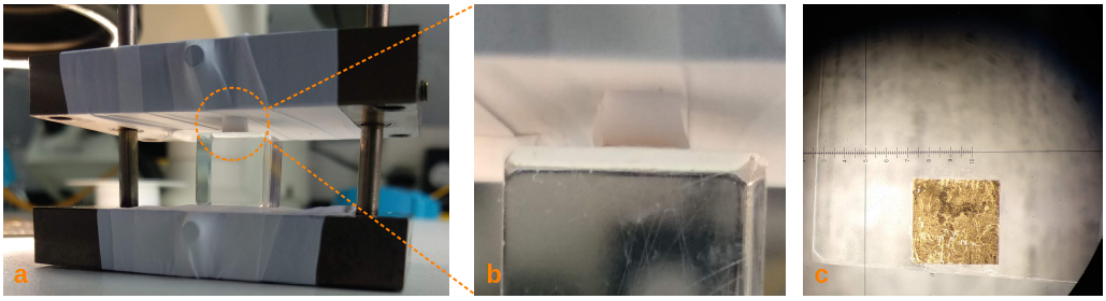

Figure 7.8: *a*: clamping system used for the gold foil gluing. To prevent any accidental damage to the crystal, the metallic structure was wrapped with PTFE tape; *b*: to avoid the wrinkling of the foil during the glue polymerization phase, a PTFE shaped with the same dimensions as the gold pad was used to make pressure on it; *c*: the glued gold foil after polymerization.

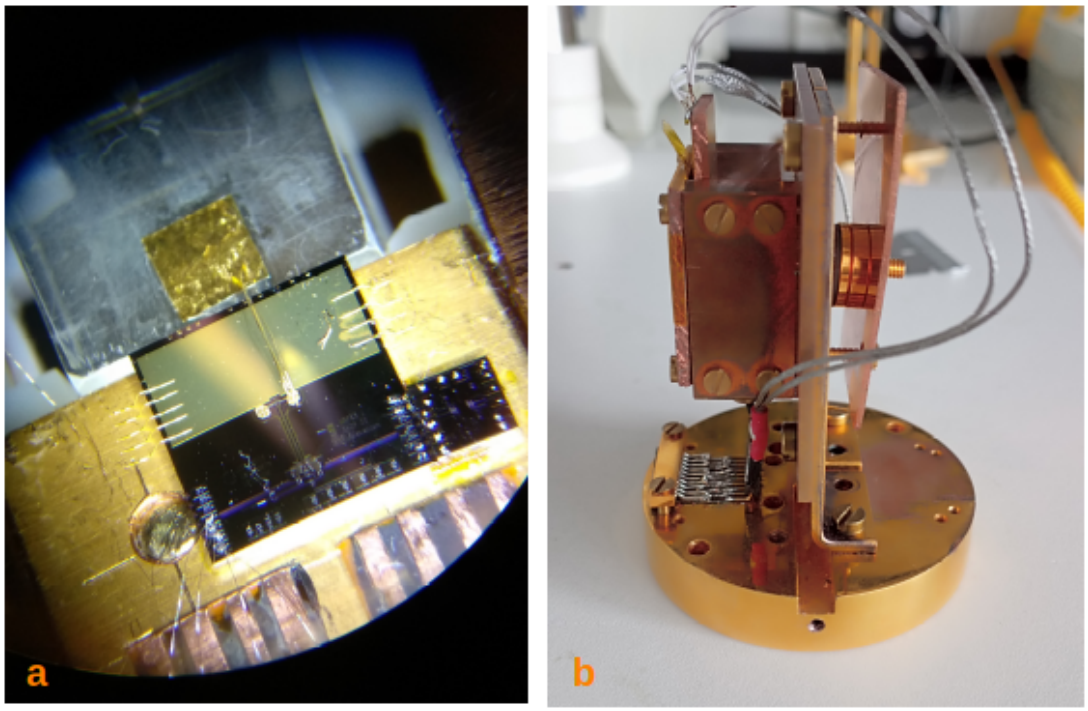

Figure 7.9: *a*: magnification of the detector. The thermal link between the absorber and sensor was guaranteed by three gold wires; *b*: detector holder. The ^{55}Fe-^{109}Cd source used in the first tests was maintained also for these measurements.

the first one more focused on the very low energy region and the second one on the gamma energy region. The data are treated similarly to what was already presented in the analysis of the previous detector configurations: pathological events are removed by cuts in the chi-square vs. pulse height plot, and the temperature fluctuations are corrected to extract the best energy resolution.

In figure 7.10 the energy spectra obtained with this new detector configuration. We can immediately observe that we are not able to well discriminate the 5.9 keV and 6.4 keV X-rays peaks, indicating a worse energy resolution (the FWHM energy resolutions are shown in table 7.3). The evaluated baseline resolution is 630 keV.

Table 7.3: FWHM energy resolutions evaluated at the most intense source peaks for both short and large dynamic ranges.

Energy [keV]	short d.r E_{res} [eV]	large d.r. E_{res} [eV]
5.9	666±7	781±2
22.0	697±16	750±11
25.0	730±80	979±32

Besides the energy peaks originated by the source, there are peaks originated by the natural radioactivity (^{40}K and ^{238}U decay chain). Furthermore, not identified peaks are present in the low energy region already observed in other spectra at the same energies, confirming that they are most likely due to fluorescence emissions coming from the surrounding materials. The evaluated sensitivity for this configuration is 44.6 $\mu\Phi_0$/keV. The rise time and decay time evaluated for a 22 keV mean pulse are 2.1 ms and 14 ms respectively. The considerable loss of sensitivity and the worsening energy resolutions compared to the first and second configurations could be probably attributed to the fact that the glue interface is deteriorating the energy of the collected phonons. Therefore, at the current state of the art, the glued gold foil is still not an alternative to the evaporated gold pad.

7.3 Conclusions

In this chapter we presented some detector configurations developed in an investigation addressed to face the hygroscopic nature of the Li_2WO_4 crystal. The first option taken into account is the evaporation of the gold pad (200 nm) directly onto the crystal surface.

Unfortunately, the Li_2WO_4 hygroscopicity is responsible for a deterioration of the crystal surfaces and, as a consequence, a bad attachment of the gold pad. This explains the difficulties met trying to bond wires on the pad and the slow collection of the athermal phonons observed in the measurements here reported.
In the attempt to overcome these difficulties, we tried to find an unconventional way to collect phonon, gluing a thin gold foil ($3\,\mu$m) onto the freshly polished crystal surface. The few μm thick glue provides a solid layer that facilitates the bonding task. Despite this practical advantage offered by this technique, the results reported in this chapter showed the best option currently available, in terms of resolution and sensitivity, is the evaporation. The AMoRE collabiration is currently making efforts to identify the most promising technique to produce calorimeters based on hygroscopic absorbers coupled to MMCs [195].

In parallel to the detector prototyping and tests reported in this chapter, we started a new project: the production of MMCs with the motivation to become independent of the availability of the actual producer. We are designing and developing the sensors at the Centre for Nanosciences and Nanotechnologies (C2N, Palaiseau, France) following the instructions provided by the Kirchhoff Institute of Physics at Heidelberg University. More details about the MMC design and micro-fabrication are given in appendix A.

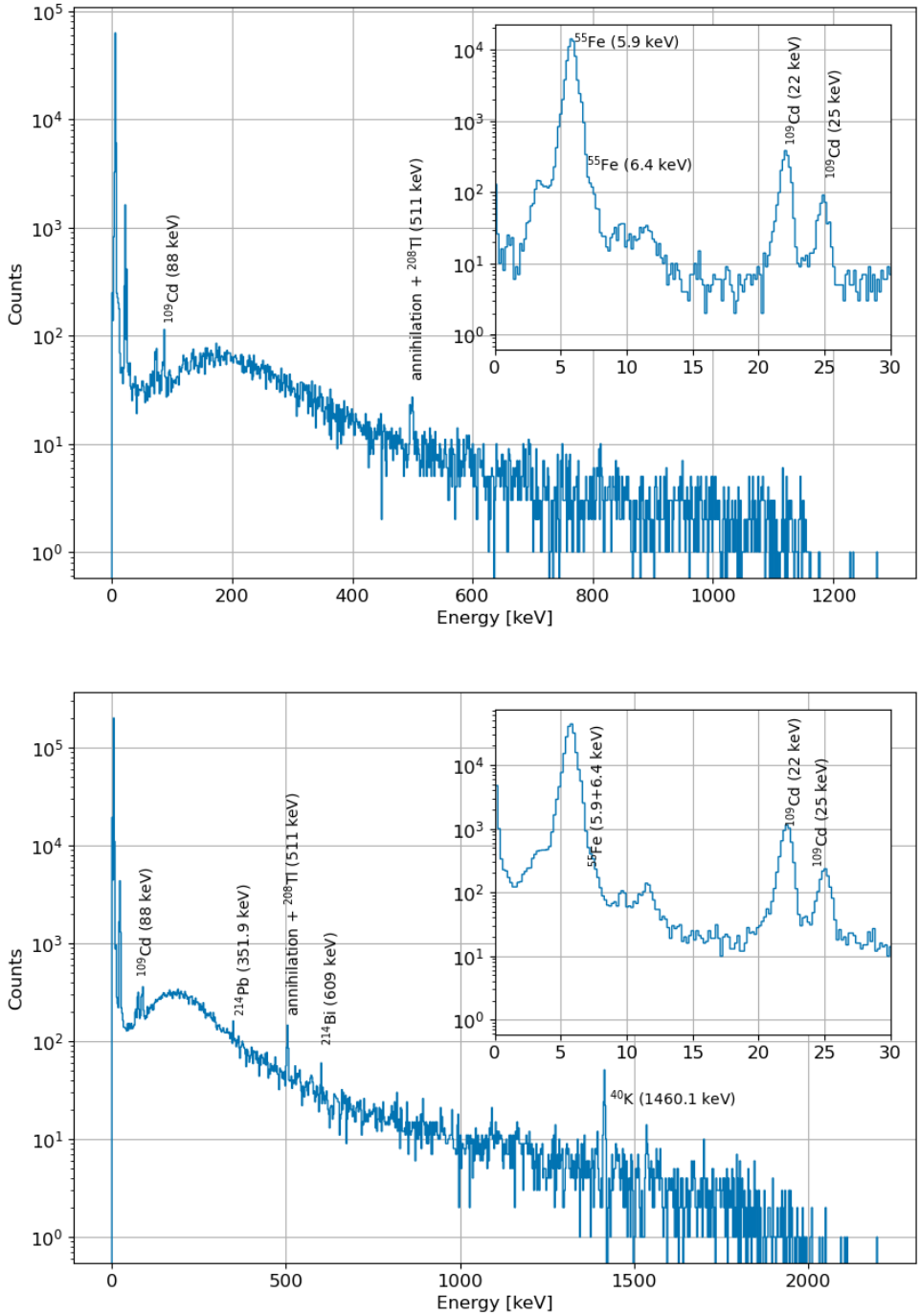

Figure 7.10: Energy spectra obtained with the third detector configuration (glued gold foil) setting a short dynamic range (*top*) and a large dynamic range (*bottom*).

Appendix A

MMC: design and micro-fabrication

In June 2021, we started a new activity aiming to produce our own MMC sensors. This new project is motivated by the fact to optimize the MMC design for the measurement of CEνNS. At the moment we started just some production tests to identify which techniques, materials, and dimensions are compatible with the features we want for our sensors and the machines available at for the production at Centre for Nanosciences and Nanotechnologies (C2N, Palaiseau, France). Here, we are benefitting the PIMENT platform and its experts in micro and nano-fabrication[1]. The ISO 4[2] clean room (appendix B.1), where the PIMENT platform is located, allows the minimization of defects due to micro dust particles that could stick on the sample surface.

A.1 MMC production steps

The description of an MMC sensor and its working principle was already depicted in chapter 2.3.2. Our first samples are realized with the micro-fabrication technique, in a multi-layer process on a silicon wafer. The production can be summarized in six steps described below [136].

[1] https://piment.c2n.universite-paris-saclay.fr/en/

[2] ISO 4 or class 10 cleanrooms are ultra-clean strictly controlled clean rooms with primary applications for nano-technology, semiconductor, biotechnology, and pharmaceutical applications.

A.1.1 Step one: the first niobium layer

- The silicon substrate is thermally oxidized by sputter depositing a ∼250 nm thick SiO_2 layer (appendix B.2.2).

- A first continuous niobium layer (thickness ∼ 300 nm) is deposited using the sputtering technique with a Plassys Sputtering MP700S, a machine equipped with four different sputter targets (Nb, Au, Pd, MgO). In order to verify the quality of the deposition, a stress test of the wafer is performed before and after the niobium deposition (appendix B.2.3).

- A thin photoresist (S1813) coating is uniformly distributed spinning the wafer (60 s/4000 rpm/200 rpm s^{-1}) and baked for 2 minutes at 100°C.

- When the photoresist is dried, the sample is properly placed in a Heidelberg DWL 66 fs, a maskless lithography laser writer (appendix B.3.3). The meander drawing is uploaded in GDS format to the Laser machine software. Once the techniques, the parameters, and the geometry of the MMCs series will be optimized, a more convenient technique will be adopted: optical lithography (appendix B.3.4). It consists of the realization of a customized mask that allows producing several samples at the same time on the same silicon wafer just by exposing it to a UV light. Compared to the laser writing, this solution is faster, it makes easier the correct alignment of the sample in the multi-layer process, it guarantees the reproducibility of the chips, and it is less expensive assuming to have already the mask (appendix B.3.4.1).

- With a specific solvent the areas not exposed to the laser are removed.

- The samples undergo a fluorine Reactive Ion Etching (RIE, see appendix B.4). While monitoring the etching of the niobium with a laser, the plasma attacks the sample surface removing layers of material until the SiO_2 is reached. The niobium covered with the photoresist are protected from the dry etching.

- Finally, the remaining photoresist is removed with a solvent. Since some traces could remain, the wafer can be additionally exposed to plasma O_2 etching for 3 minutes.

Reached this point, we can we can verify the critical current of the meander.
In figure A.1, an example of MMC meanders we produced to identify the techniques to adopt and the best parameters for our future large production.

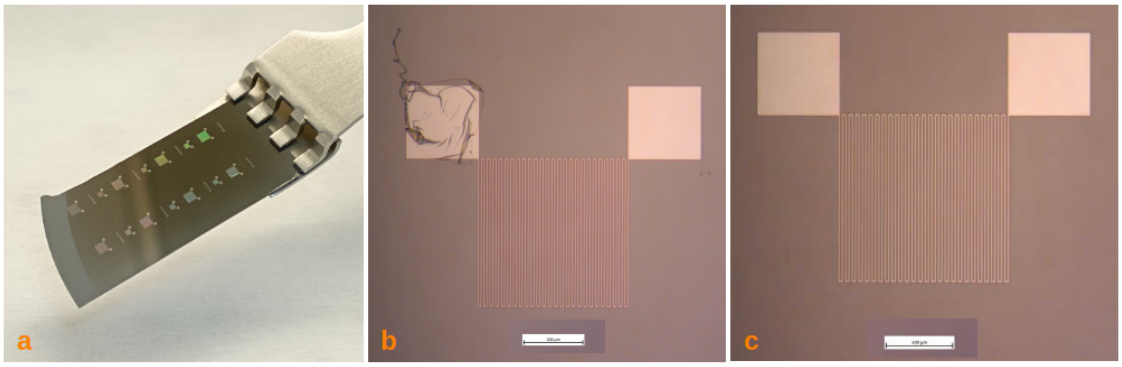

Figure A.1: *a*: example of 14 niobium meanders produced on a unique silicon wafer following the steps described in this section; *b*: magnification of one of the meanders. On the left pad, we can clearly seen traces of photoresist after the cleaning with a suitable solvent. They can be removed exposing the sample to a plasma O_2 etching; *c*: example of meander perfectly cleaned.

When the full steps will be optimized, we will be ready to produce and test in a cryogenic detector our first MMCs characterized by a simple geometry including the contact pads and superconducting heat switch (figure A.2 *a*).

A.1.2 Step two: insulation layers

- A thin photoresist coating is once again uniformly distributed spinning the wafer. Bond pads and connection areas to the second niobium layer must be protected from the insulation layer. They will be exposed to the UV light (or laser writer). Thereafter, the photoresist unexposed is removed with a specific solvent.

- The niobium structures must be electrically isolated from the subsequent metallic layers. According to the Kirchhoff Institute of Physics (KIP) Heidelberg procedure [136], the next step would be the oxidation of the niobium layer by anodization: the sample should be put in a solution of ethylene glycol ($C_2H_6O_2$), water and ammonium pentaborate ($NH_4B_5O_8$) in a ratio of 25:19:4 and the first niobium layer

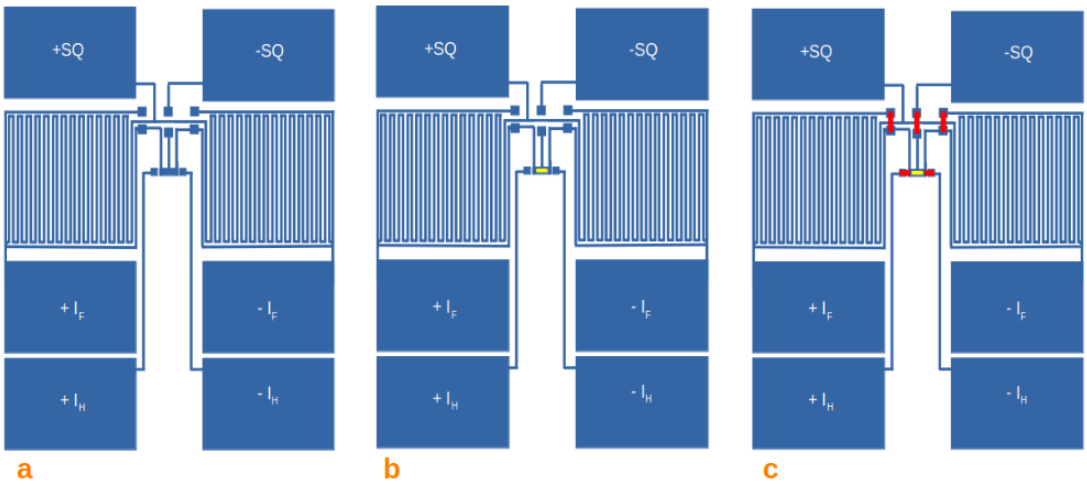

Figure A.2: Simplified geometry planned to be used for the first series of "homemade" MMCs, inspired by the Kirchhoff Institute of Physics (KIP) Heidelberg. *a*: step one. In blue the first niobium layer; *b*: step three. In yellow the heater; *c*: step four. In red the second niobium layer.

should be kept at a positive potential of 25 V (compared to a reference electrode). Following this recipe, a 50 nm thick Nb_2O_5 layer should be created. Unfortunately, at C2N there is no possibility to make the niobium anodization, therefore an alternative solution was investigated. The technique we are currently considering is the deposition of 50 nm thick Al_2O_3 via Atomic Layer Deposition (ADL)[3] technique to ensure uniformity of the dielectric layer, followed by 250 nm thick SiO_2 layer.

- Then, pads and connection parts protected by the photoresist are opened with the lift-off technique.

A.1.3 Subsequent steps

Step three: superconducting heat switch

From this step, just a general idea of the production steps is reported: all the layers described must be present but the techniques could vary and the dimensions must still be decided.

- The sample is once again coated with a photoresist layer and the heater area is

[3]https://piment.c2n.universite-paris-saclay.fr/en/equipement-piment/99/

defined by laser lithography.

- The heater element of the MMC (element in yellow in figure A.2 *b*) currently used to consists of an AuPd film. We do not have the possibility to use this alloy in the machines at our disposal. Therefore, we will try to deposit a 100-200 nm thick palladium layer via sputtering.

Step four: the second niobium layer

- The wafer is covered by the photoresist coating, exposed to the laser writing lithography and cleaned.
- Thereafter, the second niobium layer is sputtered (elements in red in figure A.2 *c*).
- The remaining photoresist is removed via lift-off process.

Step five: SiO_2 insulation of the niobium layer

- A new photoresist coating is uniformly distributed onto the wafer surface. Then, it is once again exposed to the laser lithography to protect the contact pads and some connection areas.
- A SiO_2 layer is deposited via sputtering onto the wafer surface.
- Contact pads and connections areas protected by the photoresist are opened with the lift-off technique.

Step six: gold electroplating

- The photoresist coating is distributed on the wafer which undergoes the lithography.
- A first thin (~ 2 nm) sticking niobium layer is evaporated.
- A gold layer of few μm thickness is created via electroplating.
- The photoresist is then removed by lift-off technique. The MMC sample is finally ready.

In conclusion, we are still at an early stage but we are confident that we will be able to produce our own MMCs and test the first prototypes very soon.

Appendix B

Micro-fabrication nuggets: an overview of the main methods

In the following chapter, I summarize the main micro-fabrication methods fundamental for MMC production and on which I was trained by the C2N experts.

B.1 Clean Room

In micro-fabrication, the reproducibility o a device is fundamental. Therefore, a high-quality clean room is essential. We can summarize the main contamination problems that we can meet as:

- **Dust particles**. During a deposition, the dust particles present in the air can settle on the substrate surface. If the micro-fabricated structures have a size of the order of these particles, they can be responsible for a change of dimensions or an interruption of a part of the device, causing a failure. These defects if present can be observed immediately after the fabrication by a microscopical inspection;
- **Traces of chemicals**. Chemicals are used during different phases of micro-fabrication. If the chemical is not removed leaving traces, it can provoke etching or deposition effects;
- **Metallic Ion Contaminants (MICs)**. Ion impurities in micro-fabricated circuits can have a severe impact on the electrical properties of the device. In particular, MICs are impurities present in most chemicals normally used during the

fabrication process. If not enough pure chemical is used, these impurities can be embedded and migrate into the sensitive areas. They affect the device in terms of performance and reliability since problems can appear a long time after the production.

For these reasons, it is fundamental to realize nano and micro-fabrications in suitable[1] clean rooms. Every clean room has a rigid dressing protocol since people are a major source of contamination in the clean room: a person can generate 100000-1 million particles/min (skin flakes, hair, oils, and perspiration) in addition to millions of particles produced by clothes. A such clean environment is possible thanks to a continuous laminar flow from the ceiling (where high-efficiency particulate arrest (HEPA) filters are present) to the floor. Moreover, individual workstations equipped with HEPA filters and vertical laminar flows are provided for the manipulation of wafers.
In addition to the air purity monitoring, in a clean room, there is also a severe control of:

- temperature, important for the reproducibility of chemical processes;
- humidity, it can affect some processes such as the adherence of a photoresist;

B.2 Physical vapor deposition (PVD)

The primary applications of PVD technology are the deposition of metal lines, pads, and contacts that are present on a silicon wafer surface. In this section, the two main PVD techniques are showed

B.2.1 Vacuum (or thermal) evaporation

The vacuum evaporation is performed by exposing a target substrate to the desired material vapor. This technique can be used to evaporate metals and dielectric materials.

This result is not achievable just by heating up the material source. We have 3 factors to take into account [196]:

[1]The clean rooms are classified in classes according to the amount and size of aerosols floating in the room. The lower the class number, the higher the quality of the clean room. Usually, clean rooms devoted to micro-fabrication are classified as class 10.

- **vapour creation**: starting from a solid source, the vapour flux Φ_e is described by the Hertz-Knudsen equation:

$$\Phi_e = \frac{1}{A_e} \cdot \frac{dN}{dt} = \frac{\alpha \cdot N_A \cdot (P_V - P)}{\sqrt{2\pi \cdot M \cdot R \cdot T}} \tag{B.1}$$

where A_e is the metal source area, N the number of gas molecules, α the sticking coefficient (it is a value between 0 and 1, i.e. the ideal case), N_A is the Avogadro constant, P_V the vapor pressure of the source material, P the reactor pressure, M the molar mass, R the gas constant and T the temperature.

The maximum evaporation rate is achievable by heating up the source in a vacuum chamber where $P \sim 0\,\text{Pa}$ while P_V increases with T, and the probability of residual gas contamination is reduced. There are two techniques used to heat up the material source:

  - by electron beam (figure B.1 *a*): an emitter produces an electron whose path is controlled by a magnetic field produced by an anode to hit and heat uniformly the metal source until this latter melts in the crucible;
  - by a resistive heater (figure B.1 *b*): the source is placed in a crucible made of high-temperature resistant material that is surrounded by tungsten coils in which a current flows;

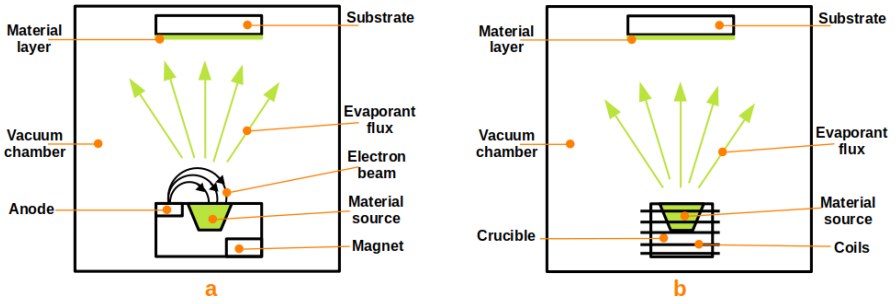

Figure B.1: Schematic drawing of PVD machines based on electron beam gun (*a*) and resistive heater (*b*).

- **vapor flux towards the substrate**: the evaporation is possible when the atoms of the source gain enough energy to beat the binding energy and become gaseous.

Leaving the source, they travel along straight lines until they strike a surface (the substrate or the walls of the vacuum chamber) condensing there and creating a thin layer. It has a very directional flux from the source to the substrate. The mean free path λ of the evaporated atoms is defined by:

$$\lambda = \frac{\eta}{p} \cdot \sqrt{\frac{\pi \cdot RT}{2M}} \tag{B.2}$$

where η is the gas viscosity, P the reactor pressure, R the gas constant, T the temperature and M the molar mass. This technique has a risk of shadow formation that is responsible for a less smooth film morphology.

- **condensation on the surface**: because of the directionality of the evaporant flux, if the substrate presents 3D structures this technique has two drawbacks: a not uniform evaporated layer and a shadow effect that prevents the deposition of the evaporant. To avoid these problems, the most modern vacuum evaporators are provided with rotating planetary systems that allow the repositioning of the substrates during the evaporation process.

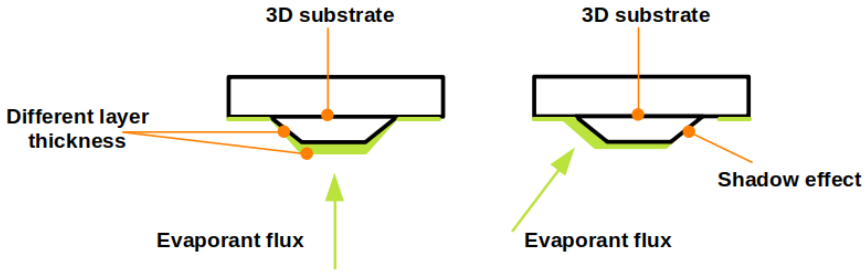

Figure B.2: Schematic representation of the not uniform evaporation (*left*) and the shadow effect (*right*).

B.2.1.1 The lift-off technique (lithography + vacuum evaporation)

This technique is particularly useful when we need to work with materials difficult to etch. The procedure itself requires a few seconds according to the involved material and dimensions. Figure B.3 is schematically representing the lift-off process:

- the substrate is covered with a photoresist that is patterned with lithography and

development. The material source emits the evaporant depositing onto the surfaces of photoresist and exposed substrate a layer (figure B.3 *a*);

- then, the sample is immersed into a solvent. Note that the photoresist is designed to leave branches through which the solvent can penetrate attacking it from the uncovered areas and removing it (figure B.3 *b*);
- Finally, the substrate is rinsed first with the solvent to eliminate some photoresist residuals and then with ultra-pure water. At the end, just the material pattern remains (figure B.3 *c*).

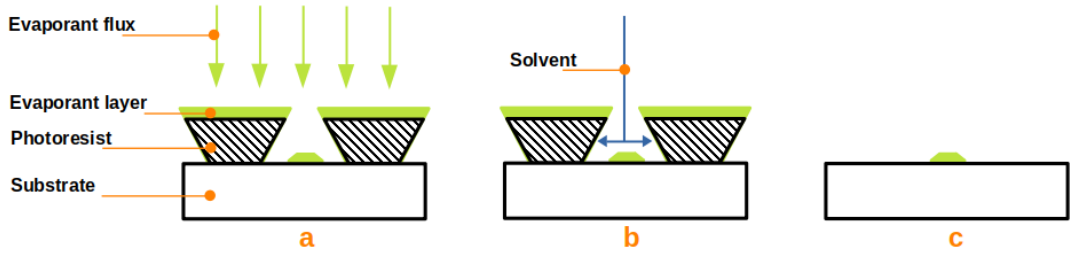

Figure B.3: Schematic representation of the lift-off process. Details in the text.

B.2.1.2 Stencil lithography technique

This technique is particularly useful in case we need to create very fragile structures. A stencil consisting of a thin membrane is positioned at close vicinity of the substrate surface (figure B.4 *a*). The material is deposited with the vacuum evaporation technique onto the stencil and the exposed areas of the substrate (figure B.4 *b*). Removing mechanically the stencil, we have instantaneously the micro-structured pattern without using any chemical process figure B.4 *c*.

B.2.2 Sputtering

The sputtering technique allows the creation of very thin films characterized by good adhesion and excellent coverage of micro-structures [197]. The working principle of the sputtering technique is the physical removal of target atoms via ion bombardment and delivering them to the substrate surface.

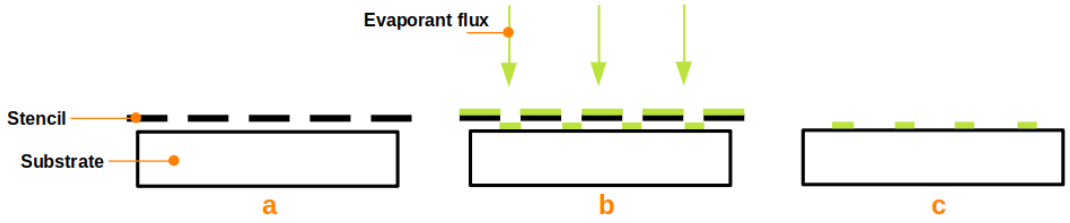

Figure B.4: Schematic representation of the stencil lithography. Details are reported in the text.

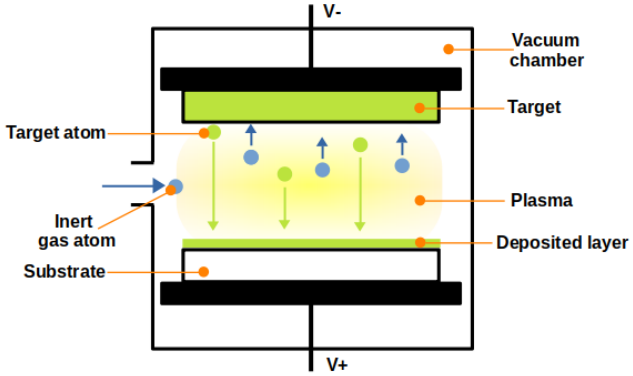

Figure B.5: Schematic representation of the sputtering. The distance between the two electrodes is rather small (typically ∼15 cm).

In figure B.5, a schematic representation of the sputtering machine is shown. It consists of a vacuum chamber equipped with electrodes: when the air is pumped out, the chamber is filled with an inert gas (usually argon) until the pressure reaches the order of 10 to 100 mTorr. Then, a high voltage, defined according to the Paschen's law, is applied between two electrodes, causing the gas breakdown and creating plasma[2] [198]: an avalanche of electrons and ions globally neutral. The Paschen's law, defining

[2]At low bias, the current we can measure is the background ionization, i.e. gas atoms ionized by photons coming from the environment and their corresponding free electrons. When the voltage is drastically increased (∼1 kV), electrons and ions responsible for the background ionization gain sufficient energy to ionize other gas atoms. Therefore, for a given voltage we are increasing the current exponentially, reaching the so-called *dark discharge* regime: the plasma is still not ready to be used since unstable and not enough energetic. When the bias is further increased, the gas breakdown happens (*glow discharge* regime). The ions hitting the cathode cause the ejection of secondary electrons that are responsible for the plasma survival.

the breakdown voltage V_B necessary to enter the glow discharge regime, is reported in equation B.3, where P is the vacuum chamber pressure, d the distance between the electrodes, γ_{2e} is the secondary electron emission coefficient, A and B are constants.

$$V_B = \frac{B \cdot P \cdot d}{ln(A \cdot P \cdot d) - ln\left(ln\left(1 + \frac{1}{\gamma_{2e}}\right)\right)} \tag{B.3}$$

Therefore, the gas ions are accelerated towards the cathode and they hit the target which is made of the material chosen for layer deposition. Impacting, target material atoms are ejected and, crossing the plasma, they settle onto the substrate surface creating a thin layer.

In DC sputtering, the plasma is created by applying a DC bias voltage between the electrodes. In these configurations, the anode usually is grounded.

Despite the simplicity of this system (figure B.6 *a*), there are a couple of drawbacks that we need to take into account dealing with it:

- we can deposit only conductive materials. On the contrary, if we decide to deposit an insulating material, the ions will hit and charge the target, stopping the self-sustainment of the plasma;
- this configuration needs an additional cooling system for the substrate because the plasma electrons, under the repulsive force of the cathode, will hit and heat up the substrate.

B.2.2.1 RF sputtering

The RF sputtering differs from the DC sputtering in the plasma generation, applying a high-frequency RF voltage between the electrodes (figure B.6 *b*). This technique offers some advantages compared to DC sputtering:

- insulating films deposition: since the sign of the voltage applied at the electrodes is alternated, positive and negative charges will be periodically deposited onto the target that will globally result neutral (as long as frequencies higher than 5 MHz are applied[3]);

[3] At lower frequencies than 50 kHz, the charges accumulated during one period are enough to charge the target and stop the plasma. At lower frequencies than 5 MHz, the ions will not be sufficiently accelerated to provoke the target atoms ejection

- higher deposition rates;
- lower power consumption.

The main drawback of depositing insulating materials is the necessity of additional cooling systems for both the target and the substrate.

B.2.2.2 Magnetron sputtering

The magnetron sputtering takes advantage of the magnetic field generated by a magnet that is located behind the cathode. The magnetic field allows the confinement of the electron close to the cathode, increasing their interaction rate with argon atoms and therefore the ionization efficiency. As a consequence, we can apply lower voltages obtaining a higher purity deposition. Moreover, being the electrons confined, their probability to hit the substrate heating is reduced: we don't need anymore a substrate cooling system.

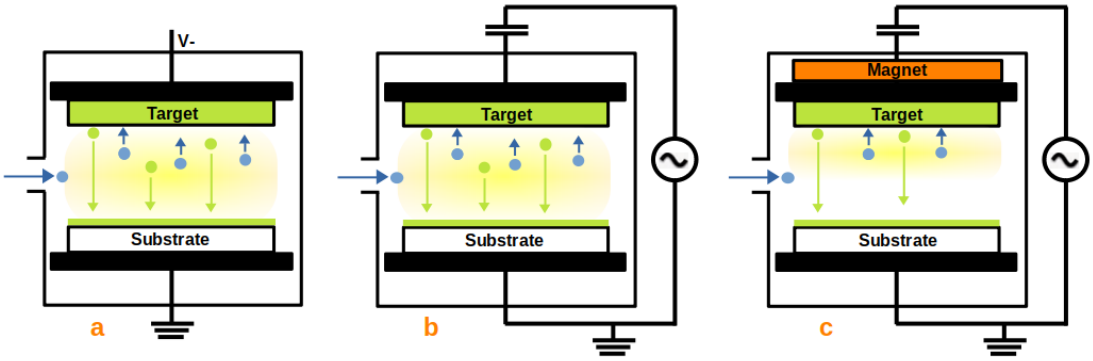

Figure B.6: Schematic representation of the three sputtering systems: DC sputtering (a), RF sputtering (b) and magnetron sputtering (c).

B.2.3 Stress in thin films

Before and after deposition, it is important to verify the stress in the sample. We can identify two stress categories:

- **intrinsic stress**: it is complex to evaluate since it depends on many factors, such as the material and microstructure of the film, the technique adopted for the

deposition, and set parameters. It is not uniform over the thickness of the film and can be reduced by annealing;

- **extrinsic stress**: the film and the substrate on which the film is thin film is deposited are characterized by a different thermal expansion coefficient. In other words, underwent at the same temperature variation (for example during the cooling down subsequent to the PVD process), they can expand or contract differently generating a tensile or compressor stress that could be responsible for the deformation of the sample (figure B.2.3).

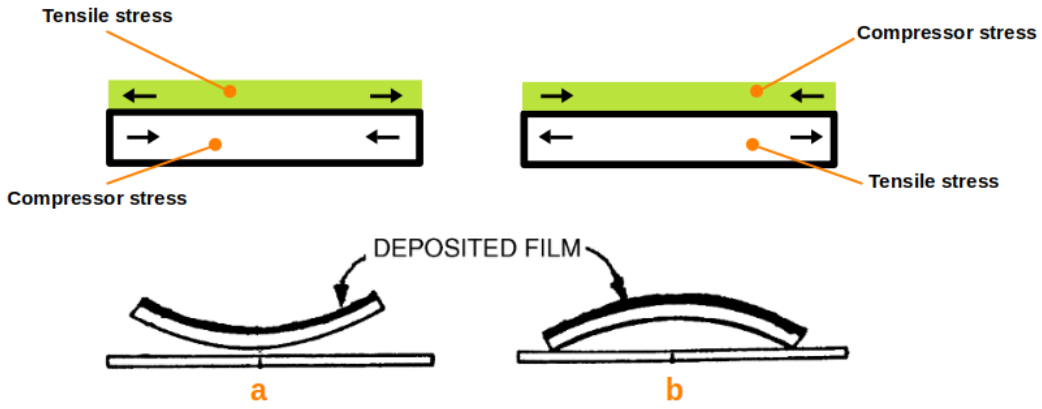

Figure B.7: Examples of stress cases that can occur. The thin film, initially hot, is deposited onto a cold substrate. It adheres well the surface but, cooling down at room temperature. However, because of the different thermal expansion coefficients of the two materials, the film experiences a tensile stress while the substrate a compressor stress (a) or vice versa (b). In the first case, the tensile stress generates a concave bending of the film that lead to cracks [197]. In the second case, the compressor stress causes a convex bending of the film that could lead to buckling.

Thus, it is important to measure the radius of curvature of the sample before and after the film deposition with a mechanical profilometer: knowing the thickness of the substrate and the film, the stress in the thin film through can be estimated through the Stoney equation:

$$\sigma_f = \frac{E_s}{6 \cdot (1 - \nu_s)} \cdot \frac{t_s^2}{t_f} \cdot \left(\frac{1}{r_{sf}} - \frac{1}{r_s} \right) \tag{B.4}$$

where E_f is the film Young's modulus[4], ν_f the Poisson ratio[5] of the film, t_s and t_f the thickness of the substrate and the film respectively, r_s is the curvature radius of the sample before the film deposition and $r_s f$ is the curvature radius of the sample after the deposition.

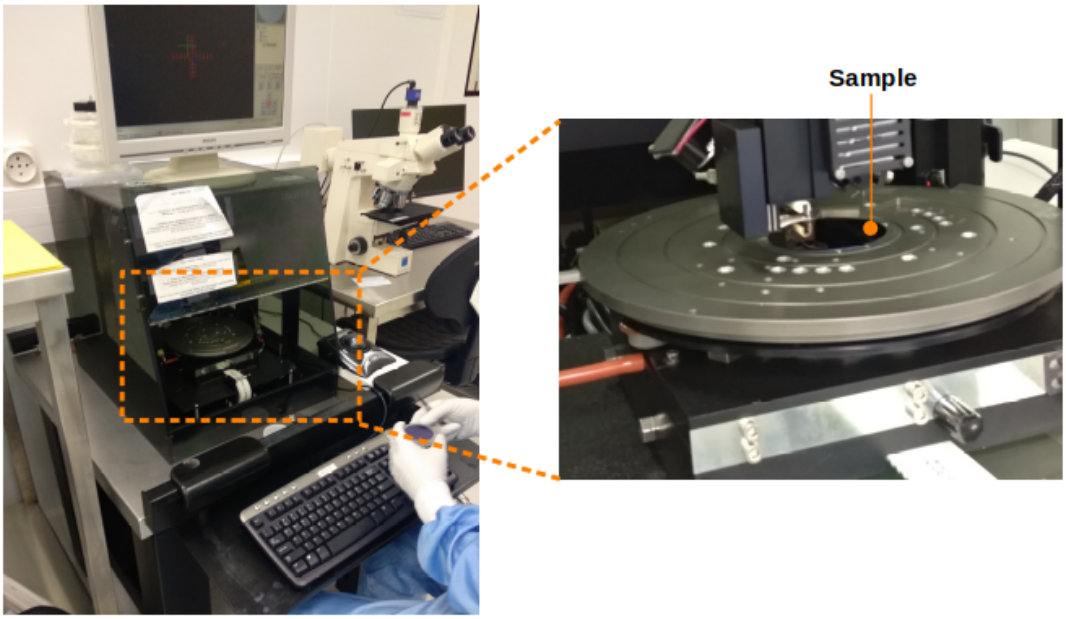

Figure B.8: Mechanical profilometer used for the stress evaluation. A sensitive stylus run along a two dimensional cross section of the surface (*inset*), measuring the parameters necessary for the stress evaluation.

B.3 Lithography

This technique allows the transfer of the desired pattern from the design to a film thanks to the combination of a radiation-sensitive layer, so-colled *photoresist*, and radiation. The lithography process can be summarize the following steps:

- preparation of the substrate;
- resist coating;

[4]It is the ratio of the stress applied to the material and the strain, both measured along the longitudinal axis of the sample.

[5]It represents the degree of transversal deformation in presence of longitudinal monodirectional stress

- exposure to radiation;
- developer bath;
- stripping process (after the etching or lift-off).

B.3.1 Photoresist coating

Once the sample (i.e. substrate + thin film to be patterned) is cleaned to eliminate any dust particles that could create defects in the device, a selected photoresist is dispensed onto the sample which is held in a resist spinner by a vacuum chuck. The high-speed spinning (1500-8000 rpm, depending on viscosity and desired thickness) which it undergoes, allows the deposition of a well-controlled and uniform thickness of photoresist and, thanks to the centrifugal force, eliminates the excess quantities. Then, the sample is heated at ∼75-100°C to remove any residual solvents in the photoresist, and stress and to improve the adherence of the new layer to the sample. Depending on the writing area, we can choose a positive or negative resist :

- positive resist: it is made of a base resin, a photosensitizer compound, and an organic solvent. When it is exposed to radiation, the existing chemical bonds of the resist are broken. The exposed regions are more soluble, and therefore can be removed easily in the developer step (figure B.9, *left*).
- negative resist: it is made of polymers combined with a photosensitizer compound. When it is exposed to the radiation, the resist is polymerized creating new chemical bonds (*cross-link*). The new cross-linked polymer has a higher molecular weight which makes it less soluble: the pattern created is the inverse of the exposed areas (figure B.9, *right*).

Besides the pattern polarity we need, the photoresistor is firstly selected according to the required lithography resolution that is determined by the intrinsic sensitivity[6] of the photoresist.

B.3.2 Lithography techniques

We have two main approaches to making lithography. The first one is the laser writing where the area to be exposed is scanned with a laser. The time required for this first

[6]It is the required incident energy so that the photochemical reaction could occur

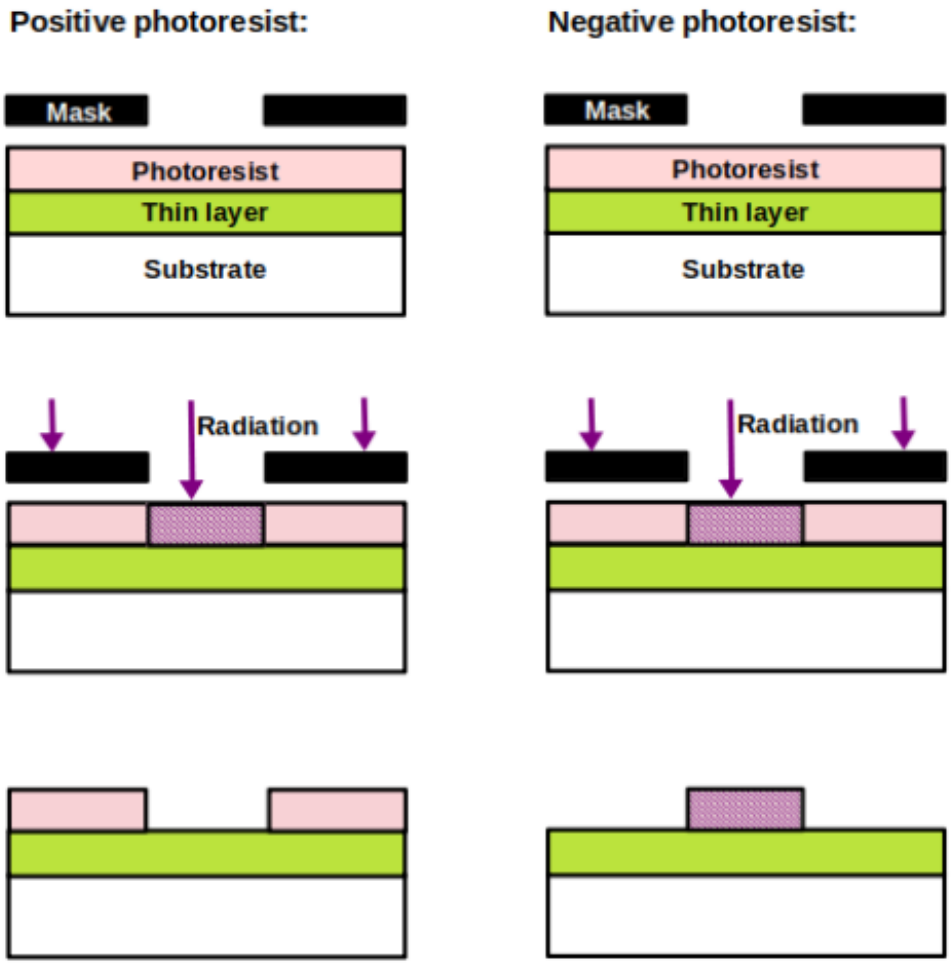

Figure B.9: Different behavior of a positive (*left* and negative (*right*)) photoresist exposed to radiation. At the bottom, the result after development.

technique depends on the surface area to be exposed and the dose necessary to chemically modify the photoresist to obtain the desired resolution. The process could require a few minutes as many hours. For these reasons, it is mainly used for prototyping and photomask production. The second one consists in exposing the sample to the radiation through a photomask. This process requires a few seconds and allows the production of many elements at the same time.

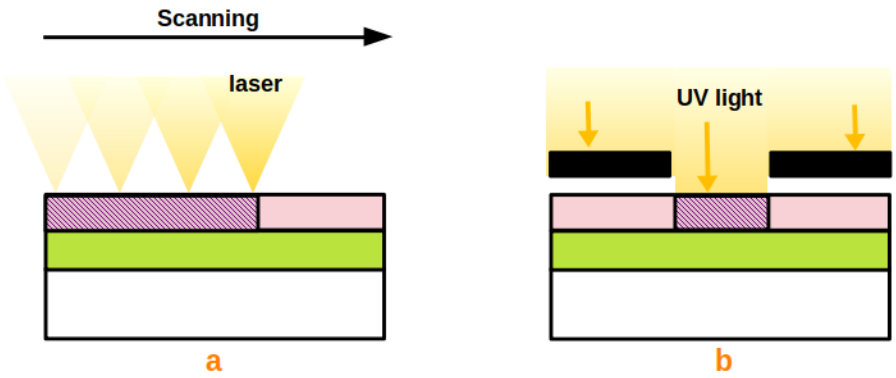

Figure B.10: Schematic representation of laser writing lithography (a) and UV lithography (b).

B.3.3 Laser writing lithography

A laser writer is composed of a laser light source and a complex system of optics in charge to shape the beam before reaching the sample to be treated. The desired pattern, saved in a CAD file, is uploaded to the laser writer software. Surface areas are progressively exposed in series to the laser light whose intensity can be tuned also during the writing phase (figure B.10 a). This feature allows the so-called *grey-scale lithography*, namely the fabrication of 3D structures that otherwise would be impossible to produce by planar exposition to the radiation (for example, the UV lithography). Laser writers are equipped with different lens write head magnifications that can be exchanged to adapt the surface writing to the required resolution; the typical resolution of this technique is 600-800 nm.

B.3.4 Optical lithography

It is the most used lithography technique in micro-fabrication since it allows to pattern large wafers with μm scale structures in a few seconds. The UV lithography is based on the usage of photomasks: thick quartz coated with a thin opaque chromium pattern. The radiation will be blocked in correspondence with the chromium drawing a pattern on the unshielded photoresist (figure B.10 b). A mask aligner correctly locates the wafer to the mask. Distance between mask and wafer, exposure intensity, and dose are tuned. The optical lithography can be based on three different kinds of exposure systems [199]:

- **contact exposure** (figure B.11 *a*): no gap between mask and photoresist. The advantage is a very good resolution (∼1μm) but the price to pay is the damage of the mask or the wafer over time and the risk of mask contamination. The Minimum Features Size (MFS) estimated for contact exposure is defined as:

$$MFS = \sqrt{d \cdot \lambda} \tag{B.5}$$

where λ is the light wavelength and d is the thickness of the photoresist;

- **proximity exposure** (figure B.11 *b*): well controlled gap g of order few μm between mask and photoresist. Compared to the contact exposure, we lose resolution (∼5-10 μm) but we don't have damage or contamination problems. Therefore, the MFS estimated becomes:

$$MFS \approx \sqrt{(d+g) \cdot \lambda} \tag{B.6}$$

- **projection lithography** (figure B.11 *c*): the mask is held by a stage above a projection lens which focuses the patterns accurately onto a wafer placed on a wafer stage: there is no contact between the two, hence there is no risk of contamination or mask damage. However, the optical magnification system on which it is based allows to reach a high-resolution (below 20 nm), that's why they are very expensive machines. The drawback is that the water can't be entirely exposed at once, but we need to repeat the exposure several times. The resolution depends on the wavelength λ, the numerical aperture NA, and the resist process conditions k_1 (equation B.7)

$$R = k_1 \cdot \frac{\lambda}{NA} \tag{B.7}$$

Besides the R, in optical lithography, another important parameter is the Depth Of Focus (DOF). Indeed, since the resist has a non-zero thickness, we need a large DOF to obtain a sharp pattern through the entire resist thickness. The DOF is determined by the numerical aperture NA, the wavelength λ, and technological properties k_2 such as the specific lithography system and photoresist process (equation B.8).

$$DOF = k_2 \frac{\lambda}{(NA)^2} \tag{B.8}$$

The only way to optimize R and DOF at the same time is to optimize the parameters k_1 and k_2.

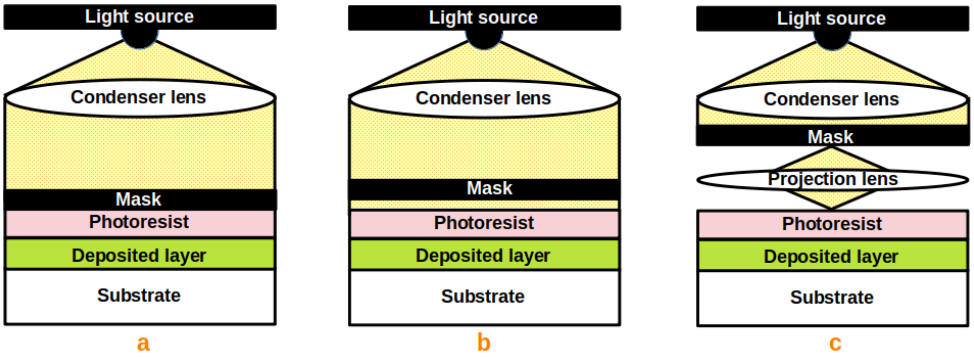

Figure B.11: Schematic representation of the three basic types of exposures: contact (a), proximity (b) and projection (c).

B.3.4.1 Photomask fabrication

As already mentioned, a photomask is thick quartz coated with a pattern made of a thin layer of opaque chromium. The radiation will be blocked in correspondence with the chromium drawing a pattern on the unshielded photoresist. In order to produce it, we have several steps to follow:

- the quartz substrate is covered with a thin ($<\mu$m) positive photoresist;
- the sample is exposed to the laser writer radiation that draws the desired pattern onto the photoresist surface;
- the sample is treated with the developer showing the drawn pattern;
- the sample is therefore etched to transfer the pattern to the chromium layer;
- the remaining photoresist now can be removed with solvent. The mask is ready to be used for UV lithography.

B.3.5 E-beam lithography

The e-beam lithography was created with the intention to overcome the optical diffraction limit ($\sim \lambda/2$) typical of optical lithography. where h is the Planck's constant, m is the electron mass, and v is the electron velocity. The electrons are extracted from an electron gun through the thermionic effect or field electron emission and accelerated in the vacuum chamber towards a system of lenses, blankers, and deflectors in charge to

correct eventual aberrations and focus the beam into a few nm order. The wafer to treat is placed on an alignment stage controlled by optical interferometers, in diametrically opposite positions with respect to the radiation source. As the photons, we can be derive the wavelength for the electrons as well thanks to the De Broglie equation:

$$\lambda = \frac{h}{mv} \tag{B.9}$$

In the e-beam lithography, the resolution is not limited by wave properties but by other effects (spin focusing, charging...). An important factor that influences the resolution is the electrons scattering: high-energy electrons penetrating a solid material will interact with its atoms and electrons. In particular, because of the inelastic scattering, the electrons can transfer part of their energy to the electrons of the material, generating a chain reaction that chemically modify the photoresist in the areas adjacent to the exposure (*proximity effect*). This effect can be corrected with three methods: dose correction, pattern size compensation, and background exposure compensation. However, with this technique, we can reach MFS values below the 20 nm. As a drawback, this technique requires more time (thus, it is more expensive) compared to the optical one since this machine uses a single electron beam to write.

B.4 Dry etching: Reactive Ion Etching

The dry etching is a procedure in which the material surface is physically removed layer by layer in correspondence of the areas that are not locally protected by the photoresist layer [200]. There are several dry techniques to achieve this result; to name a few, we have reactive ion etching, deep reactive ion etching, ion sputtering etching, reactive gas etching, laser micromachining, electrodischarge micromachining, etc. For the MMC production, we are mainly interested in reactive ion etching (RIE). The RIE happens in plasma. Let's assume that the substrate to treat is silicon. A typical gas used to etch is the carbon tetrafluoride (CF_4), an inert gas that becomes highly reactive at the plasma state. This state of the matter can be reached by applying a high voltage that is responsible for the ionization of the gas molecules, hence the production of radicals and electrons (reaction B.10).

$$CF_4 + e^- \rightarrow CF_3^+ + F + 2e_- \tag{B.10}$$

The fluorine atoms interact with the wafer atoms creating a new volatile compound with the silicon, the SiF_4, that is eliminated by the vacuum system (reaction B.11).

$$Si + 4F+ \rightarrow SiF_4 \tag{B.11}$$

Besides the reaction B.10, an electron interaction can also produce a neutral specie through the reaction B.12 which is reactive and leads to B.11 as well.

$$CF_4 + e^- \rightarrow CF_3 + F + e_- \tag{B.12}$$

At the same time, the CF_3 radicals can be absorbed by the wafer surface and then recombined with the fluorine forming CF_4 molecules again.

Since in the MMC production we need to etch until the silicon layer, we are interested in the reactions B.10 and B.12. But RIE can be used also with other gasses obtaining different effects. For example, using C_4F_8 gas we can deposit a fluorocarbon polymer chain onto the wafer surface. The result is the passivation of the film. If we select argon gas, the Ar^+ ions are accelerated towards the sample, and, hitting its surface, they physically remove silicon atoms generating an anisotropy in the etching. The photoresist mask, exposed to the same impacts, will be consumed limiting the etching extended over time.

Bibliography

[1] G. Angloher et al. "Exploring CEvNS with NUCLEUS at the Chooz nuclear power plant". In: *The European Physical Journal C* 79.12 (Dec. 2019), p. 1018. ISSN: 1434-6044. DOI: 10.1140/epjc/s10052-019-7454-4. arXiv: arXiv:1905.10258v1. URL: http://link.springer.com/10.1140/epjc/s10052-019-7454-4.

[2] Riccardo Cerulli. *Shielding power of the cryogenic oyer veto*. July 2020.

[3] Wolf Pauli. *Pauli letter collection: letter to Meitner*. 1932.

[4] Edoardo Amaldi. "From the discovery of the neutron to the discovery of nuclear fission". In: *Physics Reports* 111.1 (1984), pp. 1–331. ISSN: 0370-1573. DOI: https://doi.org/10.1016/0370-1573(84)90214-X. URL: https://www.sciencedirect.com/science/article/pii/037015738490214X.

[5] Enrico Fermi. "An attempt to a β rays theory basic assumptions of the theory". In: *Il nuovo cimento* 1 (1934), pp. 1–17. URL: https://virgilio.mib.infn.it/~zanotti/FNSN/FNSN_files/FNSN/Beta-decay/Fermi-beta-decay-1934.pdf.

[6] F. Reines and C. L. Cowan. "Detection of the free neutrino". In: *Physical Review* 92.3 (1953), pp. 830–831. ISSN: 0031899X. DOI: 10.1103/PhysRev.92.830.

[7] B. T. Cleveland et al. "Update on the measurement of the solar neutrino flux with the Homestake chlorine detector". In: *Nuclear Physics B (Proceedings Supplements)* 38.1-3 (1995), pp. 47–53. ISSN: 09205632. DOI: 10.1016/0920-5632(94)00732-B.

[8] R. Davis. "Solar neutrinos. II. Experimental". In: *Phys. Rev. Lett.* 12.11 (1964), pp. 303–305. DOI: https://doi.org/10.1103/PhysRevLett.12.303.

[9] John N Bahcall. "The solar-neutrino problem". In: *Scientific American* May (1990), pp. 54–61. URL: https://www.scientificamerican.com/magazine/sa/1990/05-01/.

[10] Peter A. Sturrock and Mark A. Weber. "Comparative analysis of GALLEX-GNO solar neutrino data and SOHO / MDI helioseismology data: Further evidence for rotational modulation of the solar neutrino flux". In: *Astrophys. J.* 565 (2002), pp. 1366–1375. DOI: 10.1086/323220. arXiv: astro-ph/0103154.

[11] J. Abdurashitov et al. "Solar neutrino flux measurements by the Soviet-American gallium experiment (SAGE) for half the 22-year solar cycle". In: *Journal of Experimental and Theoretical Physics* 95 (Jan. 2002), pp. 181–193. DOI: 10.1134/1.1506424.

[12] K. S. Hirata et al. "Search for day / night and semiannual variations in the solar neutrino flux observed in the Kamiokande-II detector". In: *Phys. Rev. Lett.* 66 (1991), pp. 9–12. DOI: 10.1103/PhysRevLett.66.9.

[13] D. Waller for the SNO Collaboration. "Recent results from the Sudbury Neutrino Observatory". In: *European Physical Journal C* 33 (2004), s823–s825. ISSN: 14346052. DOI: 10.1140/epjcd/s2003-03-908-3.

[14] D. R. Artusa et al. "Exploring the neutrinoless double beta decay in the inverted neutrino hierarchy with bolometric detectors". In: *European Physical Journal C* 74.10 (2014), pp. 1–19. ISSN: 14346052. DOI: 10.1140/epjc/s10052-014-3096-8. arXiv: 1404.4469.

[15] E. Majorana. "Teoria simmetrica dell'elettrone e del positrone". In: *Ettore Majorana Scientific Papers: On occasion of the centenary of his birth* (2006), pp. 201–233. DOI: 10.1007/978-3-540-48095-2_10.

[16] David Griffiths. *Introduction to Elementary Particles*. 1987. DOI: 10.1002/9783527618460.

[17] F. J. Hasert et al. "Observation of neutrino-like interactions without muon or electron in the Gargamelle neutrino experiment". In: *Physics Letters B* 46.1 (1973), pp. 138–140. ISSN: 03702693. DOI: 10.1016/0370-2693(73)90499-1.

[18] Daniel Z. Freedman. "Coherent effects of a weak neutral current". In: *Physical Review D* 9.5 (1974), pp. 1389–1392. ISSN: 05562821. DOI: 10.1103/PhysRevD.9.1389.

[19] D. Akimov et al. "Observation of coherent elastic neutrino-nucleus scattering". In: *Science* 357.6356 (2017). ISSN: 10959203. DOI: 10.1126/science.aao0990.

[20] A. Drukier and L. Stodolsky. "Principles and applications of a neutral-current detector for neutrino physics and astronomy". In: *Physical Review D* 30.11 (1984), pp. 2295–2309. ISSN: 05562821. DOI: 10.1103/PhysRevD.30.2295.

[21] D. Freedman. "The weak neutral current and its effects in stellar collapse". In: *Annu. Rev. Nucl. Sci.* 27 (1977), pp. 167–207. DOI: 10.1146/annurev.ns.27.120177.001123.

[22] R. Strauss et al. "Gram-scale cryogenic calorimeters for rare-event searches". In: *Physical Review D* 96.2 (2017), pp. 2–8. ISSN: 24700029. DOI: 10.1103/PhysRevD.96.022009. arXiv: 1704.04317.

[23] Julien Billard, Joseph Johnston, and Bradley J. Kavanagh. "Prospects for exploring New Physics in Coherent Elastic Neutrino-Nucleus Scattering". In: *JCAP* 11 (2018), p. 016. DOI: 10.1088/1475-7516/2018/11/016. arXiv: 1805.01798 [hep-ph].

[24] M. Aker. "Direct neutrino-mass measurement with sub-electronvolt sensitivity". In: *Nature Physics* 18.2 (2022), pp. 160–166. DOI: 10.1038/s41567-021-01463-1.

[25] Mark W. Goodman and Edward Witten. "Detectability of certain dark-matter candidates". In: *Physical Review D* 31.12 (1985), pp. 3059–3063. ISSN: 05562821. DOI: 10.1103/PhysRevD.31.3059.

[26] Manfred Lindner, Branimir Radovčić, and Johannes Welter. "Revisiting large neutrino magnetic moments". In: *Journal of High Energy Physics* 2017.7 (2017), pp. 1–12. ISSN: 10298479. DOI: 10.1007/JHEP07(2017)139. arXiv: 1706.02555.

[27] R.L Workman. "Review of Particle Physics". In: *Particle Data Group* (2022).

[28] C. Giunti and W. Kim. *Neutrino Physics and Astrophysics*. Oxford University Press, 2007. ISBN: 9780198508717. DOI: DOI:10.1093/acprof:oso/9780198508717.001.0001.

[29] B. C. Cañas et al. “Future perspectives for a weak mixing angle measurement in coherent elastic neutrino nucleus scattering experiments”. In: *Physics Letters, Section B: Nuclear, Elementary Particle and High-Energy Physics* 784 (2018), pp. 159–162. DOI: 10.1016/j.physletb.2018.07.049. arXiv: 1806.01310. URL: https://doi.org/10.1016/j.physletb.2018.07.049.

[30] M. Cadeddu et al. “New insights into nuclear physics and weak mixing angle using electroweak probes”. In: *Phys. Rev. C* 104.6 (2021), p. 065502. DOI: 10.1103/PhysRevC.104.065502. arXiv: 2102.06153 [hep-ph].

[31] B. C. Canas et al. “The weak mixing angle from low energy neutrino measurements: a global update”. In: *Phys. Lett. B* 761 (2016), pp. 450–455. DOI: 10.1016/j.physletb.2016.08.047. arXiv: 1608.02671 [hep-ph].

[32] M. Cadeddu et al. “Average CsI neutron density distribution from COHERENT data”. In: *Phys. Rev. Lett.* 120.7 (2018), p. 072501. DOI: 10.1103/PhysRevLett.120.072501. arXiv: 1710.02730 [hep-ph].

[33] C. G. Payne et al. “Coherent elastic neutrino-nucleus scattering on ^{40}Ar from first principles”. In: *Phys. Rev. C* 100.6 (2019), p. 061304. DOI: 10.1103/PhysRevC.100.061304. arXiv: 1908.09739 [nucl-th].

[34] M. B. Tsang et al. “Constraints on the symmetry energy and neutron skins from experiments and theory”. In: *Phys. Rev. C* 86 (2012), p. 015803. DOI: 10.1103/PhysRevC.86.015803. arXiv: 1204.0466 [nucl-ex].

[35] P. -G. Reinhard and W. Nazarewicz. “Information content of a new observable: The case of the nuclear neutron skin”. In: *Phys. Rev. C* 81 (2010), p. 051303. DOI: 10.1103/PhysRevC.81.051303. arXiv: 1002.4140 [nucl-th].

[36] G. Hagen et al. “Neutron and weak-charge distributions of the ^{48}Ca nucleus”. In: *Nature Phys.* 12.2 (2015), pp. 186–190. DOI: 10.1038/nphys3529. arXiv: 1509.07169 [nucl-th].

[37] C. Giunti. “General COHERENT constraints on neutrino nonstandard interactions”. In: *Phys. Rev. D* 101.3 (2020), p. 035039. DOI: 10.1103/PhysRevD.101.035039. arXiv: 1909.00466 [hep-ph].

[38] J. Barranco, O. G. Miranda, and T. I. Rashba. “Probing new physics with coherent neutrino scattering off nuclei”. In: *JHEP* 12 (2005), p. 021. DOI: 10.1088/1126-6708/2005/12/021. arXiv: hep-ph/0508299.

[39] Takaaki Kajita. "Nobel Lecture: Discovery of atmospheric neutrino oscillations". In: *Reviews of Modern Physics* 88.3 (2016), pp. 1–7. ISSN: 15390756. DOI: 10.1103/RevModPhys.88.030501.

[40] T. S. Kosmas et al. "Probing light sterile neutrino signatures at reactor and Spallation Neutron Source neutrino experiments". In: *Phys. Rev. D* 96.6 (2017), p. 063013. DOI: 10.1103/PhysRevD.96.063013. arXiv: 1703.00054 [hep-ph].

[41] J. D. Vergados, H. Ejiri, and F. Šimkovic. "Theory of neutrinoless double-beta decay". In: *Reports on Progress in Physics* 75.10 (2012). ISSN: 00344885. DOI: 10.1088/0034-4885/75/10/106301. arXiv: 1205.0649.

[42] Wei Liao, Xiao-Hong Wu, and Hang Zhou. "Electron events from the scattering with solar neutrinos in the search of keV scale sterile neutrino dark matter". In: *Phys. Rev. D* 89.9 (2014), p. 093017. DOI: 10.1103/PhysRevD.89.093017. arXiv: 1311.6075 [hep-ph].

[43] Alexey Konovalov. "COHERENT at SNS and CsI[Na] effort update". In: *Magnificent CEvNS* (2020). URL: https://indico.cern.ch/event/943069/contributions/4066385/attachments/2143819/3612953/M7s_Konovalov%20(1).pdf.

[44] D. Baxter et al. "Coherent elastic neutrino-nucleus scattering at the European Spallation Source". In: *Journal of High Energy Physics* 2020.2, 123 (Feb. 2020), p. 123. DOI: 10.1007/JHEP02(2020)123. arXiv: 1911.00762.

[45] Kate Scholberg. "Prospects for measuring coherent neutrino-nucleus elastic scattering at a stopped-pion neutrino source". In: *Phys. Rev. D* 73 (2006), p. 033005. DOI: 10.1103/PhysRevD.73.033005. arXiv: hep-ex/0511042.

[46] Patrick Huber. "On the determination of anti-neutrino spectra from nuclear reactors". In: *Phys. Rev. C* 84 (2011), p. 024617. DOI: 10.1103/PhysRevC.85.029901. arXiv: 1106.0687 [hep-ph].

[47] J. Billard et al. "Coherent Neutrino Scattering with Low Temperature Bolometers at Chooz Reactor Complex". In: *J. Phys. G* 44.10 (2017), p. 105101. DOI: 10.1088/1361-6471/aa83d0. arXiv: 1612.09035 [physics.ins-det].

[48] B. R. Davis et al. "Reactor anti-neutrino spectra and their application to anti-neutrino induced reactions". In: *Phys. Rev. C* 19 (1979), pp. 2259–2266. DOI: 10.1103/PhysRevC.19.2259.

[49] Michel Spiro and Daniel Vignaud. "Neutrino physics and astrophysics". In: *Nucl. Phys. A* 654.1-2 (1999). Ed. by B. Frois, D. Goutte, and D. Guillemaud-Mueller, pp. C350–C372. DOI: 10.1016/S0375-9474(99)00263-8.

[50] Aldo Ianni. "Solar neutrinos". In: *Prog. Part. Nucl. Phys.* 94 (2017), pp. 257–281. DOI: 10.1016/j.ppnp.2017.01.001.

[51] G Bellini et al. "Geo-neutrinos". In: *Progress in Particle and Nuclear Physics* 73 (2013), pp. 1–34. ISSN: 0146-6410. DOI: https://doi.org/10.1016/j.ppnp.2013.07.001. URL: https://www.sciencedirect.com/science/article/pii/S0146641013000732.

[52] A Bellerive et al. "The Sudbury Neutrino Observatory". In: *Nuclear Physics B* 908 (2016), pp. 30–51. ISSN: 0550-3213. DOI: 10.1016/j.nuclphysb.2016.04.035. URL: http://dx.doi.org/10.1016/j.nuclphysb.2016.04.035.

[53] M. Agostini et al. "Comprehensive geoneutrino analysis with Borexino". In: *Phys. Rev. D* 101.1 (2020), p. 012009. DOI: 10.1103/PhysRevD.101.012009. arXiv: 1909.02257 [hep-ex].

[54] Daniel Pershey. "New results from the COHERENT CsI[Na] Detector". In: *Beam Physics with a Booster Accumulator Ring BAR* (2020). URL: https://theory.fnal.gov/events/event/new-results-from-coherent-2/.

[55] D. Akimov et al. "First Measurement of Coherent Elastic Neutrino-Nucleus Scattering on Argon". In: *Phys. Rev. Lett.* 126.1 (2021), p. 012002. DOI: 10.1103/PhysRevLett.126.012002. arXiv: 2003.10630 [nucl-ex].

[56] C. Buck et al. "A novel experiment for coherent elastic neutrino nucleus scattering: CONUS". In: *Journal of Physics: Conference Series* 1342.1 (2020), pp. 6–11. ISSN: 17426596. DOI: 10.1088/1742-6596/1342/1/012094.

[57] G. Heusser. "Low-radioactivity background techniques". In: *Ann. Rev. Nucl. Part. Sci.* 45 (1995), pp. 543–590. DOI: 10.1146/annurev.ns.45.120195.002551.

[58] G. Heusser et al. "GIOVE: a new detector setup for high sensitivity germanium spectroscopy at shallow depth". In: *European Physical Journal C* 75.11 (2015), pp. 1–16. ISSN: 14346052. DOI: 10.1140/epjc/s10052-015-3704-2. arXiv: 1507.03319.

[59] H. Bonet et al. "Constraints on Elastic Neutrino Nucleus Scattering in the Fully Coherent Regime from the CONUS Experiment". In: *Physical Review Letters* 126.4 (2021), p. 41804. ISSN: 10797114. DOI: 10.1103/PhysRevLett.126.041804. arXiv: 2011.00210. URL: https://doi.org/10.1103/PhysRevLett.126.041804.

[60] H. Bonet et al. "Novel constraints on neutrino physics beyond the standard model from the CONUS experiment". In: *JHEP* 05 (2022), p. 085. DOI: 10.1007/JHEP05(2022)085. arXiv: 2110.02174 [hep-ph].

[61] C. Augier et al. "Ricochet Progress and Status". In: *19th International Workshop on Low Temperature Detectors*. Nov. 2021. arXiv: 2111.06745 [physics.ins-det].

[62] Enectali Figueroa-Feliciano. "Ricochet Progress and Status". In: *Magnificent CEvNS 2021* (2021). URL: https://indico.cern.ch/event/1075677/contributions/4544711/attachments/2324471/3958967/Figueroa%20Magnificent%20CEvNS%202021.pdf.

[63] Henry T. Wong. "Coherent neutrino-nucleus elastic scattering with reactor and solar neutrinos". In: *Neutrino 2018 - 28th International Conference on Neutrino Physics and Astrophysics, Conference Proceedings* June (2018).

[64] H. T. Wong et al. "Search of neutrino magnetic moments with a high-purity germanium detector at the Kuo-Sheng nuclear power station". In: *Physical Review D - Particles, Fields, Gravitation and Cosmology* 75.1 (2007), pp. 1–16. ISSN: 15507998. DOI: 10.1103/PhysRevD.75.012001. arXiv: 0605006 [hep-ex].

[65] A K Soma et al. "Characterization and performance of germanium detectors with sub-keV sensitivities for neutrino and dark matter experiments". In: *Nuclear Instruments and Methods in Physics Research A* 836 (2016), pp. 67–82. DOI: 10.1016/j.nima.2016.08.044.

[66] M. Deniz et al. "Measurement of $\bar{\nu}_e$-electron scattering cross section with a CsI(Tl) scintillating crystal array at the Kuo-Sheng nuclear power reactor". In: *Physical Review D - Particles, Fields, Gravitation and Cosmology* 81.7 (2010). ISSN: 15507998. DOI: 10.1103/PhysRevD.81.072001. arXiv: 0911.1597.

[67] Henry Tsz-King Wong. "Taiwan EXperiment On NeutrinO — History and Prospects". In: *The Universe* 3.4 (2015), pp. 22–37. DOI: 10.1142/S0217751X18300144. arXiv: 1608.00306 [hep-ex].

[68] G. Agnolet et al. “Background Studies for the MINER Coherent Neutrino Scattering Reactor Experiment”. In: *Nucl. Instrum. Meth. A* 853 (2017), pp. 53–60. DOI: 10.1016/j.nima.2017.02.024. arXiv: 1609.02066 [physics.ins-det].

[69] Adam Anderson. “Phonon-based position determination in SuperCDMS iZIP detectors”. In: *Journal of Low Temperature Physics* 176.5-6 (2014), pp. 959–965. ISSN: 15737357. DOI: 10.1007/s10909-013-1015-2.

[70] P. Adari et al. “Descriptions of rising low-energy spectra”. In: *EXCESS workshop* January (2022), pp. 1–44. arXiv: 2202.05097. URL: http://arxiv.org/abs/2202.05097.

[71] Bhaskar Dutta et al. “Sensitivity to oscillation with a sterile fourth generation neutrino from ultra-low threshold neutrino-nucleus coherent scattering”. In: *Phys. Rev. D* 94.9 (2016), p. 093002. DOI: 10.1103/PhysRevD.94.093002. arXiv: 1511.02834 [hep-ph].

[72] Alexis Aguilar-Arevalo et al. “Exploring low-energy neutrino physics with the Coherent Neutrino Nucleus Interaction Experiment”. In: *Phys. Rev. D* 100.9 (2019), p. 092005. DOI: 10.1103/PhysRevD.100.092005. arXiv: 1906.02200 [physics.ins-det].

[73] Alexis Aguilar-Arevalo et al. “Search for light mediators in the low-energy data of the CONNIE reactor neutrino experiment”. In: *Journal of High Energy Physics* 2020.4 (2020). ISSN: 10298479. DOI: 10.1007/JHEP04(2020)054. arXiv: 1910.04951.

[74] Javier Tiffenberg et al. “Single-electron and single-photon sensitivity with a silicon Skipper CCD”. In: *Phys. Rev. Lett.* 119.13 (2017), p. 131802. DOI: 10.1103/PhysRevLett.119.131802. arXiv: 1706.00028 [physics.ins-det].

[75] Liron Barak et al. “SENSEI: Direct-Detection Results on sub-GeV Dark Matter from a New Skipper-CCD”. In: *Phys. Rev. Lett.* 125.17 (2020), p. 171802. DOI: 10.1103/PhysRevLett.125.171802. arXiv: 2004.11378 [astro-ph.CO].

[76] Brenda Aurea and Cervantes Vergara. “The CONNIE experiment : latest results and upgrade”. In: *Magnificent CEνNS* (2021). URL: https://indico.cern.ch/event/1075677/contributions/4556661/attachments/2323744/3957553/BrendaCervantes_CONNIE_M7s2021.pdf.

[77] Chris Hagmann and Adam Bernstein. "Two-phase emission detector for measuring coherent neutrino-nucleus scattering". In: *IEEE Trans. Nucl. Sci.* 51 (2004). Ed. by J. D. Valentine, pp. 2151–2155. DOI: 10.1109/TNS.2004.836061. arXiv: nucl-ex/0411004.

[78] B. A. Dolgoshein, V. N. Lebedenko, and B. U. Rodionov. "New Method of Registration of Ionizing-particle Tracks in Condensed Matter". In: *ZhETF Pisma Redaktsiiu* 11 (June 1970), p. 513.

[79] RED-100 Collaboration. "Status of the RED-100 experiment". In: *Magnificent CEνNS* (2021).

[80] D. Yu Akimov et al. "First ground-level laboratory test of the two-phase xenon emission detector RED-100". In: *JINST* 15.02 (2020), P02020. DOI: 10.1088/1748-0221/15/02/P02020. arXiv: 1910.06190 [physics.ins-det].

[81] V. Belov et al. "The νGeN experiment at the Kalinin Nuclear Power Plant". In: *JINST* 10.12 (2015), P12011. DOI: 10.1088/1748-0221/10/12/P12011.

[82] I Alekseev et al. "First results of the ν GeN experiment on coherent elastic neutrino-nucleus scattering". In: *arXiv e-prints* (2022), pp. 1–6. arXiv: arXiv:2205.04305v2.

[83] D. Akimov et al. "The COHERENT Experimental Program". In: *2022 Snowmass Summer Study*. Apr. 2022. arXiv: 2204.04575 [hep-ex].

[84] J. Colas et al. "Development of data processing and analysis pipeline for the RICOCHET experiment". In: (Nov. 2021). arXiv: 2111.12856 [physics.ins-det].

[85] A. Aguilar-Arevalo et al. "The CONNIE experiment". In: *Journal of Physics: Conference Series* 761.1 (2016). ISSN: 17426596. DOI: 10.1088/1742-6596/761/1/012057. arXiv: 1608.01565.

[86] D.Y. Akimov et al. "Status of the RED-100 experiment". In: *Journal of Instrumentation* 12.06 (2017), pp. C06018–C06018. DOI: 10.1088/1748-0221/12/06/c06018.

[87] R. Strauss et al. "The ν -cleus experiment: a gram-scale fiducial-volume cryogenic detector for the first detection of coherent neutrino–nucleus scattering". In: *European Physical Journal C* 77.8 (2017), pp. 1–14. ISSN: 14346052. DOI: 10.1140/epjc/s10052-017-5068-2. arXiv: 1704.04320.

[88] P. Debye. "Zur Theorie der spezifischen Warmen". In: *Annalen der Physik* 344 (1911), pp. 789–839. DOI: 10.1002/andp.19123441404.

[89] Frank Pobell. *Matter and Methods at Low Temperatures*. 2007. ISBN: 9783540463566. DOI: 10.1007/978-3-540-46360-3.

[90] Charles Kittel. *Introduction to Solid State Physics*. 8th ed. Wiley, 2004, p. 704.

[91] L. Hehn et al. "Improved EDELWEISS-III sensitivity for low-mass WIMPs using a profile likelihood approach". In: *European Physical Journal C* 76.10 (2016). ISSN: 14346052. DOI: 10.1140/epjc/s10052-016-4388-y. arXiv: 1607.03367.

[92] R Agnese et al. "Nuclear-recoil energy scale in CDMS II silicon dark-matter detectors". In: *Nuclear Instruments and Methods in Physics Research Section A: Accelerators, Spectrometers, Detectors and Associated Equipment* 905 (2018), pp. 71–81. ISSN: 0168-9002. DOI: https://doi.org/10.1016/j.nima.2018.07.028. URL: https://www.sciencedirect.com/science/article/pii/S0168900218308568.

[93] HyangKyu Park. "The AMoRE: Search for Neutrinoless Double Beta Decay in 100 Mo". In: *Nucl. Part. Phys. Proc.* 273-275 (2016). Ed. by M Aguilar-Benìtez et al., pp. 2630–2632. DOI: 10.1016/j.nuclphysbps.2015.10.012.

[94] G. Angloher et al. "Results on light dark matter particles with a low-threshold CRESST-II detector". In: *European Physical Journal C* 76.1 (2016), pp. 1–8. ISSN: 14346052. DOI: 10.1140/epjc/s10052-016-3877-3. arXiv: 1509.01515.

[95] G. Angloher et al. "The COSINUS project: perspectives of a NaI scintillating calorimeter for dark matter search". In: *European Physical Journal C* 76.8 (2016), pp. 1–6. ISSN: 14346052. DOI: 10.1140/epjc/s10052-016-4278-3. arXiv: 1603.02214.

[96] Denys Poda and Andrea Giuliani. "Low background techniques in bolometers for double-beta decay search". In: *International Journal of Modern Physics A* 32.30 (2017). ISSN: 0217751X. DOI: 10.1142/S0217751X17430126. arXiv: 1711.01075.

[97] Luis Gonzalez-Mestres. "Large, real time detectors for solar neutrinos and magnetic monopoles". In: *LAPP-EXP-89-16* (Jan. 1989), pp. 55–61. URL: https://inis.iaea.org/collection/NCLCollectionStore/_Public/22/052/22052194.pdf.

[98] C Bobin et al. "Alpha/gamma discrimination with a CaF2(Eu) target bolometer optically coupled to a composite infrared bolometer". In: *Nuclear Instruments and Methods in Physics Research Section A: Accelerators, Spectrometers, Detectors and Associated Equipment* 386.2 (1997), pp. 453–457. ISSN: 0168-9002. DOI: https://doi.org/10.1016/S0168-9002(96)01185-0. URL: https://www.sciencedirect.com/science/article/pii/S0168900296011850.

[99] J. B. Birks. "Scintillations from Organic Crystals: Specific Fluorescence and Relative Response to Different Radiations". In: *Proc. Phys. Soc. A* 64 (1951), pp. 874–877. DOI: 10.1088/0370-1298/64/10/303.

[100] J.B. Birks. *The Theory and Practice of Scintillation Counting*. Pergamon Press, 1964, p. 664. DOI: 10.1016/c2013-0-01791-4.

[101] L. Gironi. "Development of cryogenic detectors for rare event searches". PhD thesis. Università degli Studi di Milano-Bicocca, 2010. URL: https://cuore.lngs.infn.it/sites/default/files/phd_unimib_033675.pdf.

[102] A. Armatol et al. "Toward CUPID-1T". In: (Mar. 2022). arXiv: 2203.08386 [nucl-ex].

[103] W. R. Armstrong et al. "CUPID pre-CDR". In: (July 2019). arXiv: 1907.09376 [physics.ins-det].

[104] Dounia Lila Helis. "Searching for neutrinoless double-beta decay with scintillating bolometers". PhD thesis. Université Paris-Saclay, 2021. URL: https://tel.archives-ouvertes.fr/tel-03442659/document.

[105] Denys Poda. "Scintillation in Low-Temperature Particle Detectors". In: *MDPI Physics* 3.3 (2021), pp. 473–535. DOI: 10.3390/physics3030032. URL: https://hal.archives-ouvertes.fr/hal-03287559.

[106] Dmitry Yu. Akimov et al. "Coherent elastic neutrino-atomic nucleus scattering — recently discovered type of low-energy neutrino interaction". In: *Uspekhi Fizicheskih Nauk* 189.02 (2019), pp. 173–186. ISSN: 0042-1294. DOI: 10.3367/ufnr.2018.05.038356.

[107] Andrea Giuliani and Alfredo Poves. "Neutrinoless double-beta decay". In: *Advances in High Energy Physics* 2012 (2012). ISSN: 16877357. DOI: 10.1155/2012/857016.

[108] P. Belli et al. “Experimental searches for rare alpha and beta decays”. In: *European Physical Journal A* 55.8 (2019). ISSN: 1434601X. DOI: 10.1140/epja/i2019-12823-2. arXiv: 1908.11458.

[109] Leszek Roszkowski, Enrico Maria Sessolo, and Sebastian Trojanowski. “WIMP dark matter candidates and searches - Current status and future prospects”. In: *Reports on Progress in Physics* 81.6 (2018). ISSN: 00344885. DOI: 10.1088/1361-6633/aab913. arXiv: 1707.06277.

[110] H. Ejiri and S. R. Elliott. “Solar neutrino interactions with the double beta decay nuclei of ^{82}Se, ^{100}Mo and ^{150}Nd”. In: *Phys. Rev. C* 95.5 (2017), p. 055501. DOI: 10.1103/PhysRevC.95.055501. arXiv: 1703.06915 [nucl-ex].

[111] H. Ejiri, J. Engel, and N. Kudomi. “Supernova neutrino studies with Mo-100”. In: *Phys. Lett. B* 530 (2002), pp. 27–32. DOI: 10.1016/S0370-2693(02)01349-7. arXiv: astro-ph/0112379.

[112] K. Zuber. “Spectroscopy of low energy solar neutrinos using CdTe detectors”. In: *Physics Letters, Section B: Nuclear, Elementary Particle and High-Energy Physics* 571.3-4 (2003), pp. 148–154. ISSN: 03702693. DOI: 10.1016/j.physletb.2003.07.070. arXiv: 0206340 [astro-ph].

[113] A. H. Abdelhameed et al. “A new limit on the resonant absorption of solar axions obtained via 169Tm-containing bolometer”. In: *Journal of Physics: Conference Series* 2103.1 (2021), pp. 1–7. ISSN: 17426596. DOI: 10.1088/1742-6596/2103/1/012142. arXiv: arXiv:2004.08121v1.

[114] K. Jakovcic et al. “A Search for solar hadronic axions using ^{83}Kr”. In: *Radiat. Phys. Chem.* 71 (2004). Ed. by Malcolm Cooper and Dudley Creagh, pp. 793–794. DOI: 10.1016/j.radphyschem.2004.04.095. arXiv: nucl-ex/0402016.

[115] M. Krcmar et al. “Search for solar axions using Li-7”. In: *Phys. Rev. D* 64 (2001), p. 115016. DOI: 10.1103/PhysRevD.64.115016. arXiv: hep-ex/0104035.

[116] Shigetaka Moriyama. “Proposal to search for a monochromatic component of solar axions using ^{57}Fe”. In: *Nuclear Physics B - Proceedings Supplements* 72.1-3 (1999), pp. 183–186. ISSN: 09205632. DOI: 10.1016/S0920-5632(98)00522-2. arXiv: 9504318 [hep-ph].

[117] C.W.E Eijk. "Inorganic Scintillators for Thermal Neutron Detection". In: *Radiation Measurements* 59 (Aug. 2004), pp. 337–342. DOI: 10.1016/j.radmeas.2004.02.004.

[118] Zane Bell et al. "Neutron Detection with Cryogenics and Semiconductors". In: *physica status solidi (c)* 2 (Mar. 2005), pp. 1592–1605. DOI: 10.1002/pssc.200460840.

[119] M. Martínez et al. "Scintillating bolometers for fast neutron spectroscopy in rare events searches". In: *Journal of Physics: Conference Series* 375.PART 2 (2012), pp. 8–12. ISSN: 17426596. DOI: 10.1088/1742-6596/375/1/012025.

[120] E. E. Haller et al. "NTD Germanium: A Novel Material for Low Temperature Bolometers". In: *Neutron Transmutation Doping of Semiconductor Materials* (1984), pp. 21–36. DOI: 10.1007/978-1-4613-2695-3_2.

[121] A. Fleischmann et al. "Metallic magnetic calorimeters". In: *AIP Conference Proceedings* 1185 (2009), pp. 571–578. ISSN: 0094243X. DOI: 10.1063/1.3292407.

[122] A. Aliane et al. "Design and fabrication process of silicon micro-calorimeters on simple SOI technology for X-ray spectral imaging". In: *Nuclear Instruments and Methods in Physics Research, Section A: Accelerators, Spectrometers, Detectors and Associated Equipment* 594.2 (2008), pp. 210–214. ISSN: 01689002. DOI: 10.1016/j.nima.2008.06.029.

[123] E. Haller, Kohei Itoh, and Jeffrey Beeman. "Neutron Transmutation Depot (NTD) Germanium Thermistors for Submillimetre Bolometer Applications". In: 388 (Nov. 1996), p. 115.

[124] Masatoshi Imada, Atsushi Fujimori, and Yoshinori Tokura. "Metal-insulator transitions". In: *Rev. Mod. Phys.* 70 (4 Oct. 1998), pp. 1039–1263. DOI: 10.1103/RevModPhys.70.1039. URL: https://link.aps.org/doi/10.1103/RevModPhys.70.1039.

[125] N. F. Mott. "Metal-Insulator Transitions". In: *Pure and Applied Chemistry* 52.1 (1980), pp. 65–72. ISSN: 13653075. DOI: 10.1351/pac198052010065.

[126] D. McCammon. "Semiconductor thermistors". In: *Topics in Applied Physics* 99 (2005), pp. 35–62. ISSN: 03034216. DOI: 10.1007/10933596_2.

[127] Boris I Shklovskii and Alex L Efros. “Variable-Range Hopping Conduction”. In: *Electronic Properties of Doped Semiconductors*. Berlin, Heidelberg: Springer Berlin Heidelberg, 1984, pp. 202–227. ISBN: 978-3-662-02403-4. DOI: 10.1007/978-3-662-02403-4_9. URL: https://doi.org/10.1007/978-3-662-02403-4_9.

[128] A. L. Efros and B. I. Shklovskii. “Coulomb gap and low temperature conductivity of disordered systems”. In: *Journal of Physics C: Solid State Physics* 8.4 (1975). ISSN: 00223719. DOI: 10.1088/0022-3719/8/4/003.

[129] C. Enss, ed. *Cryogenic particle detection*. Vol. 99. Topics in applied physics. Berlin, Germany: Springer, 2005.

[130] M. Bühler and E. Umlauf. “A magnetic bolometer for single-particle detection”. In: *Epl* 5.4 (1988), pp. 297–301. ISSN: 12864854. DOI: 10.1209/0295-5075/5/4/003.

[131] E. Umlauf and M. Bühler. *Development of a Magnetic Calorimeter for Neutrino Detection*. ELSEVIER B.V., 1989, pp. 309–317. DOI: 10.1016/b978-0-444-87414-6.50025-0. URL: http://dx.doi.org/10.1016/B978-0-444-87414-6.50025-0.

[132] C Enss, R E Lanou, and H J Marls. “Metallic magnetic bolometers for particle detection”. In: *J Low Temp Phys* 93 (1993), pp. 709–714.

[133] M. A. Ruderman and C. Kittel. “Indirect exchange coupling of nuclear magnetic moments by conduction electrons”. In: *Physical Review* 96.1 (1954), pp. 99–102. ISSN: 0031899X. DOI: 10.1103/PhysRev.96.99.

[134] A. Fleischmann et al. “Low Temperature Properties of Erbium in Gold”. In: *Journal of Low Temperature Physics* 118.1-2 (2000), pp. 7–21. ISSN: 00222291. DOI: 10.1023/a:1004654401827.

[135] Ch. Enss. *Cryogenic Particle Detection*. Vol. 94. 2003. ISBN: 9783642105050. URL: http://link.springer.com/10.1007/b12169.

[136] Daniel Hengstler. “Development and characterization of two-dimensional metallic magnetic calorimeter arrays for the high-resolution X-ray spectroscopy”. PhD thesis. Ruperto-Carola-University of Heidelberg, Germany, 2017. URL: http://archiv.ub.uni-heidelberg.de/volltextserver/23815/1/Dissertation.pdf.

[137] John Clarke and Alex I. Braginski. *The SQUID Handbook*. Vol. 1. 2005, pp. 1–395. DOI: 10.1002/3527603646.

[138] L. Marini. "The CUORE experiment : from the commissioning to the first 0 $\nu\beta\beta$ limit". PhD thesis. University of Genoa, 2018, p. 184.

[139] C. Alduino et al. "CUORE-0 detector: design, construction and operation". In: *JINST* 11.07 (2016), P07009. DOI: 10.1088/1748-0221/11/07/P07009. arXiv: 1604.05465 [physics.ins-det].

[140] A. Alessandrello et al. "Methods for response stabilization in bolometers for rare decays". In: *Nuclear Instruments and Methods in Physics Research, Section A: Accelerators, Spectrometers, Detectors and Associated Equipment* 412.2-3 (1998), pp. 454–464. ISSN: 01689002. DOI: 10.1016/S0168-9002(98)00458-6.

[141] Éric Aubourg et al. "Measurement of electron-phonon decoupling time in neutron-transmutation doped germanium at 20 mK". In: *Journal of Low Temperature Physics* 93.3-4 (1993), pp. 289–294. ISSN: 00222291. DOI: 10.1007/BF00693435.

[142] A. Alessandrello et al. "Development and optimization of a modular bolometer to search for rare decays". In: *Czechoslovak Journal of Physics* 46.SUPPL. 5 (1996), pp. 2893–2894. ISSN: 00114626. DOI: 10.1007/BF02570433.

[143] Tianzhuo Zhan et al. "Thermal boundary resistance at Si/Ge interfaces by molecular dynamics simulation". In: *AIP Advances* 5.4 (2015). ISSN: 21583226. DOI: 10.1063/1.4916974. URL: http://dx.doi.org/10.1063/1.4916974.

[144] M. Pedretti. "The single module for CUORICINO and CUORE detectors: test, construction and modelling". PhD thesis. University of Insubria, 2004. URL: https://www.roma1.infn.it/exp/cuore/thesis/phd/Pedretti_phd.pdf.

[145] P. Das, R. Bruyn de Ouboter, and K. W. Taconis. "A Realization of a London-Clarke-Mendoza Type Refrigerator". In: *Low Temperature Physics LT9* (1965), pp. 1253–1255. DOI: 10.1007/978-1-4899-6443-4_133.

[146] G. Frossati. "Obtaining ultra-low temperatures by dilution of 3He into 4He". In: *JOURNAL DE PHYSIQUE* 39.8 (1978), pp. C6–1578.

[147] A.T.A.M. De Waele. "Introduction to dilution refrigeration". In: (2009), pp. 1–15. URL: http://cryocourse2011.grenoble.cnrs.fr/IMG/file/Lectures/2011-deWaele-DilFridge.pdf.

[148] A.T.A.M. De Waele. "Basic operation of cryocoolers and related thermal machines". In: *Journal of Low Temperature Physics* 164.5-6 (2011), pp. 179–236. ISSN: 00222291. DOI: 10.1007/s10909-011-0373-x.

[149] Kurt Uhlig. "3He/4He dilution refrigerator with pulse-tube refrigerator precooling". In: *Cryogenics* 42.2 (2002), pp. 73–77. ISSN: 0011-2275. DOI: https://doi.org/10.1016/S0011-2275(02)00002-4. URL: https://www.sciencedirect.com/science/article/pii/S0011227502000024.

[150] John C. Mather. "Bolometer noise: nonequilibrium theory". In: *Applied Optics* 21.6 (1982), p. 1125. ISSN: 0003-6935. DOI: 10.1364/ao.21.001125.

[151] B. Mauri. "Optimization and characterization of TeO2 bolometers for Double Beta Decay with sensitivity to surface events". Master's thesis. University of Milano-Bicocca, 2019.

[152] E. Olivieri et al. "Vibrations on pulse tube based Dry Dilution Refrigerators for low noise measurements". In: *Nuclear Instruments and Methods in Physics Research, Section A: Accelerators, Spectrometers, Detectors and Associated Equipment* 858 (2017), pp. 73–79. ISSN: 01689002. DOI: 10.1016/j.nima.2017.03.045. arXiv: 1703.08957.

[153] R. Maisonobe et al. "Vibration decoupling system for massive bolometers in dry cryostats". In: *Journal of Instrumentation* 13.8 (2018). ISSN: 17480221. DOI: 10.1088/1748-0221/13/08/T08009. arXiv: 1803.03463.

[154] S. Pirro. "Further developments in mechanical decoupling of large thermal detectors". In: *Nuclear Instruments and Methods in Physics Research, Section A: Accelerators, Spectrometers, Detectors and Associated Equipment* 559.2 (2006), pp. 672–674. ISSN: 01689002. DOI: 10.1016/j.nima.2005.12.197.

[155] C. Arnaboldi et al. "CUORE: A cryogenic underground observatory for rare events". In: *Nuclear Instruments and Methods in Physics Research, Section A: Accelerators, Spectrometers, Detectors and Associated Equipment* 518.3 (2004), pp. 775–798. ISSN: 01689002. DOI: 10.1016/j.nima.2003.07.067. arXiv: 0501010 [hep-ex].

[156] H. D. Pinckney et al. "The Thermal Conductance of Sapphire Ball Based Detector Clamps". In: (Nov. 2021). DOI: 10.1007/s10909-022-02777-x. arXiv: 2111.05217 [physics.ins-det].

[157] Michele Mancuso. "Development and optimization of scintillating bolometers and innovative light detectors for a pilot underground experiment on neutrinoless double beta decay". PhD thesis. Université Paris-Saclay, 2016.

[158] E. Gatti and P. F. Manfredi. "Processing the signals from solid-state detectors in elementary-particle physics". In: *La Rivista del Nuovo Cimento* 9.1 (1986), pp. 1–146. ISSN: 0393697X. DOI: 10.1007/BF02822156.

[159] D. M. Chernyak et al. "Rejection of randomly coinciding events in ZnMoO4 scintillating bolometers". In: *European Physical Journal C* 74.6 (2014), pp. 1–6. ISSN: 14346052. DOI: 10.1140/epjc/s10052-014-2913-4.

[160] Hawraa Khalife. "CROSS and CUPID-Mo : future strategies and new results in bolometric search for 0 $\nu\beta\beta$". PhD thesis. université Paris-Saclay, 2021.

[161] Riham Mariam et al. "Determination of L-X ray absolute emission intensities of 238Pu, 244Cm, 237Np and 233Pa radionuclides using a metallic magnetic calorimeter". In: *Spectrochimica Acta - Part B Atomic Spectroscopy* 187.November 2021 (2022). ISSN: 05848547. DOI: 10.1016/j.sab.2021.106331.

[162] V Wagner. "Exploring CEvNS of Reactor Neutrinos with the NUCLEUS Experiment". In: *17th International Conference on Topics in Astroparticle and Underground Physics (TAUP 2021)* (2021). URL: https://indico.ific.uv.es/event/6178/contributions/15578/attachments/9254/12000/NUCLEUS-TAUP-VWagner.pdf.

[163] Johannes Felix Martin Rothe. "Low-Threshold Cryogenic Detectors for Low-Mass Dark Matter Search and Coherent Neutrino Scattering". PhD thesis. Technischen Universität München.

[164] F. Ardellier et al. "Double Chooz: A Search for the neutrino mixing angle θ_{13}". In: (June 2006). arXiv: hep-ex/0606025.

[165] G Heusser. "Low-Radioactivity Background Techniques". In: *Annual Review of Nuclear and Particle Science* 45.1 (1995), pp. 543–590. DOI: 10.1146/annurev.ns.45.120195.002551. URL: https://doi.org/10.1146/annurev.ns.45.120195.002551.

[166] Glenn F. Knoll. *Radiation Detection and Measurement, 3rd ed.* 3rd edition. New York: John Wiley and Sons, 2000. ISBN: 978-0-471-07338-3.

[167] Andreas Erb and Jean Côme Lanfranchi. "Growth of high-purity scintillating CaWO4 single crystals for the low-temperature direct dark matter search experiments CRESST-II and EURECA". In: *CrystEngComm* 15.12 (2013), pp. 2301–2304. ISSN: 14668033. DOI: 10.1039/c2ce26554k.

[168] Joseph A. Formaggio and C. J. Martoff. "Backgrounds to sensitive experiments underground". In: *Annual Review of Nuclear and Particle Science* 54 (2004), pp. 361–412. ISSN: 01638998. DOI: 10.1146/annurev.nucl.54.070103.181248.

[169] G. Boireau et al. "Online monitoring of the Osiris reactor with the Nucifer neutrino detector". In: *Physical Review D* 93.11 (2016), pp. 1–17. ISSN: 24700029. DOI: 10.1103/PhysRevD.93.112006.

[170] C. Aberle et al. "Large scale Gd-beta-diketonate based organic liquid scintillator production for antineutrino detection". In: *Journal of Instrumentation* 7.6 (2012). ISSN: 17480221. DOI: 10.1088/1748-0221/7/06/P06008.

[171] Chloé Goupy. *First estimate of backgrounds at sub-keV energies for the NUCLEUS CEνNS experiment*. June 2022. DOI: 10.5281/zenodo.6767550. URL: https://doi.org/10.5281/zenodo.6767550.

[172] G. Angloher et al. "Results from 730 kg days of the CRESST-II Dark Matter search". In: *European Physical Journal C* 72.4 (2012), pp. 1–22. ISSN: 14346052. DOI: 10.1140/epjc/s10052-012-1971-8. arXiv: 1109.0702.

[173] J. Åström et al. "Fracture processes observed with a cryogenic detector". In: *Physics Letters, Section A: General, Atomic and Solid State Physics* 356.4-5 (2006), pp. 262–266. ISSN: 03759601. DOI: 10.1016/j.physleta.2006.03.059. arXiv: 0504151 [physics].

[174] X. F. Navick, D. L'Hôte, and R. Tourbot. "Ionization measurement at very low temperature for nuclear and electron recoils discrimination by ionization-heat simultaneous measurement for dark matter research". In: *Nuclear Instruments and Methods in Physics Research, Section A: Accelerators, Spectrometers, Detectors and Associated Equipment* 442.1 (2000), pp. 267–274. ISSN: 01689002. DOI: 10.1016/S0168-9002(99)01232-2.

[175] V. Wagner et al. "Development of a compact muon veto for the NUCLEUS experiment". In: (2022). arXiv: 2202.03991. URL: http://arxiv.org/abs/2202.03991.

[176] M Vivier and F Jeanneau. "Nucleus planning and BA timeline". In: *NUCLEUS general meeting* (2022).

[177] A. J. Tavendale and G. T. Ewan. "A high resolution lithium-drift germanium gamma-ray spectrometer". In: *Nuclear Instruments and Methods* 25.C (1963), pp. 185–187. ISSN: 0029554X. DOI: 10.1016/0029-554X(63)90183-6.

[178] G. T. Ewan and A. J. Tavendale. "Application of high resolution lithium-drift germanium gamma-ray spectrometers to high energy gamma-rays". In: *Nuclear Instruments and Methods* 26.C (1964), pp. 183–186. ISSN: 0029554X. DOI: 10.1016/0029-554X(64)90072-2.

[179] R. H. Pehl et al. "Accurate determination of the ionization energy in semiconductor detectors". In: *Nuclear Instruments and Methods* 59.1 (1968), pp. 45–55. ISSN: 0029554X. DOI: 10.1016/0029-554X(68)90342-X.

[180] E. Armengaud et al. "First results of the EDELWEISS-II WIMP search using Ge cryogenic detectors with interleaved electrodes". In: *Phys. Lett. B* 687 (2010), pp. 294–298. DOI: 10.1016/j.physletb.2010.03.057. arXiv: 0912.0805 [astro-ph.CO].

[181] Emeline Queguiner. "Analysis of the data of the EDELWEISS-LT experiment searching for low-mass WIMP". PhD thesis. Université Claude Bernard Lyon 1, 2019. URL: https://tel.archives-ouvertes.fr/tel-02025002/document.

[182] National Instruments. *Device specification NI 6366*. URL: http://imserc.northwestern.edu/downloads/nuled%20usb%206366.pdf.

[183] Paul Horowitz and Winfield Hill. *The art of electronics; 3rd ed.* Cambridge: Cambridge University Press, 2015. URL: https://cds.cern.ch/record/1981307.

[184] A. Broniatowski et al. "A new high-background-rejection dark matter Ge cryogenic detector". In: *Physics Letters, Section B: Nuclear, Elementary Particle and High-Energy Physics* 681.4 (2009), pp. 305–309. ISSN: 03702693. DOI: 10.1016/j.physletb.2009.10.036. arXiv: 0905.0753.

[185] Claudio Arnaboldi et al. "The programmable front-end system for CUORICINO, an array of large-mass bolometers". In: *IEEE Transactions on Nuclear Science* 49 II.5 (2002), pp. 2440–2447. ISSN: 00189499. DOI: 10.1109/TNS.2002.803886.

[186] C. Arnaboldi, X. Liu, and G. Pessina. "The preamplifier for CUORE, an array of large mass bolometers". In: *IEEE Nuclear Science Symposium Conference Record* (2009), pp. 389–395. ISSN: 10957863. DOI: 10.1109/NSSMIC.2009.5401681.

[187] "Space-and-surface charge neutralization of cryogenic Ge detectors using infrared LEDs". In: *AIP Conference Proceedings* 1185 (2009), pp. 310–313. ISSN: 0094243X.

[188] L. Thulliez et al. "Calibration of nuclear recoils at the 100 eV scale using neutron capture". In: (2020), pp. 1–6. eprint: 2011.13803. URL: http://arxiv.org/abs/2011.13803.

[189] Chloé Goupy et al. "COV cylindric crystals". In: *NUCLEUS general meeting* (2022).

[190] F Jeanneau, M Vivier, and E. Mazzucato. "COV Status and Open Issues". In: *NUCLEUS COV meeting* (2022).

[191] A. Aliane et al. "First test of a Li2WO4(Mo) bolometric detector for the measurement of coherent neutrino-nucleus scattering". In: *Nuclear Instruments and Methods in Physics Research, Section A: Accelerators, Spectrometers, Detectors and Associated Equipment* 949.July 2019 (2020), p. 162784. ISSN: 01689002. DOI: 10.1016/j.nima.2019.162784. URL: https://doi.org/10.1016/j.nima.2019.162784.

[192] C. Alduino et al. "CUORE-0 detector: Design, construction and operation". In: *Journal of Instrumentation* 11.7 (2016). ISSN: 17480221. DOI: 10.1088/1748-0221/11/07/P07009.

[193] E. Armengaud et al. "Performance of the EDELWEISS-III experiment for direct dark matter searches". In: *Journal of Instrumentation* 12 (June 2017). DOI: 10.1088/1748-0221/12/08/P08010.

[194] Valentina Novati. "Sensitivity enhancement of the CUORE experiment via the development of Cherenkov hybrid TeO bolometers". PhD thesis. Université Paris-Saclay, 2018. URL: https://tel.archives-ouvertes.fr/tel-01963790.

[195] S.R. Kim. *Poster presentation at 19 Int. Workshop on Low Temp. Detectors (LTD-19)*. July 2021.

[196] Stephen M. Rossnagel. "Physical vapor deposition". In: *Handbook of Semiconductor Manufacturing Technology, Second Edition* (2007), pp. 15–1–15–27. ISSN: 0010-180X. DOI: 10.4011/shikizai1937.68.710.

[197] Mark Jackson. *Micro- and Nanofabrication*. 2005, pp. 1–32. ISBN: 9783662443941. DOI: 10.1201/9781420028270.ch1.

[198] M.J. Madou. *Fundamentals of Microfabrication : The Science of Miniaturization*. 2nd ed. CRC PRESS, 2002. ISBN: ISBN 0-8493-0826-7. URL: https://www.researchgate.net/publication/31755433_Fundamentals_of_Microfabrication_The_Science_of_Miniaturization_MJ_Madou.

[199] Zheng Cui. *Nanofabrication: principles, capabilities and limits*. Springer, 2008. ISBN: 978-0-387-75576-2. DOI: 10.1007/978-0-387-75577-9.

[200] Sami Franssila. *Introduction to Microfabrication*. Wiley Online Library, 2010, pp. 1–518. ISBN: 9781119990413. URL: http://onlinelibrary.wiley.com/book/10.1002/9781119990413.